ATOMIC-SCALE STRUCTURAL CHARACTERIZATIONS OF FUNCTIONAL EPITAXIAL THIN FILMS

A Dissertation

by

YUANYUAN ZHU

Submitted to the Office of Graduate Studies of
Texas A&M University
in partial fulfillment of the requirements for the degree of

DOCTOR OF PHILOSOPHY

Chair of Committee,	Haiyan Wang
Committee Members,	Donald Naugle
	Andreas Holzenburg
	Rusty Harris
Intercollegiate Faculty Chair,	Ibrahim Karaman

August 2013

Major Subject: Materials Science and Engineering

ABSTRACT

A precise understanding of the fundamental correlation between synthesis, microstructure and physical properties is of vital importance towards rational design of improved functional epitaxial thin films. With the presence of heterogeneous interface and associated inhomogeneous lattice strain, film microstructure becomes sensitive to subtle interfacial perturbations and hence may exhibit intriguing physical properties. Control of the epitaxial film functionality requires accurate knowledge of the actual film chemistry, interfacial defects and associated strain field.

This dissertation reports in-depth microstructural characterization of the intrinsic chemical inhomogeneity in selected epitaxial thin films including superconducting $Fe_{1+y}Te_{1-x}Se_x/SrTiO_3$(STO) heterogeneous systems, the flux-pinning defects at both of conversional $YBa_2Cu_3O_{7-\delta}$ (YBCO)/substrate lateral interfaces and vertical interfaces of YBCO&$BaSnO_3$(BSO) nanocomposite films, and the misfit dislocation core configurations of STO/MgO and MgO/STO heterostructures pair, using the state-of-the-art aberration-corrected scanning transmission electron microscopy (C_S-corrected STEM) in combination with geometric phase analysis (GPA).

For the first time, the local atomic arrangement of Te and Se as well as interstitial Fe(2) has been clearly revealed in superconducting $Fe_{1+y}Te_{1-x}Se_x$/STO epitaxial films. We found that the film growth atmosphere can greatly affect the film stoichiometry, the homogeneity of Se/Te ordering and thus the overall film superconductivity.

YBCO/substrate interface mismatch and YBCO&BSO vertical interface contact have been explored through substrate selection and doping-concentration variation. We observed a diverse nature of intrinsic defects in different YBCO/substrate heterosystems; thermal stable defects capable of maintaining individual strain field have been found effective in flux-pinning. Along the vertical heterointerface of YBCO/BSO, misfit dislocations were found throughout the film thickness. It adds another dimension to the flux-pinning landscape design.

Four basic misfit dislocation core configurations of a STO/MgO heterosystem have been identified, and found strongly dependent on the actual interface disordering such as substrate atomic-height steps and interdiffussion. To precisely quantify the heterointerface lattice strain, we first conducted systematic investigations on the accuracy of STEM-based GPA. Follow our protocol, 1 pm accuracy has been proven in the STEM fast-scan direction with a spatial resolution less than 1 nm. The effectiveness and reliability of this optimized GPA strain profile were demonstrated in both applications of a relaxed STO/MgO and a partially strained $LaAlO_3$/STO heterointerfaces, respectively.

You can believe what you see, as long as you understand how you see.

- Severin Amelinckx

ACKNOWLEDGEMENTS

At no time during my graduate career did I consider any accomplishments without the help, guidance and love of those around me. There are many to whom I must show gratitude for their guidance, compassion, professionalism, support and wisdom.

I would like to thank my parents, who raised me to have an inquisitive and stubborn disposition of character. They are awesome in their own way, which is not as easy as it appears. I thank my "sister", Xiaoyu, for reminding me the concept of hometown no matter how far I travel. I thank my friends (you know who you are), for their presence in my life helping keep me sane during the doctoral process.

I thank my advisor, Dr. Haiyan Wang, who is one of the most energetic people and also of the most passionate ones about thin film science and technology I've ever known. I owe her a lot of gratitude for being the best cheerleader when I stuck, and for constantly encouraging me pursuing high quality work and not less. I would like to thank my committee members, Dr. Donald Naugle, Dr. Andreas Holzenburg, Dr. Phillip Hemmer and Dr. Rusty Harris for their supports and great advices guiding me through the doctoral research.

I would like to thank all my colleagues for their teaching, help and fruitful discussions: Dr. Zhenxing Bi, Dr. Joon-Hwan Lee, Dr. Chen-Fong Tsai, Dr. Michelle Myers, Dr. Aiping Chen, Li Chen, Fauzia Khatkhatay, Qing Su, Liang Jiao, Wenrui Zhang, Jie Jian and Clement Jacob. I would like to acknowledge Dr. Zhiping Luo at MIC for significant help with EDX and crystal structure modeling.

I would like to acknowledge Dr. Christian Kisielowski, Dr. Andrew Minor, Dr. Jim Ciston, Dr. Peter Ercius, Dr. Colin Ophus and Chengyu Song at National Center for Electron Microscopy, Lawrence Berkeley National Laboratory for inspiring discussions and collaboration on several research topics.

I would also like to acknowledge funding from the Air force Office of Scientific Research, Department of Energy, and the National Science Foundation. I would like to thank Jan Gerston, Jane Cavlina, Marissa Mancuso, Claudia Samford, John Turner and Doreen Ah Tye for their timely help and support as well.

TABLE OF CONTENTS

Page

LIST OF FIGURES

Page

LIST OF TABLES

Page

CHAPTER I

INTRODUCTION

1.1. Overview

Within materials science and engineering there exists the desire to control a materials composition, crystal structure and defects with atomic precision. The central theme in epitaxy thin film growth is to achieve single-crystal-like quality with desired functionality through interface design. Over the past several decades, epitaxy has become one of the most significant phenomena in modern functional thin film materials science and thin film device technology.

When one crystal is grown epitaxially over another crystal having different lattice parameters, the film crystal accommodates the misfit by elastic strain. Misfit that is not completely accommodated by the elastic strain is relaxed by generating misfit dislocations. The division of misfit between the elastic strain and the misfit dislocations is based on various factors such as the lattice mismatch rate, the thickness of the film and the bonding at the interface. In fact, due to the film-substrate lattice thermal expansion difference and imperfections in substrate crystal such as surface step terrace, interface structures are typically complicated and difficult to control.

The structural property of epitaxial thin films challenges modern microstructural characterization techniques, for it requires evaluations of both film collective crystallographic quality and individual atom deviations at the interface. With advances

of spherical aberration correction in transmission electron microscopy and developments in corresponding digital imaging process techniques, we are entering the era of genuine atomic resolution and precise atomic structure quantification. The expectation is that by faithful characterizing the overall epitaxy quality as well as heterogeneous interface structures at atomic scale, a rational design can be made regarding function.

1.2 Thin film epitaxy

1.2.1 Epitaxy and its advantages

Original from two Greek roots, *epi*, meaning "resting upon" and *taxis* which means "ordered arrangement"; epitaxy refers to an oriented overgrowth. Epitaxial thin films then represent a group of single-crystal-like thin films, grown in a way of following one or two crystallographic orientation of a seed crystalline substrate.[1] On the contrary, if the overlayer either forms a random out-of-plane orientation with respect to the crystalline substrate or does not form an ordered crystal structure, this is called non-epitaxial growth. Fig. 1.1(a) shows an artist's rendition of the initial stage of thin film synthesis process. In epitaxial growth, as illustrated in Fig. 1.1(b), the film ad-atoms are locked into preferred crystallographic sites at the surface of the seed substrate. Although epitaxy wasn't introduced in literature until the pioneer study of the French mineralogist Louis Royer in the 1920s,[2] for many years the phenomenon of epitaxy continued to be the center of scientific interests from fundamental materials science investigation- to practical electronic device engineering.

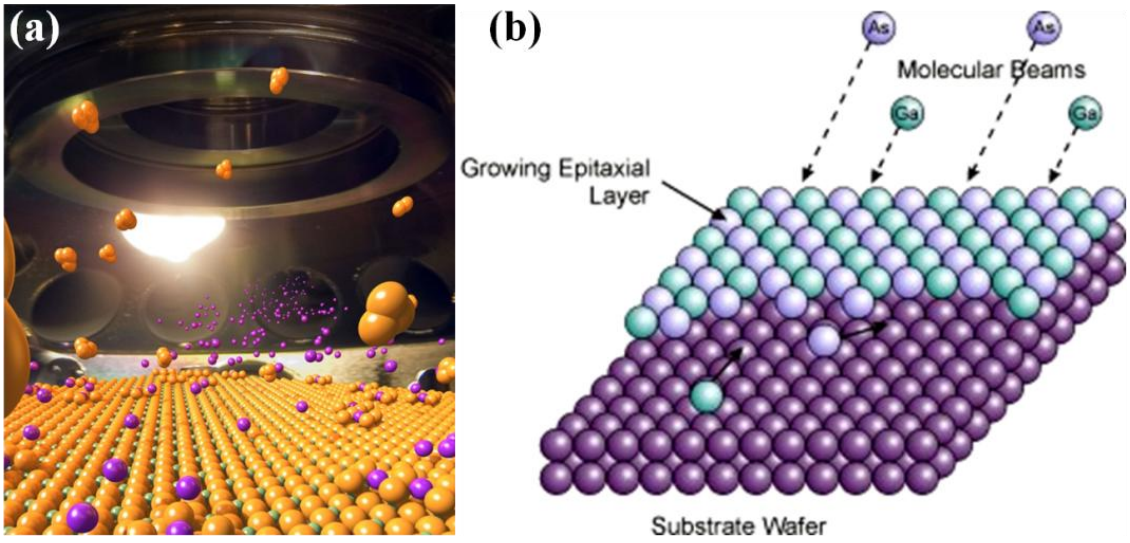

Figure 1.1. Schematic illustrations of (a) the initial stage of thin film growth when ad-atoms start to pile up on single-crystalline substrate surface and (b) the epitaxial layers formed by locking ad-atoms into preferred crystallographic sites at the surface of the substrate.

In general, there are two categories of epitaxial structures. In the case that an add-on thin film shares the same type of material as the substrate, it is called homoepitaxy; otherwise, it is a heteroepitaxy. One typical example of homoepitaxy is the deposition of silicon on silicon wafers as the first step in the fabrication of integrated circuit transistors.[3] This processing step has been proved to lead to a dramatic progress in the yield of early bipolar transistors.[4] Thus, in terms of materials synthesis and optimization, the advantages of epitaxial growth for homogeneous structures are,

(1) To produce films with a higher purification than the substrate;

(2) To fabricate films with tunable doping concentrations;

In the case of heterogeneous systems,

(3) To integrate crystalline layers of different materials;

(4) To create new materials that cannot be grown in the form of equilibrium single crystal.

Heteroepitaxy is the more common phenomenon, since affordable high quality single-crystalline substrates are available in few material systems; and more importantly, heteroepitaxial growth enables new physical properties[5 6] and new phases[7] that cannot be obtained in bulk forms. So the main study subject of this dissertation focuses on the heterogeneous epitaxy.

1.2.2 Heteroepitaxy lattice misfit

At the interface of a heterogeneous system, besides the stoichiometry differences between the heteroepitaxial thin film and its substrate, interface lattice mismatching is essential to film epitaxy quality as well as to the interface structures.[8, 9] To understand the epitaxial relationship and the nature of the interfacial defects, some fundamental concepts in epitaxial thin films are introduced. The epitaxial relationship including crystallographic orientation between the heteroepitaxial layer and the substrate can be predicted based on the argument of lattice fitting. Usually, but not always, the contacting planes and directions that lead to the best lattice fit determine the film-substrate epitaxial relationship. [1]

One of the most important quantities that characterize epitaxy is the lattice misfit rate *f*. It is defined as,

$$f = 2 \times \frac{(a_s - a_f)}{(a_s + a_f)} \tag{1.1}$$

where a_s and a_f refer to the unstrained bulk lattice parameters of the film and the substrate in contact. Based on the value of the lattice misfit *f*, the heterogeneous epitaxy can be generally divided into three types. As shown in Fig. 1.2(a), when *f* is very small, i.e. $a_s \approx a_f$, it is called lattice-matched epitaxy. There is nearly no interfacial-bond straining; and then the heteroepitaxial interface is essentially like that of the homoepitaxy. However, this case is relatively rare. The second type of heteroepitaxy, as shown in Fig. 1.2(b), is the strained lattice-mismatched epitaxy. Although it could be different from one material to another, it has proposed that the lattice misfit *f* in this case is in a range from 1% to 8%,[10] as the film and substrate lattice parameters become substantially different. At the interface, the film layers strain elastically to match the same interatomic spacing as the substrate laterally. Then the thin film in-plane strain is defined as,

$$\varepsilon = \frac{(a_s - a_f)}{a_f} \tag{1.2}$$

where it assumes the strained film lattice is equal to a_s; the " - "sign of ε means the film is in compression and if it is a " + "sign it refers to tension. Such highly strained heteroepitaxy is usually observed in very thin initial film layers that grow pseudomorphically and leads to defect-free coherent heterointerface.

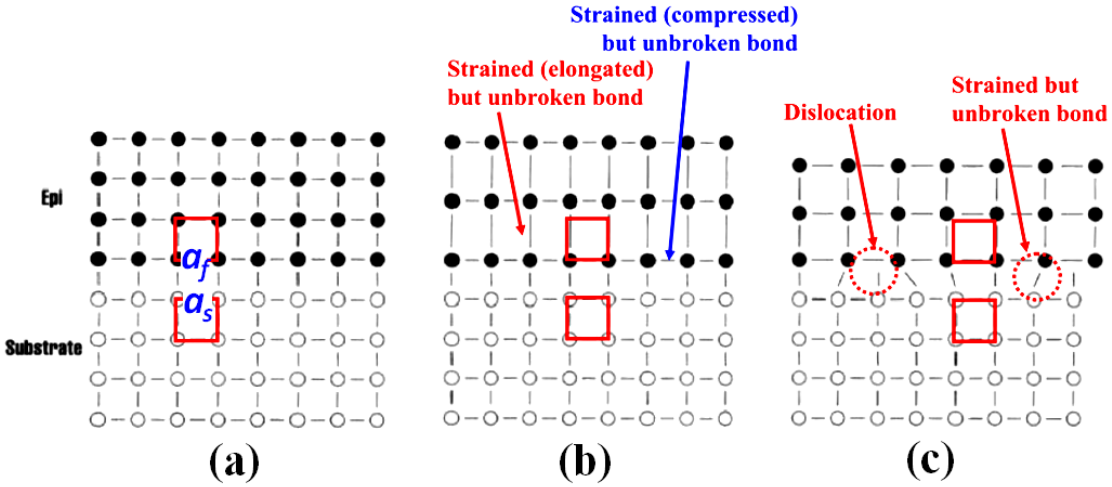

Figure 1.2. Schematic illustrations of the three major types of heteroepitaxy (a) the lattice-matched heteroepitaxy; (b) the coherently strained lattice-mismatched heteroepitaxy and (c) incoherently relaxed lattice-mismatched heteroepitaxy.

As the epilayer grows thicker, the rising elastic strain ε will eventually exceed the energy required for generating misfit dislocation arrays. As illustrated in Fig. 1.2(c), the initially strained film lattice decomposed (ideally) into an incoherent heterointerface where a portion of the ε is relieved by dislocations. The misfit dislocation spacing D_s can be estimated by,

$$D_s = \frac{a_s \times a_f}{|a_s - a_f|} \tag{1.3}$$

The misfit dislocations are separated in spacing D_s by lattice regions of relatively good fit. Instead of growing by one-to-one lattice matching, integral multiples of lattice planes match across the film–substrate interface. This is also called the domain matching epitaxy (DME), and the domain size equals to integral multiples of planar spacing.[10] At this incoherent relaxed lattice-mismatched heteroepitaxy, the residual film strain can be calculated as,

$$\varepsilon_{res.} = \frac{(ma_s - \mathrm{n}a_f)}{na_f} \tag{1.4}$$

where m and n are the integrals of the domain-matched substrate and the film, respectively. $\varepsilon_{res.}$ is usually at least one order smaller than the ε in equation (1.2) before the domain matching.

1.2.3 Epitaxial thin film microstructure hierarchy

For most technological applications, it is desired that the deposited epitaxial thin film form an ideally single-crystalline layer that has one well-defined orientation with respect to the seed substrate, i.e. single-crystal-like epilayer. However, in practical epitaxial growth, due to factors such as - interaction nature of the materials, the effects of film-substrate wetting, differences in lattice thermal expansion and surface step terraces,[11, 12] the actual film microstructure can be complicated in terms of both crystallographic and stoichiometry properties.[13] In general, the microstructure of epitaxial films can be illustrated in an hierarchy shown in Fig. 1.3 with examples of representative defects.[14]

Having this microstructure hierarchy in mind is extremely important towards establishing a valid structure-performance correlation for heterogeneous systems. A global microstructural evaluation on thin film phase/stoichiometry uniformity and crystalline quality is absolutely necessary before the attempt of relating the atomic-level interfacial defects to the overall film physical properties. In the main content of this dissertation, research topics are presented following the sequence of the epitaxial thin film hierarchy, from the top macroscopic film chemical inhomogeneity (Chapter III), to

microscopic film crystalline orientation (Chapter IV and V) and then to atomic-scale film interface defects and associated film lattice strain (Chapter VI and VII). Even in the later in-depth atomic scale analysis, the overall film epitaxial quality has been evaluated and achieved by optimizing deposition condition to lay a fairly regular crystalline background for further defect investigation. Meanwhile, film microstructure in turn depends on the initial heterogeneous interface structures. Atomic level characterization on these interfacial defects is essential for understanding the epitaxial growth mechanism and thin film defect-property correlation, and thus for rational interface property design.[15, 16] And it has been conducted in each individual research topic with different focuses. Thus, the heterogeneous interface structure and associated defects are the main topic of this dissertation.

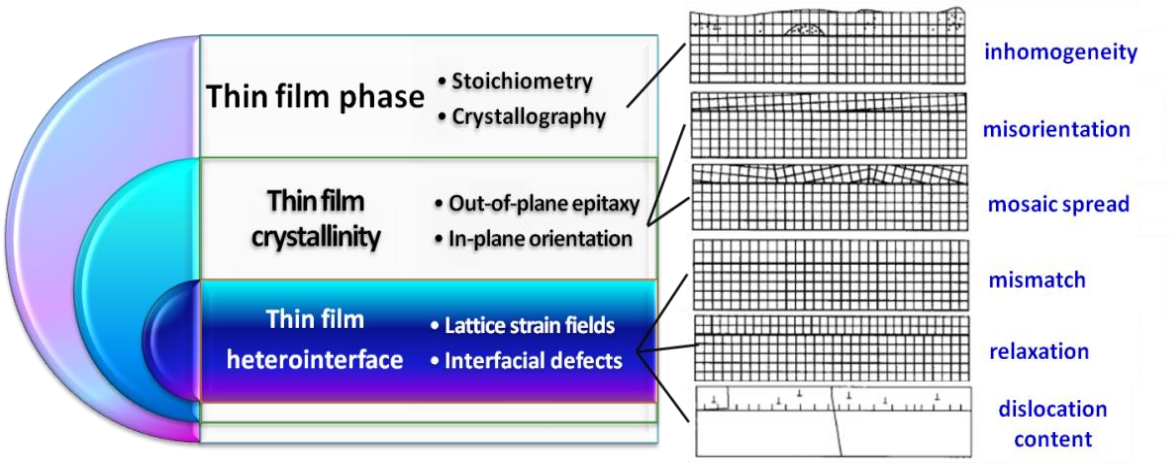

Figure 1.3. Thin film microstructure hierarchy and corresponding representative defects[14].

1.2.4 Different varieties of interfacial imperfections

Perfect crystal can be obtained, hypothetically, only at absolute zero; at all real temperatures, crystals are imperfect. This is also true for epitaxial thin films. Additionally, in practical epitaxy growth, film/substrate lattice and chemical mismatch and any disturbance during the initial film nucleation and post strain relaxation can introduce disordering. Examples of crystal defects commonly observed in epitaxial films are schematically presented in Fig. 1.4.

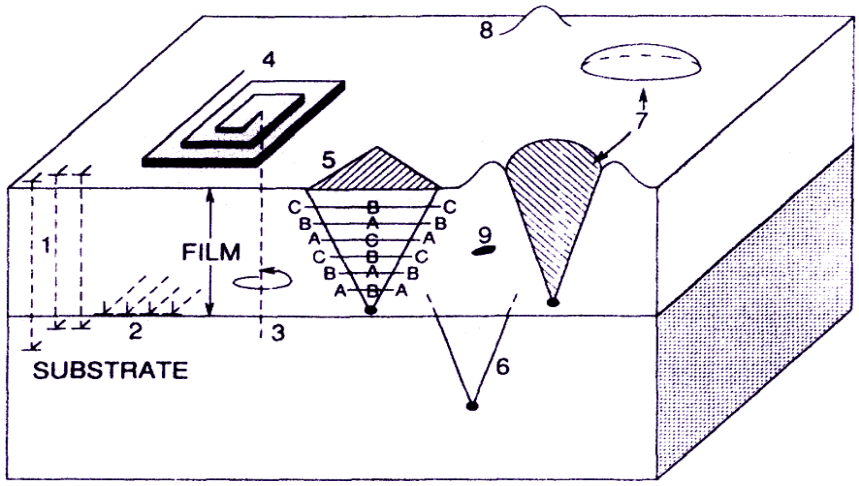

Figure 1.4. Schematic illustration of crystal defects in epitaxial films. 1, Threading edge dislocations; 2, interfacial misfit dislocations; 3, threading screw dislocations; 4, growth spiral; 5, stacking faults in film; 6, stacking faults in substrate; 7,oval defect; 8, hillock; 9, precipitate or void. [1]

It is well known that defects such as dislocations, stacking faults and twins affect materials performance by lowering carrier concentrations and mobility in electronic device or by enhancing flux-pinning effects in high temperature superconducting thin films. Semiconductor films, although are now considered largely “defect free”; in high quality silicon films there are about 10 dislocations/cm^2 while for GaAs films the

dislocation density is still in the order of $10^2/cm^2$. Among those interfacial defects, misfit dislocations attracted more attentions than others in high-performance epitaxy films. Extensive experimental efforts and theoretical investigations have demonstrated that the highly defective localized misfit dislocations and chemistry disorders have dramatic impacts on epitaxial thin film properties.[17-20] As shown in Fig. 1.2, misfit dislocations are also features of incoherently relaxed lattice-mismatched heteroepitaxy, different from the coherently strained epilayer. Another important epitaxial film property associated with misfit dislocations is the short/long-range lattice strain. Around a misfit dislocation line, the atoms are misaligned from their perfect lattice sites, creating a strain/stress field. This (residual) lattice strain was found strongly influences the defective nature of the heterogeneous interface.[21, 22]

Early epitaxial semiconductor films were usually characterized by standard X-ray and electron diffractions, which are essentially averaged results over a large number of lattice units. Slight crystal imperfections in high quality epitaxial films such as the misfit dislocations and associated strain are around the size of a few atomic length; this atomic structures requires atomic-scale characterization.

1.3 Functional heterosystems studied

1.3.1 Superconducting $FeSe_{0.5}Te_{0.5}$ epitaxial films

Superconductivity, the phenomenon of zero electrical resistance and expulsion of magnetic fields, is one of the most fascinating topics in solid-state physics (and also in

materials science). The discovery of superconductivity in iron-pnictide Fluorine-doped lanthanum iron arsenide ($LaFeAsO_{1-x}F_x$) in 2008,[23] has stimulated great research interest in the field. - So far, there are more than fifty new iron-based superconductors have been discovered. Based on chemical composition, they are usually divided into these four structure groups as demonstrated in Fig. 1.5(a).

It is noted that all the iron-based superconductors share a common building block of the Fe-centered-chalcogen/pnicogen tetrahedral sheet (as highlighted in yellow in Fig. 1.5(a)).[25] Among the four representative structural groups of the iron-based superconductors, iron selenide (FeSe) of the 11 structure consisting of only the superconducting layers without the La(O, F) "charge reservoir'' layer);[26] it provides a simple and arsenic-free system for studying the pairing mechanism for these new superconductors.[27]

The critical transition temperature (T_C), below which the material becomes superconducting, of FeSe is about 8K as noted in Fig. 1.5(a). This T_C can be further increased through materials engineering, for example, by incorporating isovalent dopants such as Te.[28] Although $Fe_{1+y}Te$ is not superconducting but exhibits long-range antiferromagnetic order with a distinct wave vector (π, 0),[29] the ternary compounds $Fe_{1+y}Te_{1-x}Se_x$ has a T_C of about 15 K at the optimized tellurium concentration of 50%.[28] At room temperature, as shown in Fig. 1.5(b), the crystal structure of $FeSe_{0.5}Te_{0.5}$ has been identified as the P4/nmm tetragonal phase with anti-PbO structure in space group #129.[26] One characteristic of the isovalent $FeSe_{0.5}Te_{0.5}$ is that the selenium and tellurium

share the chalcogen site, but at different z-coordinates and thus bonding angles and bonding lengths with Fe, which could lead to a lower local symmetry.[26]

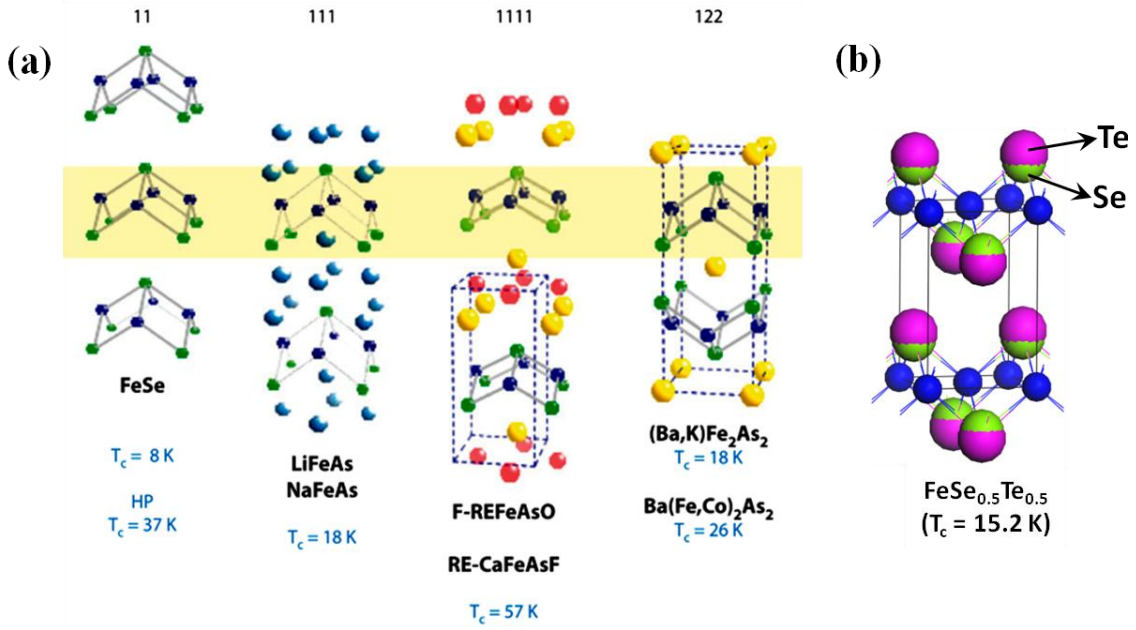

Figure 1.5. (a) The four representative structural groups of the iron-based superconductors.[30] (b) The tetragonal atomic model of the arsenic-free $FeSe_{0.5}Te_{0.5}$ at room temperature.

Materials science investigations towards the correlations between iron-based superconductor performance and microstructure have found that $Fe_{1+y}Te_{1-x}Se_x$ compounds are more tolerable to structural imperfections such as stoichiometry disorder, large angle grain boundaries.[25] For example, the superconductivity of $Fe_{1+y}Te_{1-x}Se_x$ can persist over a wide doping range (x) of Se for Te,[31] and of Fe(2)-interstitial doping (y).[29] Transport critical current density through bicrystal grain boundary (GB) was found to maintain above 10^{-3} A/cm^2 up to a GB angle of ~ 9° in cobalt-doped $BaFe_2As_2$ epitaxial films; whereas the GB angle of only ~ 5° for $YBa_2Cu_3O_{7-\delta}$.[32] Additionally, although the

superconducting transition temperatures of $Fe_{1+y}Te_{1-x}Se_x$ are typically lower than those of iron pnictide, iron chalcogenides exhibit lower anisotropies with very high upper critical field slopes near the superconducting transition temperatures. This suggests that $Fe_{1+y}Te_{1-x}Se_x$ thin films can be applied as high-field superconductors with less rigid requirements in film epitaxy quality.

On the other hand, however, the critical superconducting temperature of Fe-based superconductors, Fe-Te-Se system in particular, has been found to be very sensitive to lattice (or bond length) modification. Efforts such as applying external pressure, isovalent doping (chalcogen) have been made for reaching higher in the Fe-based superconductors. Recently, a 21K onset T_C was reported in an epitaxy $FeTe_{0.5}Se_{0.5}$ thin film grown by pulsed-laser deposition (PLD).[33] While Bellingeri *et al* [33] attributed the 21K onset T_C in their 200-nm-thick film to the compressive effect from the $LaALO_3$ (a ~ 3.789Å) substrate; Geetha Kumary *et al* [34] observed lower T_C in also PLD film on LAO (~ 11.5K) than that of on $SrTiO_3$ (T_C ~14K), both of which are even thinner (~ 100 nm). In fact, it has been demonstrated in semiconducting and ferroelectric oxide thin films that interfacial structures are typically complicated and difficult to predict, for factors such as the film-substrate lattice thermal expansion difference and surface step terraces.[11, 35] In-depth characterization on Fe-based superconducting thin film local atomic structure and interface defects, which is essential for understanding the unique stoichiometry inhomogeneity,[36] magnetic fluctuations[37] and lattice strain modification in Fe-based superconducting thin films, however, is quite limited at present.

1.3.2 $YBa_2Cu_3O_{7-x}$ (YBCO) epitaxial thin films and flux-pinning effects

Ever since superconductivity was discovered in mercury by Onnes in 1911, one of the most attractive applications for these zero-resistance superconductors is to use them as electrical cables that can carry current any distance with no loss (proposed firstly also by Onnes). As the scientific study on the mechanism of superconductivity has remained as an attractive curiosity, interests in industrial application of superconductors were renewed in 1987 with M. K. Wu and P. Chu's discovery of superconductivity in yttrium barium copper oxide $YBa_2Cu_3O_{7-x}$ (YBCO) at an ever-achieved high critical transition temperature of 93 K,[38] brought this long-standing dream of resistance-free cable one step further. The crystal structure of superconducting YBCO is presented in Fig. 1.6(a) in the orthorhombic structure of *Pmmm* (space group #47) with lattice constant of a = 3.82 Å, b = 3.89 Å and c = 11.68 Å. For the first time a material, called Type II high-temperature superconductors represented by YBCO, had been found that would reach a superconducting state at temperature warmer than liquid nitrogen (i.e. T_C > 77 K), a economically available coolant. One essential requirement for electric power application is for superconducting materials be formed into copper-wire-like long and robust cable. However, high-temperature superconductor YBCO is ceramic in nature. Epitaxial growth of an YBCO superconducting coating on a thin supporting tape has become one of the most important research directions for YBCO-related research. [39-41] In this dissertation, we didn't address - the mechanism of superconductivity, but have focused on the materials science of one of the most commercial valuable Type II superconductor, YBCO thin films.

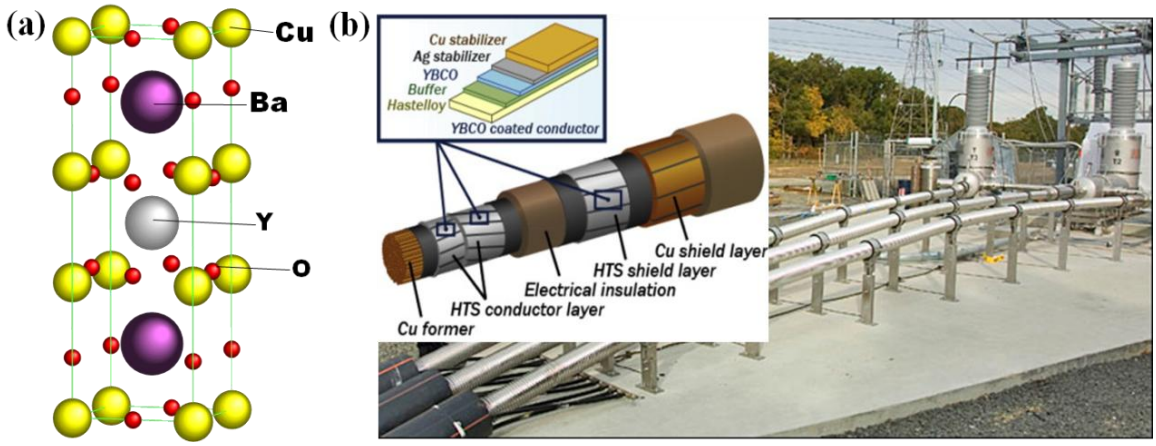

Figure 1.6. (a) The orthorhombic crystal structure of $YBa_2Cu_3O_{7-x}$(YBCO) superconductor. (b) Construction of a typical YBCO superconducting cable and power transportation facility.

After decade's efforts in perfecting YBCO superconducting coating, recently, commercial YBCO superconducting cable has been starting to be used in electric power transportation by a few companies. [42-44] An illustration of the construction of a typical YBCO superconducting cable is presented in Fig. 1.6(b). For example, one of these companies, Superpower, conducted a superconducting cable project of 10 km of YBCO wire in Albany, New York. These projects partly answered the questions to the commercial viability of superconducting cable; meanwhile, they have raised the new challenge in substantial improvement of YBCO's performance. Based on the performance/cost ratio at the present, the new high-temperature superconducting cable is over 10 times more expensive than the conventional copper wire. [45] In the logic of higher performance translates to lower cost, we expect to make the YBCO superconducting cable being able to transport as much electrical power as possible within the same wire, i.e. a higher current density (J_C). To boost the superconducting

performance of YBCO, factors affect the value of J_C have been intensively studied and can be generally summarized as the following four aspects.

First of all, material imperfections, such as cracks, voids or secondary phase, was considered that partially block the superconducting current. Fortunately, as the development of thin film synthesis optimization, we now can produce YBCO thin films with quite high purity. Secondly, the *a*-axis growth YBCO, was considered as a degradation of the film epitaxial quality. The structural feature of YBCO, as shown in Fig. 1.6(a), is layered crystallographic ceramics, which results in an extremely directional superconductivity. Strict maintenance of the specific crystallographic orientation of YBCO *c*-axis in parallel to the film growth direction is necessary for a uniformly high J_C. The third factor is the so-called weak-link effect.[46] This effect arises from the out-of-plane misorientation between adjacent grains, causes an exponential decrease in J_C. As discussed above, the anisotropic superconducting nature of YBCO requires highly crystalline alignment not only along the *c* axis but also in the *ab* planes.[47] The experimental results have shown that the YBCO thin film deposited on the Rolling Assisted Biaxial Textured (RABiT) substrate has a comparable J_C value to those on single-crystal substrates. [48]

The last and maybe the most important factor is the flux-pinning effect,[49-51] which relates to the physical nature of Type II superconductive materials. As we know, a perfect superconductor exhibits zero electrical resistance as well as perfect diamagnetism. Type II superconductors are far from perfect. They allow external applied magnetic field to penetrate into the superconductor and form a mixed state. In Type II

superconductor, this penetration occurs in the form of tubes, called vortices. As shown schematically in Fig. 1.7(a), an individual vortex has a core radius equals to the coherence length ξ and the penetration depth λ determines the spread of the surrounding outer region. Outside of each tube-shape vortex, the superconducting electrons can flow without resistance; while within it, it is a nonsuperconducting state. When carrying an electric current as in power transportation, a lateral force known as the Lorentz force F acts on the vortices. This process is schematically illustrated in Fig. 1.7(b). The greater the transport current *J* the greater the F on each vortex and results in vortex motion -, which dissipates energy and causes electrical resistance to appear in the superconductor.[52] To maintain the superconducting state, an opposite force is needed to pin the vortices.

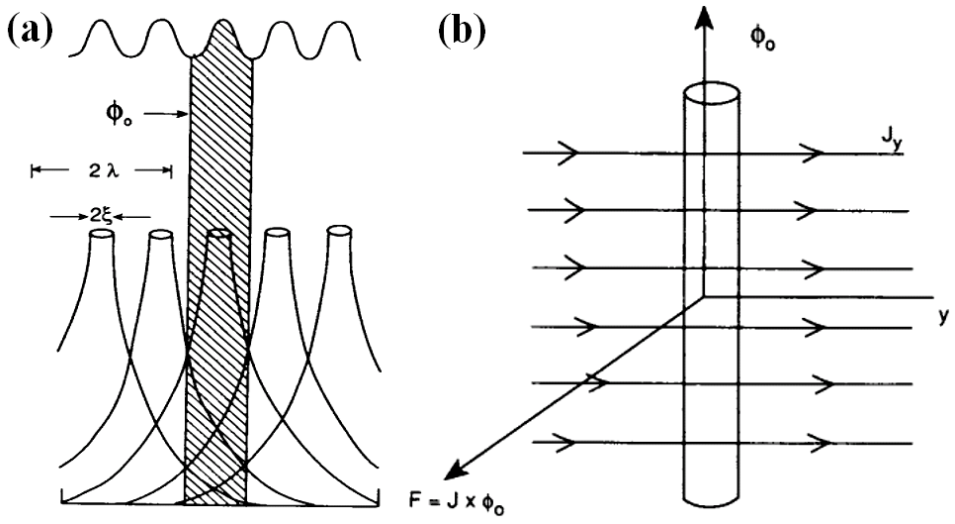

Figure 1.7. (a) The magnetic field (top) from a group of overlapping vortices. ξ is the coherence length and λ is the penetration-depth. (b) Schematic illustration of vortices in Type II superconductor, which allow magnetic field to penetrate and of Lorentz force *F* exerted on a vortex by a perpendicular transport current *J*.

In Type II superconductors, the flux-pinning force maintaining the vortices in their position often arises from crystallographic defects. Materials scientists have been trying to enhance J_C by introducing defects into YBCO in a controllable manner. Generally speaking, one rule for flux-pinning defects engineering is to introduce high density of nano-size defects without compromising the crystallinity of YBCO matrix. Table 1.1 lists representative researches of defects engineering of YBCO thin films and their effectiveness in improving J_C. MacManus-Driscoll and her colleagues doped $BaZrO_3$ nanoparticles in YBCO.[53] Although the doped sample shows slightly lower self-field J_C, the in-field J_Cs are improved 1.5–5 folds at high field. The angular dependence of J_C in 1T field plot shows a shift upwards in 0 degree, which indicates strong pinning defects along the c axis. And the TEM observation confirmed this. The doped YBCO has columnar defects with a density of at least $0.4*10^{11}$ cm^{-2}. Y_2O_3 could also serves as the secondary phase to improve flux pinning.[54] Results showed that small additions of Y_2O_3 improve the critical transition temperature T_C and self-field J_C effectively. As to in-field performance, this doping improves J_C in the low field regime. The angular dependence of J_C in 1T filed plot shows the upward shift of the x = 1.1 sample in all angles suggest the presence of extra random defects. In addition, $BaSnO_3$ doping brought some interesting results in J_C enhancement.[55] Although both T_C and self-field J_C were reduced by this doping, in-field J_C was found to be enhanced considerably. Since J_C is proportional to $B^{-\alpha}$, this much smaller α illustrate that the rate of fall in J_C with the applied magnetic field in the doped sample was very low as compared to regular YBCO samples, especially at low T. The reversed relationship in angular dependent J_C is also

interesting. TEM observation found that high density misfit dislocation and stacking faults generated at the interfaces of YBCO and BSO may responsible for this. Therefore, in addition to acting as flux pinning centers by themselves, the nanoparticles can also create defects, such as strain fields surrounding the particles, stacking faults, and dislocations, that can potentially enhance the flux pinning.

When deposition condition is varied, doped nanoparticles could grow larger and become nanopatch, even continuous nanolayers or thicker interlayers. Many works have been done in this field. One of the most studied secondary phases is CeO_2, which has near-perfect lattice mismatch with YBCO. Before introducing CeO_2, scientists had tried CeO_2 nanopatch,[56] CeO_2 nanolayer,[57]. Flux pinning was found to be slightly improved at low fields or low measurement temperatures compared to pure YBCO. However, Foltyn and co-workers[58] successfully overcame the barriers to the 1000 A/cm width limit by introducing 40nm-thick CeO_2 interlayer into YBCO to produce thick film with a total thickness of 3.5 micrometer. Compare to a 3.7 micrometer YBCO single layer, whose J_C is 1.3 MA/cm, this 3.5 micrometer multilayer has a J_C of 4.0 MA/cm. One explanation of this enhancement is that the CeO_2 interlayers serve as starting templates for the growth of subsequent high-quality YBCO layers, reducing the microstructure degradation when the film getting thicker, by acting as stating templates for the growth of subsequent high-quality YBCO layers. Moreover, misfit defects effect could be another possible explanation.

Table 1.1. Representative studies on flux-pinning engineering of J_C improvement in YBCO epitaxial films.

Thin film engineering	Film Properties			Flux-pinning Effects				Major Defects (cm^{-2})
	Synthesis Methods	Film t (μm)	Lattice Misfit f	Film defects features	T_C (K)	Jc^{self} (MA/cm^2) & Jc^H		
$BaZrO_3$-nanoparticles[53]	PLD (STO / IBAD-MgO)	0.5 ~ 1.7	9%	10 nm nanoparticles with a density of $3*10^{10}$ cm^{-2}	↓87.5 ~ 92	↓1.5~2.6	↑ 1.5~5-fold	Columnar defects ($0.4*10^{11}$)
Y_2O_3-nanoparticles[54]	PLD (STO / IBAD-MgO)	~ 1	2.3%	20~45 nm nanoparticles	↑97	↑~5.5	↑in low filed; ↓in high filed	extra random defects
$BaSnO_3$-nanoparticles[55]	PLD (LAO / Ni-W MS)	~ 0.3	~7%	10 nm nanoparticles with a density of $3.5*10^{11}$ cm^{-2}	↓88 ~90	↓~1	↑ low decreasing rate in H (α~0.23);	Misfit dislocation & SF (~10^{11})
CeO_2-nanopatch[56]	PLD (STO)	~ 0.3	0.31%	$t(YBCO)/t(CeO_2)_n$ (nm) = $(11/2\sim3)_{20}$	↓88 ~ 90	> 1	↑ at low field; ↓at moderate filed;	\
CeO_2-nanolayer[57]	PLD (STO)	~ 0.5		$t(YBCO)/t(CeO_2)_n$ (nm) = $(15/5\sim8)_{22}$	↓88	↓ by 0.6	↑at low field & at low T	misfit dislocations ($160*10^{11}$ cm^{-2})
CeO_2-interlayer[58]	PLD (STO buffer MgO)	3.5		$t(YBCO)/t(CeO_2)_n$ (nm) = $(550/40)_3$	\	↑4.0	\	\
YBa_2CuO_5 (Y211) particles[59]	PLD (STO / LAO)	~ 2	2~7%	$(Y211/Y123)_n$ $4*10^{11}$ MA/cm^2	↓88 ~90	↑4	↑ by a factor of 2~3 (77 K)	Pseudo-columnar defects
$BaZrO_3$ (doped in target)[60]	PLD (STO)	~ 1	9%	Single layer YBCO(BZO)	\	\	Variable	Random Particles; Columnar Defects (CD)
$BaZrO_3$ & CeO_2[61]	PLD (RABiTS)	~ 1	BZO (9%); CeO_2 (a:0.3; b:1.4%)	1. Single-layer YBCO(BZO)	\	1.2	↑in-field (α=0.27<0.5>); ↑ J_C (H//c) ↓ J_C (H//ab)	\
				2. BCO(BZO)/CeO_2		↑	↑in-field (α~0.34); ↑ J_C(H//c)	BZO~ $3.9*10^{11}$ cm^{-2}; CD
				3.YBCO(BZO)/YBCO		↑	↑in-field (α~0.34); ↑ J_C(H//ab)	BZO;CD; stacking defects

Besides adding one kind of defects, materials scientists have also tried to introduce both nanoparticles and interlayer to improve the J_C of YBCO. These kinds of films can be called as nanocomposites. Haugan introduced YBCO 211 particles by a growth of alternating multilayers of ultrathin layers.[59] The advantage of doing so is that it has some degree of control over the nanoparticle dispersion parameters compared to the conventional doping. Results showed that both self-field and in-field J_C have been improved. The authors claimed that this is due to the pseudo-columnar defects. Recently, scientists designed the main defects from random particles to columnar defects in BZO doped YBCO,[60] simply by changing the deposition parameters such as substrate temperature or repetition rate. They also suggested that growth kinetics is the main factor in the formation of directional pinning defects.

Kang and his colleague introduced CeO_2 as interlayer into BZO doped YBCO.[62] They also made single-layer BZO-doped YBCO and misfit-free YBCO multilayer as comparison. Because of the columnar defects and BZO nanodots, the composited YBCO, has the highest in-field J_C and a small α value. However, for the applied magnetic field in parallel to *ab* plane, a more pronounced upward shift was observed in YBCO interlayer sample. This indicated that the planar defects at interface are different for both interlayers. As discussed in above cases, one conclusion we could draw is that by modifying defects in YBCO thin film, a J_C enhancement in all directions and fields is achievable.

On the other hand, historically, the J_C of epitaxial YBCO thin films was found 10–100 times higher than YBCO single crystals, when the films were first produced in

the late 1980s.[63, 64] Due to the large density of defects inherent in thin-film growth, vortices were pinned intensively. As shown in Fig. 1.8, there are various kinds of inherent defects in YBCO thin films.[45] Note that there are certain similarities of Fig. 1.8 with Fig. 1.4; so this is also called the thin film effect. Any film defects as well as their associated strain fields, which locally disturb the crystalline perfection, are candidates of flux pinning sites. These intrinsic defects include random pinning, such as point defects, and correlated pinning defects, which arises from linear or planar defects. The task of enhancing J_C of YBCO thin films has been become more specific. That is to uncover which of these film defects are beneficial for pinning vortices, and to engineering those flux-pinning effective defects without obstructing current. Theoretically, scientists estimated the upper limit of J_C at 77 K is about 60 MA/cm^2,[65] but the best measured value in experiment is around 7 MA/cm^2.[58] So there are potentials for further J_C improvement. The history of superconductor development is still in its early stage.

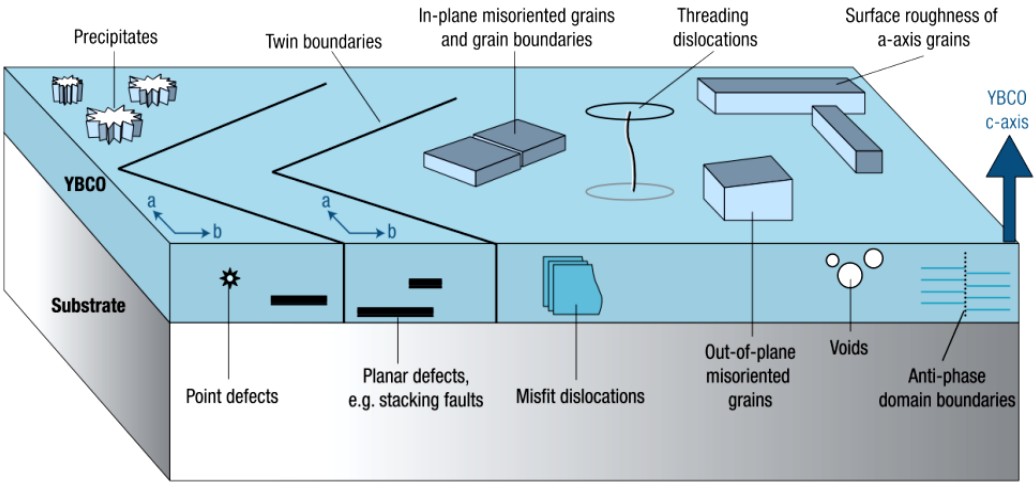

Figure 1.8. Variety of intrinsic defects in YBCO thin films.[45]

1.3.3 Perovskite oxide epitaxial thin films

Complex oxides represent a variety of smart materials systems in which the physical and chemical properties of the oxides can be tuned through adjusting the anion deficiency or cation valence states. In the big family of functional complex oxides, those with perovskite structure are particularly interesting, exhibiting various physical properties. For example, perovskite $La_xSr_{1-x}MnO_3$ and $La_{0.7}Ca_{0.3}MnO_3$ are ferromagnetic conductors; $LaMnO_3$ and $LaFeO_3$ are antiferromagnetic insulators; YBCO which can be considered as a layered-perovskite structure is a high temperature superconductor as discussed in the previous section.

The crystal structure of an ideal cubic perovskite oxide, with a general formula of ABO_3, is demonstrated in Fig. 1.9. It consists of an array of corner-sharing BO_6 octahedra with a larger A cation at the body-center position. Almost all perovskite oxides share a similar lattice parameter around 4.0 Å.

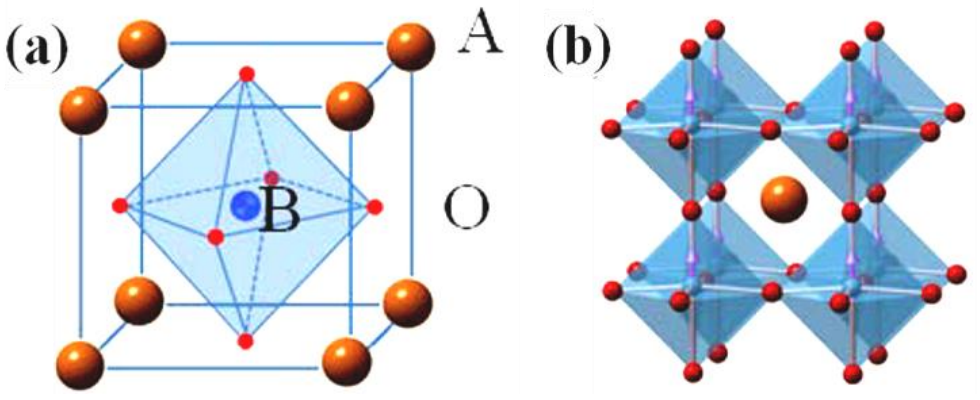

Figure 1.9. (a) Schematic illustration of ABO_3 perovskite structure. (b) The corner-sharing oxygen octahedra in perovskite structure.

The perovskite structure is quite stable as far as the overall charge of A and B is +6 and the ionic radius of A-cation is larger than that of the B-cation. Thus, perovskite structure accommodates a wide range of valence states which make many elements acceptable in this structure. There are three categories: $A^{+1}B^{+5}O_3$ (A = Na, Ag, K; B = Nb, Ta, I), $A^{+2}B^{+4}O_3$ (A = Ba, Sr, Ca, Pb; B = Ti, Mn, Fe, Zr, Sn, Hf, Mo) and $A^{+3}B^{+3}O_3$ (A = La, Pr, Sm, Bi, Y; B = Fe, Cr, Co, Mn, Ti, V, Al). Depending on the ionic radii of the A-or B-site cation, the actual perovskite oxides show a distorted cubic structure with lower crystal symmetry. Typical distortions include tilting of the octahedra or cation displacement within the octahedra, which leads to ferroelectricity in $BaTiO_3$.

If a cation A with a large size similar to oxygen (e.g., Sr) is incorporated at the center of the unit cell and Re is replaced by another small cations B (e.g., Ti), $SrTiO_3$ (STO) perovskite unit cells can be obtained. STO is not only a prototype perovskite but also one of the most important complex functional oxides. Its significance in electronic oxides is like silicon in semiconductors. The microstructure of STO, especially defect structures such as dislocation cores, has been intensively studied using the most advanced electron microscopy techniques at the time (Fig. 1.10).

More interestingly, as STO grows as thin films form, exotic physical properties such as room-temperature ferroelectricity,[66] conductivity[5] or even superconductivity[6] has been observed at the heterogeneous interface. Understanding the nature of the epitaxial interface disordering holds the key of rational functionality control and future oxide electronic device design.

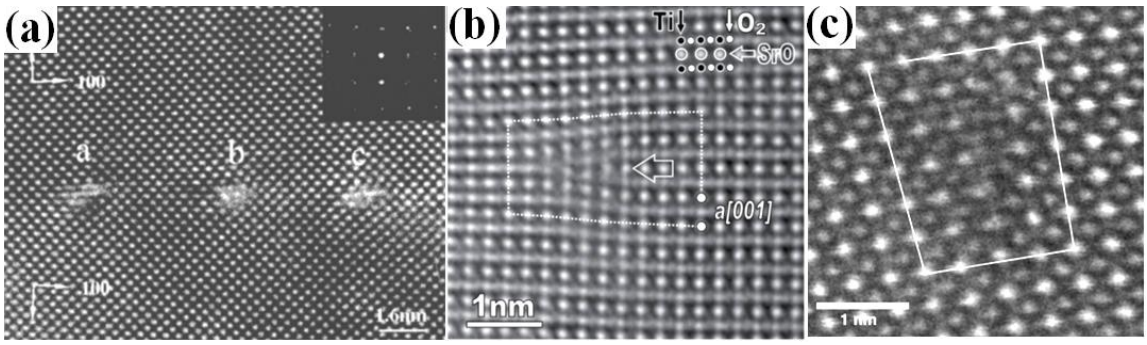

Figure 1.10. (a) A HRTEM micrograph,[67] (b) a Cs-corrected HRTEM image under the negative spherical aberration imaging (NCSI) condition[68] and (c) a C_S-corrected STEM image[69] of the dislocation core structures of single crystal $SrTiO_3$.

1.4 C_S-corrected STEM in functional heteroepitaxial structures

1.4.1 The era of spherical-aberration correction

To understand the world around us, humankind have been in the process of developing and advancing tools to improve our (poor) eyesight so as to look into the very small of the universe. Although optical microscopy is still very much used in biology (since Hooke's Micrographia in 1665) and in classical metallurgy, its principle limitation in terms of resolution by the wavelength of light (in the order of 10^4 angstrom) was stated by Ernst Abbe at the end of the 19th century. Inspired by Paul Dirac's theory of particle/wave duality, and the demonstration of magnetic field focusing an electron beam by Hans Busch, Ernst Ruska and Max Knoll took up the resolution challenge.[70] In 1933, a capability of resolving to 500 angstrom was achieved in Ruska's the first prototype electron microscope. This resolution leap is clearly shown in Fig. 1.11 in green. A few years later, the first STEM was developed by Manfred von Ardenne in

1938.[71] Since the 1950s, the resolution record of TEM and STEM has been steadily improved from 10 angstrom[72] to around 2 angstrom in most commercial instruments (without correction) currently.

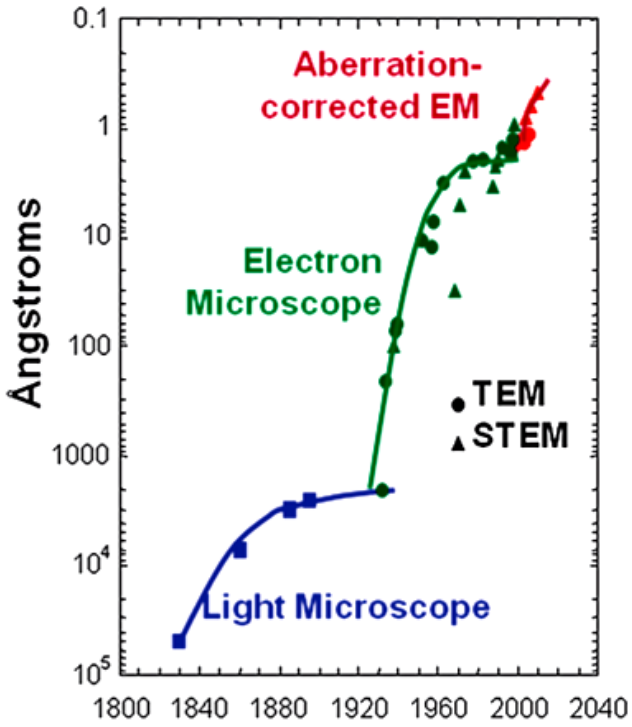

Figure 1.11. The evolution of spatial resolution versus years of optical microscopes and electron microscopes.[73] Two historical leaps in resolution are demonstrated in different colors.

Soon after the invention of the first TEM, in 1936, Otto Scherzer showed that the spherical aberration was unavoidable for rotationally symmetric electron lenses.[74] And interestingly, in his prophetic lecture "There's Plenty of Room at the Bottom" given in 1959, Richard Feynman simply responded "why must the field be symmetric?" Indeed, sophisticated electron-optical components designed to break this rotational symmetry

composed to the key idea of aberration correctors (theoretical study on aberration correction by Scherzer in 1947).[75] The impact of spherical aberration correctors on electron microscopy is evident from Fig. 1.11 (highlighted in red). It opens a new level of sub-angstrom resolution and more importantly a genuine atomic resolution.[76]

1.4.2 Atomic resolution in C_S-corrected electron microscopy

Before spherical aberration correction, "high resolution micrograph" is the proper term to be used for TEM images obtained in conventional uncorrected microscope. Although a high resolution micrograph shows a periodic pattern consisting of black or white dots, superficially resembling an atomic lattice under certain conditions, the information of individual atomic site is in principle not accessible.[77] This rather common misunderstanding of "dot-like contrast" to "atomic resolution" makes it easy to underestimate the revolutionary progress of aberration correction. A brilliant discussion on the significance of C_S-corrected electron microscopy to the entire scientific community, materials science in particular, was given by Dr. Urban.[78] Few works that were capable of atomic-scale resolution involved exit plane-wavefunction (EPWF) reconstruction from a focal series.[79, 80] In EPWF calculation the spherical aberrations were corrected post-experimentally to a certain extent by software. However, these early studies were focused on the collective crystal properties such as lattice parameters and crystal symmetry rather than on individual atoms.

So what is atomic resolution? A correct definition has been given only recently: "resolving a structure with atomic resolution means that the information must be entirely

local on the atomic level. Any change in the position or occupancy of an atomic site in the sample must show up in the image as an individual signal localized only at the corresponding atomic position."[77, 78] Another description of atomic resolution given by Dr. Van Tendeloo is that "to determine where are the atoms, which atom is it and what is its electronic configuration?"[81] One demonstration of the genuine atomic resolution is presented in Fig. 1.12. Any local changes on the oxygen column marked in the $SrTiO_3$<110> model have been faithfully reflected in the image with aberration-correction. Thus, strictly speaking, only the micrographs obtained in modern aberration-corrected microscopes match this standard.

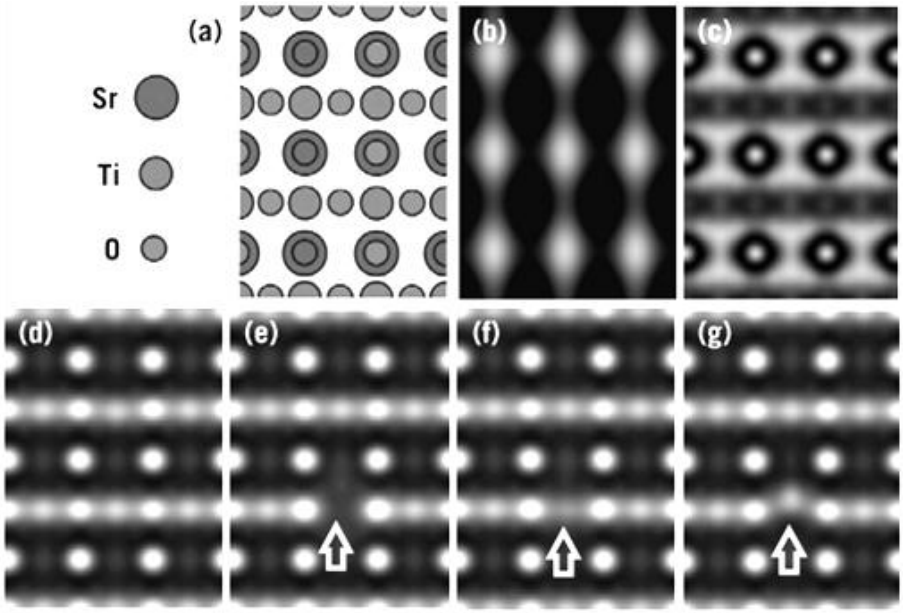

Figure 1.12. Demonstration of atomic resolution by simulation micrographs for oxygen occupancy in $SrTiO_3$. (a) Crystal model of $SrTiO_3$ in <110> zone axis. Simulated HRTEM images under (b) Scherzer condition without C_S-correction, (c) positive phase contrast optimum condition with C_S-correction, (d) the negative spherical aberration imaging (NCSI) condition. NCSI images with oxygen column (arrow) set to (e) occupancy of 0, (f) occupancy of 0.5 and (g) displacement up by 50 pm.[77]

The effects of spherical aberration corrector on STEM imaging are well understood from the aspect of the probe forming lens (the condenser lens).[82] Together with development in high-brightness Schottky-field emission electron source, C_S-correction STEM allows a larger beam convergence angle which provides a small electron probe of sub-angstrom point-to-point resolution of high current. An interesting comparison of Graphene experimental HR-STEM images before and after aberration is shown in Fig. 1.13. The C_S-corrected STEM image in Fig. 1.13(b) provides us with not only the individual atomic positions but also the type of the elements in terms of atomic weight (Z-contrast).

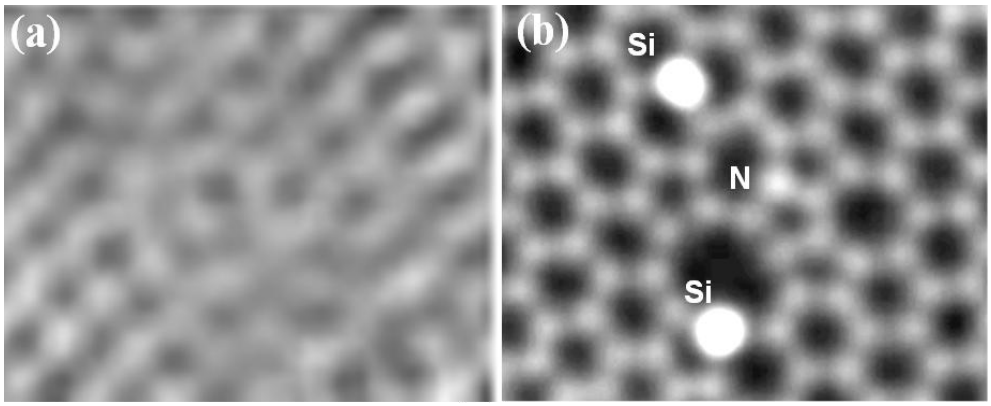

Figure 1.13. HR-STEM micrograph of Graphene (a) before[83] and (b) after[84] probe C_S-correction.

1.4.3 C_S-corrected STEM for functional heteroepitaxial structures

Modern aberration-corrected (scanning) transmission electron microscopy provides us with the power of revealing materials structure with a genuine atomic resolution. This is not just looking into a sample with a better resolving capability;

instead, the power of the technique is that it could link the local physical property directly to atomic-level information – the old dream of material science.[78] In the field of materials science, almost all the applications tend towards scale miniaturization. Functional epitaxial thin films, in particular, are approaching the dimensions of the ultimate building block – the atom. Crystallographic defects at heterogeneous interfaces involve atoms deviating from their equilibrium bulk positions. From a collective view point, it gives rise to inhomogeneous lattice strain; to individual atom (or ion), it is possible contribute to electronic structure modification.

Extensive studies on materials structure-property relationships with in-depth characterizations using C_S-corrected electron microscopy have been conducted. Recent C_S-corrected (S)TEM progress on complex oxides, [85, 86] semiconductors, [87] quantum dots and quantum wires[88] and metal oxide catalysts [89] have been reviewed. Here, considering functional epitaxial thin films are the major topic and C_S-corrected STEM is the main atomic-resolution characterization method of this dissertation, representative studies which fit both categories are summarized and listed in Table 1.2.

Table 1.2. Recent research highlights in atomic-scale C_S-corrected STEM for various heterogeneous systems

Heteroepitaxial systems		**Major observation (&C_S-corrected STEM techniques)**	**Ref.**
Superconductor heterointerfaces	$YBa_2Cu_3O_{7-x}$ /$La_{0.67}Ca_{0.33}MnO_3$ interface	Coherent interfaces, free of defects, in absence of measurable chemical interdiffussion (C_S-STEM imaging & EELS)	90
	$La_{0.7}Ca_{0.3}MnO_3/YBa_2Cu_3O_7$ /$La_{0.7}Ca_{0.3}MnO_3$ heterostructures	The same stacking sequence at both top and bottom cuprate interfaces (Cs-STEM imaging & EELS)	91
	$YBa_2Cu_3O_{7-x}/SrTiO_3$,/$LaAlO_3$, /MgO and /YSZ interfaces	Identifying of interface atomic contact, intrinsic YBCO film defects (C_S-STEM imaging & intensity profile)	92
	$Fe_{1+y}Se_{1-x}Te_x/SrTiO_3$ interface	The spatial relationship of Se, Te and interstitial Fe (C_S-STEM imaging & intensity profile)	93
	Oxide/Nb(elemental Type II superconductor) interface	Revealing the interfacial stacking sequence; directly visualization of hydrogen atoms in bulk beta-NbH (C_S-ABF/ HAADF STEM imaging, EELS, ultraviolet laser-assisted local-electrode atom-probe tomography)	94
Perovskite heterointerfaces	YSZ (Y_2O_3-stabilized ZrO_2)/$SrTiO_3$ interface	Atomic reconstruction of the interface structure is suggested as a high-mobility plane for the observed ionic conductivity (C_S-STEM imaging & EELS)	95
	$LaVO_3/SrTiO_3$ multilayer	Quantitative characterization on the intermixed amounts of vanadium (C_S-STEM imaging & EELS elemental mapping)	96

Table 1.2. Continued

Heteroepitaxial systems		Major observation (&C_S-corrected STEM techniques)	Ref.
Perovskite heterointerfaces	$La_{1-x}Sr_xCoO_3/SrTiO_3$ interface	Nanoscale CoO precipitates in the $La_{1-x}Sr_xCoO_3$ thin film; mapping the chemistry of interfaces atomic plane by atomic plane, including light elements Such as O. (C_S-STEM imaging & EELS elemental mapping)	86
	$CaTiO_3/SrTiO_3$ interface	Misfit dislocation core characterization (C_S-STEM imaging & EELS elemental mapping)	86
	$La_{0.7}Sr_{0.3}MnO_3/SrTiO_3$ multilayer	Developed a statistical hypothesis testing method to distinguish different atomic column types and to identify the nature of unknown columns with good accuracy and precision (C_S-STEM imaging, intensity profile and statistical parameter estimation)	97
	$BiFeO_3/La_{0.7}Sr_{0.3}MnO_3$ interface	Characterizing the octahedral tilts by quantitative unit-cell-by-unit-cell mapping (C_S-STEM imaging, intensity profile and low-loss EELS imaging)	98
	$SrRuO_3/La_{0.7}Sr_{0.3}MnO_3$ interface	Quantification of cation displacements at the interface, and density functional calculations based on the observation. (C_S-STEM imaging, intensity profile and EELS)	99
	a single-unit-cell layer of $LaAlO_3/SrTiO_3$	Simultaneous determination of local structural and chemical features of the interface on an atomic scale (C_S-EM imaging and sophisticated numerical image simulation procedures)	100
	$BiFeO_3/La_{0.7}Sr_{0.3}MnO_3/SrTiO_3$	Direct atomic displacement mapping at ferroelectric interfaces. (C_S-STEM imaging and intensity profile)	101

Table 1.2. Continued

Heteroepitaxial systems		**Major observation (&C_S-corrected STEM techniques)**	**Ref.**
Other important heterostructures	Metal/metal interfaces, e.g. Ni-base superalloy γ/ γ' interface	The determination of the true atomic-scale structure and change in chemical composition across the complex order-disorder γ/ γ' interface. (C_S-STEM imaging, intensity profile and energy filtered TEM imaging)	102
	Metal/oxide interfaces, e.g. Au/Ce-based oxides (heterogeneous catalysts)	Direct evidence about subtle structural changes taking place at nanometer-sized Au/ceria oxide interfaces. (C_S-STEM imaging, intensity profile and EELS)	103
	Ni/LaNbO4 interface (composite anodes for solid-oxide fuel cells)	Revealing the absence of reaction or inter-diffusion layers at the interface and changes in the valence state of Ni and in the electronic structure of La. Comparison of experimental results to density functional calculations. (C_S-STEM imaging and EELS)	104
	Si/insulating oxide interface, Si/Y2O3/Pr2O3/Si heterostructures	Realizing compressed, fully relaxed, as well as tensile-strained Si films; the interface structures were precisely analyzed at the atomic scale. (C_S-STEM imaging and EELS)	105
	BN monolayer with C and O impurities	Demonstration of atom-by-atom structural and chemical analysis of all radiation-damage-resistant atoms in Graphene sheets. (C_S-STEM imaging, intensity profile and quantitative analysis)	84

In all of these applications of C_S-corrected STEM on heterogeneous structures, a quantitative analysis down to atomic scale is extremely important. As that have been demonstrated in a few studies already,[99, 104] experimental determined defective structures with atomic-scale description in combination with density functional calculations are a powerful tool for understanding the atomic origin of materials properties. All the structure-property relationships are unambiguously coded in the positions of individual atoms.[81] To evolve from understanding to design, faithful and precise experimental quantitative characterization is the bridge between physical properties and materials synthesis and engineering.

This atomic quantification involves multiple challenges, including precise measurement of individual and collective atom displacements to a few picometer accuracy,[98, 99, 101] determination of the occupancy of an individual atomic column[96, 97] and detecting and distinguishing light elements.[84, 86, 94] As the microscopy techniques have developed with genuine atomic resolution, corresponding progresses have also been made to extract structural properties from microscopic atomic arrangements. Numerical image simulation has demonstrated its capability of simultaneous determination of local structural and chemical features of the interface at atomic scale.[100] Digital imaging processing methods in real space such as peak finding [106, 107] and the statistical parameter estimation,[97] and the methods working from reciprocal space such as geometric phase analysis (GPA)[108] have gradually replaced human eye-inspection, giving a more reliable and reproducible quantification procedure.

The efforts of electron microscopists have given aberration-corrected TEM and STEM the power to reveal genuine atomic structures with unprecedented precision. It is now up to materials scientists to apply this power into their materials needs.

CHAPTER II

RESEARCH METHODOLOGY

2.1 Pulsed laser deposition (PLD)

Epitaxial films may be grown from gaseous or liquid precursors. Typical thin film deposition techniques can be classified into three categories: (1) Physical vapor deposition (PVD) techniques include electron-beam evaporation, molecular beam epitaxy (MBE), pulsed laser deposition (PLD) and magnetron sputtering; (2) Chemical vapor deposition (CVD) involving chemical reactions and surface absorptions in techniques, such as low-pressure CVD (LPCVD), plasma-enhanced CVD, metal-organic CVD and atomic layer CVD (ALD); (3) Liquid phase epitaxy (LPE) and solution-based techniques (sol-gel and polymer assisted deposition).[109] With those systems, the film density, microstructure, stoichiometry as well as other properties can be easily controlled.

PLD is one of the physical vapor deposition systems for thin film processing. Since laser assisted thin film deposition was initially carried out in 1960s, Dijkkamp and Venkatesan demonstrated deposition of $YBa_2Cu_3O_7$ (YBCO) as a high temperature superconducting material by laser deposition method in 1987.[110] Currently pulsed laser deposition (PLD) - is applied for high quality thin film fabrication. PLD techniques fit the growth of almost all materials and can provide good film stoichiometry for complex composites.[111]

Basic operational mechanism for this system is mainly depending on the laser ablation after the pulsed laser hits the surface of the target material inside of a vacuum chamber. Once the pulsed laser strikes the target material, the evaporated materials from the target can fly through the plasma plume and deposit on the surface of the substrate. Thus, because the film deposition is carried out directly by the laser process, this technique is relatively simpler than other methods. For the film processing, high vacuum -in the chamber is required. Before the deposition, base pressure of the chamber should be reduced -to 10^{-7} mbar range. The pressure can be controlled by mechanical and turbo molecular pumps. - The high spatial coherent beam of the lasers allows extreme focusing and directional irradiation with high energy densities.

With such a monochromatic laser light, it can be possible to have narrow band excitation of the laser. The pulsed excitation of the laser maintains the transient resolution. Then, based on these capabilities, PLD -shows several advantages over other deposition techniques such as evaporation or chemical vapor deposition methods.[112] First, PLD can produce the high quality stoichiometric films with complex composites, maintaining the low contamination levels. And almost all metals and complex ceramic materials can be processed. Multi-targets can be used to grow single or multi layer thin films. During the deposition, extra gases such as O_2 or N_2 can be introduced as maintaining the film stoichiometry of oxides and nitrides. Finally, the film properties can be varied by in situ control. Therefore, based on these advantages, different thin film properties can be achieved.[113]

The schematic diagram of the PLD experimental setup is illustrated by the Fig. 2.1. In the chamber, multiple target holders are located face to face with the substrate holder. The targets could be mounted on the target holders at which the surface of the target is 45 degree tilted respect to the incident direction of the excimer laser beam. Once a high power laser strikes the target through the optical focusing lens, it can generate the heat energy to vaporize the target materials. Under the laser ablation, the evaporated materials can travel in the plasma plume to the surface of the substrate attached on the substrate holder positioned about 3~5 cm away from the surface of the target. During the thin film deposition, the substrate temperature can be tuned in the range between room temperature and 1050 K.

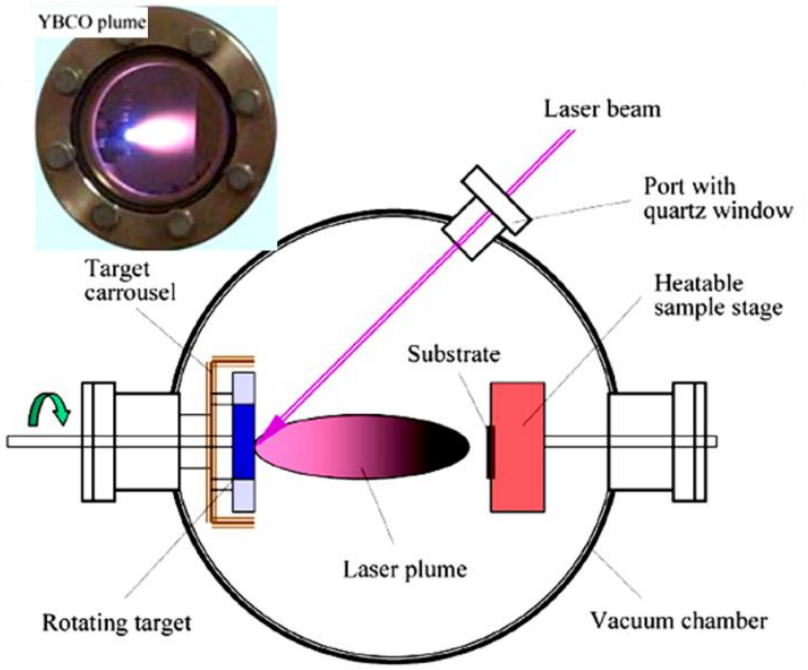

Figure 2.1. Schematic diagram of the pulsed laser deposition (PLD) system. The inset is an example of the laser plume during superconductor YBCO epitaxial film deposition.

There are several parameters that affect the quality of the thin films, such as repetition rate of the laser pulse, substrate temperature, laser energy density, distance between the target and substrate and partial gas pressure of the chamber. - - The partial pressure of the gas in the chamber highly affects the surface coverage of the plume. For example, under high partial gas pressure, the mean free path of adatom from the plume can be reduced after it collides with the -gas atoms. Then the plum can cover the relatively small area of the substrate. Meanwhile, as the mean free path of the adatom increases under high vacuum condition, the plume can cover the larger area of the substrate. Therefore, under such various deposition conditions of PLD system, growth of different structures of the thin films is possible. In order to comprehend the mechanism of PLD processing, study of the interaction between the laser and target is essential. The interactions during -laser ablation should be understood based on physical phenomenon with equilibrium and non-equilibrium processes which can be determined by the physical properties of laser and target materials.

Once the pulsed laser beam strikes the target, laser radiation is absorbed by the target surface. As electromagnetic energy transferred from the laser to target, it can be converted to different forms of energy source, such as electronic excitation, thermal, chemical and mechanical energies, to evaporate the target material. During the evaporation, usually other processes such as ablation, excitation, plasma formation and exfoliation are accompanied. Eventually, these processes generate a plasma plume that is a mixture of energetic atoms, molecules, electrons, ions, clusters, micron-sized solid

particulates and molten globules. The short mean free path after the collision between the species results in the rapid expansion of the plum from the target surface. [114]

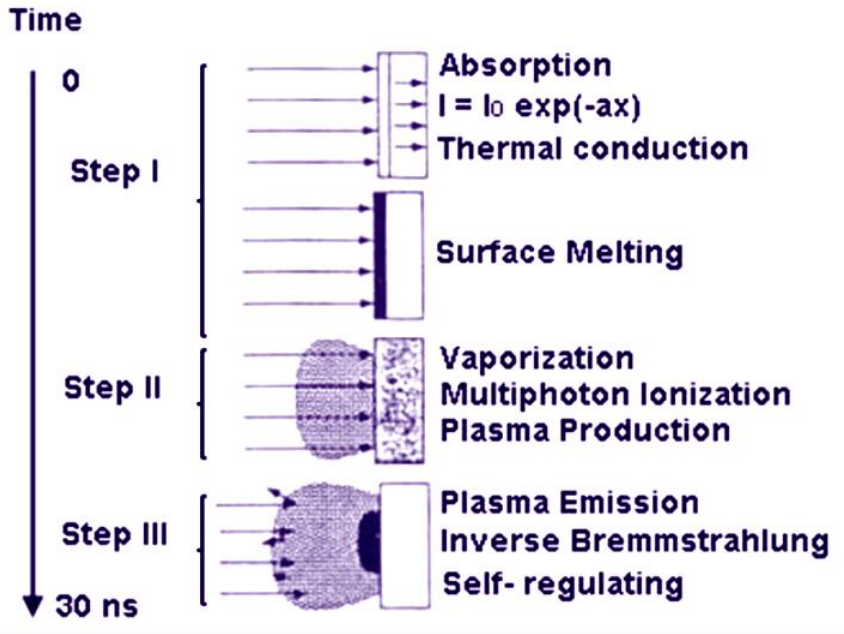

Figure 2.2. Representation of the laser target interaction stages during the short pulsed laser period.

To -understand the mechanism of the plum formation, detailed descriptions of the formation of the plume during the laser-target interaction are shown in Fig. 2.2. Once a laser pulse impacts on the target surface with -intensity $-I_0 \cdot \exp(-\alpha x)$, the interaction process can be explained with three different steps until a plume is formed within a few nanoseconds. In the first step, - starting with the laser pulse, the target materials is evaporated during the interaction between the laser and target. During the second step, further interaction between the evaporated materials and laser enhances the formation and expansion of the isothermal plasma. Finally, during the third step, the

plasma can expand anisotropically under adiabatic conditions. This step is initiated at the end of the pulse.

2.2 Global thin film microstructure characterizations

2.2.1 X-ray diffraction (XRD)

X-ray diffraction (XRD) is one of the most widely used nondestructive crystal structure analysis techniques used to determine -the lattice constant and orientation of the crystal. Its application for the thin film materials can help to identify the strain effect along the interface between the film and substrate, which may suggest more a detailed study of the defects in the film. Fig. 2.3 shows the schematic set up of X-ray spectrometer.

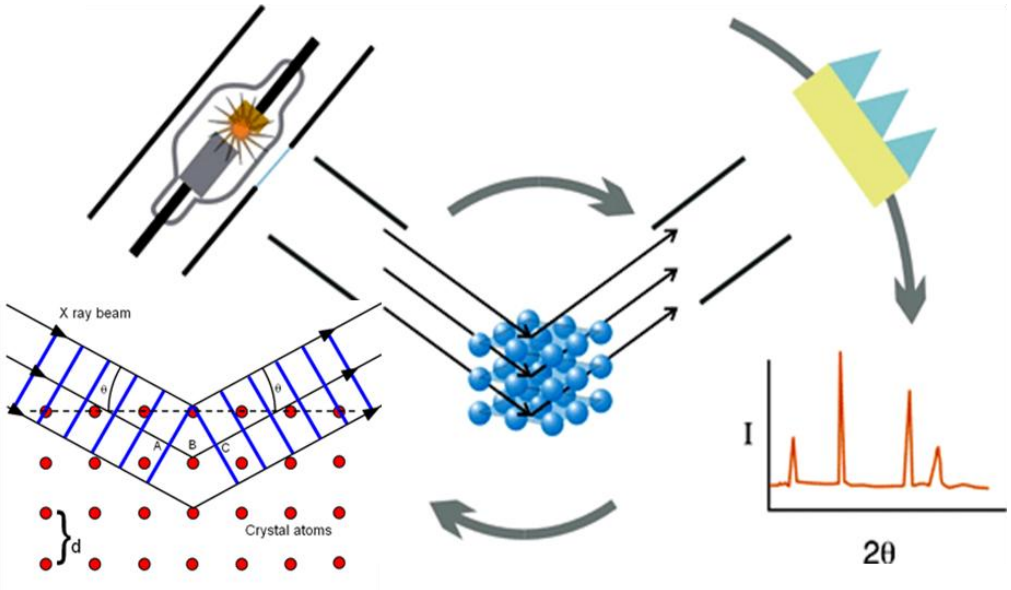

Figure 2.3. Schematic illustration of X-ray spectrometer and Bragg's law.

In its use two -factors should be considered. First, the incident and its reflected X-ray beam lie in a plane orthogonal to - the reflecting plane. Second, the incident beam and diffracted beam form an angle 2θ. In the schematic, the diffracted beam can be measured by rotating the detector-. The lattice spacing *d* of the sample studied can be deduced from the measured diffraction angle θ - based on the Bragg's law,

$$d \cdot sin\theta = n\lambda \tag{2.1}$$

where the λ is the wave length of the X-ray. Once the parallel and monochromatic incidental X-ray beam interacts with the sample -, it is diffracted by a set of crystal planes spaced with *d* along a certain direction. A diffraction peak is formed at a corresponding angle θ governed the Bragg's law. Finally, based on the shape and position of the peak, sample crystal structure can be characterized. Particularly, the information from the width and degree of the intensity peak is essential to determine the crystallinity of the material based on grain size.

As shown in Fig. 2.4, the features of diffraction patterns (illustrated in Debye cones) can be directly correlated to the crystallinity property of the samples. When a - amorphous or powder sample is characterized, the XRD result is a complete Debye cone. When analyzing this type of sample any linear scan through the Debye cones will give an accurate powder pattern. This "linear scan" is exactly how a conventional Bragg-Brentano powder diffraction system works. However, when a system is not a completely amorphous (texture measurement) --, the result is an incomplete Debye cone. Possible reasons for the variance of the peak width is from the relationship between the spectral width of the X-ray source and the diffracted angle θ. Increase of the peak

width can be caused by misorientation of textured -crystal -.[115] - Additional to the peak width variation, the intensity of the peak could also be affected by the textured crystal. In other words, the peak intensity is highly affected by the crystallinity of the sample.

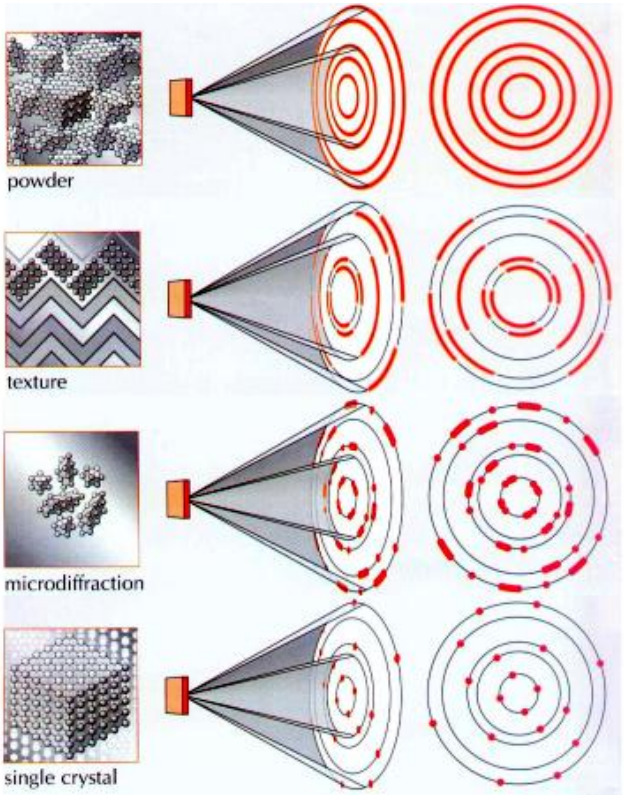

Figure 2.4. Schematic illustration of the crystallinity property of the sample and the features of diffraction patterns.[116]

If the atomic arrangement is irregular, the constructive and destructive interference won't form a sharp peak due to random phase. And then, the intensity of the X-ray beam can be estimated by the summation of all the X-ray intensities scattered. However, if the beam hits a well-oriented crystal, and the refracted beam could be

explained based on Bragg's law. Therefore, a material with high crystallinity can have higher intensity than that with a low crystallinity or is amorphous -. In additional to the information about grain size and crystallinity of materials, X-ray diffraction technique can also analyze the strain effect for thin films based on the peak position the intensity- as illustrated in Fig. 2.5.

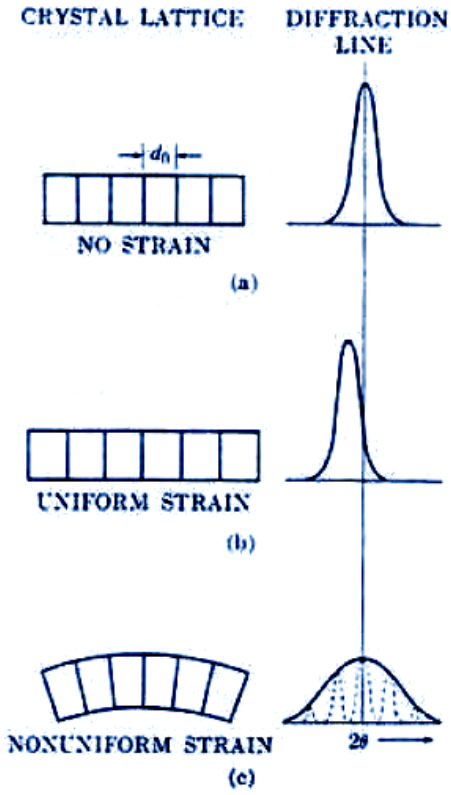

Figure 2.5. The effect of lattice strain on the peak width, intensity and position.

If there is an uniform tensile strain in a thin film sample, the out-of-plane *d*-spacing of the sample can be smaller than its bulk value.[117] On the other hand, the film

samples that are under a uniform compressive strain, the *d*-spacing can become larger. Therefore, the corresponding peak position could be shifted to the lower angle under the compressive strain and the higher angle under tension (Fig. 2.5(b)). However, as the thin film is under nonuniform strain with which the top area of the film is under the tensile strain and the bottom area near the interface between the film and substrate is under the compressive strain, XRD peak shows the increase of the width with a lower intensity caused by the imperfect crystal orientation (Fig. 2.5(c)). Then only preferred orientation which is perpendicular to the beam direction contributes to the peak intensity.

2.2.2 Transmission electron microscopy (TEM)

Transmission electron microscopy (TEM) is one of the most important microstructure characterization techniques due to its high measurement resolution (compared to diffraction-based methods like the XRD above), and for its capabilities to determine the materials' chemical, geometric and the electronic properties. Historically, electron beam was introduced as the light source in microscopes due to the resolution limitation in traditional optical microscopes imposed by the wavelength of visible light. Today, TEM has become more versatile than ever; analytical electron microscopy (AEM) is well developed, including the conventional TEM, high-angle annular dark field (HAADF) STEM, Energy Dispersive X-ray Spectrometer (EDX) and electron energy loss spectroscopy (EELS) and so on. In this dissertation, extensive TEM and STEM studies have been conducted to characterize the heterogeneous structures of functional epitaxial films, from the global crystallinity to defect details. Considering that

STEM has a lot in common with TEM in terms of the instrumental setup, fundamentals of electron microscope are presented in this section with focus on the conventional TEM (CTEM). TEM facilities include the JEOL JEM-2010 microscope (200KV, LaB_6 filament with 0.23nm point resolution), FEI Tecnai F20 super-twin (200KV, ZrO_2/W Schottky field emitter with 0.27 point resolution), Philips CM200F analytical electron microscope with a point-to-point resolution of 0.20 nm. In addition to the regular single-tilt and double-tilt holders, beryllium double-tilt holder has also been used for Energy Dispersive X-ray Spectrometer (EDX) experiments.

2.2.2.1 Electron scattering theory

The nature of the electron is a low mass and negatively charged particle; it can be easily deflected by atoms (the electrons or the nucleus of an atom) of materials in interest. The electron scattering caused by these Coulomb interactions is the foundation of all electron microscopy and analytical techniques. Fig. 2.6(a) illustrates a variety of electron scattering processes as a result of an electron beam interacting with a thin solid section. Each of the scattered electron signals represents some specific aspect of the sample studied, and can be collected and displayed as an image or spectrum in SEM or AEM. TEM utilizes the electrons that go through a specimen, i.e. transmission electrons. In Fig. 2.6(a), the four types of forward scattering are presented, which contribute most of the signals used in TEM and STEM.

Typically, the scattering is described - as elastic or inelastic (particle nature), i.e. describing of scattering that causes no loss of energy and measurable loss of energy,

respectively. One the other hand, we can also consider the wave nature of electron beam and refer the scattering as coherent (remain in phase) and incoherent. The nature of the electron-matter scattering can result in different angular distributions. As shown here, at a relatively low forward scattering angle, inelastic scattering is almost always incoherent. Coherent elastic beams at a medium scattering angle are denoted as Bragg scattering, which contains information on the crystal potential within the lattice. At higher angles (> 10°) elastic scattered electrons are more incoherent. Also, multiple electron scattering can happen -at different angles. If the TEM specimen is very thin (usually a reasonable assumption with a well prepared sample), we often approximate the scattering to a single scattering event. It is generally considered that the more scattering events the greater the angle of scatter. Then it is difficult to interpret the images, diffraction patterns and spectra gathered at different scattering angles when an electron is scattered many times (approximate > 20 times).

As discussed above, the angular distribution of electron scattering is fundamentally important in -TEM. Fig. 2.6(b) illustrates these angles, including the incidence/convergence semiangle of the source electron beam α, collection semiangle β and general scattering semiangle θ. -TEM and STEM -use the objective aperture and detectors to collect a certain fraction of the scattering angular distribution.

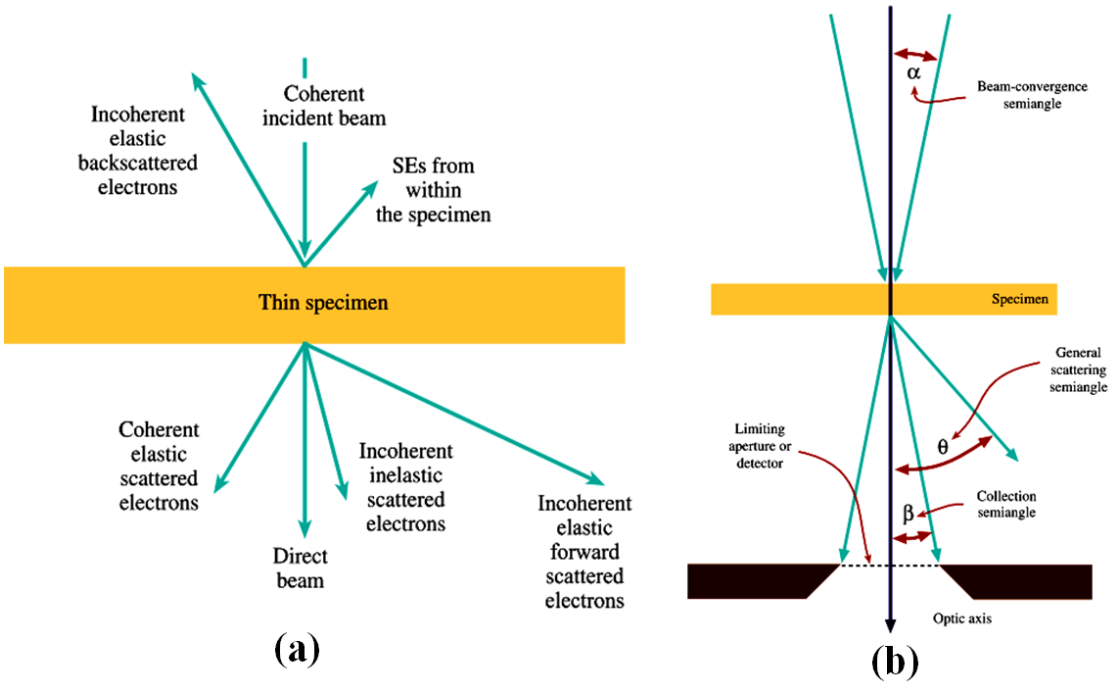

Figure 2.6. (a) Different kinds of electron scattering from a thin TEM specimen, which permits electrons to be scattered in both the forward and back directions. (b) Important angles (i.e., semi-angles) in (S)TEM. All the angles are measured from the optic axis, an imaginary line along the length of the TEM column.[118]

2.2.2.2 Instrumental aspect of electron microscopes

As shown in Fig. 2.7(a), a modern AEM includes various analytical techniques; whereas, conventionally all TEMs contain three essential components, as illustrated in Fig. 2.7(b), (1) the illumination system, (2) the electromagnetic lens system (objective lenses and sample stage) and (3) the imaging system. The illumination system consists of the gun and the condenser lenses; in general, it takes electrons from the source and transfers them to the specimen. The electron source is critical to the performance of the microscope. The thermionic source and the filed-emission source are the two most commonly used TEM guns, while the cold-field source is used in a dedicated STEM. No

one source is the best for all application aspects of TEM; stringent requirements are applied for a particular beam of electrons to meet one's specification. By controlling the condenser lens, the illumination system can be operated in two principle modes: parallel beam, which is used for TEM imaging and diffraction; and convergent beam for STEM imaging and microanalysis. The objective lens system is the heart of a TEM, for it is where all electron-matter interactions and fundamental TEM operations (TEM bright/dark field imaging and electron diffraction) take place. The resolving power of a TEM, i.e. resolution, depends largely on the objective lens, which forms the first image. For the state-of –the-art aberration-corrected TEM, the corrector is applied to the objective lens to minimize its spherical aberration, and boost the HRTEM resolution. Finally, the imaging system consists of two lens systems, one for magnifying the image or the diffraction pattern produced by the objective lens, and the other for projecting it onto the screen. The magnifying lenses are referred as the intermediate and diffraction lenses. Alternatively, in STEM, an electron detector coupled to a camera system (TV or CCD) is used to display the STEM image. Since there are at least three magnifying lenses in a TEM, the objective, intermediate and projector lenses, the overall magnification is calculated as the product of the individual magnifying powers of all of the lenses in the system.

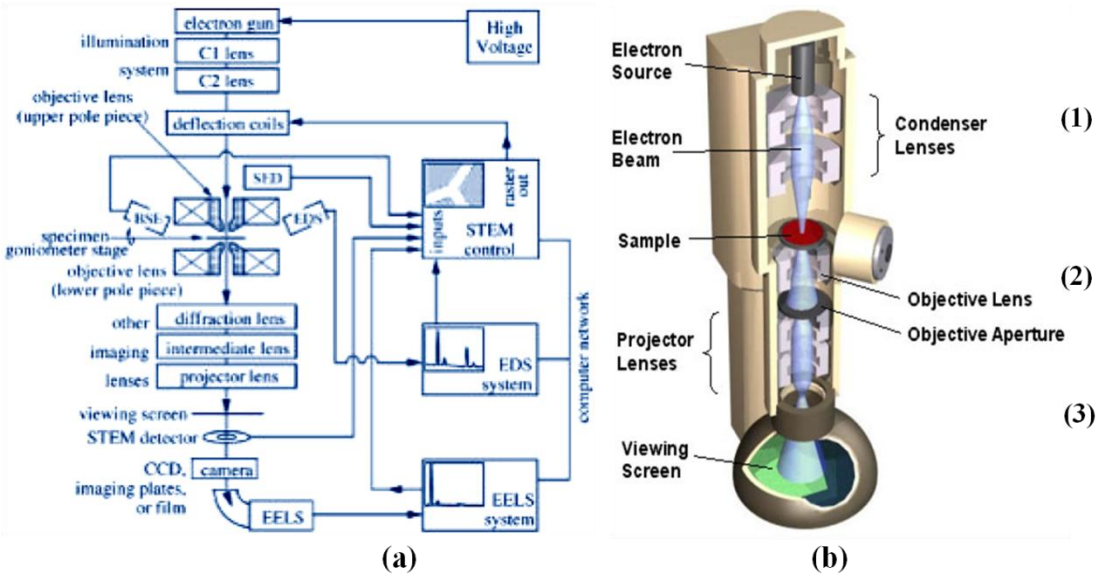

Figure 2.7. (a) The block diagram of a TEM system with various analytical capabilities. (b) Schematic illustration of the three major components of a typical TEM.

2.2.2.3 Electron diffraction

Electron diffraction is a powerful tool in conventional TEM for determining the crystallographic features of a specimen in interest. Coherent scattering events caused by sample periodic lattice can be recorded in the back focal plane of the objective lens. The generation of the electron diffraction spots is schematically illustrated in Fig. 2.8. Since the wavelength of the electron beam is very short (smaller than the lattice distance of most materials), the diffraction angle θ is very small. The Ewald reflection sphere could overlap the low level diffractions - for active state of crystalline plane reflection. The diffraction pattern has characteristic diffraction spots related to the reciprocal lattice vectors of the crystal. Although selected area electron diffraction (SAED) has a much higher spatial resolution compared to XRD, the smallest sample region it characterizes is limited by the size of the selective aperture (usually > 150 nm in diameter).

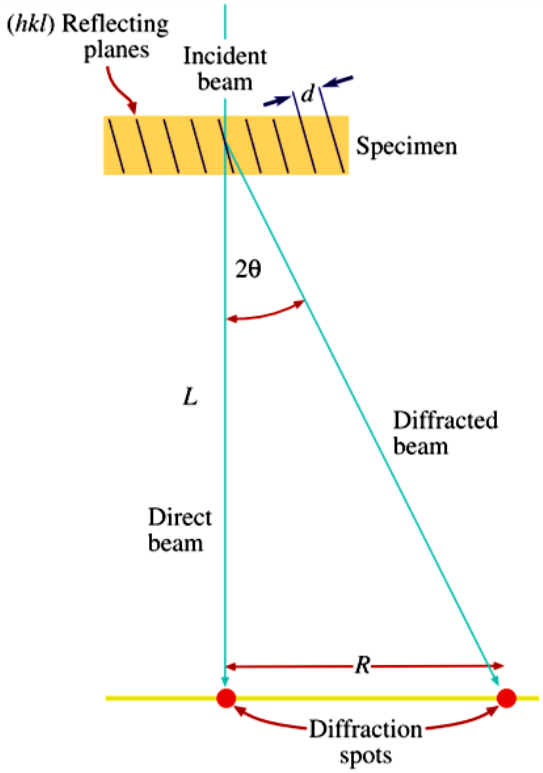

Figure 2.8. A schematic illustration of the generation of electron diffraction spots. The spacing R between the direct beam and a scattering maximum is reciprocal to the lattice distance d. L is the camera length.

2.2.2.4 High resolution transmission electron microscopy

The role of a microscope (electron microscope or optical) in terms of forming an image is that it transforms each point on the specimen into an extended region in the image. The mathematical expression of the extended region in the image which corresponds to the point r is:

$$g(r) = \int f(r')h(r-r')dr' = f(r) \otimes h(r) \qquad (2.2)$$

where, *f(r)* is a specimen function, *h(r)* is the point spread function and $\otimes$ means convolution which Indicates the two functions are "folded together". The term *h(r-r')* is

a weighting term telling us how much each point in the specimen contributes to each point in the image. In reciprocal space, (2.2) can be written as,

$$G(g) = H(g)\,F(g) \tag{2.3}$$

where $\boldsymbol{g}$ is called the spatial frequency. The factors contributing to $H(\boldsymbol{g})$ include: the aperture function $A(\boldsymbol{g})$, the envelope function $E(\boldsymbol{g})$ and the aberration function $B(\boldsymbol{g}) = exp\{-i\chi(g)\}$. This limits the resolution.

One the other hand, the interaction between an electron of energy E and the crystal potential φ(r) is given by the Schrödinger equation,

$$[-\frac{h^2}{8m\pi^2}\nabla^2 - e\phi(r)]\psi(r) = E\psi(r) \tag{2.4}$$

where m is the relativistic electron mass and h is Planck's constant. The Schrödinger equation above cannot be solved directly without making various approximations. Depending on how the problem is formulated, one can derive the most common solutions to the electron wave field at a position T within the specimen. In the Weak Phase Object Approximation (WPOA), the phase of the electron wave function after traversing a specimen of thickness T is given as,

$$\psi(x,y,z=T) \approx \psi(x,y,z=0) = exp[-i\sigma V_p(x,y)T] \approx 1 - i\sigma V_p(x,y)T \tag{2.5}$$

where $V_p(x,y)$ is the average potential per unit length, and σ is an interaction constant. The WPOA only applies to very thin specimens of the order of a few tenths of angstrom, depending on the atomic number of the atoms in the structure.

Applying the WPOA to the above optical system (2.2), then the specimen function $f(r) = 1 - i\sigma V_p(r)T$, and accordingly the wavefunction in the image is given by $[1\text{-}i\ \sigma V_p(r)T] \otimes h(r)$. As shown in (2.3), the complex convolution can be avoided by

writing the expressions in reciprocal space. Thus, the effect of the microscope lenses is described by modifying the exit plane wave using the aberration function $B(\boldsymbol{g})$ in the form,

$$\psi_i(g) = \psi(g) exp\{-i\chi(g)\} \tag{2.6}$$

The lens aberrations, with a core $\chi(\boldsymbol{g})$ of the exponential, produce relative phase shifts of the electron waves associated with individual rays. A simplified but frequently used form is thus obtained writing with the third-order spherical aberration parameter and the objective lens defocus parameter,

$$\chi(g) = \frac{1}{4} Cs\, \lambda^3 g^4 + \frac{1}{2} Z\lambda g^2 \tag{2.7}$$

where C_S is spherical aberration. The phase contrast transfer function (CTF) is defined as $-\sin 2\pi\chi(\boldsymbol{g})$. An example of a CTF for a 200 kV TEM with field emission gun (FEG) is presented in Fig. 2.9 under two important phase contrast conditions. To form images, resolution is not sufficient and contrast is also required. HRTEM is based primarily on phase contrast. This means that the information on the specimen structure is largely provided by locally varying phase shifts of the electron waves. Because phases cannot be seen, HRTEM faces the problem -that phase information must be converted into amplitude information. Scherzer proposed that the phase shifts described by the aberration function depending on $\boldsymbol{g}$ may be a solution. However, the result is far from ideal since the phase changes depend in a highly nonlinear fashion on $\boldsymbol{g}$. On the basis of equation (2.7), Scherzer derived the following relations for optimum phase contrast,

$$Z_S = -(\frac{4}{3} Cs\lambda)^{1/2} \tag{2.8}$$

$$d_S = g_S^{-1} = \frac{1}{2}(3Cs\lambda^3)^{1/4} \quad (2.9)$$

where Z_S is the so-called Scherzer defocus and d_S is the Scherzer or point-resolution limit. Under the Scherzer defocus, as shown in the CTF in Fig. 2.9(a), the modulus of the transfer function is close to -1 (phase shift close to $\pi/2$) over a certain range. And this is achieved at the price of rapid contrast oscillations for $\boldsymbol{g} > 4$ nm^{-1}. An objective lens aperture must be used to avoid the associated artifacts in the image by preventing beams corresponding to the rapid contrast oscillations for $\boldsymbol{g} > 4$ nm^{-1} from contributing to the image.

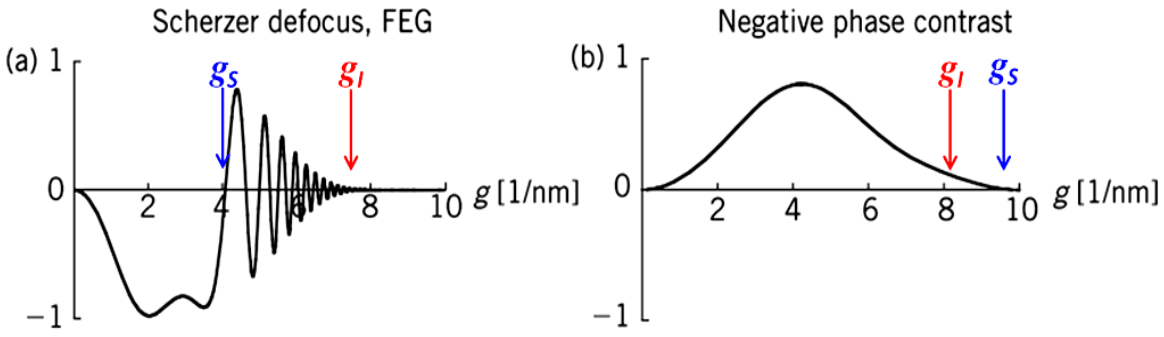

Figure 2.9. (a) Contrast transfer function (CTF) − sin $2\pi\chi(g)$ for a 200 kV electron microscope equipped with a field-emission gun (FEG). (b) The CTF for NCSI conditions in the aberration-corrected instrument. Although the modulus of the CTF is apart from the maximum, no contrast oscillations occur and the whole range of g up to the information limit is contributing to the image.[77]

Consequently, in the conventional uncorrected HRTEM, even under the optimum phase contrast at Scherzer defocus, the information on sample details corresponding to the high spatial frequency range between g_S and the information limit g_I is lost, despite the fact that this information is transferred by the optical system. This is why

conventional HRTEM images are not atomic resolution images. In comparison, in Fig. 2.9(b), the transfer characteristic of C_S-corrected HRTEM under the negative spherical aberration imaging (NCSI) condition is extended up to the limit g_I without oscillation. The detailed atomic information from high space Fourier component is then transferred and recorded in the image.

2.3 Atomic-scale thin film microstructure characterization

2.3.1 The limits of HRTEM in resolving heterointerface structure

In phase-contrast-dominant HRTEM images, it is known that the image contrast reverses with sample thickness and microscope focus.[119, 120] In the works of this dissertation, high-angle annular dark-field scanning transmission electron microscopy (HAADF-STEM) has been chosen over HRTEM images in investigating the defective feature of various heterogeneous interfaces. One main reason is that, as shown in Fig. 2.10, at the heterointerface of $LaAlO_3/SrTiO_3$ (LAO/STO), where the lattice varies rapidly due to the strain introduced by the lattice mismatch; in a representative HRTEM image (Fig. 2.10(a)), it is difficult to achieve a response for the contrast transfer function that is flat enough to avoid the inversion of contrast at the strained heterointerface. On the other hand, a STEM image (Fig. 2.10(b)) taken from the same TEM sample, shows well defined contrast maxima, which is crucial for later the image-based lattice strain measurement in Chapter VII. Similarly, In the case of a $SrTiO_3$/MgO (STO/MgO) heterogeneous interface, misfit dislocations were generated to relax the large lattice

mismatch (~ 8%). In HRTEM, a high density of misfit dislocations and associated defects introduce even greater local lattice distortions, and resulting contrast reversals.

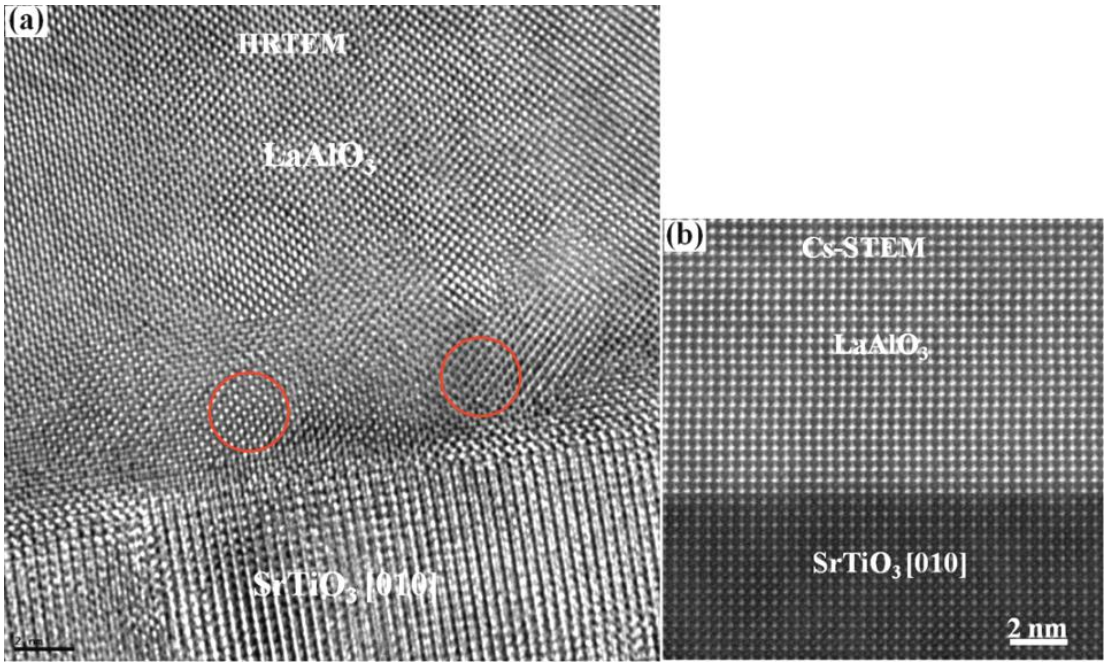

Figure 2.10. (a) A representative HRTEM image and (b) a C_S-corrected HAADF-STEM image of the LAO/STO heterointerface in <100>. Both images were taken from the same TEM cross section specimen.

Additionally, in the case of layered perovskite YBCO epitaxial thin films, HRTEM images, as presented in Fig. 2.11 (a) and (b), have difficulties to identify the exact atomic arrangement of the intrinsic planner defects, even though HRTEM simulations have been also applied. In comparison, the corresponding C_S-corrected STEM images (Fig. 2.11 (c) and (d)) show details about the number of the inserting CuO-planes as well as the orientation of the planner defects (details see Chapter IV).

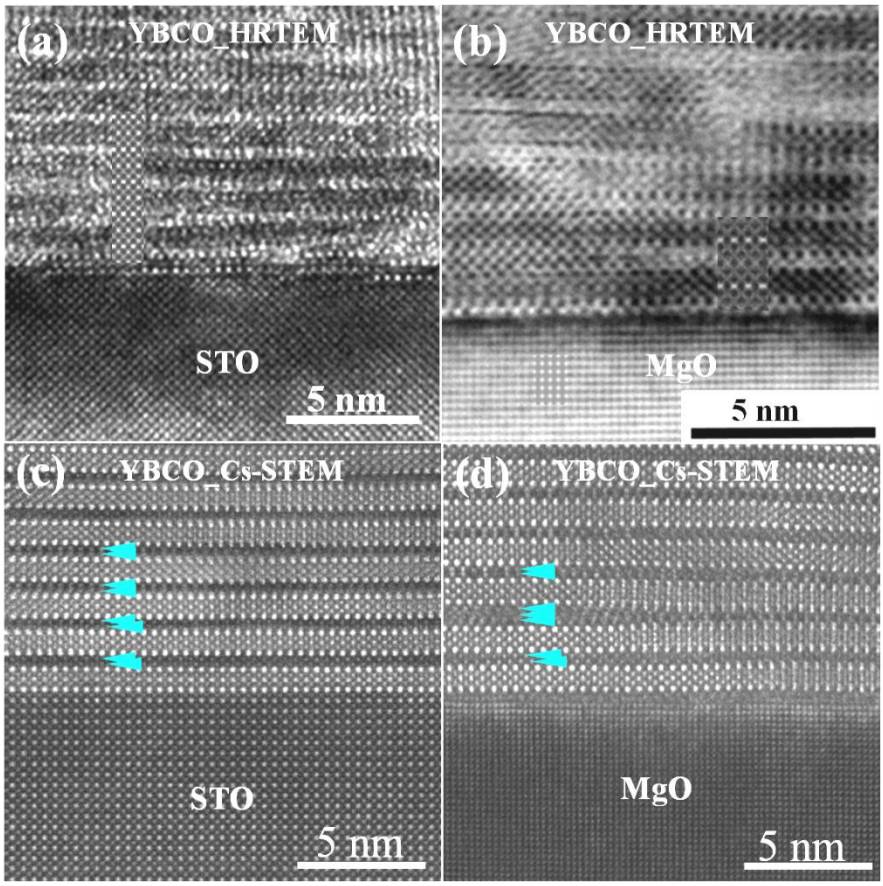

Figure 2.11. Representative HRTEM images of superconducting YBCO thin films on (a) STO and on (b) MgO substrate. (c) and (d) C_S-correction HAADF-STEM images of the same TEM samples.

Thus, we have adopted STEM imaging to study the heteroepitaxial structures for the following reasons, (1) the contrast of STEM images is less sensitive to local sample variations; it has been experimentally confirmed that no contrast reversal in STEM up to a wide range of focus and foil thickness;[121] (2) STEM allows high resolution images to be taken from thicker foils to minimize surface relaxation,[122, 123] maintaining a authentic strain condition in the epitaxial film; (3) Z-contrast STEM image adds another dimension for mapping lattice chemistry distribution at the same time.

2.3.2 Aberration-corrected scanning transmission electron microscopy

The origin of scanning transmission electron microscopy (STEM) dates back to 1938 when Manfred von Ardenne published the first results from an "Electron Raster-microscope" that displayed a 40 nm resolution in the scan direction. The first Z-contrast image was obtained by a ADF detector collecting from the inelastically scattered electrons by a spectrometer at the base of the microscope.[124] The benefit of STEM imaging is the incoherent character, which excludes phase contrast within the image allowing the images to be directly interpretable from the sample structure.[125] Overall the application of spherical aberration correction is more successful in STEM than HRTEM mode, exhibiting 0.47 Å resolution[126] compared to C_S-corrected HRTEM which limited around 0.8 Å[127] in 2009. The collection of high-resolution images with simultaneous analytical methods makes STEM a very powerful nanoscale analytical instrument.

2.3.2.1 STEM image formation and Z-contrast imaging

Electron beam scans across a specimen -causes the convergent probe to scatter electrons forming a site specific convergent beam electron diffraction (CBED) pattern. Information in the image is dependent on the detector position and size since only a portion of the information scattered by the sample is collected. As shown in Fig. 2.12, the ADF detector collects high angle scattered electrons about the optic axis, and displays the elastically scattered information in ADF STEM images. Altering the

collecting angular range of the ADF detector can change the information transferred to the image, providing the ability to select signals of interest.

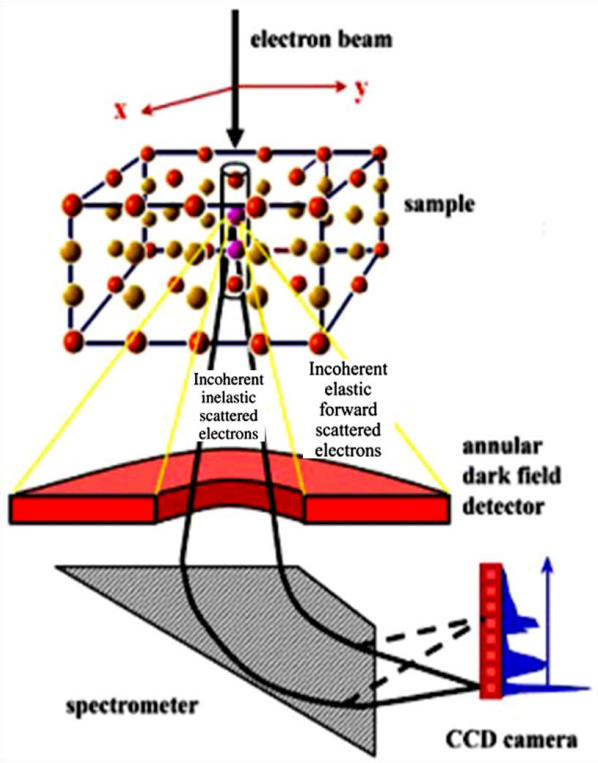

Figure 2.12. Schematic illustration of the formation of STEM image. In STEM the probe is scanned across the specimen. For each position of the probe, electrons are collected by a bright field or annular dark field detector. A spectrometer can also be used to record an electron energy-loss spectrum.

In STEM, the focused probe forms a cone of illumination in which the partial plane-wave components compose the amplitude of the probe wave function, with the magnitude dependent on the convergence angle and the phase dependent on the lens aberrations and defocus value. Under these conditions, it has been shown that the wavefunction exiting the crystal may be composed of the 1s Block states and match

fairly well to experimental images since these states impose the strongest scattering interaction.[128] The 1s states minimally overlap with neighboring atoms and therefore are the most localized in real space.[125] The contribution of different states depends on the depth within the crystal as well as the probe position on forming intensity peaks over atomic positions within the specimen.

In regards to the transfer function for STEM imaging, there are no contrast reversals as we previously discussed in the condition of HRTEM. The incoherent transfer function is a smooth decaying positive function. The resolution for incoherent imaging imposes a different resolution limit than HRTEM, allowing for higher resolution with ADF STEM at the same wavelength and spherical aberration values, [129]

$$r_{incoherent} = 0.43\ (Cs\lambda^3)^{1/4} \tag{2.10}$$

In the absence of multiple scattering, the intensity variations in the image are proportional to the mass and thickness changes.[125] The scattering of the incident electron wave to high angles caused by Rutherford scattering from the atomic nuclei gives rise to incoherent atomic number (Z) contrast imaging. Through this model the electron is scattered more strongly by atoms with a higher mean inner potential, therefore a higher Z. The exponential relationship between the intensity in the image and the atomic number varies between 1.6 to 1.9 for a given microscope setup.[130] This analysis simplifies the interpretation of the image since phase contrast is not a component.

2.3.2.2. Spherical aberration correction in STEM

Spherical aberration is one of the major intrinsic aberrations that limit the spatial resolution in modern electron microscopy. Aberration-corrected STEM techniques are well recognized currently for their high spatial resolution and high sensitivity for chemical analysis.[131] The electron probe size and thus the spatial resolution of STEM imaging and chemical analysis are mainly limited by the third-order spherical aberration coefficient (C_S), which is unavoidable for conventional rotationally symmetric magnetic lenses. This limitation can be overcome by using a series of multipole lenses that break the rotational symmetry.[132]

Two different types of spherical aberration correctors for STEM instruments are now commercially available from Nion Company[82] and Corrected Electron Optical Systems(CEOS).[133] The Nion probe C_S-correctors are specially designed for dedicated VG STEM instruments, and consist of three octupoles and four quadrupoles that are placed between the second condenser lens and the scan coils before the objective lens of the instrument schematically illustrated in Fig. 2.13(a). The CEOS C_S-correctors, based upon a design first proposed by Rose,[133] are designed to fit into most modern (S)TEM instruments. It consists of two hexapoles and several additional coupling lenses, which are also located between the condenser lenses and the objective lens of the (S)TEM instrument as shown in Fig. 2.13 (b).

Thus, an spherical aberration-corrector uses sophisticated electron optics (with ~ 100 independent elements), that are tuned and diagnosed by computer programs to

produce a very small electron probe, down to sub-angstrom, has been achieved in scanning transmission electron microscopy (STEM) [126, 134].

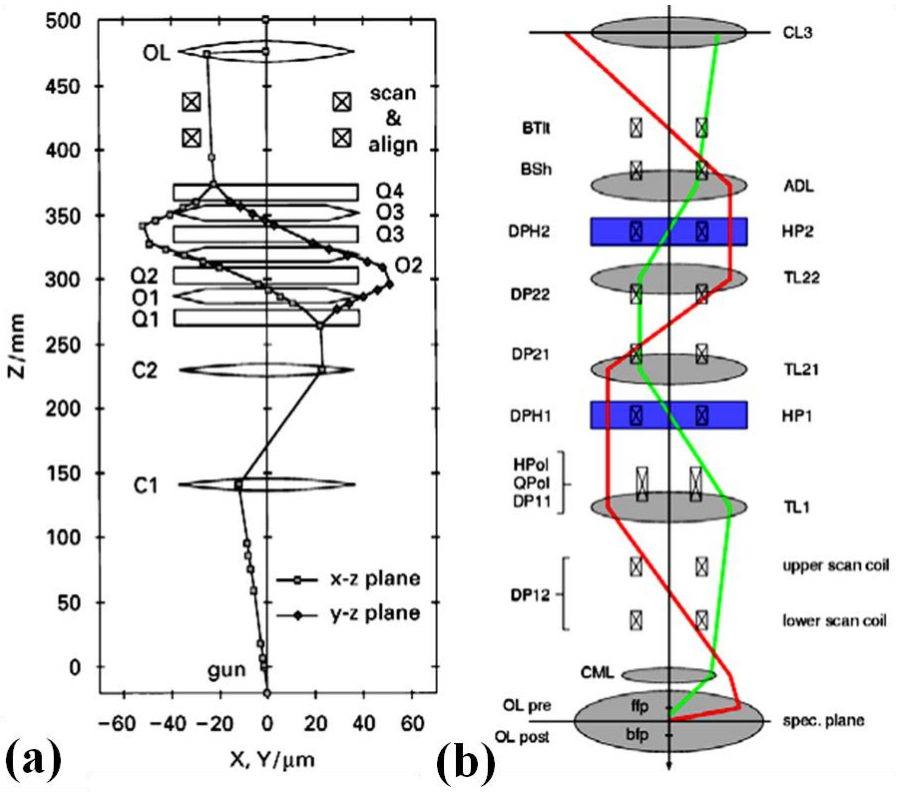

Figure 2.13. Schematic diagram of the principal electron optical elements of C_S correctors developed by (a) Nion Co.[82] and by (b) CEOS for STEM, and their first-order electron trajectories. The electron gun is situating at the bottom and top of (a) and (b) respectively.

2.3.2.3. Practical C_S-corrected STEM set up

In the works of this dissertation, TEAM 0.5,[135] a modified FEI Titan microscope with a special high-brightness Schottky-field emission electron source and an improved hexapole-type illumination aberration corrector, was employed. By correcting the spherical aberration up to the fifth-order using the illumination aberration corrector,

TEAM 0.5 allows a larger beam convergence angle which provides a small electron probe of high current.

The sophisticated design of C_S-correctors requires computer-aided measurement of all the axial aberrations of the microscope system and automatic tuning of all the magnetic components for an optimum performance. Zemlin tableaus[136] are employed to tune the CEOS C_S-correctors, in which a systematic series of images from standard Au nanoparticles samples are taken at various beam tilt angles at both under and over focus conditions. As shown in the screen shot in Fig. 2.14, images of the electron probe, as well as the precise astigmatism and defocus values at each beam tilt angle, can then be determined by deconvoluting the paired under/over-focus images in the control software. By repeating this process at various beam tilt angles, the magnitude of all the aberration coefficients can be deduced. The lens setting of the corrector can then be tuned accordingly to compensate the aberration of the microscope objective lens. After aberration correction, the large flat central disk presented in Fig 2.14 indicates that the C_S-free region has been extended to a larger convergent angle, and effectively a shaper electron probe (higher intense and smaller diameter).

One of main advantages of the aberration-corrected STEM is thus a significant improvement in the spatial resolution as high as 0.5 angstrom (also the electron probe size).[137] This sub-angstrom electron probe is much smaller than a typical lattice spacing of 2 angstrom, which helps minimize the transverse interference effects between neighboring atomic columns.[138] All ADF-STEM micrographs in this dissertation were recorded in TEAM 0.5 with a convergence semi-angle of 17 mrad after fine-tuning of

the probe corrector at 300 kV to a flat-phase angle of over 25 mrad (typical residual aberration coefficients are listed here[126]). Unless stated otherwise, an ADF detector inner semi-angle of 68 mrad was used for the Z-contrast imaging, which gave reasonable signal-to-noise ratios.

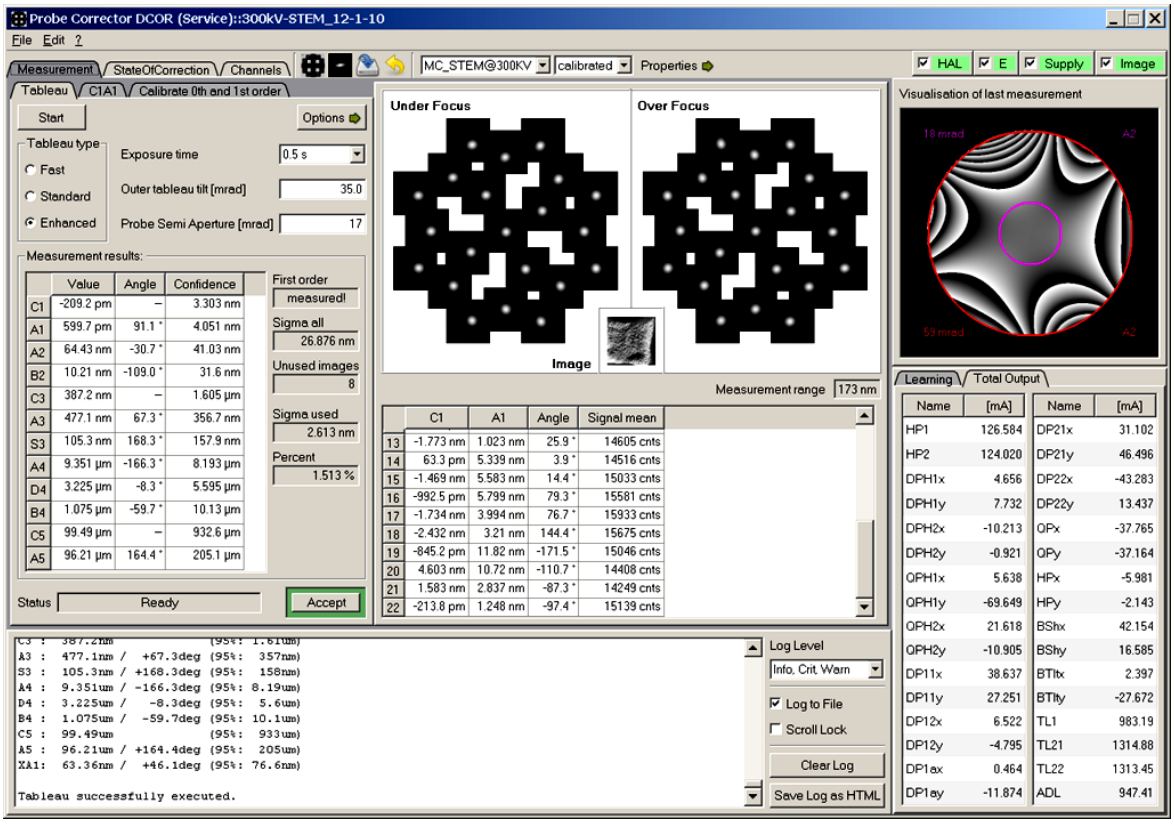

Figure 2.14 Screen shot of the CEOS control software showing the Zemlin tableau and the aberration values determined from the electron probe shape at various tilting angles. The result was obtained on the TEAM 0.5 microscope.

2.3.3 Geometric phase analysis (GPA)

2.3.3.1. GPA algorithm

In this dissertation, a commercial program, a plug-in of Digital Micrograph (DM 1.8.3 package, HREM Research Inc.), was used for geometric phase analysis. Developed by Hÿtch and colleagues,[108] the geometric phase algorithm reconstructs the displacement field utilizing Fourier filtering centered around two non-collinear Bragg vectors of the power spectrum generated from a high resolution micrograph. The vectorial representation of the displacement field is,

$$u(r) = -(1/2\pi)[Pg_1(r)a_1 + Pg_2(r)a_2] \quad (2.11)$$

where r is a position in the image, a_1 and a_2 are the associated lattice vectors of g_1 and g_2 in real space. $Pg_1(r)$ and $Pg_2(r)$ are the two geometric phase images presenting the local deviation in two chosen set of lattice planes from a reference lattice. The "phase" in GPA does not refer to the electron wave function, but to the position of image contrast maxima, so it is called "geometric" phase. In this study, for the cubic structures two low-order vertical vectors g_1 = [020]* and g_2 = [002]* were usually selected. Then, the derivation of the displacement field gives strain field in a principle direction,

$$\varepsilon_{xx} = \partial u_x(r)/\partial x,\ \varepsilon_{yy} = \partial u_y(r)/\partial y \text{ and } \varepsilon_{xy} = \tfrac{1}{2}\,(\partial u_x(r)/\partial y + \partial u_y(r)/\partial x) \quad (2.12)$$

Thus the biaxial strains of ε_{xx} (in-plane), ε_{yy} (out-of-plane) and ε_{xy} (shear strain) are derived to illustrate the local lattice displacement from the reference lattice. For additional mathematical and theoretical discussion of GPA, please see.[108, 139]

Note that the strain determined by GPA here is a relative value. For example, in the case of interface lattice strain, where the substrate lattice are usually selected as reference, then $\varepsilon_{xx}^{GPA} = \varepsilon_{xx}^{relative} = (a^{local} - a^{sub})/a^{sub}$; the sign of the ε means that the measured local lattice is larger ('+') or smaller ('-') than the reference lattice. In this study, reference regions with a size of 256 × 256 pixel were selected for all 1024 × 1024 pixel images (and 128 × 128 pixel reference for the images of 512 × 512 pixels). The relative strain can be easily transformed into the conventional strain when the reference lattice parameter and the bulk material lattice are known, $\varepsilon_{xx}^{absolute} = (a^{local} - a^{bulk})/a^{bulk}$; or one can simply calculate the actual local lattice parameters (of the thin film, as the substrates are usually a standard crystal with a known lattice parameter) for further analysis. GPA generates strain maps with color contour directly illustrating the location relative strain. Unless state otherwise a scale range of -10% to +10% was applied to all strain maps for consistency.

2.4 Thin film physical property measurement

The superconducting properties of the YBCO and the $Fe_{1+y}Te_{1-x}Se_x$ epitaxial thin films have been conducted in a Physics Property Measurement System (PPMS 6000 Quantum Design) with R-T measurement and a vibrating sample magnetometer (VSM) head and resistivity options. This system is very powerful and can achieve magnetic fields up to ±9 T and a temperature range of 1.9 K to 400 K. The VSM measurement noise is less than 5×10^{-7} emu. There are two resistivity options. AC transport option is

optimized for samples from nΩ to kΩ and thus can be used to measure highly conducting materials such as metals. DC resistivity option is optimized for samples whose resistance is in the range of ~Ω to ~MΩ and thus can be used to measure the conducting (also for superconductors such as YBCO at room temperature) and semiconducting materials. It can measure a resistance up to 5×10^6 Ω.

Fig. 2.15(a) shows the PPMS basic components. The black container is the EverCool Dewar system. The right side blue box is the control area network electronics tower for VSM option. Fig. 2.15(b) shows the sample motor and detection coil set for VSM option. After loading the VSM sample in center of the magnet, the induced voltage can be detected by oscillating the sample near a detection coil. There are two different types of VSM measurements. The first type is studying the magnetization vs. magnetic field (M-H) of perovskite oxide thin films. In these measurements, a magnetic field is applied in parallel to (in-plane) or perpendicularly (out-of-plane) to the film surface.

In this dissertation, the superconducting properties of YBCO and $Fe_{1+y}Se_{1-x}Te_x$ epitaxial thin films were characterized using resistivity–temperature (R–T) measurement by a four point probe method from 2 to 300 K in the PPMS. Both the self-field and in-field critical current densities (J_C) were measured under an applied magnetic field up to 7 T at various temperatures (2 K, 4 K or 5 K and 7 K) by the VSM in the PPMS. As for magnetic characterization, due to that the restraining force F_p is always against flux motion, a flux density gradient is then established across the sample. It causes hysteresis of the magnetic moment (M) during the magnetization of a hard superconductor.

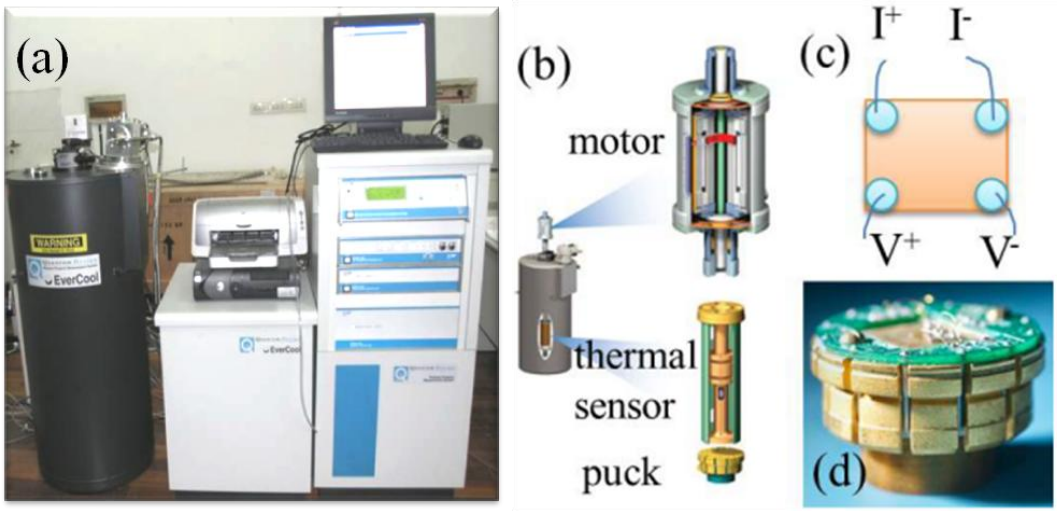

Figure 2.15. (a) The PPMS equipment used in the laboratory. (b) The sample motor drive and detection coil set for VSM option and sample puck for resistivity option. (c) The typical van der Pauw measurement setup. (d) Sample puck for resistivity option.

The magnetization difference ΔM between up and down branches is proportional to J_c, according to the Bean model in the situation where the H is applied along the film surface. For the geometry with H applied perpendicular to the film, which is the most important scenario for most of the applications, the modified Bean model is applied:

$$J_c = 20\Delta M/[2(1 - w/3l)] \tag{2.13}$$

where w and l is the width and length of the film and M here is the magnetic moment per volume. The above equation was used to transfer the measured magnetization difference to the superconductor property parameter critical current density.

CHAPTER III

ATOMIC-SCALE INVESTIGATIONS OF INTRINSIC CHEMICAL INHOMOGENEITY IN SUPERCONDUCTING $Fe_{1+y}Se_{1-x}Te_x$ EPITAXIAL FILMS*

3.1 Overview

The spatial relationship of the intrinsic chemical inhomogeneity of Te, Se and the interstitial iron (iron in 2c Wyckoff sites Fe(2)) in the $Fe_{1+y}Te_{1-x}Se_x$ system has been studied in this work with the state-of-the-art aberration-corrected scanning transmission electron microscopy (Cs-corrected STEM). By comparing two highly epitaxial $Fe_{1+y}Te_{1-x}Se_x$ films prepared by standard pulse-laser deposition, we found the film growth atmosphere can greatly affect the stoichiometry, the homogeneity of Se/Te ordering, and thus superconducting properties. For the first time, the local atomic arrangement of the Te and Se as well as Fe(2) has been clearly revealed. Films grown in a vacuum environment exhibit near-randomly distributed Se/Te and highly localized Fe(2), with a relatively higher superconducting transition temperature. The significance of the chemical inhomogeneity has been discussed in relation to the scale of the coherence length in iron chalcogenide superconductors.

---

*This chapter is reprinted with permission from "Atomic-scale investigations of intrinsic chemical inhomogeneity in superconducting Fe1+ySe1-xTex epitaxial films" by Y. Zhu, L. Chen, J. Ciston and H. Wang, Journal of Physical Chemistry C, in press (2013). Copyright © 2013 American Chemical Society.

3.2 Introduction

Since the discovery of superconductivity in $LaFeAsO_{1-x}F_x$ in 2008,[23] iron-based superconductors have attracted great research interest as an alternate, non-cuprate unconventional high temperature superconductor.[140] The discovery of arsenic-free iron selenide (FeSe) with a critical transition temperature (T_C) around 8 K provides a model system to study the superconducting mechanism of iron-based superconductors.[27] The T_C of FeSe can be further boosted by applying external pressure (T_C = 36 K at 8.9 GPa)[141] or by incorporating isovalent dopants such as Te.[28] More interestingly, the T_C of the ternary compounds $Fe_{1+y}Te_{1-x}Se_x$ is almost doubled at the optimized tellurium concentration of 50% (15 K, in bulk),[28] even though the other end phase, $Fe_{1+y}Te$, is not superconducting but exhibits long-range antiferromagnetic (AFM) order with a distinct wave vector (π, 0).[29] In contrast to their simple crystalline structure (anti-PbO tetragonal structure, without a La(O, F) "charge reservoir'' layer),[26] $Fe_{1+y}Te_{1-x}Se_x$ compounds tend to accommodate significant nonstoichiometric disordering.[25]

There are generally three major types of chemical inhomogeneity in $Fe_{1+y}Te_{1-x}Se_x$: (1) impurity phases, such as Fe_7Se_8,[142] Fe_3O_4[143] etc., whose origin is attributed to the complexity of the Fe chalcogenide phase diagram[144] and possible oxygen contamination;[145] (2) iron interstitials (i.e. Fe(2)[146]), appear to always partially occupy the 2c site in the chalcogen layer;[147, 148] (3) congeneric phases with different Se/Te ratios, attributed to the distinct *z*-coordinates of the Se and Te ions (and different bonding angles and bonding lengths with Fe) in $Fe_{1+y}Te_{1-x}Se_x$ crystals yielding a lower

symmetry.[26] The presence of these stoichiometry fluctuations is often accompanied by crystallographic imperfections such as lattice distortion,[26] crystal mosaicity[149] and planar defects such as grain/phase boundaries.[32] Lattice disordering can in turn affect the compound's chemical inhomogeneity and thus the superconducting properties. In particular, $Fe_{1+y}Te_{1-x}Se_x$ thin films were found be able to either further boost the T_C (e.g. onset T_C = 21 K[33]) [150] or destroy the superconductivity [151], owing to the interface strain modification.[152]

The effects of chemical inhomogeneity in the $Fe_{1+y}Te_{1-x}Se_x$ system are closely tied to the delicate interplay between magnetism and the superconductivity.[153, 154] Since most of the type one foreign impurities are magnetic, they usually suppress the superconductivity of the parent phase.[145] Similarly, the type two inhomogeneity in the form of iron interstitials also suppresses superconductivity of the parent FeSe and the $Fe_{1+y}Te_{1-x}Se_x$ compounds[143, 149, 155] through charge-carrier localization.[149] However, experiments on $Fe_{1+y}Te_{0.5}Se_{0.5}$ with different Fe(2) concentrations found a positive correlation between small amounts of Fe(2) and T_C.[147] In the case of Te/Se inhomogeneity, some studies reported nonuniform distribution of Te and Se ions with phase-segregated regions ranging from sub-micron[156] to tens of nanometers (in clusters).[157] Others proposed that Se and Te could be organized in regular fashions as a supercell.[158] A scanning tunneling microscopy (STM) study investigated the topography of a freshly cleaved $FeSe_{0.55}Te_{0.45}$ single-crystal; the results yielded small Te- (or Se)-rich phases of only a few angstroms in *ab*-direction.[159] Recent physical property studies pointed out that in $Fe_{1+y}Te_{1-x}Se_x$ single crystals greater structural inhomogeneity leads to

a better overall superconductivity.[142, 149] The exact spatial relationship between the Te and Se (and Fe(2)) is crucial for providing the structural origin for the candidate pairing mechanism related to (π, π) spin fluctuation[160] and the competing or coexisting magnetic correlations.[29, 154]

To explore this issue, we conducted systematic microstructural characterizations to investigate stoichiometry inhomogeneity in superconducting $FeSe_{0.5}Te_{0.5}$ (nominal) films. In this work, we focused on two $FeSe_{0.5}Te_{0.5}$ films, one deposited under a controlled oxygen atmosphere and the other grown in vacuum. The average film crystallographic properties were examined by X-ray diffraction (XRD) and electron diffraction. Chemical inhomogeneity was firstly examined by energy dispersive X-ray analysis (EDX) in transmission electron microscope (TEM), and the vacuum-grown iron-rich sample with a higher T_C was studied using high resolution aberration-corrected scanning transmission electron microscopy (Cs-corrected STEM). In particular, the occupancy of the Te and Se and the distribution of Fe(2) were examined atomic-column-by-atomic-column leading to a schematic 3D model of $FeSe_{0.5}Te_{0.5}$ lattice. Moreover, the heterogeneous interface structures of $FeSe_{0.5}Te_{0.5}/SrTiO_3$ including substrate steps, interface contact and misoriented film grains were directly observed and discussed with atomic models.

3.3 Experimental

The deposition of the $Fe_{1+y}Te_{1-x}Se_x$ films was conducted by a standard pulsed-laser deposition (PLD) technique (KrF excimer laser λ = 248 nm) using a target with nominal composition of $FeSe_{0.5}Te_{0.5}$. In this work, we focused on the microstructure of two $Fe_{1+y}Te_{1-x}Se_x$ films, up to a thickness of approximately 150 nm, grown on single crystal $SrTiO_3$(100) substrates in vacuum (~10^{-4} Pa) and in a controlled oxygen atmosphere (~10^{-2} Pa with a base pressure in vacuum), respectively. The details on target processing and deposition parameters can be found elsewhere.[161]

A systematic microstructural characterization was conducted via XRD (BRUKER D8 powder X-ray diffractometer), energy dispersive X-ray analysis (EDX), selected-area electron diffraction (SAED) and Cs-corrected STEM. EDX and SAED were performed using a JEOL JEM-2010 equipped with a beryllium double-tilt holder, an Oxford instruments ATW type EDX detector and INCA Energy TEM platform. All EDX spectra were obtained at the electron transparent regions of the TEM specimen with a spatial resolution about 30 nm.[162] Estimated from the commercial single-crystalline $SrTiO_3$ substrate, an analytical EDX error of ± 2% was achieved. In this work, TEAM 0.5,[135] a modified FEI Titan microscope equipped with a special high-brightness Schottky-field emission electron source as well as two improved hexapole-type spherical aberration correctors was employed. Correcting the spherical aberration up to fifth-order by the illumination aberration corrector, TEAM 0.5 allows a larger beam convergence angle, providing a small electron probe of high current. One of main

advantages of the aberration-corrected STEM is a significant improvement spatial resolution, which has been demonstrated to be as high as 0.5 Å.[137] All annular dark-field (ADF) STEM micrographs in this report were recorded in TEAM 0.5 with a convergence semi-angle of 17 mrad after fine-tuning of the probe corrector at 300 kV to a flat-phase angle of over 25 mrad (typical residual aberration coefficients are listed here[126]). ADF detector inner semi-angles of 43 mrad and 68 mrad were used. Cross-sectional TEM specimens were prepared through a conventional TEM sample preparation routine including cutting, gluing, grinding, polishing, and final precision ion polishing.

3.4 Results and discussion

The crystal structures of both $Fe_{1+y}Te_{1-x}Se_x$ films have been identified as the P4/nmm tetragonal phase (anti-PbO structure, space group #129[26]) by XRD.[161] No impurity phase, such as Fe_7Se_8[142] or Fe_3O_4[143] commonly observed in single crystal $Fe_{1+y}Te_{1-x}Se_x$, were found in either of our thin films. In Figs. 3.1(a) and 3.1(b), EDX spectra were acquired from 10 distinct electron-transparent areas of the two TEM specimens to determine the local film stoichiometry. Surprisingly, the oxygen-grown film (onset T_C = 11.4 K) is a slightly iron-deficient phase with an average composition of $Fe_{0.96}Se_{0.57}Te_{0.43}$; the vacuum-grown film with a higher transition temperature (onset T_C = 12.5 K)[161] is a Fe-rich phase with an average composition of $Fe_{1.10}Se_{0.55}Te_{0.45}$. In the

oxygen-grown film, the local film composition varies considerably from one region to another, with anti-correlated concentrations of Fe and Te.

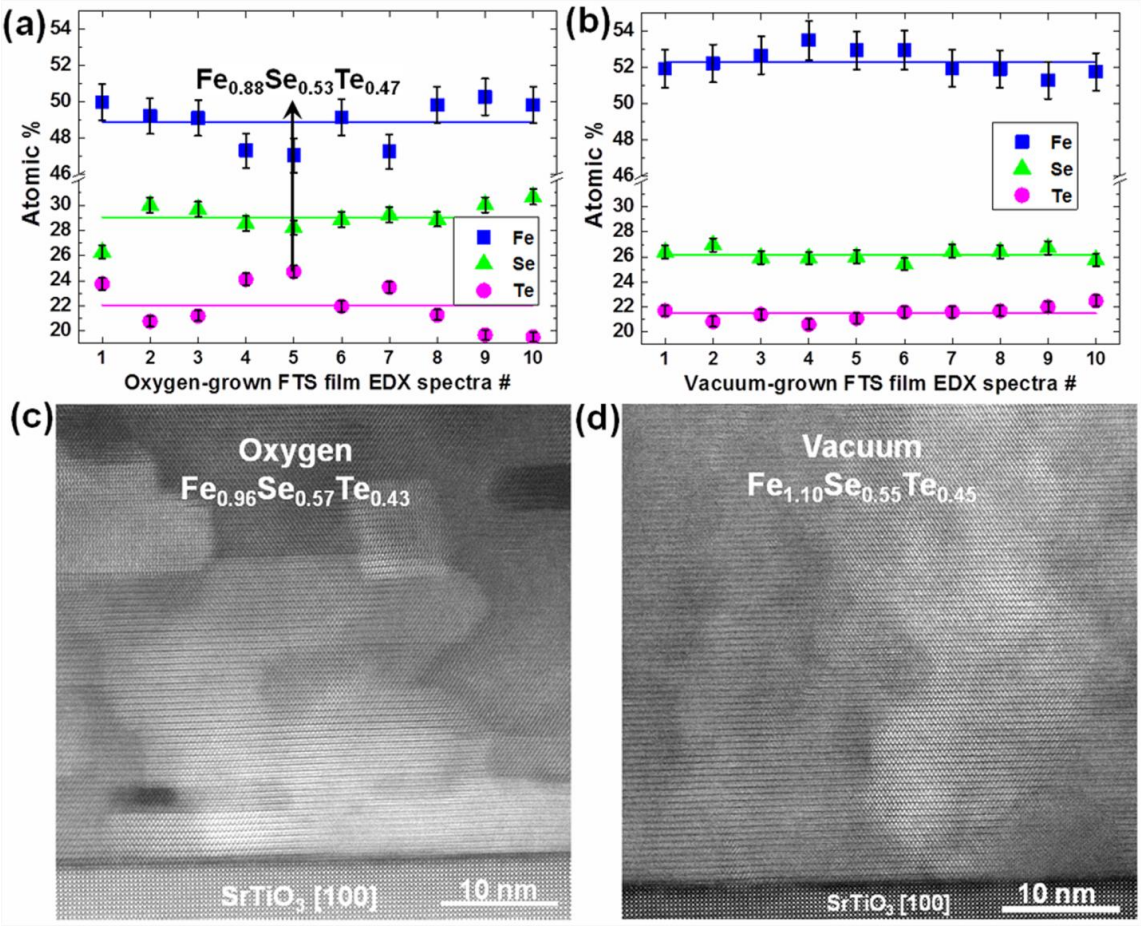

Figure 3.1. (a) Iron, selenium and tellurium concentrations of 10 distinct regions as determined by Energy dispersive X-ray spectroscopy (EDX) of oxygen-grown and (b) the vacuum-grown $FeSe_{0.5}Te_{0.5}$ (nominal) films. The mean concentrations for each element are noted by solid horizontal lines. (c) and (d) show STEM overviews of the two films (not from the same region as the EDX data). The averaged film stoichiometry was noted in the STEM image accordingly.

Te-rich (Fe-deficient) regions were directly observed in later STEM study, shown in a representative cross-section STEM micrograph of Fig. 3.1(c), as bright

clusters about 10 nm to 50 nm in diameter with a rectangular shape (estimated from over 10 STEM micrographs in medium magnification). The tellurium segregation was also found in radio frequency sputtering $Fe_{1+y}Te_{1-x}Se_x$ films even after annealing[156] and in single crystals of superconducting $FeTe_{0.65}Se_{0.35}$ with narrow Fe-deficient "white bands".[142] In comparison, the vacuum-grown $Fe_{1.10}Se_{0.55}Te_{0.45}$ film presents less noticeable heterogeneity, as demonstrated in Figs. 3.1(b) and 3.1(d). The observed contrast in the STEM images contains a partial contribution from diffraction contrast due to the moderately low ADF collection angle (both Figs. 3.1(c) and 3.1(d) were obtained using 43 mrad)[163] as well as to the in-plane grain misorientation.

The vacuum-grown films exhibited a high degree of epitaxy as confirmed by the sharp out-of-plane (00*l*) reflections in the SAED patterns, shown in Figs. 3.2(a) to 3.2(c). Using the STO substrate as reference, the $Fe_{1.10}Se_{0.55}Te_{0.45}$(FST) film lattice parameters were calculated to be a = 3.80 Å, c = 5.86 Å, which agrees well with previous reports on PLD thin films (c = 5.84 ~ 5.89 Å).[33] The (0*l*0) reflections of the FST film are indexed in green, and remain regardless of the selected areas. The predominant in-plane texture orientation was found to be $[100]_{FST}$ || $[100]_{STO}$. It is noted that there are other film in-plane orientations in this vacuum-grown film. In Figs. 3.2(b) and 3.2(c), for example, the minor $[210]_{FST}$ // $[100]_{STO}$ and $[310]_{FST}$// $[100]_{STO}$, were observed as additional film orientations together with the dominant $[100]_{FST}$ one. The angles between these film grains are large, e.g. 26.56° and 18.43° between [210] and [100], and between the [310] and [100], respectively. The impacts of these large angle grain boundaries and associated weak-link effects[164] on the critical current density ($J_c^{\text{self-filed}}$ in particular), as indicated in

our previous reports,[161] are not significant. This is likely because the misoriented film grains represent only a minor fraction of the whole, and are not continuous throughout the film.

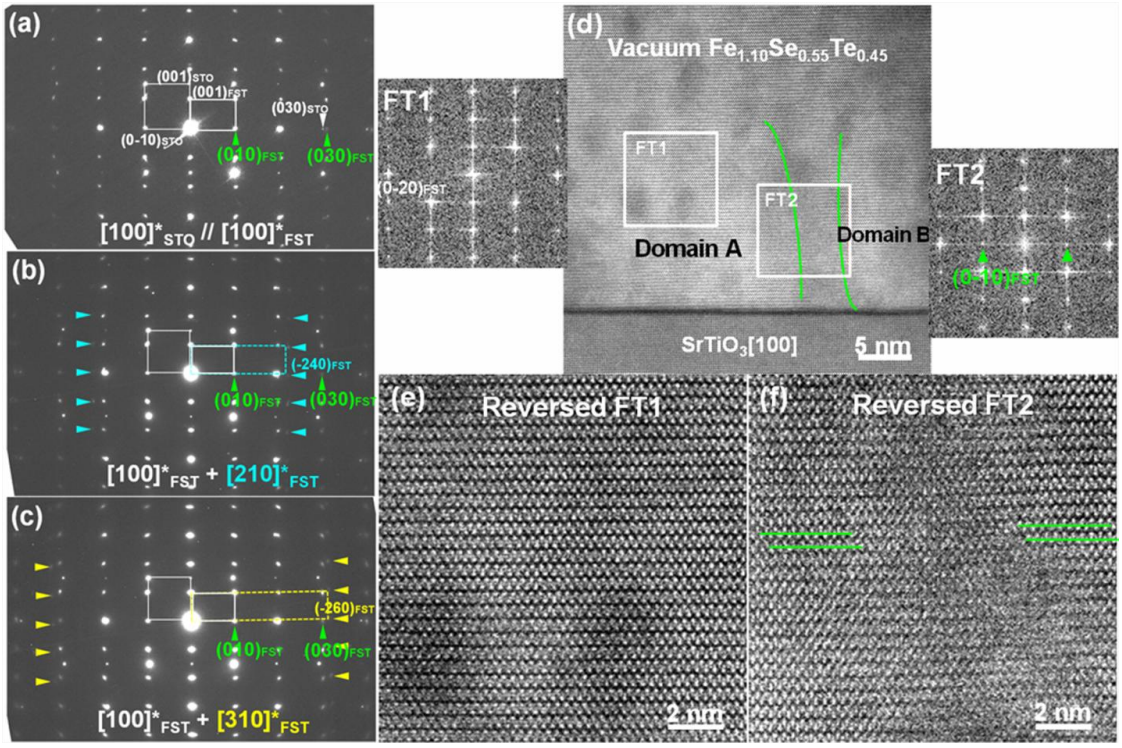

Figure 3.2. (a)-(c) Representative SAEDs of the superconducting vacuum-grown $Fe_{1.10}Se_{0.55}Te_{0.45}$ film. Additional minor in-plane misoriented grains were indexed in color in (b) and (c). The orientation relationship was determined and noted in each SAED. (d) An STEM micrograph and Fourier transforms form film local lattice. (e) and (f) are magnified regions of Fig. 3.2(d) corresponding to the areas of FT1 and FT2. The kinematically forbidden reflections (010) and (030) are indicated with green triangles.

Another interesting observation in the SAEDs of the vacuum-grown $Fe_{1.10}Se_{0.55}Te_{0.45}$ epitaxial film is the presence of the forbidden reflections of (0l0), l = odd integral (marked by green triangles in Figs. 3.2(a) to 3.2(c) and were also observed

in the film SAED without STO substrate). These additional (010) and (030) reflections could be related to dynamical diffraction effects, stacking defects in the film, or a preference of Se or Te in the occupancy of the chalcogen site.[157] To further verify the microstructure origin of these observed forbidden reflections, a local Fourier transforms (FT) survey (of 10-nm-by-10-nm selected region, about 15 times smaller than the smallest selected aperture in SAED) was performed in the STEM images. As shown in the representative Figs. 3. 2(d) to 3.2(f), the forbidden (010) reflections appear only at the regions across two film lattice domains (e.g. FT2). These reflections remain extinct (e.g. FT1), as expected in the superconducting tetragonal symmetric $Fe_{1+y}Se_{1-x}Te_x$ phase without Se/Te ordering,[26] in the regular film regions such as Fig. 3.2(e). Thus, in our case the observed forbidden reflections in SAED are likely due to a net scattering - from a stacking defect associated with slightly misaligned film domains (Fig. 3.2(f)). As discussed above, our EDX, SAED and Fourier transform analysis shows that by modifying deposition atmosphere the superconducting PLD $Fe_{1+y}Te_{1-x}Se_x$ thin films can present different overall and local stoichiometry. Obvious chemical inhomogeneity, appearing as nano-size Te-rich clusters, was observed in the iron deficient $Fe_{0.96}Se_{0.57}Te_{0.43}$ film deposited in controlled oxygen condition. The vacuum-grown film, on the other hand, maintains chemical inhomogeneity to a much finer length scale (Figs. 3.1(b) and 3.1(d)).

To overcome the limited spatial resolution of the EDX, we applied high resolution Cs-corrected STEM on the vacuum-grown superconducting Fe-rich $Fe_{1.10}Se_{0.55}Te_{0.45}$ film to examine the exact spatial relationship between the Te, Se and

the Fe(2) on an atomic column scale. In Fig. 3.3, a representative cross-section STEM micrograph under the dominant [100] zone axis presents the atomic arrangement of the $Fe_{1.10}Se_{0.55}Te_{0.45}$ film. For many materials, Cs-corrected STEM micrographs can provide relatively direct interpretation in terms of atom column positions (no contrast reversal up to a wide range of focus and foil thickness).[121] In the enlarged film region (Fig. 3.3(b)), the brighter dots represent the Te/Se atomic columns, and the less bright Fe-column-chains are located in between the Te/Se-triangle lattice; this is consistent with a standard anti-PbO lattice in [100] projection (Fig. 3.3(c)). Since the EDX analysis suggests excess iron (y = 0.1), which was reported to occupy the interstitial 2*c* sites,[29] we applied intensity line profile across the chalcogen planes for verification. As illustrated in a line profile inserted in Fig. 3.3(b), it is clear that there is no additional intensity peak in between any two adjacent chalcogen peaks, indicating that the 2*c* sites are not occupied. Intensity line profile was also conducted in HR-STEM micrographs under different view fields of the vacuum-grown $Fe_{1.10}Se_{0.55}Te_{0.45}$ film, similar results have been repeatedly observed (as the inset in Fig. 3.3(b)) in the absence of the Fe(2). This suggests that there are regions in this $Fe_{1.10}Se_{0.55}Te_{0.45}$ iron-rich thin film adopt only the anti-PbO crystal structure without significant interstitial iron. This is reasonable considering only a very small amount of additional iron was found in the EDX analysis. Since Fe(2) is related to charge carrier localization,[148] the observed dominant Fe(2)-free grain here is likely to be beneficial for the overall superconductivity which agrees well with the high T_C measured in this film.[161]

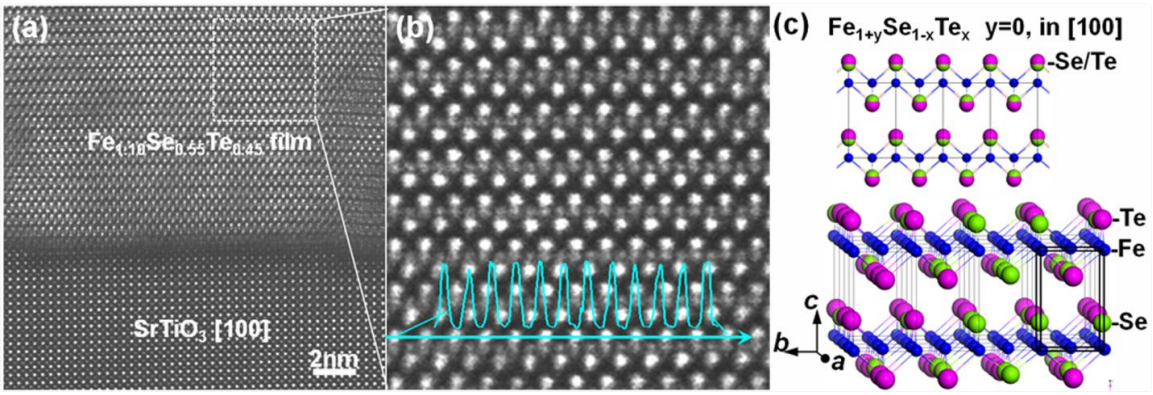

Figure 3.3. (a) High resolution Cs-corrected STEM image of the dominant [100]-oriented vacuum-grown $Fe_{1.10}Se_{0.55}Te_{0.45}$ film on the $SrTiO_3$(100) substrate. (b) The enlarged view of the atomic lattice of the $Fe_{1.10}Se_{0.55}Te_{0.45}$ thin film. Intensity line profile along the marked chalcogen plane is inserted. (c) A [100] projection and the corresponding three-dimensional 4 × 4 × 1 (unit cell) atomic model of the tetragonal anti-PbO structure free of interstitial Fe(2). The unit cell is marked by solid lines.

Furthermore, we noticed that in Fig. 3.3(b) the intensities of the chalcogen columns were quite uniform throughout this local film region (4.5 nm by 4.5 nm), indicating that the Te/Se occupancy within each individual column (about 15 nm thick in the e-beam direction based on STEM simulation) is nearly constant. The lack of apparent order of Se/Te ions is in agreement with the extinction of kinematically forbidden reflections in the local single-grain Fourier transform analysis (Figs. 3.2(d) and 3.2(e)). The same speculation was made from x-ray diffraction data of a $Fe_{1+y}Te_{1-x}Se_x$ single crystal lacking superlattice peaks.[158] Therefore, as schematically illustrated in the 4 × 4 × 1 atomic model in Fig. 3.3(c) where Se (large purple spheres) and Te (small green spheres) ions occupy distinct lattice sites (different chalcogen height from the iron plane), there is no regular ordering of their distribution in the Fe(2)-free regions of the superconducting $Fe_{1.10}Se_{0.55}Te_{0.45}$ film. These observations support the previous STM

finding that $Fe_{1+y}Te_{1-x}Se_{x,}$is electronically homogenous despite its apparent chemical inhomogeneity, which requires that the inhomogeneous phase size be smaller than the superconducting coherence length (ξ_C).[159] Other reports indicate a very small ξ_C = 5.1 Å,[149] only about one unit cell size of FeTe or of FeSe. As illustrated in Fig. 3.3(c), the unit cell chemistry is altered by simply substituting any of the eight tetrahedral parents Te (or Se) with the foreign Se (or Te) ions. Because of the z-coordinates of the Te and Se are distinctly different and both slightly shifted from the parent ternary phase structure,[26] the lowered local crystal symmetry could activate spin fluctuations to proximate a magnetic quantum critical point that is crucial for pairing.[24] Thus, a random distribution of the Te and Se throughout the $Fe_{1+y}Te_{1-x}Se_x$ seems more reasonable and more likely to achieve the superconductivity.

One remaining question concerns the excess iron atoms in the $Fe_{1.10}Se_{0.55}Te_{0.45}$ film. The excess iron appears to be highly localized, and are only visible in a few regions investigated by STEM. One such example, in Fig. 3.4, was found near the boundary between two different in-plane orientated film grains. As demonstrated in the enlarged STEM micrograph in Fig. 3.4(b), three film regions were identified and marked by I, II and III according to their different atomic arrangements. Region I was identified as the [210]-oriented grain, region II is a [100]-oriented grain similar to Fig. 3.3, and region III is the transitional area between the two. In the [100]- oriented grain in region II, the interstitial iron is directly resolvable in the STEM image. Shown in the magnified region II in Fig. 3.4(c), interstitial iron atoms were found in the chalcogen planes indicated by white arrows; an intensity line profile also confirmed the presence of the interstitial iron

as additional peaks marked by stars between the chalcogen columns. False intensities between atomic columns reported previously[165] due to large electron probe in abnormal shape or very high signal-to-noise ratio,[165, 166] can be avoided in the aberration-corrected TEAM 0.5 microscope.[135] Thus, the atomic-scale observation in Fig. 3.4(c) is in good agreement with the [100] projection model with the interstitial irons in Fig. 3.4(d). It is also noted that chalcogenide layer becomes blurry and less distinctive in the presence of interstitial iron. The Fe(1) sheet, in particular, seems being disrupted by the emergence of the Fe(2). Although the effect of lattice distortions or incoherent reflections along the electron-beam direction on imaging cannot be completely ruled out, it is possible that the suggested magnetic coupling between the Fe(2) and the adjacent Fe(1) sheet in nonsuperconducting $Fe_{1+y}Te$[155] could also happen locally in this ternary compound. The distribution of the Fe(2), circled in Fig. 3.4(b), it is limited in a dimension to about 2 nm × 1 nm. This structural feature is schematically illustrated in Fig. 3.4(d). We also compared the intensity value of the line profiles, and found that the ones along the Fe(2)-column are obviously lower than (< 40%) that along the Fe(1) in the parent lattice. It indicates that the interstitial iron does not persist through the full thickness of the film, which is in agreement with the small lateral dimension of the Fe(2) in Fig. 3.4(b). This might explain why Fe(2) was scarce in STEM observation, since certain degree of occupancy is needed to allow it to be outstanding from the image background. Thus, although the Fe(2) has been linked to charge-carrier localization and short-range magnetic orders,[149] the effects of these isolated superconductivity-suppressing phases

appear to be localized because the overall $Fe_{1.10}Se_{0.55}Te_{0.45}$ film remains superconducting with a T_C of 12.5 K.

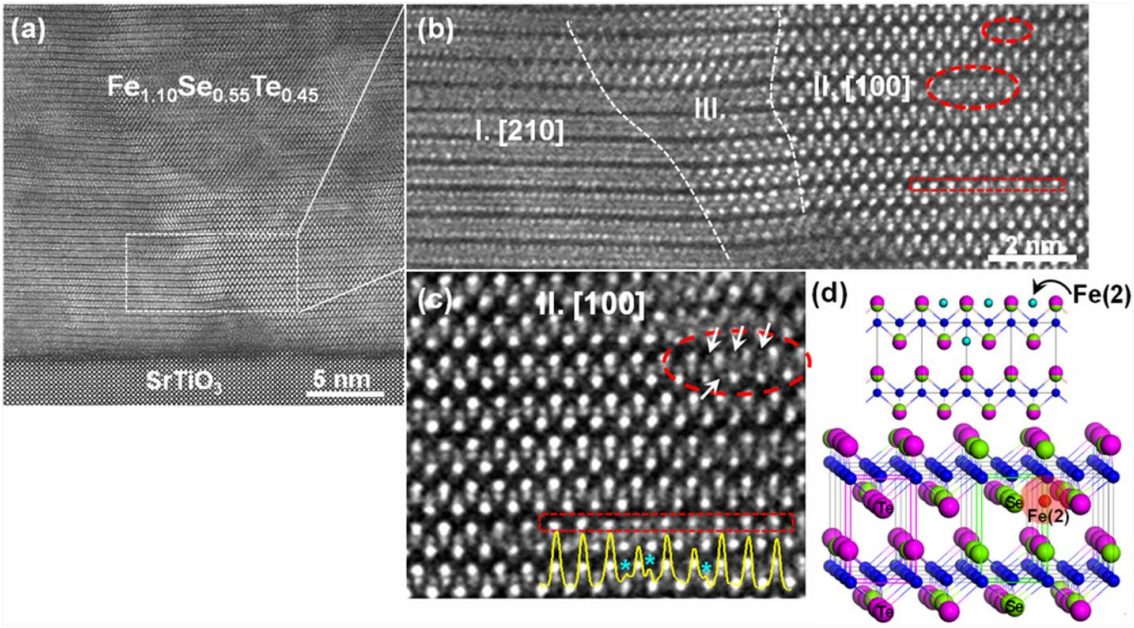

Figure 3.4. (a) STEM overview of the interface between two different in-plane orientated film grains in the vacuum-grown $Fe_{1.10}Se_{0.55}Te_{0.45}$ film. (b) Enlarged intersection region with three regions: I in [210] orientation, II in [100] orientation, and III is a transition region between the two. (c) Enlarged atomic STEM image of the region II in [100] with nanoscale interstitial-iron phases. Intensity line profile shown along the marked chalcogen plane. Interstitial iron peaks are noted by stars. (d) A schematic illustration of the spatial relationship of Te, Se and Fe(2) in the parent FST lattice.

Cs-corrected STEM has also been applied to investigate the atomic structure of the heterogeneous $Fe_{1.10}Se_{0.55}Te_{0.45}$(FST)/$SrTiO_3$ interface. As shown in a typical STEM micrograph in Figs. 3.5(a) and enlarged 3.5(b), a sharp interface is observed, without obvious interdiffussion. Fourier filtering using the shared (020) Bragg reflection of FST and STO (in Fig. 3.5(c)) reveals four misfit dislocations with nonperiodic spacing (5 nm

to 9 nm) above the heterogeneous interface. Based on the bulk lattice parameters at room temperature, i.e., $a_{STObulk}$ = 3.905 Å and $a_{FSTbulk}$ = 3.793 Å, under the major $[100]_{FTS}$ // $[100]_{STO}$ orientation, the dislocation spacing is estimated to be 13 nm for a lattice mismatch of 2.94%. However, the observed dislocation spacings are considerably smaller, suggesting a greater lattice misfit. Further analysis of the Fourier transform on the local film interfacial region, presented in Figs. 3.5(d) and 3.5(e), identified another film orientation [310] though at least part of the projected thickness. This orientation results in a much larger lattice mismatch of 10.88% and consequently a smaller dislocation spacing of 3.4 nm. This interruption in the expected lattice misfit caused by multiple misoriented film grains may explain the dislocation spacing variations observed above (Fig. 3.5(c)). Although it was theoretically proposed that the film strain state could be designed through substrate selection,[167] the real film strain state depends not entirely on the ideal misfit rate; interface defects, practical orientation relations and structural imperfections all strongly affect misfit dislocation spacing, and thus the film strain. On the other hand, it is noted that the emergence of the unit-cell-height step (marked by a yellow dash line in Fig. 3.5(b)) at the STO substrate surface does not interrupt the in-plane continuity of the local iron chalcogenide film. Although the film planes are slightly buckled, no defects such as antiphase boundaries[15] were observed at the substrate steps. The robustness of the iron chalcogenide layer was also demonstrated at large-angle grain boundaries in Fig. 3.4(a). The enlarged interface region in Fig. 3.5(f), the Se/Te-plane serves as the starting film layer with the substrate terminated at a TiO_2 layer. This atomic interface contact of chalcogen-plane/TiO_2 remains the same

even after the substrate surface steps. Thus the observed robustness of the iron chalcogenide layer might explain why many high temperature superconductors including cuprates are exhibit a layered structure[168] as suggested in the 'updated' Matthias's rule for searching new superconducting materials.[24]

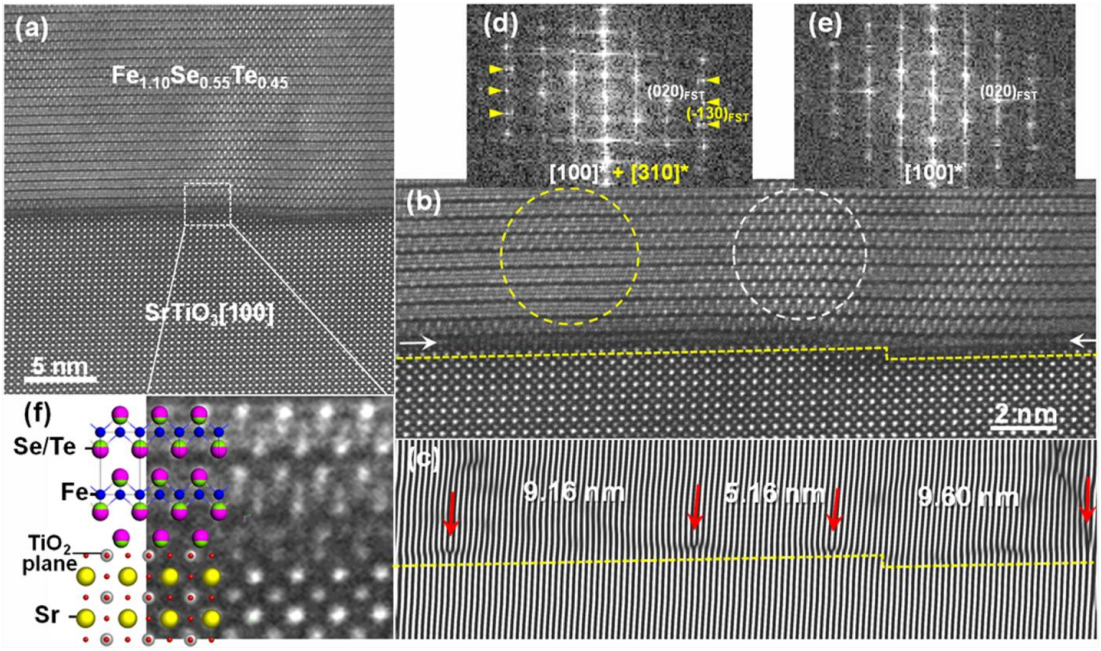

Figure 3.5. (a) An overview of the heterointerface of the $Fe_{1.10}Se_{0.55}Te_{0.45}$/STO under [100]. (b) The enlarged interface atomic arrangement. The STO substrate surface terrace with a one-unit-cell-height step is marked by a dashed line to guide the eye. (c) The (020) Bragg-filtered image of (b). Misfit dislocations are marked by arrows with dislocation spacings. (d) and (e) Fourier transforms of the two regions selected from (b). (f) The enlarged atomic arrangement of the interface contact. The atomic-projection models of the FTS tetragonal lattice and the STO along the [100] are inserted.

3.5 Conclusions

In summary, we characterized the microstructure, in particular the intrinsic chemical inhomogeneity, of two impurity-free superconducting $Fe_{1+y}Te_{1-x}Se_x$ thin films deposited under two growth atmospheres. In the iron deficient $Fe_{0.96}Se_{0.57}Te_{0.43}$ film grown in controlled oxygen, Te-rich clusters with a dimension of 10 nm to 50 nm were observed presenting obvious chemical inhomogeneity. In the case of the vacuum-grown Fe-rich $Fe_{1.10}Se_{0.55}Te_{0.45}$ film, which has a higher superconducting transition temperature, EDX shows mild local stoichiometry variation. Careful Fourier transform analysis and intensity profiles on high resolution Cs-corrected STEM micrographs identify a nearly random distribution of the Te and Se. The resulted local asymmetry away from the ideal tetragonal lattice was then found to be likely in a similar dimension to the coherence length ξ_C of the superconducting $Fe_{1+y}Te_{1-x}Se_x$. The potential proximities to a magnetic quantum critical point due to this atomic-level lattice symmetry oscillation might hold the key for the spin fluctuation mediated superconductivity. On the other hand, the occupancy of interstitial iron atoms was found to be highly localized in the matrix lattice in regions of approximately 1 nm diameter. The primary structural Fe(1) sheets become "disturbed" in the presence of the Fe(2), indicating possible iron-iron magnetic interaction. In addition, our study on the heterogeneous $Fe_{1.10}Se_{0.55}Te_{0.45}/SrTiO_3$ interface demonstrates that the in-plane grain misorientation can influence the interface strain by modifying the misfit dislocation distribution. The iron chalcogenide layer was found to be very robust, and able to

tolerate defective structure such as large-angle grain boundaries and substrate surface steps. Overall, this work provides atomic-scale insight into the fundamental crystal chemistry and actual lattice imperfections of the isovalent-doped $Fe_{1+y}Te_{1-x}Se_x$ superconducting thin films.

CHAPTER IV

ATOMIC INTERFACE SEQUENCE, MISFIT STRAIN RELAXATION AND INTRINSIC FLUX-PINNING DEFECTS IN DIFFERENT $YBa_2Cu_3O_{7-\delta}$ HETEROGENEOUS SYSTEMS

4.1 Overview

To explore the interface effects on enhancing critical current density in $YBa_2Cu_3O_{7-\delta}$ (YBCO) thin films, four heterogeneous systems, two of which with small opposite lattice misfit (i.e., the YBCO/STO (~ 1.6%) and the YBCO/LAO (~ -1.6%)), and the other two with relatively large opposite mismatch (i.e., the YBCO/MgO (~ 8.9%) and the YBCO/YSZ (~ -5.9%)), were selected and synthesized by pulsed-laser deposition. A detailed microstructure analysis including XRD, TEM and the state-of-the-art Cs-corrected STEM imaging, and a thorough superconducting property characterization including critical transition temperature (T_c) and critical current density ($J_c^{self\text{-}field}$ and $J_c^{in\text{-}field}$ (H//c)) were conducted for all four heterogeneous systems. The results reveal that the YBCO intrinsic defects, driven by the interface mismatch of different strain states, present a diverse nature in their distribution and density, and thus different flux-pinning performance under various measurement conditions. This study provides an in-depth insight on the microstructure-property correlation in a strongly correlated electronic system, the YBCO heterogeneous structures.

4.2 Introduction

Research on the microstructure and superconducting properties of $YBa_2Cu_3O_{7-\delta}$ (YBCO) thin films has been of great interests since the discovery of the high-temperature superconductivity in copper oxide materials [38]. A significant J_c leap happened when YBCO was made into a thin film form for the first time, where the J_c (~ 2.2 MA/cm^2 at 77 K zero field) was 10 to 100 times higher than that of the bulk YBCO single crystals [63, 64]. However, the YBCO-based coated conductor faces the frequently observed thickness-dependence issue, i.e., the J_c decreases dramatically as the film grows thicker. Later, a multilayer approach that has several thin YBCO layers stacked through heterogeneous interfaces, was proposed and it can maintain a high self-field J_c^{self} up to 4.0 MA/cm^2 at 75 K with a total YBCO film thickness of 3.5 μm [58]. Interfacial defects, unfortunately in a wide variety [45], were considered as the flux-pinning centers account for these great improvements [48]. On the other hand, tremendous efforts have been made towards incorporating external defects of various types and dimensions into the superconducting YBCO matrix to enhance its flux pinning properties under applied magnetic field [53, 59, 60, 169].

Among all the defects incorporated into YBCO matrix for successful self-field and in-field performance enhancements, intrinsic film defects such as threading dislocations [170, 171], misfit dislocations [172], stacking faults [173, 174] etc. are considered to be the most promising candidates. And the formation of these potential vortex pinning sites are closely related to the YBCO thin film initial nucleation [175-177] and lattice strain

relaxation [178]. However, little work has been done to understand the intrinsic flux-pinning defects and their correlations to the film growth [171].

In this paper, controlled YBCO-based heterogeneous interface systems were deposited and compared to address the above questions. Four systems including one pair with small substrate-introduced lattice mismatch but opposite strain state (-1.57% and 1.55%) and another pair with relatively large misfit (-5.88% and 8.93%), were established through the substrate selection (table 1). Considering that the film defects are usually near the interface and the lattice strain fields could extent into certain depth, a film thickness of approximate 150 nm was chosen for all samples. In particular, we conducted a systematic microstructure study on the four YBCO heterogeneous interface systems starting with determining their atomic interface sequence, which was found to be crucial to thin film epitaxial growth [179]. Then correlations between the film initial nucleation and misfit relaxation, the YBCO characteristic layered structure and intrinsic film defects formation, as well as their roles in the overall J_c in field performance were discussed.

4.3 Experimental

The YBCO thin films on four different commercial single crystalline substrates - $SrTiO_3$ (001), $LaAlO_3$ (001), MgO (001) and YSZ (yttria-stabilized zirconia) (001) - were prepared by a standard pulsed-laser deposition (PLD) technique (with a KrF excimer laser λ = 248 nm). Starting with commercial oxide powders, a YBCO target

with 10% additional Y_2O_3 was prepared through a conventional target processing procedure (details can be found elsewhere [180]). The depositions were carried out at the same substrate-to-target distance of 5 cm, target temperature of 780°C, an oxygen pressure of 200 mTorr, a laser energy of 300 mJ and a repetition rate of 5 Hz, following by annealing under 200 Torr of oxygen at 550°C for 30 minutes. All the YBCO samples were deposited under the same conditions and are with a similar film thickness of 150 nm. The YBCO superconducting properties including critical transition temperature (T_c) was measured by a standard four probe measurement in a physical property measurement system (PPMS, Quantum Design). Both the self-field and in-field critical current densities (J_c^{self} and $J_c^{in\text{-}field}$ (H//c)) were characterized from 0 T to 5 T at various temperatures (65 K, 40 K, and 5 K) by the vibrating sample magnetometer (VSM) in PPMS.

A systematic microstructure characterization was carried out via X-ray diffraction (BRUKER D8 powder X-ray diffractometer), selected-area electron diffraction (SAED), cross-sectional TEM (XTEM) and aberration-corrected scanning transmission electron microscopy (Cs-corrected STEM). SAED and XTEM were performed using a JEOL JEM-2010 microscope with a double-tilt holder. TEAM 0.5 [135], a modified FEI Titan microscope equipped with a special high-brightness Schottky-field emission electron source as well as an illumination aberration corrector capable of correcting the spherical aberration up to fifth-order, was employed. All of the high angle annular dark-field (HAADF) STEM micrographs in this report were recorded in the TEAM 0.5 microscope after a fine-tuning of the probe corrector at 300 kV (the phase

shift is effectively minimized; typical residual aberration coefficients are listed here [126]). Cross-sectional TEM foils were prepared through a conventional TEM sample preparation routine including cutting, gluing, grinding, polishing, and final precision ion polishing. Special care was taken to minimize irradiation damage during ion milling by applying polishing for longer time and milling at low angles.

4.4 Results and discussion

The overall crystallographic properties of the YBCO thin films grown on various crystalline substrates were firstly characterized by XRD. In Fig. 4.1(a), all films show primary YBCO (00*l*) peaks in typical θ-2θ scans, indicating highly *c*-axis texture of the YBCO thin films. Other than the peaks from the substrates (and small ones as indicated by dashed lines from the sample holder) no other peaks from impurity phases were observed. In the YSZ-supported YBCO, a small peak at (200) suggests a possible *a*-axis growth. The out-of-plane lattice parameters (d_c) were calculated as of 11.67 Å, 11.67 Å, 1.67 Å and 11.66 Å for the YBCO thin films deposited on the STO, MgO, LAO and YSZ, respectively. The film out-of-plane orientation was evaluated by the rocking curve of the (005) YBCO reflection (Fig. 4.1(b)). The full width at half maximum (FWHM) of the peaks demonstrate a small finite spread of 0.17° to 0.39°, suggesting excellent out-of-plane epitaxy qualities [181]. It is noted that the FWHM of the YBCO thin films grown on the STO and on the MgO are even smaller and then a better film crystallinity.

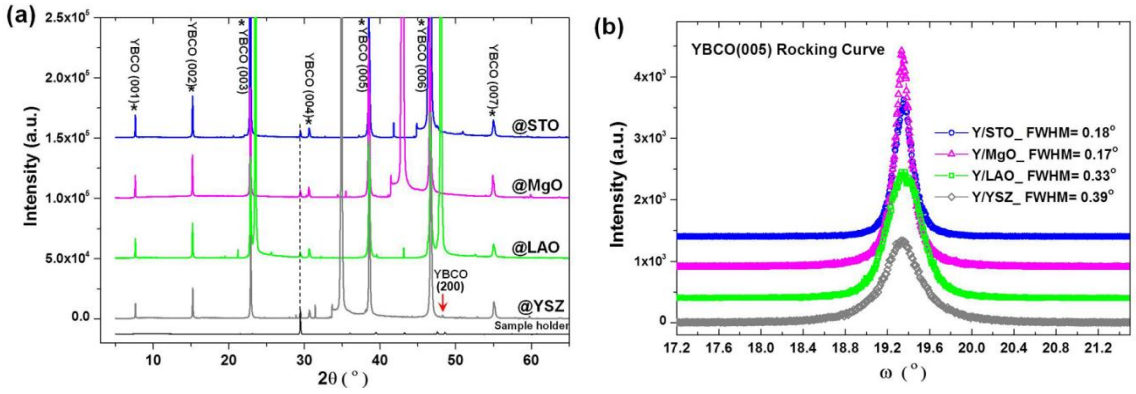

Figure 4.1. (a) The XRD θ-2θ scans of the four YBCO thin films deposited on the STO(100), MgO(100), LAO(100) and YSZ(100) single crystalline substrates. The pattern of the holder was also presented for a reference of the additional peaks. Primary YBCO (00*l*) peaks were noted for all films. A small peak at (200) was found only in the YBCO grown on YSZ. (b) The (005) YBCO rocking curve of the four films. The full width at half maximum (FWHM) are noted accordingly.

Further cross-sectional electron microscopy studies revealed the film and substrate in-plane orientation relationships. As shown in Fig. 4.2, representative cross-sectional STEM images and the corresponding SAEDs are presented for the four YBCO heterogeneous systems. The as-deposited YBCOs follow a cube-on-cube in-plane stacking on the substrates of STO (100) (Fig. 4.2(b)), LAO $(100)_{\text{pseudo-perovskite}}$ (Fig. 4.2(f)), and MgO(100) (Fig. 4.2(d)); whereas, the YBCO deposited on the YSZ substrate rotates 45° resulting in an YBCO(100)//YSZ(110) in-plane matching (Fig. 4.2(h)). Thus the film/substrate lattice misfits under the observed orientation relationships agree well with our expectations (table 1). The layered-YBCO-stacking structures, as suggested by the sharp (00*l*) reflections in all EDs and directly revealed in the atomic resolved STEM images (Figs. 4.2(a), 4.2(c), (e) and 4.2(g)), demonstrate excellent film crystallinity free of impurities such as Y_2O_3 inclusions. Although that the buckled layers were observed in

certain film regions, which is probably caused by the TEM sample preparation, most of the YBCO planes are straight without obvious damages.

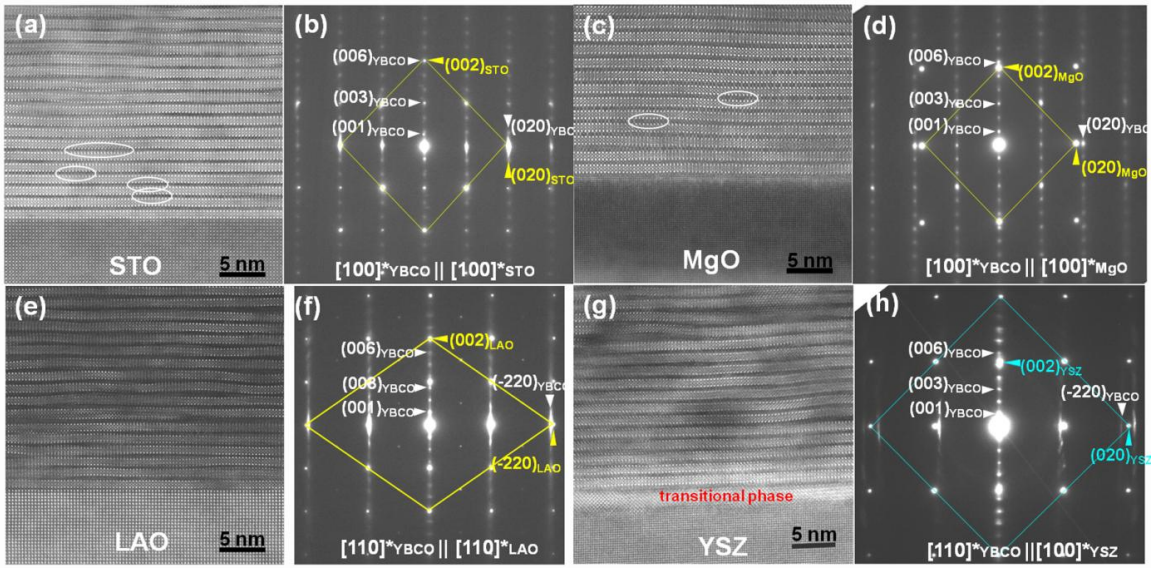

Figure 4.2. The representative cross-sectional STEM images and corresponding SAEDs of the YBCO thin films on (a, b) the STO, (c, d) the MgO, (e, f) the LAO and (g, h) the YSZ substrate. All SAEDs were indexed. The corresponding orientation relationship between the YBCO thin film and each substrate was determined and noted. The complex Frank sessile dislocations were marked by circles in (a) and (c).

The T_c values of the YBCO samples are summarized as the inset in Fig. 4.3. The film thicknesses measured in TEM are also listed. All of the YBCO thin films have a T_c above 91 K (onset) with a transition width less than 2 K. The critical current density (J_c) as a function of the applied magnetic field (H//*c*) were measured at 65 K, 40 K, and 5 K and plotted in Figs. 4.4(a) to 4.4(c), respectively, with each $J_c^{in\text{-}field}$ normalized to the corresponding $J_c^{self\text{-}field}$ as insets. Although the exact values of the $J_c^{self\text{-}field}$ vary slightly from batch to batch among all four sample batches, the overall trend of the $J_c^{in\text{-}field}$ is consistent.

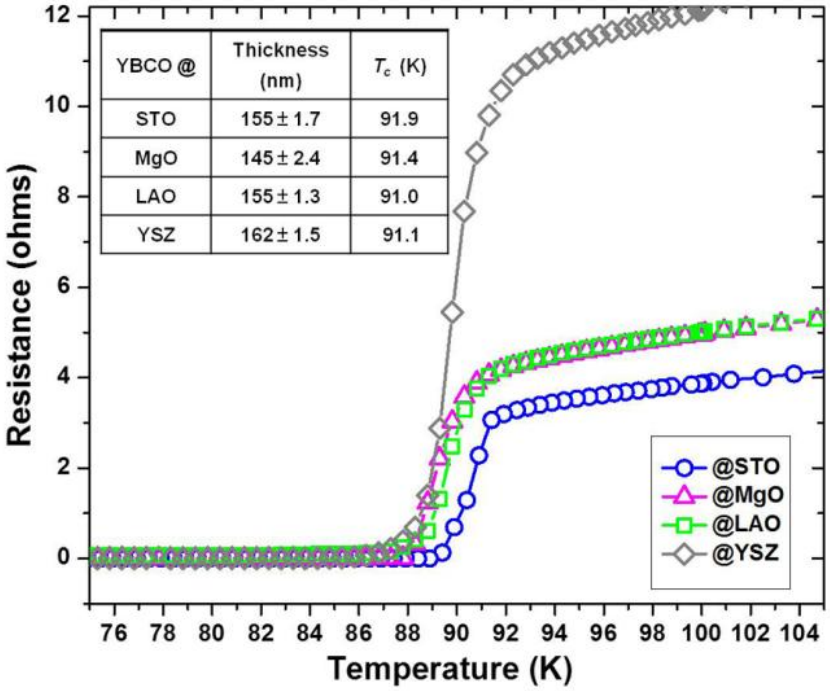

Figure4.3. *R–T* plots of the four YBCO thin films on different substrates. The inset lists the film thickness measured in TEM and the onset critical temperature T_c. Note that only one sharp superconducting transition around 90K is shown for all cases.

Several major findings based on the $J_c^{in\text{-}field}$(T) performance are: (1) the YBCO thin films grown on the STO substrates have the highest J_c at relatively high temperatures of 65 K and 40 K; (2) about the $J_c^{in\text{-}field}$ degradation rate, the YBCO/MgO films, as shown in the insets in Figs. 4.4(b) and 4.4(c), show the best pinning performance at 40 K and 5 K, possibly related to their high interfacial defects (more discussions are in section 3.3); (3) the YBCO/LAO samples are temperature- and field-sensitive and show the best performance at 5 K (Fig. 4.4(c)) while at 65 K the J_c drop dramatically as the applied field increases (Fig. 4.4(a)); (4) the YSZ is the worst substrate among the four (under this deposition condition), which is likely to be attributed to the *a*-axis-grown YBCO (Fig. 4.1(a).

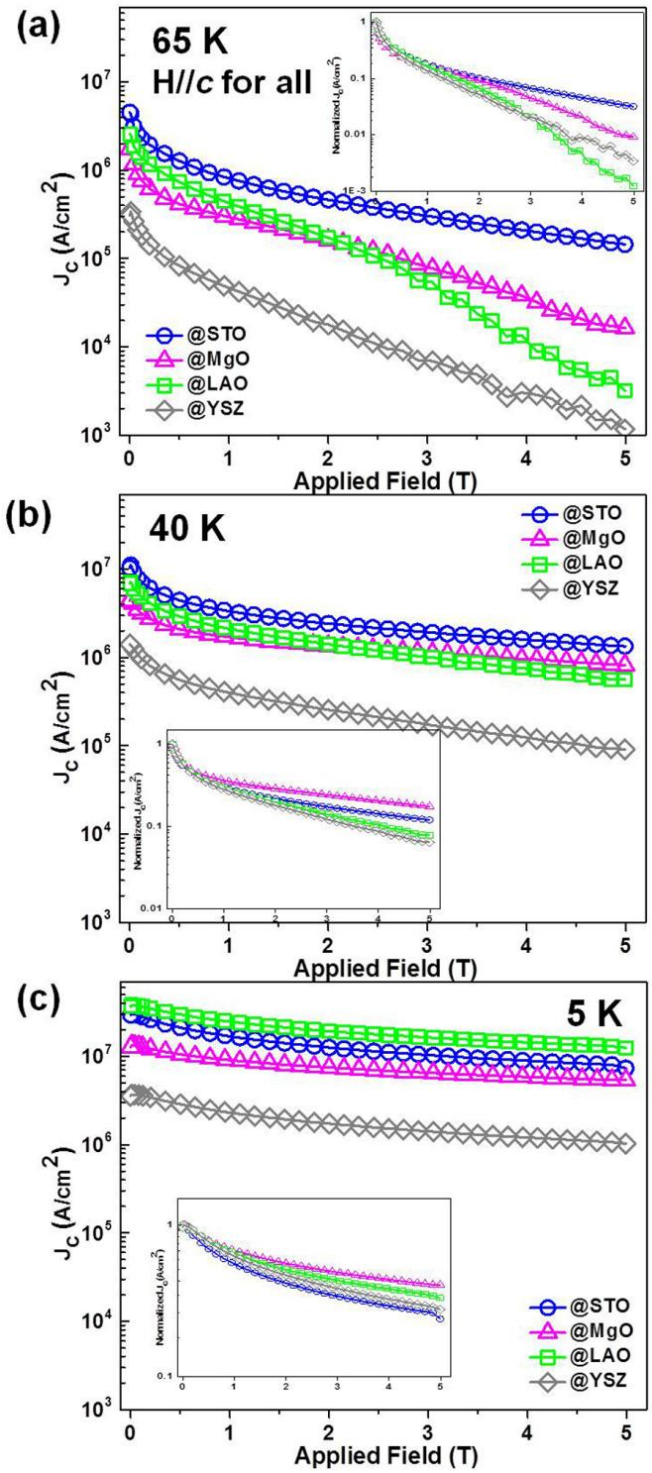

Figure 4.4. The critical current density (J_c) of the four YBCO thin films as a function of the applied magnetic field (H//c) measured at (a) 65 K, (b) 40 K, and (c) 5 K. The insets are $J_c^{in\text{-}field}$ normalized to the corresponding $J_c^{self\text{-}field}$.

4.4.1 Atomic interface contacts in different YBCO/substrate systems

Figs. 4.5(a) and 4.5(b) are the enlarged interface regions of the YBCO/STO and the YBCO/LAO samples (from Figs. 4.2(a) and 4.2(b)), respectively. Taking the advantages of the extremely small probe size of the TEAM 0.5, intuitive interpretation of the STEM image intensities in terms of atom column positions, i.e. I is proportional to Z^n (I is the image intensity; and Z is the average atomic number along the column of the scanned crystal; n = 1.5 ~ 2), is straightforward [121]. Thus high resolution Cs-corrected STEM images here provide directly interpretable atomic arrangements of the cation sublattice at the heterogeneous interfaces. In the STO substrate layers in Fig. 4.5(a), the relatively brighter dots represent the Sr-columns, and the less bright TiO-columns locate at the centers of the Sr-square lattice; all together presents a standard ABO_3 perovskite lattice in the <100> projection. Similarly, the YBCO lattice was also identified based on its brightest Ba-columns, less bright Y-columns in between and the surrounding least bright square-CuO-lattice, demonstrating a typical YBCO structure under the <100> review direction which could also be viewed as a tripled BAO_3 perovskite-like lattice in the *c*-axis direction.

Follow the periodicity of the above determined cation sublattice, the two possible YBCO/STO interface stacking sequences are: BaO-CuO_2-Y-CuO_2-(BaO-CuO-SrO)-TiO_2 or BaO-CuO_2-Y-CuO_2-(BaO-TiO_2-SrO), i.e., the CuO plane in contact with the SrO plane, or the BaO plane in contact with the TiO plane. To resolve whether the less bright plane between the two bright BaO- and SrO-plane at the interface belongs to the CuO- or the TiO_2-plane, intensity line profile was performed and the results yield an

obvious intensity as the TiO_2-plane. Thus, the TiO_2-plane is the terminating layer of the STO substrate used in this study, followed by a BaO-starting-plane in the first YBCO unit-cell-layer (illustrated by superimposed atomic projection models at the interface in Fig. 4.5(a)).

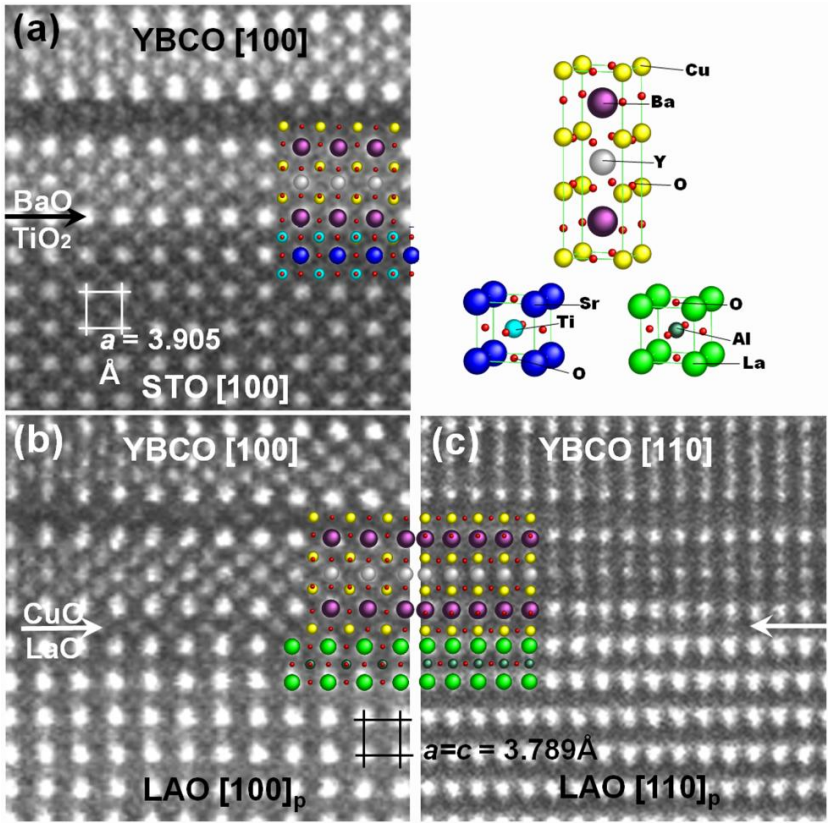

Figure 4.5. The atomic interface contact at the heterojunction of (a) the YBCO/STO under the <100> zone axis and of the YBCO/LAO along (b) the <100> and (c) the <110> zone axis. The YBCO film starting layers are noted by arrows. The projected atomic arrangements of YBCO, STO and LAO lattices were superimposed on the image.

In the case of the YBCO/LAO, similar cation sublattice analysis was applied. From both zone axis of the <100> and the <110>, the heterogeneous interface contact

was unambiguously determined as $BaO\text{-}CuO_2\text{-}Y\text{-}CuO_2\text{-}(BaO\text{-}CuO\text{-}LaO)\text{-}AlO_2$ (illustrated in Figs. 4.5(b) and 4.5(c)), i.e., the film CuO-plane is in contact with the substrate LaO-plane.

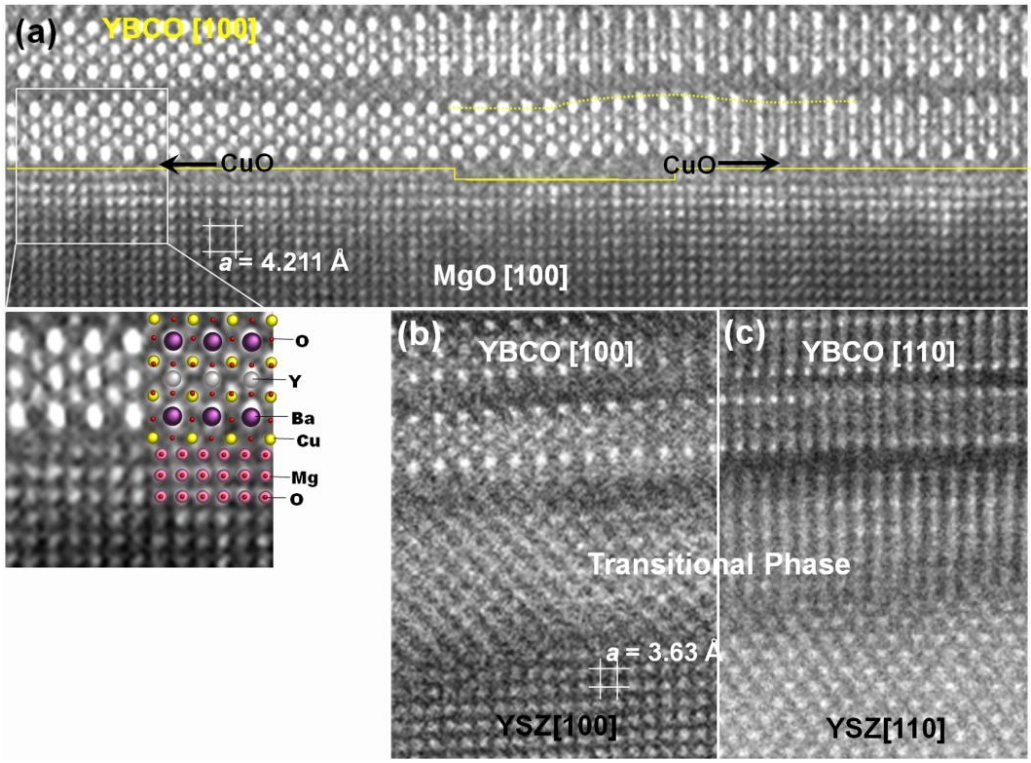

Figure 4.6. The atomic interface contact at the heterojunction of (a) the YBCO/MgO under the <100> direction and of the YBCO/YSZ along (b) the <100> and (c) the <110> zone axis. A line indicating the MgO termination layer shows the atomic-height steps at the substrate surface. The projected atomic models were superimposed on the enlarge interface of the YBCO/MgO.

The atomic interface structures of the other two heterogeneous systems, the YBCO/MgO and the YBCO/YSZ systems, are more complex as they involve a defective transitional layer. As shown in Fig. 4.6(a), at a representative interface region of the YBCO/MgO system with atomic-height surface steps which is common for the MgO

substrate, an interface contact of BaO-CuO_2-Y-CuO_2-(BaO-CuO-MgO) was determined with a certain extent of lattice distortions. While as demonstrated in Fig. 4.6(b) along the <100> zone axis and in Fig. 4.6(c) along the <110> zone axis, a 2~3 nm thick reaction layer (possible $BaZrO_3$ [182]) was found between the YBCO thin film and the YSZ substrate.

The above Cs-corrected STEM investigations clarify the previous debates on the starting atomic plane of the YBCO thin film on different (100) perovskite or cubic substrates. Our observation of BaO-CuO_2-Y-CuO_2-(BaO-TiO_2-SrO) is the only stacking sequence for the YBCO on TiO_2-terminated STO, confirming the conclusion made by Wen *et al*. using a thorough HRTEM image simulation [183]. The CuO-plane, proposed by Basu *et al.* [184] and suggested later by Ramesh [175], is identified as the film starting layer on the LAO. Our observations of the locally disordered CuO-MgO contact at the YBCO/MgO and the transitional phase on the YSZ agree well with the previous HRTEM studies [182, 185]. However it is not yet clear why different stacking sequences were observed in the different heterogeneous systems, even though the same deposition conditions and even the same deposition runs were adopted for this study.

4.4.2 Heterointerface mismatching and strain relaxation

We applied filtered Fast Fourier Transform (FFT) on the STEM micrographs (Figs. 4.2(a), 4.2(c) and 4.2(e)), the resulting (020) Bragg images and corresponding original heterogeneous interface regions of the YBCO/STO, the YBCO/LAO and the YBCO/MgO systems were enlarged and presented in Figs. 4.7(a), 4.7(b) and 4.7(d),

respectively. Due to that the emergence of the transitional phase interrupts the YBCO/substrate lattice matching (Fig. 4.2(g)), the YBCO/YSZ system was not considered in this analysis. In Fig. 4.7, horizontal lines indicating the bright BaO-plane in the first YBCO monolayer were superimposed on the exactly same positions in the corresponding (020) Bragg images to guide the view. Surprisingly, in the STO- and the LAO-supported films (Figs. 4.7(a) and 4.7(b)), not a single misfit dislocation was found in the immediate YBCO monolayer, despite that the lateral field of view here are about 30 nm, much longer than the estimated dislocation spacing of ~ 12 nm in both cases (Table 4.1). These nearly defect-free 1st-YBCO-layer suggest that the YBCO films have grown initially pseudomorphically (highly strained) on the STO and the LAO substrates. The estimated pseudomorphic layer thickness is around 1.2 nm (one unit cell height) for a lightly mismatched system such as the YBCO/STO or the YBCO/LAO systems.

Table 4.1**.** The list of the theoretical in-plane lattice misfit and the dislocation spacing calculated by bulk lattice parameters at room temperature in the selected YBCO heterogeneous systems.

Film/Sub	Bulk Lattice Constant (Å)	Misfit Rate (%) $2(a_s-a_f)/(a_s+a_f)\times100$	Misfit Dislocation Spacing $d_{002s}d_{002f}/\lvert d_{002s}-d_{002f}\rvert$(nm)
YBCO (orth.)	3.85		
STO	3.91	1.55	12.54
LAO	3.79	-1.57	12.16
MgO	4.21	8.93	2.25
YSZ	3.63	-5.88	3.18

Note: an averaged *a* over the bulk *a*- and *b*-lattice parameter was used for the YBCO for simplification. In the calculation of dislocation spacing, the d_{002s} is adopted considering the actual (002) monolayer matching.

On the contrary, as illustrated in the (020) Bragg image in Fig. 4.7(d), regular misfit dislocation arrays with an average spacing of 2.46 nm were found in the YBCO layer immediately above the MgO substrate. This observation is consistent with the theoretical prediction (~2.25 nm in Table 4.1) that a domain match epitaxy is adopted when the lattice mismatch becomes large (usually > 9%). Instead of forming a coherent interface, edge dislocations are generated at the interface to relax the large misfit strain and further lower the system energy [10]. In terms of the film growth mechanism, the observed pseudomorphical interfaces in the YBCO/STO and YBCO/LAO systems agree well with the 2D island growth mechanism proposed by a previous study on the early deposition stage; meanwhile, the misfit dislocation arrays are likely to account for the 3D Volmer-Weber growth found in the case of YBCO/MgO [178, 186]. On the other hand, the misfit dislocations at the YBCO/MgO with such a high density are probably responsible for the defective CuO/MgO contact observed in Fig. 4.6(a), for that the centers of these edge dislocations (i.e. dislocation cores) were found right at the film starting plane the CuO-plane. Additionally, the YBCO layers (not just the first monolayer but also the following ones) were found buckled at the steps of the MgO surface (marked by a dotted-line in Fig. 4.6(a)). Similar phenomenon was also observed by Traeholt *et al.*[185]. It suggests that the YBCO film lattice has already nearly fully relaxed by the defective interface and therefore can conformably grow on the surface defects.

The formation of the anti-phase boundary (APB) was reported as an effective mechanism for strain relaxation in the YBCO film grown on STO [185]. However, there is

no APB found in the YBCO on the STO or on the LAO in this study. Instead, the STEM study revealed other ways to relax the interface strain. For example, as pointed by the double arrows in Fig. 4.7(a), a remarkably high density of planar defects consisting of two sequential CuO-planes (in the conventional YBCO orthorhombic structure, only one CuO-plane) were found between nearly every YBCO layer on STO (Fig. 4.2(a)). The extra CuO-plane was identified as a stacking fault with a displacement of [0 $\mathbf{b_0}$/2 $\mathbf{c_0}$/6] [187]; when such stacking faults appear periodically with a certain sequence, new phases such as $YBa_2Cu_4O_8$ [188] or $YBa_2Cu_{3.5}O_{7.5}$ [189] were formed. However, in our case, no new phase was identified in either XRD or SAED. As illustrated in Fig. 4.8 (the enlarged circled region in Fig. 4.7(a)), the first double-CuO-plane (marked by "1") in the YBCO film presents a continuous triangle-shape atomic arrangement, suggesting that the stacking fault here is under the <100> zone axis [190]. The same structure was found in the second double-CuO-plane but only on the left side; whereas, the right double-CuO-plane aligns head-to-head indicating a <010>-projected stacking fault perpendicular to the left one. Thus, the second double-CuO-plane is no longer a simple planar defect, but are two extrinsic type Frank sessile dislocations [191]. Similar defects are also observed in the third double-CuO-plane while with a swapped orientation sequence. It is noted that they are not conventional dislocations but are consistent with the dislocation with a Burgers vector of ½[110] and a glide plane of (001) located between the two CuO layers reported previously [191].

Shown in the enlarged circled image in Fig. 4.7(a), the <100>-projected configuration of this complex dislocation is an edge dislocation with **b** = ½ [100]. These

partial edge dislocations provide extra-half-(020)-plane in YBCO, similar to that of the misfit dislocations at the interface of the YBCO/MgO system. This strongly indicates that these complex Frank sessile dislocations (two in pairs with a 90° rotation with each other) are very likely to contribute to the STO-introduced tensile strain relaxation and possibly also to the enhanced pinning properties in the YBCO/STO system.

Identical complex Frank sessile dislocations with a 90° rotation were also observed in the YBCO on the MgO. Their partial edge dislocations are noted by the circles in Fig. 4.2(c); whose density is considerably lower compared to that of those in the YBCO on STO. This again supports the hypothesis that the emerging of the complex Frank sessile dislocations is to relax the tensile lattice strain; less occurs here is due to that the misfit dislocation arrays at the YBCO/MgO interface have already relaxed most of the interface strain. On the other hand, a simpler case of the above defects, the pure 'insertion faults', were also found in the YBCO films. For example, in Fig. 4.7(d), the tripled-CuO-plane changes to a single one and then to a double-CuO-layer as marked by arrows. The transition from one CuO-plane to two presents the end of one sessile Frank loop, which also involves a partial edge dislocation but with the extra-half-inserting plane lies within the *ab*-plane suggested by previous report [191].

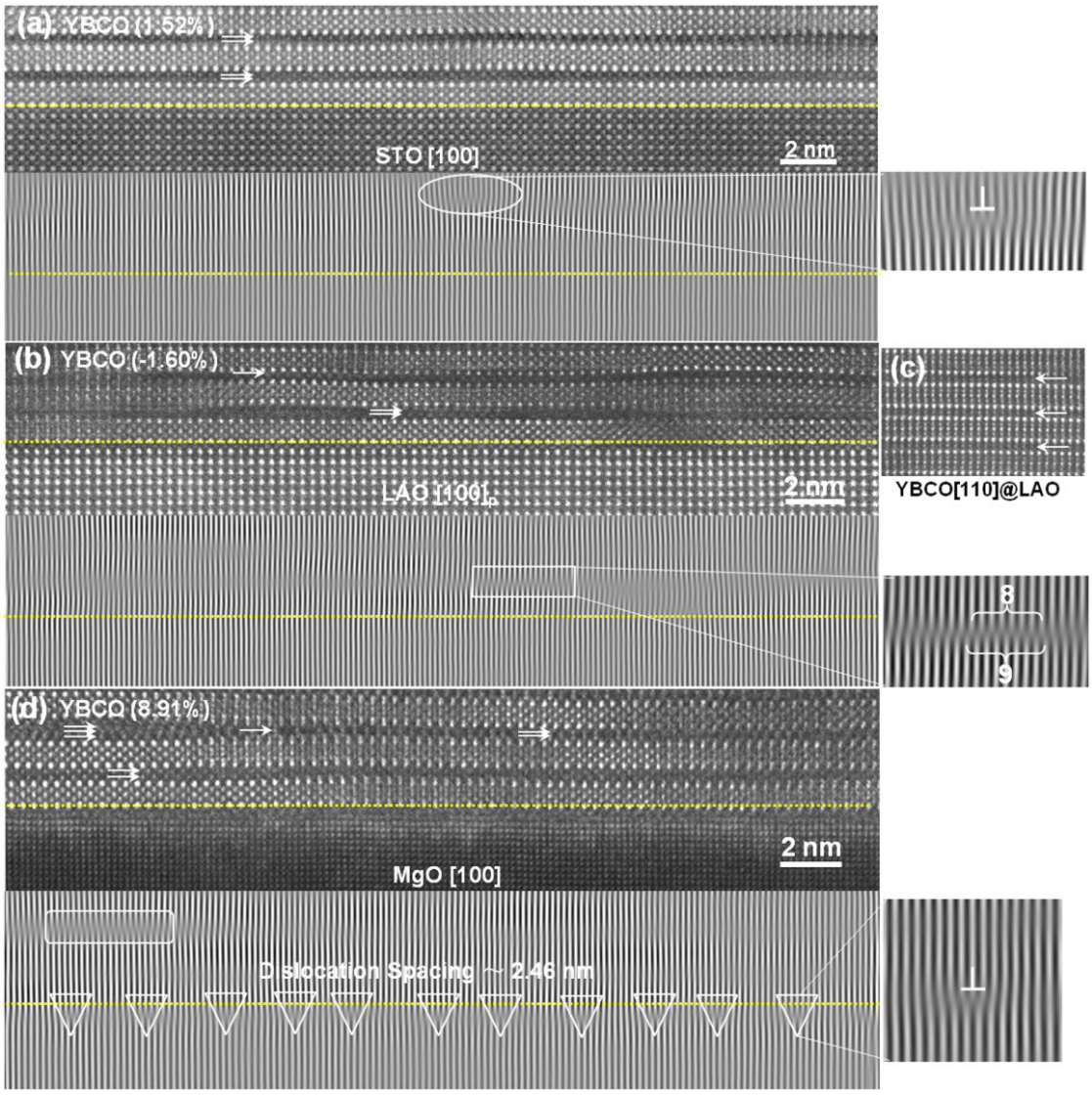

Figure 4.7. The enlarged STEM images at the interface region of Fig. 4.2 and the corresponding (020) Bragg images of the heterointerface of (a) the YBCO/STO, (b) the YBCO/LAO and (d) the YBCO/MgO in <100> projection. An additional YBCO/LAO image under the <110> direction is shown in (c). Horizontal lines indicating the bright BaO-plane in the first YBCO monolayer were superimposed on the exactly same position in the corresponding Bragg image to guide the view. Arrows in YBCO are inserted to indicate the number of the extra CuO-plane at the local area. The complex Frank sessile dislocations, the stacking faults and the misfit dislocation arrays are noted by the circle, the rectangles and the triangles in (a), (b) and (d), respectively, and were enlarged for details.

In another strained case of the YBCO/LAO, only few double-CuO-planes was found (e.g. near the substrate in Fig. 4.7(b)); standard YBCO layers with single-CuO-plane were observed from both of the <100> and the <010> zone axis (Fig. 4.7(c)). It is noted that the buckled YBCO planes in this case makes it difficult to distinguish the number and orientation of the CuO-planes. As illustrated in the enlarged rectangular area in Fig. 4.7(b), the stacking fault combined with the bulked YBCO layer here also contribute to a partial edge dislocation along the <100> projection. Unlike the partial edge dislocation observed in the YBCO/STO (inset in Fig. 4.7(a)), it presents a less rigid eight to nine (020)-plane matching, affecting a larger lattice area associating with a greater distortion. On the basis of the above observations and discussions, the YBCO/LAO might be to some extent remain strained. One reason that this YBCO film might be less relaxed may be attributed to its compressive strain state, which may not be in favor of forming YBCO film intrinsic defects such as misfit dislocations and the Frank sessile dislocations. Similar theory could be applied to the also compressed YBCO/YSZ system. Although this heterogeneous system has a smaller absolute misfit value than that of the YBCO/MgO system (Table 4.1), a transitional phase was formed prior to the YBCO growth, indicating the possibly tremendous difficulties in generating the interfacial defects for relaxing the compressive strain.

On the other hand, nucleation is not simply determined by the misfit strain alone; other critical factors driven by thermodynamics [176] or charge balance [175] could also contribute to the initial growth stage. For example, it was reported that a full 123 monolayer only form on the TiO_2-terminated substrate; while a 122+CuO_x sub-

monolayer was usually found on the SrO terminated STO [177]. Then it is possible that on the TiO_2-STO due to the formation of the CuO-capped monolayer, Frank sessile dislocations are the defects emerge later to relax the lattice strain; whereas, the nonstoichiometric 122+CuO_x layer resulting from the SrO-termination could lead to other possible lattice disorders for strain accommodation. In this case, substrate surface termination, under certain circumstance (such as proper lattice misfit), plays a significant role in determining film intrinsic defects through initial film nucleation.

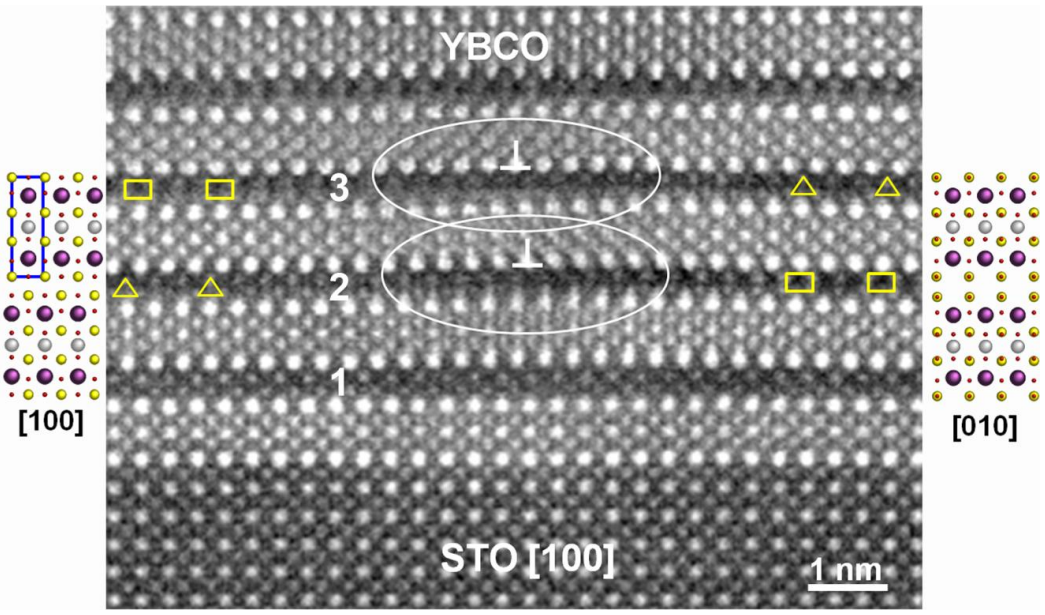

Figure 4.8. A detailed illustration of the complex Frank sessile dislocations with a 90 degree in-plane rotation in the YBCO grown on STO. The image was enlarged from Fig. 4.2(a). The first, second and third double-CuO-planes starting from the interface are marked by 1, 2 and 3. The atomic arrangements of the YBCO lattice with an extra-CuO-plane are inserted on the left in <010> projection, on the right in <100> direction. The signature triangle-shape and square-like double-CuO-plane atomic arrangements are used to determine the local lattice orientation. The partial edge dislocations are marked by the extra-half-(020)-plane in the YBCO film.

4.4.3 YBCO thin film intrinsic defects and their effects on flux pinning

As discussed in the previous section, different types of intrinsic film defects were observed in the three YBCO films that have a direct heterogeneous interfacial contact with the corresponding substrate (Fig. 4.7). The complex Frank sessile dislocations and stacking faults were found dominant in the YBCO/STO system; some of them were also observed in the YBCO/MgO (Fig. 4.2(c)), where regular misfit dislocation arrays with a density as high as about 4.1×10^{6} cm^{-1} (estimated from the observed dislocation spacing) were observed at the interface. In the case of the YBCO/LAO, few stacking faults appearing as additional CuO-planes without the 90° rotation were observed (Fig. 4.7(b)); it is likely that the YBCO films remain strained under the LAO-introduced compressive strain.

Although all of the YBCO thin films including the YBCO/YSZ show similar T_cs above 91 K, their in-field behaviors ($J_c^{in\text{-}field}$ at various temperatures) are quite different (Fig. 4.4). And these differences in the $J_c^{in\text{-}field}$(T) performance are well correlated with the corresponding intrinsic film defects observed above. For example, under the deposition condition in this work, the YBCO films grown on the STO have the highest J_c under all magnetic fields at high temperatures (Figs. 4.4(a) and 4.4(b)). The complex Frank sessile dislocations and the stacking faults in this system are very likely to be responsible for the high J_c. On one hand, the structural origin of the Frank sessile dislocation and of the stacking faults is an extra-CuO-plane, which allows the YBCO to remain the fourfold CuO-chain structure [191]; meanwhile, additional CuO-planes was found be able to increase the number of superconducting charge carriers [187], thus a

higher supercurrent density; On the other hand, the immobile nature of the complex Frank sessile dislocations, i.e. the 90° rotation between the adjacent Frank sessile loops makes them nearly impossible to move, is probably the reason that they are thermally stable flux-pinning centers less affected by temperature variation. When comparing the $J_c^{in\text{-}field}$ performance, the YBCO/MgO samples become the best at lower temperatures (e.g., 40K and 5K as the insets in Figs. 4.4(b) and 4.4(c)). Interfacial defects with a high density have been proven very effective on pinning especially at high magnetic fields [180]. The robust $J_c^{in\text{-}field}$ performance here could be resulted from the high density misfit dislocations found at the heterogeneous interface of YBCO/MgO. It is also possible that the misfit dislocations network, the Frank sessile loops (Fig. 4.2(c)) and stacking faults (Fig. 4.7(d)), all contribute to the in-field flux-pinning and result in a collective pinning effect.

Unlike the YBCO/STO and the YBCO/MgO, both films under tensile strain, the other two heterogeneous systems are expected to be in compression (Table 4.1). As aforementioned, the YBCO/LAO films probably remain strained, appearing as bulk YBCO-layers in the STEM images and also in the corresponding YBCO(005) rocking curve with a relatively large FWHM (Fig. 4.1(b)). Moreover, the stacking faults found here affect a large distorted lattice region (the inset in Fig. 4.7(b)) comparing either to the misfit dislocation core (the inset in Fig. 4.7(d)) or to the edge dislocation partial of the Frank sessile defect (the inset in Fig. 4.7(a)). A very recent study which reported similar planar defects in a vortex-pinning enhanced YBCO attributed the pinning effect to the associated nanostrain [192]. This could explain why the YBCOs/LAO samples are

superior under lower temperatures, not only in $J_c^{self\text{-}field}$ but also in $J_c^{in\text{-}field}$. But once the measurement temperature increases, due to the short of stable lattice defects to sustain the proper local strain field that pinning the vortices, the J_c dropped immediately at the presence of the magnetic field (Fig. 4.4(a)). In the case of the YBCO/YSZ, the attempt to compare it with the other systems might not be appropriate. Due to the formation of the secondary phase at the heterogeneous interface, the following YBCO film cannot be considered as grown on the single-crystal substrate anymore. As shown in the YBCO(005) rocking curve (Fig. 4.1(b)), the YBCO/YSZ has the largest FWHM which could be attributed to the out-of-plane tilting observed in the later STEM study (Figs. 4.6(b) and 4.6(c)). Additionally, since the J_c in YBCO is highly anisotropic, the present of the *a*-axis-grown YBCO (Figs. 4.1(a)) could be the one of the main reasons for its poor J_c performance.

Based on the above discussions on the YBCO film intrinsic defects and the correlations to the $J_c^{in\text{-}field}$(T) performance, an effective flux-pinning landscape should consist of a large numbers of highly localized lattice disorders (preferably to be close to the size of the vortex cores, i.e. 2 ~ 3 nm [193]). Within these disorders, thermal stable defects are essential for maintaining the individual strain field; and thus superior $J_c^{self\text{-}field}$ performance could be achieved at higher temperatures and higher applied fields.

4.5 Conclusions

In this study, four 150-nm-thick highly epitaxial YBCO heterogeneous systems with interface misfit ranging from -5.9% to 8.9% were produced. Under the same deposition condition, different heterogeneous stacking sequences and strain relaxation defects were revealed by the Cs-corrected STEM in the atomic-scale. In the slightly mismatched systems of the YBCO/STO (~ 1.6%) and the YBCO/LAO (~ -1.6%), a pseudomorphical interface with sequence of $BaO\text{-}CuO_2\text{-}Y\text{-}CuO_2\text{-}(BaO\text{-}TiO_2\text{-}SrO)$ and $BaO\text{-}CuO_2\text{-}Y\text{-}CuO_2\text{-}(BaO\text{-}CuO\text{-}LaO)\text{-}AlO_2$ was identified, respectively, suggesting an initial perfect 2D growth. In the YBCO/STO, the complex Frank sessile dislocations with a 90° rotation and the stacking faults were found dominant in the film. Owning to the large number of extra-CuO-planes and to the immobile nature of the complex defects, the YBCOs/STO system shows excellent self-field and in field J_c performance at high temperatures. In the YBCO/LAO system, however, fewer stacking faults were found, suggesting a possible strained film lattice which could provide effective flux-pinning at low temperatures. On the other hand, in the case of the two heterogeneous systems with greater lattice misfits, high density misfit dislocations (spacing ~ 2.46 nm) were found at the interface of the YBCO/MgO system (~ 8.9%) under the 3D Volmer-Weber growth, leading to the robust in-field pinning performance observed at low temperatures; whereas, a secondary phase was found formed prior to YBCO layers to accommodate the compressive stress (~ -5.9%) in the YBCO/YSZ system. This study

could lead to the further understanding of YBCO J_c-intrinsic defects dependence as well as the design of a practical flux-pinning landscape.

CHAPTER V

INTERFACIAL DEFECTS DISTRIBUTION AND STRAIN COUPLING IN THE VERTICALLY ALIGNED NANOCOMPOSITE $YBa_2Cu_3O_{7-x}/BaSnO_3$ THIN FILMS*

5.1 Overview

Here, we report the unique microstructural characteristics of $YBa_2Cu_3O_{7-x}$(YBCO)/$BaSnO_3$(BSO) nanocomposite thin films on $LaAlO_3$(LAO) substrates. The BSO secondary phase grows as self-assembled vertically aligned nanopillars uniformly distributed in the superconducting YBCO matrix. Detailed microstructure and strain studies including X-ray diffraction(XRD), cross-section and plan-view transmission electron microscopy(TEM) and geometric phase analysis(GPA) reveal that, as the BSO doping concentration varied from 2 mol% to 20 mol%, nanopillar density increased from $0.26\times10^{11}/cm^2$ to $1.44\times10^{11}/cm^2$ while the nanopillars diameter remains 7-8 nm in diameter). The YBCO strain state is affected by both lateral and vertical strains; while, the BSO lattice is strongly tuned by YBCO rather than the substrate. A high density array of dislocations in the order of 10^{13} $/cm^2$ was observed along the vertical heterointerfaces throughout the YBCO film thickness for all doping concentrations.

---

*This chapter is reprinted with permission from "Interfacial defects distribution and strain coupling in the vertically aligned nanocomposite YBa2Cu3O7-X/BaSnO3 thin films" by Y. Zhu, C. Tsai, J. Wang, J. Kwon, H. Wang, C. Varanasi, J. Burke, L. Brunke and P. Barnes, Journal of Material Research, **27**, 1763 (2012).

5.2 Introduction

Since the first demonstration of the $La_{0.7}Ca_{0.3}MnO_3$:MgO nanocomposite system,[1] the two-phase nanocomposite thin films, holding the promise for multifunctionality, have drawn extensive research interests.[2-4] For example, the $BiFeO_3$ (BFO):$CoFe_2O_4$ (CFO) nanocomposites combine ferroelectric and magnetic properties together achieving multiferroic.[5] Following that, a unique family of two-phase nanocomposite with vertical lattice alignment, termed as the vertically aligned nanocomposites (VAN), has been demonstrated in several systems.[6,7] For example, the $La_{0.5}Sr_{0.5}CoO_3$ (LSCO):$Ce_{0.9}Gd_{0.1}O_{1.95}$ (CGO) VAN was fabricated as the interfacial layer between the cathode and the electrolyte and proven to effectively increase the cell efficiency in solid oxide fuel cells.[8] More interestingly, the strain coupling along the vertical lattice matched interfaces in VAN systems can be further tuned by the diameter and density of the nanopillars.[9, 10] New functionality and unique strain coupling are attractive for future applications; however, the fundamental study on the vertical lattice matching and the nature of the defects along the vertical interfaces is scarce.

On the other hand, in the field of high-temperature superconductors (HTS) such as $YBa_2Cu_3O_{7-}$(YBCO),[11] maintaining the critical current density J_c of the film under applied magnetic field, i.e. excellent in-field performance, is one of the major challenges for practical applications.[12] One of the main approaches is to introduce nanoscale defects in YBCO matrix, which serve as the flux-pinning centers under high fields.[12, 13] These dopants have to be chemically compatible with YBCO and grow epitaxially in the

YBCO matrix. Among all of the artificial pinning centers introduced including the 0D, [14] 1D, [15, 16] and 2D [17] defects; to dates, vertically aligned nanopillars are considered to be one of the most effective pinning schemes. For example, Goyal *et al.* showed a stronger pinning effect along c-axis for $BaZrO_3$ nanorods doped YBCO films.[18] Varanasi *et al.* demonstrated the $BaSnO_3$ (BSO)-doped YBCO films with significantly enhanced c-axis pinning effects. [19, 20] Recently, Wee *et al.* chose Ba_2GdTaO_6[21] and Ba_2YNbO_6 [22] which chemically and structurally similar to YBCO as the secondary phase, achieving self-assembled growth as well as flux pinning enhancement. However, the nature of the defects and the effects of the strain [23] along the vertical interfaces that could be responsible for superconductive performance are still under investigation.

In this work, we select BSO-doped YBCO films with different doping concentrations as the typical system to investigate the microstructural origin of the VAN growth and the nature of the defects along the heterogeneous interface in the systems. The reasons BSO-doped YBCO system is chosen for this study are (1) BSO nanopillars grown epitaxially in YBCO matrix over a large thickness range; and (2) the BSO nanopillar density can be easily tuned over a wide range by controlling the doping concentration of BSO. A combination of cross-section and plan-view transmission electron microscopy (TEM) study was applied to all the VAN films with different doping concentrations for exploring the distribution and dimension of the BSO phases. The out-of-plane lattice strain and matching relation of YBCO and BSO were studied for exploring the possible growth mechanisms of the self-assembled BSO nanopillars.

5.3 Experimental

Depositions of YBCO thin films with different $BaSnO_3$ concentrations (2 mol%, 4 mol%, 10 mol%, and 20 mol %) were conducted using pulsed laser deposition (PLD). The ratio of YBCO to BSO in the resulting thin films was controlled by varying the amount of powders in the composite targets preparation. Starting with commercially available YBCO (Nexans, Hurth, Germany) and BSO (Cerac, Milwaukee, WI) powders, which were carefully weighed and well mixed to achieve four final targets with 2 mol%, 4 mol%, 10 mol%, and 20 mol% BSO in YBCO, respectively. Then, four composite films, up to a thickness of approximately 300 nm, were obtained on (100) LAO single crystal substrates. The details on target processing and deposition details can be found elsewhere. [21]

A systematic microstructural characterization was conducted via X-ray diffractometer (XRD) and TEM. Plan-view and cross-section TEM samples were prepared through a conventional TEM sample preparation routine including cutting, gluing, grinding, polishing, and final precision ion polishing. The TEM characterization was performed using a Philips CM200F analytical electron microscope with a point-to-point resolution of 0.20 nm.

5.4 Results and discussion

The overall microstructure of the YBCO/BSO films was first characterized by XRD. In Fig. 5.1(a), all the films show primarily YBCO (00*l*) peaks and BSO (002) peaks in the typical θ-2θ scans, indicating that all four composite films are highly textured along YBCO (00*l*) on LAO (001) substrates. As the BSO concentration increases from 2 mol% to 20 mol%, the corresponding BSO (002) peak intensity also increases while no other peaks from other BSO orientations or other impurity phases were observed. This suggests that the primary (002) orientation remains as BSO doping concentration increases. Under this orientation relationship of YBCO(00*l*)//BSO(00*l*)//LAO(001), the theoretical lattice misfit rate, as well as corresponding coherent matching dislocation spacing and residual strains are calculated using the bulk lattice constants for the lateral and the vertical interface, respectively. As listed in Table 5.1, in the epitaxial thin film, besides the conventional lateral lattice confinement from the substrate, a lattice misfit of ~ 5.535% between the two film phases–YBCO and BSO-is suggested.

Table 5.1. The list of theoretical in-plane and out-of-plane lattice misfit, dislocation spacing calculated by bulk lattice parameters at room temperature.

Theoretical Predictions (assuming coherent contact)	LATERAL (substrate) STRAIN LAO a_s = 3.789 Å		VERTICAL (matrix) STRAIN YBCO $c_0/3$ = 3.894 Å
	YBCO $\bar{a}_0$ = 3.852 Å	BSO a = 4.116 Å	BSO c = 4.116 Å
Bulk Lattice Misfit (%) $2(a_s-a_f)/(a_s+a_f)$	//: -1.649 YBCO in // compre.	//: -8.273 BSO in // compre.	⊥: -5.535 BSO in ⊥ compression
Dislocation Spacing (nm) $d_{002_s}d_{002_f}/\|d_{002_s}- d_{002_f}\|$	11.584	2.385	3.704

Note: for the vertical strain prediction, the d_c(001) of YBCO is divided by three, i.e. the averaged $c/3$ =3.894Å, for simplification. In the calculation of dislocation spacing, d_{002_s} is adopted considering the actual (002) monolayer matching.

It is interesting to note that, as shown in the enlarged XRD pattern in Fig. 5.1(b) with all diffraction peaks normalized based on the strongest LAO (002) peak, both YBCO (006) and BSO (002) peaks shift towards lower angles, i.e. larger out-of-plane lattice parameters, as the BSO concentration increases. The ratio of YBCO (006) / (005) peak intensity was calculated for each sample and remains relatively constant. It indicates little or no variation in oxygen stoichiometry of the YBCO matrix for all the samples, which is in agreement with the fact that all of the films were prepared under the same PLD conditions. The calculated d_c of the YBCO matrix and of the BSO secondary phase, as well as their increases as a function of doping concentration is then presented in Fig. 5.2. Comparing to the d_c of a 280-nm-thick pure YBCO thin film (~ 11.704 Å), the out-of-plane d_c of the YBCO phase in the doped thin films only shows a very small

variation. However, the d_c of the BSO secondary phase increases about 0.6% when the doping concentration rises to 20mol%.

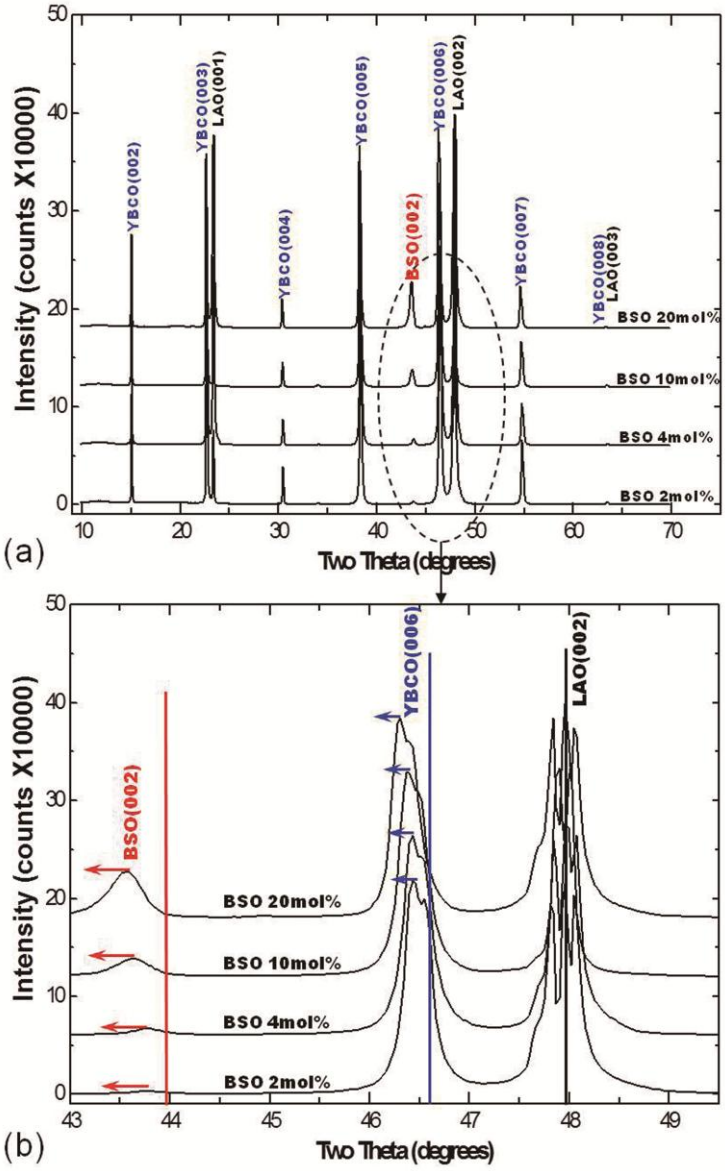

Figure 5.1. XRD θ-2θ scans of YBCO samples with 2 mol%, 4 mol%, 10 mol% and 20 mol% BSO in: (a) the full range; (b) the enlarged XRD scan showing YBCO (006) and BSO (002) peaks. All diffraction patterns are normalized with the strongest LAO (002) peak. The peak positions of bulk YBCO and BSO are noted in (b) as solid line for reference.

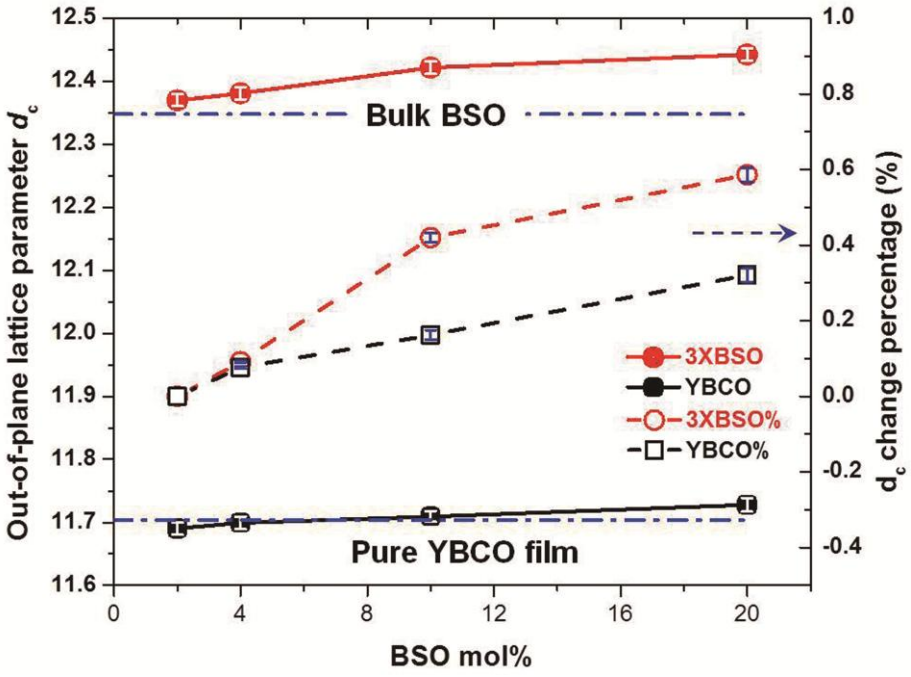

Figure 5.2. The plot of XRD out-of-plane lattice parameter and corresponding percentage variations of the YBCO and the BSO in all four samples.

To reveal how the BSO secondary phase disperses in the YBCO matrix and the related defects caused by the dopant structures, we conducted both plan-view and cross-section TEM (XTEM) studies on all the composite films. Figs. 5.3 show low magnification XTEM images of YBCO+BSO films on LAO substrates with BSO doping concentration varied from 2 mol% to 20 mol%. It is noted that nicely grown BSO nanopillars align vertically throughout the film thickness. With the increase of BSO concentration, these vertically aligned nanopillars were not growing wider; instead, their density increases accordingly. A clear illustration of the dimension and distribution of the BSO nano-columns with different doping concentrations is presented in the plan-view TEM images in Figs. 5.4. As the BSO concentration increases from Fig. 5.4(a) 2

mol% to Fig. 5.4(d) 20 mol%, the nanopillars density increases from $2.60\times10^{10}/cm^2$ to $1.44\times10^{11}/cm^2$ while the diameter of the nano-columns remained relatively constant at about 7 ~ 8 nm in diameter.

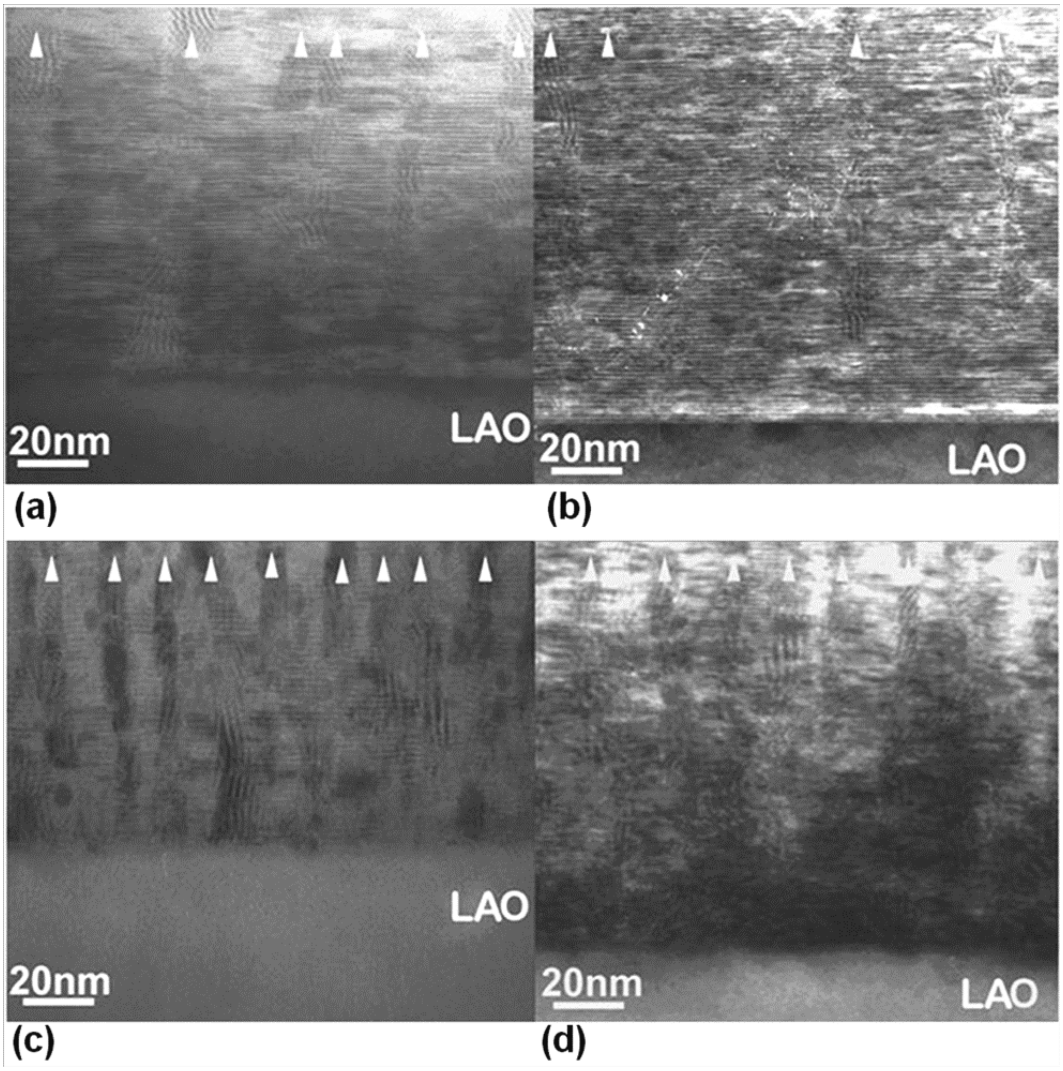

Figure 5.3. Low Magnification XTEM images of YBCO/BSO composites on LAO substrates with (a) 2 mol%, (b) 4 mol%, (c) 10 mol% and (d) 20 mol% BSO, respectively. High density vertically aligned BSO nano-columns are cleared observed in all four samples and marked as white triangles.

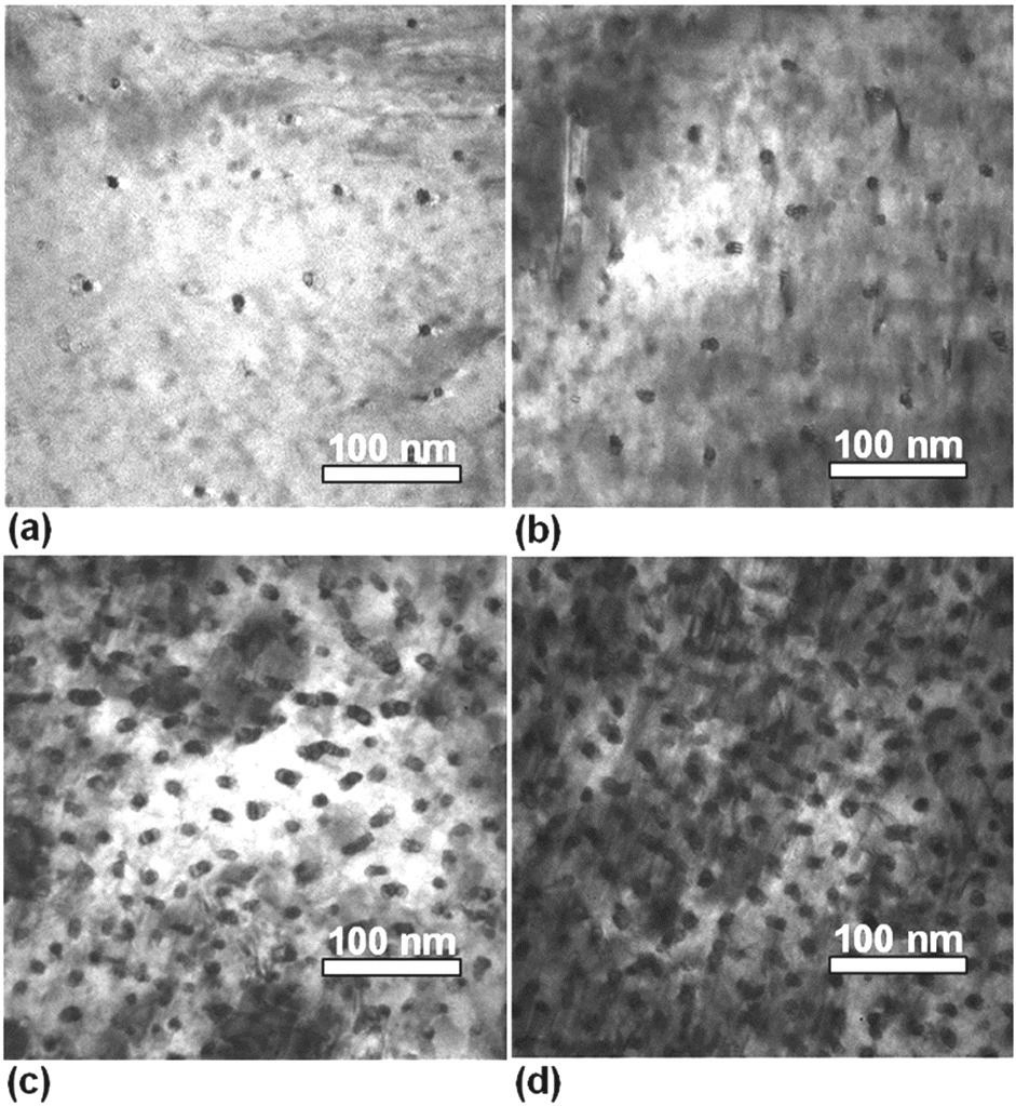

Figure 5.4. Plan-view TEM micrographs of YBCO/BSO composites with (a) 2 mol%, (b) 4 mol% (c) 10 mol% and (d) 20mol% BSO, respectively. The as-observed elliptic cross-sections of the BSO nano-columns are due to an angle between the sample surface normal and the column axis. The diameter of the BSO nano-columns was estimated from the shorter radius.

From the above XRD and TEM analysis, it is obvious that the YBCO+BSO films have grown as heteroepitaxial two-phase VAN. Different from most of the other artificial secondary phases, e.g. nanoparticles like $BaZrO_3$ (BZO) [16] and Y_2O_3 [24] or

nanolayers such as CeO_2 [17, 25] and Y_2BaCuO_6 [14], the BSO continuous nanopillars in the VAN structure grew epitaxially and simultaneously with YBCO matrix through the film thickness. Based on the Winterbottom construction [26] and recently presented guidelines to the materials selection of the self-assembled vertical nanocomposites [6], the intrinsic similarity in crystalline structures and out-of-plane lattice matching between the cubic Perovskite BSO and YBCO matrix, as well as the comparable wetting ability to the surface of (001) pseudocubic LAO substrate for both phases, lead to the tantalizing possibility of heteroepitaxy BSO in 3D (i.e., both in-plane as well as out-of-plane). Compared to another frequently used secondary addition – BZO – which forms continuous nanorods only under certain PLD conditions and many of the BZO nanorods was observed bent as film thickness increases; [27] BSO nanopillars intend to maintain the steady straight growth, despite our efforts in trying to break their continuity by raising deposition temperature during the PLD process. Thus, the proposed 3D heteroepitaxy was found to be quite robust in the PLD grown BSO/YBCO system and also in other $REBa_2Cu_3O_y$ (RE: rare-earth element) films [28]. The detailed self-assembled growth dynamics and morphology control of the nanostructures have been studied as one of the fundamental issues of the self-assembled nanocomposites [26] which are beyond the scope of this work. Here, we are trying to further investigate the lattice matching between the two phases that one occupies dominant film volume than the other; and to explore how they accommodate the challenge of an extra heterogeneous interface achieving the VAN structure.

The strain state of the 300 nm-thick YBCO+BSO VAN film is determined by two competing factors, i.e., the lateral strain from the substrate and the vertical strain between the two phases. To determine which one is dominant, the ratios of the vertical to lateral interface areas for BSO and YBCO in 2 mol% and 20 mol% samples are listed in Table 5.2, respectively.

Table 5.2. Calculations of the vertical to lateral interface areas ratios of the BSO and the YBCO in the VAN films with 2 mol% and 20 mol% BSO, respectively.

BSO concentration	**2 mol%**	**20 mol%**
the BSO nano-column density (**per cm^2** of the film/sub interface)	2.60×10^{10}	1.44×10^{11}
BSO/Sub interface area (cm^2)	$\pi r^2\times2.60\times10^{10} = 1.31\times10^{-2}$	$\pi r^2\times1.44\times10^{11} = 7.23\times10^{-2}$
BSO/YBCO vertical interface area (cm^2)	$2\pi rh\times2.60\times10^{10} = 1.96$	$2\pi rh\times1.44\times10^{11} = 10.85$
$\frac{\text{vertical interface area}}{\text{lateral interface area}}$ of BSO	$\frac{1.96}{1.31\times10^{-2}} = \frac{10.85}{7.23\times10^{-2}} = \frac{2h}{r} =$**150**	
$\frac{\text{vertical interface area}}{\text{lateral interface area}}$ of YBCO	$\frac{1.96}{1-1.31\times10^{-2}} =$ **1.99**	$\frac{10.85}{1-7.23\times10^{-2}} =$ **11.70**

Note: r refers to the radius of the BSO nano-column which is about 4 nm measured by TEM; h = 300 nm is the film thickness.

For BSO, apparently the vertical interface area between BSO and YBCO is much larger (about 150 times larger) than the lateral interface, due to the very small BSO nanopillar diameter. This suggests that the vertical strain is dominant in the BSO nano-columns, and it seems not affected by the doping concentration. According to the theoretical predications listed in Table 5.1, since BSO has a larger c-lattice parameter of

4.116 Å than the c/3 of YBCO (3.894 Å), a large vertical compression (~ 5. 385%) is expected in BSO in the ideal coherent lattice matching.

However, as shown in Fig. 5.5, the practical vertical BSO/YBCO interface suggests otherwise. HRTEM images of the 4 mol% and 20 mol% samples, and their corresponding fast Fourier filtered images are shown in Figs. 5.5(a) and 5.5(b), 5.5(c) and 5.5(d), respectively. Along the interface between BSO and YBCO, localized dislocation-like contrast (marked as white "T" in Figs. 5.5(b) and 5.5(d)) was observed in both samples. Taking the 4 mol% sample for instance, the misfit dislocation spacing (d_M) measured here in Fig. 5.5(b) is only ~ 3 nm, indicating a domain matching epitaxy (DME) [29] where 14 of (002) BSO lattices match with 15 of (006)YBCO lattices. Under such matching condition, the residual strain in BSO yields a vertical tension ~ 1.3%. The same filtered Fast Fourier Transformation (FFT) was applied to the HRTEM images taken at the vertical interfaces from samples with different doping concentrations. Although it is not conclusive that the VAN film with higher BSO concentration has a smaller d_M, a d_M ~ 2nm, resulting in an even larger residual strain ~ 4% in BSO, is observed at a section of vertical interface in the 20mol% sample.

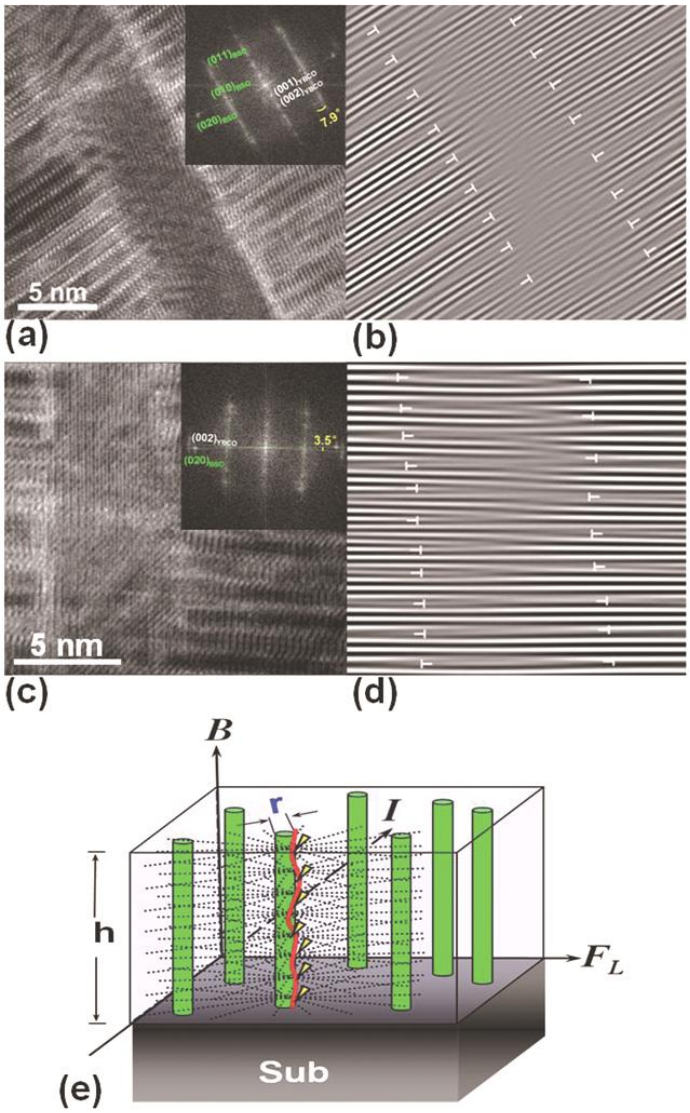

Figure 5.5. TEM observations at the BSO-YBCO vertical interface and the schematic illustration of the flux-pinning effect of the vertical interfacial defects under applied magnetic fields. HR-XTEM images and corresponding filtered Fast Fourier Transform (FFT) images are shown in (a) and (b), (c) and (d) for the 4 mol% and 20 mol% film, respectively. Misfit dislocations are marked as white "T" along the vertical interface. In (e), the thickness of the YBCO thin film is noted as h; the radius of the nanopillar is noted as r, respectively. When transport current (I) is applied under the magnetic field (B), the resulting Lorentz force (F_L) moves vortices toward right (showing by curved vortices line in red), dissipating energy and causing the electric resistivity to occur. The Vertical-interfacial-defects and their effects in pinning the vortices lines are illustrated in terms of the defects density. The misfit dislocation lines are noted as dotted lines around each doping phase.

Based on the theoretically predicted dislocation spacing (Table 5.1), the ideal dislocation spacing is ~ 3.7 nm, yielding a very small residual compression ~ -0.05% in the BSO (guided by the black arrows in Fig. 5.6).

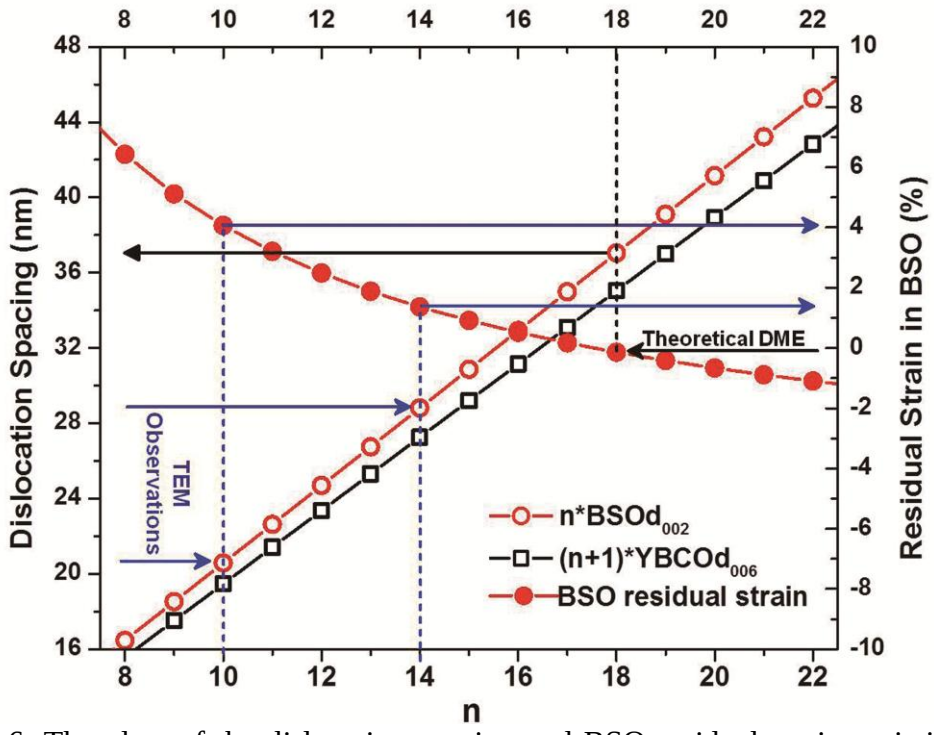

Figure 5.6. The plots of the dislocation spacing and BSO residual strain variation as a function of the domain epitaxy matching n. Black arrows and dashed lines guide the view of theoretical domain matching epitaxy; blue lines guide the TEM observed matching results in the YBCO/BSO nanocomposite film. The practical dislocation spacing (or domain size), as shown, is smaller than the theoretical prediction, resulting in the reverse in the vertical strain state of BSO.

However, practically, the dislocation spacing along the vertical interface is smaller (2~3 nm) than the theoretically calculated value, as illustrated by blue arrows in Fig. 5.6. This modified DME, thus, introduces considerably large residual tension in the BSO.

Moreover, besides the above lattice extension/compression, local lattice rotation related to the tilting growth of the BSO nanopillars, is also observed in the VAN films, especially those with low BSO concentration. As shown in Fig. 5.7(a), a BSO nanopillar in a 4 mol% film has a ~ 6° tilt off the c-axis. It is surrounded by an amorphous-like area with a thickness of 2-3 unit cells (~2.5nm).

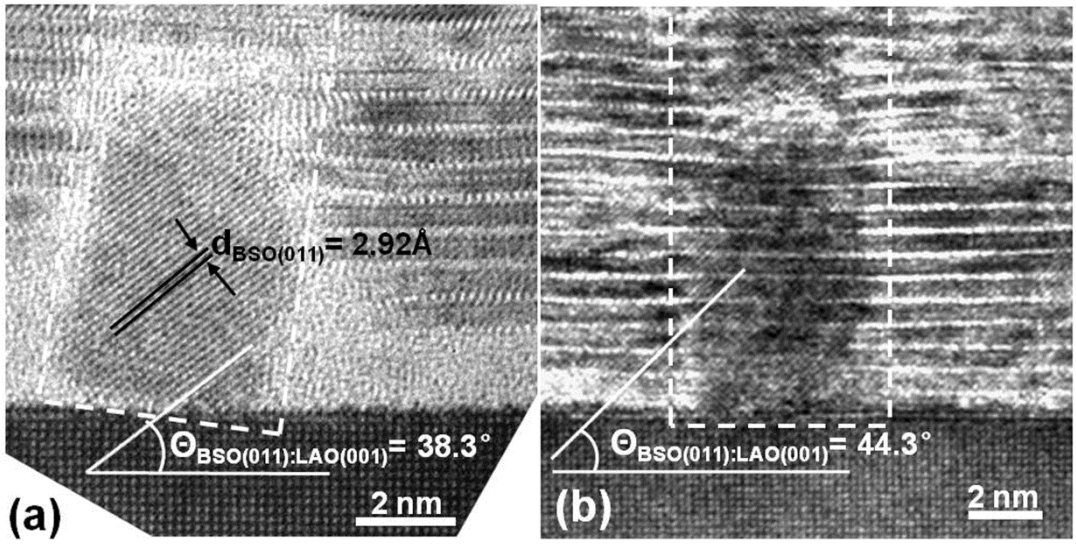

Figure 5.7. The enlarged XTEM images of the film/substrate regions of the YBCO+BSO film with (a) 4 mol% and (b) 20 mol% BSO, respectively. The BSO nanopillars' tilting angles are characterized by the angle between the BSO(011) and LAO(001), which is 45° in idea case.

While in the samples with higher BSO doping concentrations, such as Fig. 5.7(b), a thinner amorphous region (~ 1nm) is found mainly on the left side of a straighter BSO nanopillar in the 20 mol% sample. From our experience, the emerging of amorphous-like layers between YBCO and substrate could be introduced by TEM foil preparation. Whereas, these observed tilting growth is more likely attributed to the large

lattice mismatch between BSO and LAO substrate (~ -8.273%). Since YBCO is competing with BSO during the initial film growth, it's could be difficult for BSO to grow laterally and become wide enough to form domain matching epitaxy. One effective way of relieving this large lateral strain is tilting the BSO nanopillars slightly off the c-axis. And this titling growth could, in turn, impact the local out-of-plane and in-plane contact lattice relationship.

In all, a great number of dislocations with spacing 2 ~ 3 nm were observed along each BSO-YBCO vertical interface, and the dislocation density increases as the number of BSO nanopiller increases. Conventionally, interfacial defects, especially misfit dislocations, are of great interests in functional oxide thin films [30]. For example the film-substrate interfacial defects are believed to be responsible for the high J_c of YBCO and attribute to the thickness dependence effect of YBCO films. [31] For this BSO-YBCO VAN case, the BSO nanopillars as well as the defects along the interfaces between the BSO and YBCO are the effective pinning centers for the enhanced in-field performance. [19, 20] A recent study on $BaZrO_3$ doped YBCO films (BZO/YBCO) shows that the strain induced oxygen stoichiometry variation along the interfaces could also affect YBCO's superconducting performance. [23] In the BSO/YBCO case, the T_c of YBCO maintains a high value of >87K for all concentrations. [20] Therefore the effects of oxygen stoichiometry variation in the BSO/YBCO case might not be as strong as that in the BZO/YBCO case. A schematic illustration of the defect distribution and corresponding pinning effects of the VAN YBCO thin films is presented in Fig. 5.5(e). Under the applied magnetic field (B), the resulting Lorentz force (F_L) could move vortices toward

right (illustrated by the red vortices' line), dissipating energy and causing the electric resistivity to occur. As illustrated here, the vertically-aligned BSO nanopillars can provide the possibility of arranging the pinning centers throughout the YBCO film thickness and achieving a much stronger pinning effect especially for high field applications. The above defects analysis and discussions agrees well with the J_c results measured in applied magnetic field, [20] which showed an obvious enhancement in $J_c^{in\text{-}field}$ (H//*c*) as the YBCO doped with higher BSO concentrations. Therefore, although the accurate control on the density of the vertical interfacial defect is complex, VAN configuration is a promising approach for introducing and, more importantly, distributing the flux-pinning defects throughout the film thickness and forms a 3D defect network.

5.5 Conclusions

In conclusion, we have conducted in-depth microstructural characterizations on the PLD-grown BSO/YBCO VAN to explore the growth mechanism and vertical strain tuning of VAN. In all four YBCO films with the BSO doping concentration varied from 2 mol% to 20 mol%, continuous BSO nanopillars with nearly constant diameters of around 7-8 nm, grow epitaxially and distribute randomly in the YBCO matrix. XRD results suggest a strong lattice strain tuning between the YBCO matrix and the doped BSO nanopillars as a function of the nanopillar density. It was noted that along their vertical heterogeneous interfaces, a high density of dislocations in the order of 10^{13} /cm^2

is found throughout the YBCO film thickness. These high density vertical interfacial defects could act as strong c-axis pinning centers and be responsible for the high field performance of YBCO films regardless of the film thickness.

CHAPTER VI

CS-CORRECTED STEM INVESTIGATION OF DISLOCATION CORE CONFIGURATIONS AT A $SrTiO_3$/MgO HETEROGENEOUS INTERFACE*

6.1 Overview

The heterostructures and interfacial defects in a 40-nm-thick $SrTiO_3$ (STO) film grown epitaxially on a single-crystal MgO (001) were investigated using aberration-corrected scanning transmission electron microscopy (Cs-corrected STEM) and geometric phase analysis (GPA). The interface of STO/MgO was found to be of the typical domain-matching epitaxy (DME) with a misfit dislocation network having a Burgers vector of ½ $\boldsymbol{a}_{STO}$ <100>. Our studies also revealed that the misfit dislocation cores at the heterogeneous interface display various local cation arrangements in terms of the combination of the extra-half inserting plane and the initial film plane. The type of the inserting plane, either the SrO- or the TiO_2- plane, alters with the actual interfacial conditions. Contrary to previous theoretical calculations, the starting film planes were found to be dominated by the SrO layer, i.e. a SrO/MgO interface. In certain regions, the starting film planes change to the TiO_2/MgO interface because of atomic steps at the MgO substrate surface.

---

*This chapter is reprinted with permission from "Cs-corrected STEM investigation of dislocation core configurations at a SrTiO3/MgO heterogeneous interface" by Y. Zhu, C. Song, A. Minor and H. Wang, Microscopy and Microanalysis, in press (2013).

6.2 Introduction

The exact nature of the interface structure and its associated defects has been a long-standing question for studies of thin film mechanical and physical properties [22, 194]. Significantly different from their bulk counterparts, many oxide thin films, almost all with heterogeneous interfaces, behave as strongly correlated electronic systems [195]. In these confined structures, multiple coupling states - charge (electronic), orbital (and/or spin) and inhomogeneous lattice strain - interact, and become very sensitive to subtle structural perturbations and hence present novel properties [196]. Studies on typical perovskite $SrTiO_3$ (STO) thin films have showed that dislocation cores have a distinct local composition [68], and can switch the film electrical properties [197]. Ferroelectric barium strontium titanate ($Sr_{1-x}Ba_xTiO_3$) grown on MgO [198], is considered as one of the most promising high-κ dielectric candidates for replacing SiO_2 in MOS gates downsizing [199]. The film quality and functionality are largely dependent upon the heterogeneous interface structure, i.e. interfacial defects and lattice strains [197, 200].

Although rocksalt MgO has one neutral (001) surface, perovskite STO allows for two types of (001) termination, the SrO- or TiO_2-planes, which could enable different chemical bonding at the interface. For the interface contact of STO/MgO, previous first-principle calculations suggested that starting the STO film growth with a TiO_2 layer is preferred due to its thermodynamic stability [201] and that it is in favor of strain relaxation [202]; whereas, experimentally it was not conclusive [203]. In fact, due to the coupling effects at the confined heterogeneous interface [196], together with the film-substrate lattice

thermal expansion difference and surface step terraces [11, 12], interfacial structures are typically complicated and difficult to predict [13].

Owing to the development of aberration corrected electron microscopy, sub-angstrom resolution is readily achieved in high-resolution transmission electron microscopy (HRTEM) as well as in scanning transmission electron microscopy (STEM) [126]. Except for few special cases of channeling effect [204], one of the most advantageous aspect of STEM is its capability of faithfully recording image contrast as a function of lattice atomic number Z, i.e. the contrast does not reverse for a wide range of specimen thickness and imaging focus [121]. Therefore, it becomes possible to distinguish the atomic columns consisting of different elements, such as the TiO- and Sr-columns in STO. Due to the large lattice mismatch between STO and MgO (about 7.54% estimated by $2(a_s-a_f)/(a_s+a_f)$ using bulk lattice parameters at room temperature), a misfit dislocation network is expected. Although the dislocation core structures of STO were intensively studied in bulk samples [69] or at homogeneous interfaces [205], reports on the misfit dislocations at the heterogeneous interface of functional oxides are limited to very few systems [15, 16] and so far there is no such report for the interface of STO/MgO.

Here, we present a detailed interfacial structure analysis on a pair of oxide heterostructures - STO/MgO and MgO/STO - using aberration-corrected high resolution scanning transmission electron microscopy (Cs-corrected STEM) in combined with geometric phase analysis (GPA) [108]. GPA is an image processing method used for mapping lattice displacement and has been successfully applied to misfit dislocations and their associated strain fields [206-208]. Important details of the interface structure at the

partially coherent heterointerface, such as the termination planes, cation disorder, and nature of the substrate terraces, were investigated at the atomic scale. In particular, we focused on the misfit dislocations observed at the heterogeneous STO/MgO interface. The type of misfit dislocation network at the heterointerface was determined by imaging in both the <100> and <110> directions; and the local cation arrangements at the dislocation cores were further revealed by applying GPA to Cs-corrected STEM images. Following this the correlations between the interface structure - the substrate steps and interdiffussion - and the misfit dislocation core configurations were discussed and compared with atomic models. Microscopy analysis of the MgO/STO system is also presented as a unique comparison study for systems with a reversed strain state.

6.3 Experimental

Two epitaxial thin films, STO on MgO and MgO on STO, were deposited by a standard pulsed-laser deposition technique (with a KrF excimer laser $\lambda = 248$ nm) using both commercial MgO and STO targets (CERAC, Inc.) and commercial single crystal MgO(100) and STO(100) substrates. The depositions were carried out at the same substrate-to-target distance of 5 cm, target temperature of 780 °C, under an oxygen pressure of 27 Pa (about 200 mTorr), with a laser energy of 300 mJ and a repetition rate of 2 Hz. Without post annealing, the samples were directly cooled down to room temperature in 4×10^4 Pa (300 Torr) of O_2. After 720 s and 600 s depositions, the resulted STO and MgO film thicknesses are around 40 nm and 15 nm, respectively.

Cross-sectional specimens were prepared through a conventional TEM sample preparation routine including cutting, gluing, grinding, polishing, and final precision ion polishing.

We employed the TEAM 0.5 TEM to investigate the interfacial configuration. TEAM 0.5 is a modified FEI Titan microscope with a special high-brightness Schottky-field emission electron source an improved hexapole-type illumination aberration corrector capable of resolving details as small as 0.05 nm (also the electron probe size) [135, 137]. All annular dark-field (ADF) STEM micrographs were recorded in TEAM 0.5 with a convergence semi-angle of 17 mrad after fine-tuning of the probe corrector at 300 kV to a flat-phase angle of over 25 mrad (typical residual aberration coefficients are listed elsewhere [126]). A moderate ADF detector inner semi-angle of 43 mrad was selected to boost the image signal-to-noise ratio for the later intensity line profile, while still maintaining a similar STEM intensity ratios as that at a higher detector inner angle.[121]

To process the high resolution ADF-STEM micrographs, GPA software (a plug-in of Digital Micrograph 1.8.3 package, HREM Research Inc.) was employed to generate the corresponding phase and strain map. For each dot-like micrograph, the geometric phase algorithm reconstructs the displacement field utilizing Fourier filtering centered around two non-collinear Bragg vectors (details see [108, 139]. The phase component of the complex image, i.e. phase image, presents the local deviation in a chosen set of lattice planes from a reference lattice; and the derivation of the complex image gives the strain field in a principle direction. The “phase” in GPA does not refer to

the electron wave function, but to the position of image contrast maxima. STEM imaging, due to its essential difference from HRTEM projection imaging, tends to introduce artificial fringe distortions during image collection. The "flyback" error, which is along the fast scan direction, is one of the major artifacts in scanning imaging[209, 210]. To minimize the "flyback" effects, we aligned the slow scan direction (orthogonal to the fast scan direction) of each STEM image parallel to principal x-axis of the strain map. This method was proved to be effective in eliminating the lattice distortion caused by the "flyback" error in the STEM image with defect-related [$-\pi$, π] phase boundaries. [210]

6.4 Results and discussion

Fig. 6.1(a) is a representative cross-sectional Cs-corrected STEM image of a 38-nm-thick STO epitaxial thin film on MgO (100) substrate acquired in <100> zone axis. Since the STEM image intensity is generally proportional to Z^n of the scanned crystal (n = 1.5 to 2.0), the enlarged interface region in Fig. 6.1(b) shows, the Sr-columns as the brightest dots with the less bright TiO-columns located at the centers of the Sr-square lattice. Together Fig. 6.1(b) presents the standard perovskite lattice in <100> projection. On the other hand, the MgO-columns have the least contrast, forming another cubic lattice in the <100> direction (Please note that the O-columns are not resolvable in the STEM images here but illustrated in the atomic models in Fig. 6.1(f)).

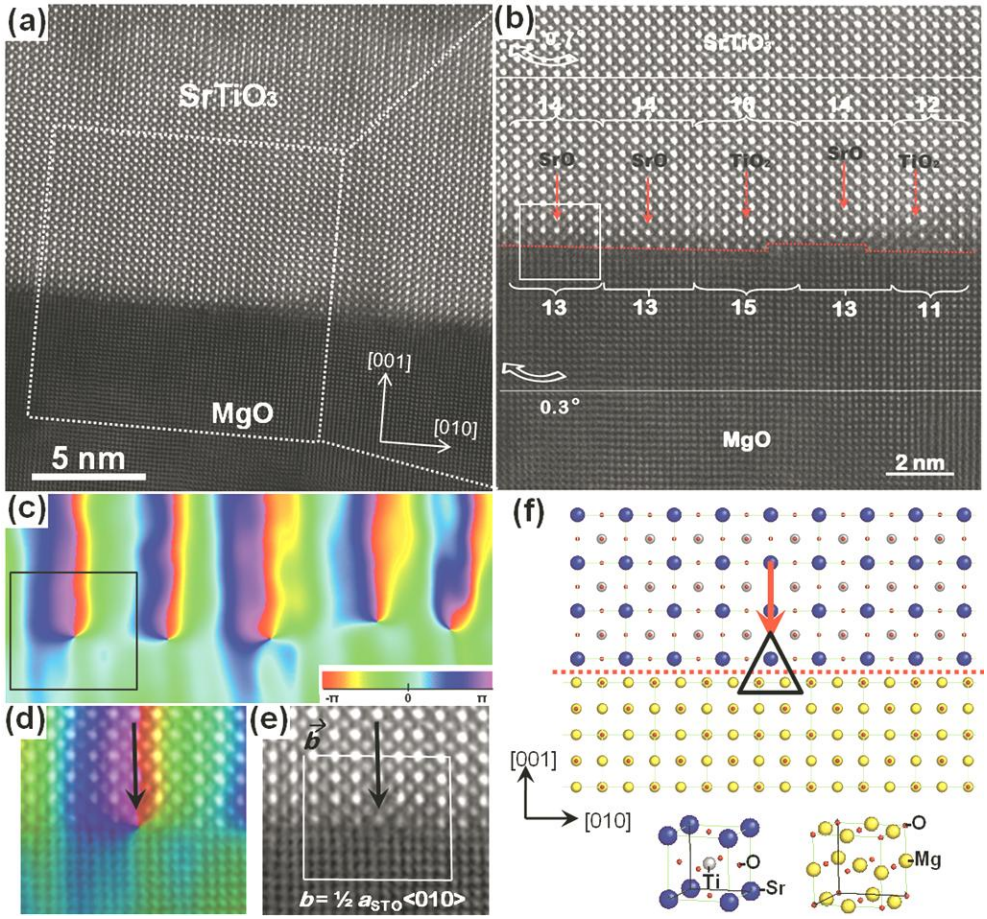

Figure 6.1. (a) A representative high-resolution Cs-corrected STEM image of the STO/MgO heterointerface in <100> zone axis. (b) Enlarged interfacial area with five misfit dislocation cores. Red vertical arrows point the extra-half planes at each dislocation core. The corresponding matching domains were bracketed with their sizes noted by the number of the STO (020) and MgO (020) lattice planes, respectively. A net lattice distortion angle of 0.7 degree and 0.3 degree was measured in the STO layer and the MgO layer, respectively, about 5 nm away from the interface. (c) The 020 phase image of the interface region obtained by applying geometric phase analysis. (d) Enlarged misfit dislocation from (b) superimposed with the corresponding phase image to show the relationship between the abrupt phase alternation and the position of the extra-half-plane. (e) A Burgers circuit applied on the same dislocation core to illustrate the misfit dislocation has a Burgers vector of ½ $\boldsymbol{a}_{STO}$<010>. (f) Schematic illustration of the dislocation core structure in (e) by atomic models of STO and MgO.

Five misfit dislocations, marked by red arrows in Fig. 6.1(b), were found at the heterogeneous interface of STO/MgO. To determine the dislocation network type, which is considered essential for describing the interface crystallographic structure [211], GPA was applied on the STEM images taken in both <100> and <110> directions. In Figs. 6.2(a) to 6.2(b), typical Cs-corrected STEM images of the STO/MgO heterointerface are presented, together with corresponding Fourier transforms, filtered Bragg images (Figs. 6.2(c) and 6.2(d)), geometric phase images (Figs. 6.2(e) and 6.2(f)) and strain field maps (Figs. 6.2(g) and 6.2(h)). Compared with the filtered Bragg images the phase images provide a better visualization of the lattice variations from the reference [108], where in this case the crystalline MgO substrate was selected as a reference. As shown in the 020 phase image (Fig. 6.2(e)) of the STO/MgO interface in <100>, the phase is approximately zero in the MgO substrate lattice, but presents significant deviations in the top STO film region. These lattice displacements correspond to the misfit dislocations in the 020 Bragg image in Fig. 6.2(c). An obvious demonstration is also shown at the convergent region of strain around the dislocation core in the in-plane-lattice-strain map E_{xx} (Fig. 6.2(g)). Thus, the distribution of these misfit dislocations as well as their spacing can be easily determined using this analysis technique.

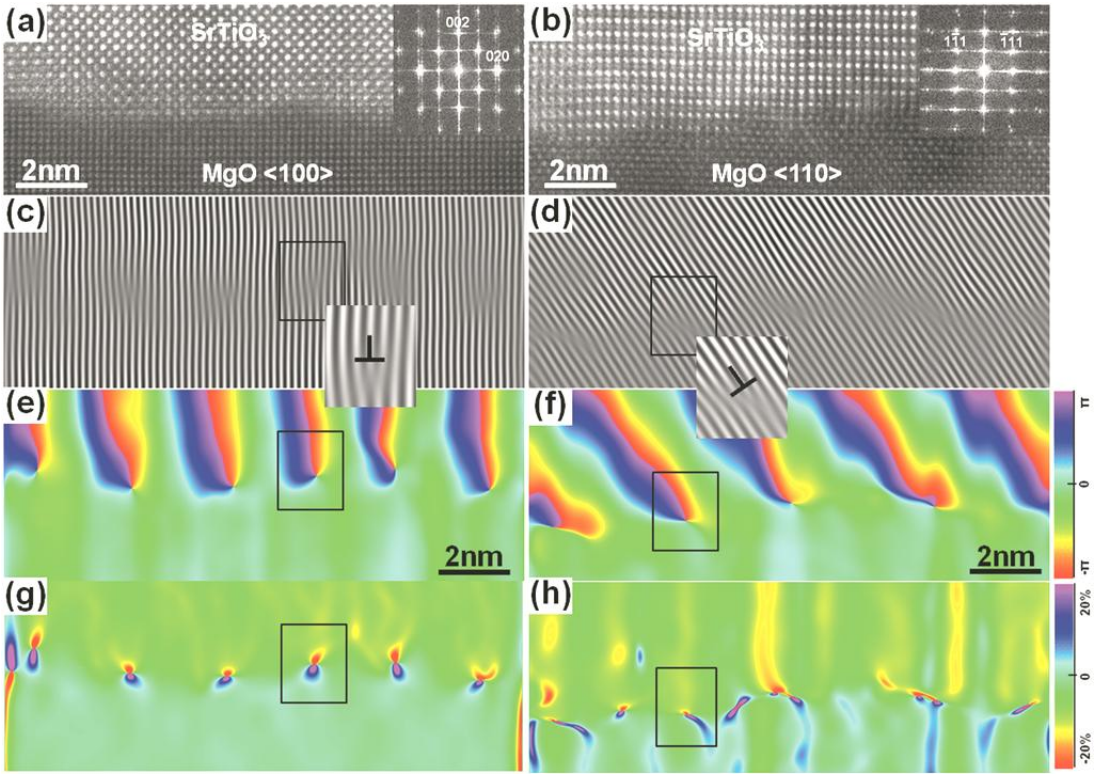

Figure 6.2. Typical Cs-corrected STEM images of the STO/MgO heterointerface in (a) <100> and (b) <110> zone axis. The inserts are corresponding Fourier transforms. (c) 020 Bragg image, (e) 020 geometric phase image and (g) the in-plane E_{xx} strain field map calculated using both 020 and 002 vectors in (a). (d) $\bar{1}11$ Bragg image, (e) $\bar{1}11$ geometric phase image and (g) the in-plane E_{xx} strain field map calculated using both $\bar{1}11$ and $1\bar{1}1$ vectors in (b).

Two criteria can be used to identify the type of dislocation network: (1) the direction in which the dislocation core could be directly observed and (2) the dislocation spacing relationship [203]. Here, in Figs. 6.2(e) and 6.2(g), the periodic edge dislocation cores were found in the <100> direction and their experimental spacing measured from the phase image was 2.67 nm, agreeing well with the theoretical estimation (the misfit dislocation spacing $d_s = (a_f \times a_s)/2(a_f - a_s)$ = 2.69 nm based on the bulk lattice parameters of the STO film and the MgO substrate). Additionally, in the <110> direction, inspecting

the STEM images by viewing the interface $(\bar{1}11)$ plane displacement variation in Figs. 6.2(d) and 6.2(f) [210] periodic dislocations are also visible. The measured spacing between these 45 degree inclined dislocation end-on yields 3.77 nm (similarly that the distance between the two components in E_{xx} strain map Fig. 6.2(g) measured as 1.89 nm), equal to the d_s of <100> after projecting in the <110> direction. This confirms that the nature of the misfit dislocations at the STO/MgO heterointerface is a <100> dislocation network. More precisely, as shown in Fig. 6.1(b), there are 14 $(020)_{STO}$ lattices that match with 13 $(020)_{MgO}$ lattices cube-on-cube. This feature of domain-matching epitaxy (DME) [10] leads to an estimated residual strain of 0.134% much smaller than the rigid lattice-matching epitaxy (LME) strain of 7.836%.

In addition, the Cs-corrected HRSTEM imaging also reveals interesting chemical information including the type of the extra-half inserting plane for the misfit dislocations, which could determine the cation sub-lattice of the misfit dislocation core. The GPA technique has shown the capability for illustrating the lattice variation reproducibly [210] and accurately [208] without human errors. When applying GPA to STEM images, not only does the lattice displacement become more visible but the chemical characteristic of the lattice can also be presented simultaneously. For example, in Fig. 6.1(d), an enlarged image of the first dislocation core in Fig. 6.1(b) is superimposed by its 020 phase image Fig. 6.1(d) and the phase changes abruptly across a edge dislocation. This π to $-\pi$ (purple to red) phase jump corresponding to a translation of half *a*-lattice fringe spacing [108] is caused by inserting the extra half plane in the STO film. Moreover, here, based on the image intensity, it is a SrO extra-half-plane sitting on the dislocation

core with a Burgers vector of ½ $\boldsymbol{a}_{STO}$<010> as demonstrated by the Burgers circuit in Fig. 6.1(e). The atomic configuration of this dislocation core is schematically illustrated in Fig. 6.1(f). The same methodology was applied to the Cs-corrected STEM images in this work in order to unambiguously determine the extra-half-plane type. At the STO/MgO heterointerface, the inserting planes are identified as either the SrO extra-half-plane or the TiO_2 extra-half-plane (here, for example in Fig. 6.1(b), 3 of SrO extra-half planes and 2 of TiO_2 extra-half-planes). Under the ideal case, in the absence of any perturbations, one single regular type of the extra-half-inserting plane, i.e. SrO- or TiO_2-plane, is expected at the dislocation core centers. The types of inserting planes observed in this study are possibly related to the interface imperfections, which is discussed later in the paper.

Unlike the STO homogeneous dislocation core structures [69, 205], the vertical inserting planes above the STO/MgO interface are observed almost perfectly parallel to each other along the [010] direction. However, the STO (002)-stacking-planes above the interfacial dislocations are not perfectly horizontal but tilting upward to the right, as shown by a curved open arrow in Fig. 6.1(b). This results in a net lattice tilting of less than 1 degree depending on the imaging areas (e.g. 0.7 degree for the area in Fig. 6.1(b)). Similar lattice bending was also observed in the MgO-substrate planes, with a smaller net tilting angle through the same region, reflecting a rumpled lattice distortion similar to previous observation [212]. This can be attributed to the fact that the heterointerface is essentially a three dimensional structure accommodating residual

lattice strains in all *a*, *b* and *c* directions; so that the rumpled (002) plane could be a result of the lattice displacement variation mainly in the out-of-plane *c* direction.

In short, the STO/MgO heterostructures with a lattice misfit larger than 7 % (at both room temperature and the deposition temperature) is a typical DME interface, where a misfit dislocations network with a Burgers vector of ½ $\boldsymbol{a}_{STO}$ <100> is generated. This introduces possible structural and chemical perturbations to the inhomogeneous strain fields.

Another key interfacial chemical feature at the STO/MgO heterogeneous interface is the starting film plane. An image intensity profile along the atomic planes at the interface was performed on all of the acquired STO/MgO STEM images. For example, two intensity line profiles at the interface are shown in Fig. 6.3 and Fig. 6.4, respectively. According to the intensity as well as the periodicity of each atomic plane (Fig. 6.3(b) and Fig. 6.4(a)), the starting thin film planes in our observations were dominated by the SrO plane, indicating a SrO/MgO contact at the interface. A previous study of the STO thin films with and without an atomic TiO_2 buffer layer on MgO showed that the misfit dislocation spacings are approximately 3.1 nm and 2.8 nm, respectively [213]. The latter case is closer to our observation of dislocation spacing, which confirms the initial growth plane of our STO film is dominated by SrO plane. However, our experimental observation is in contrast to some of theoretical calculations, based on which the TiO_2/MgO contact was preferred for thermodynamic stability [201] and for strain relaxation [202].

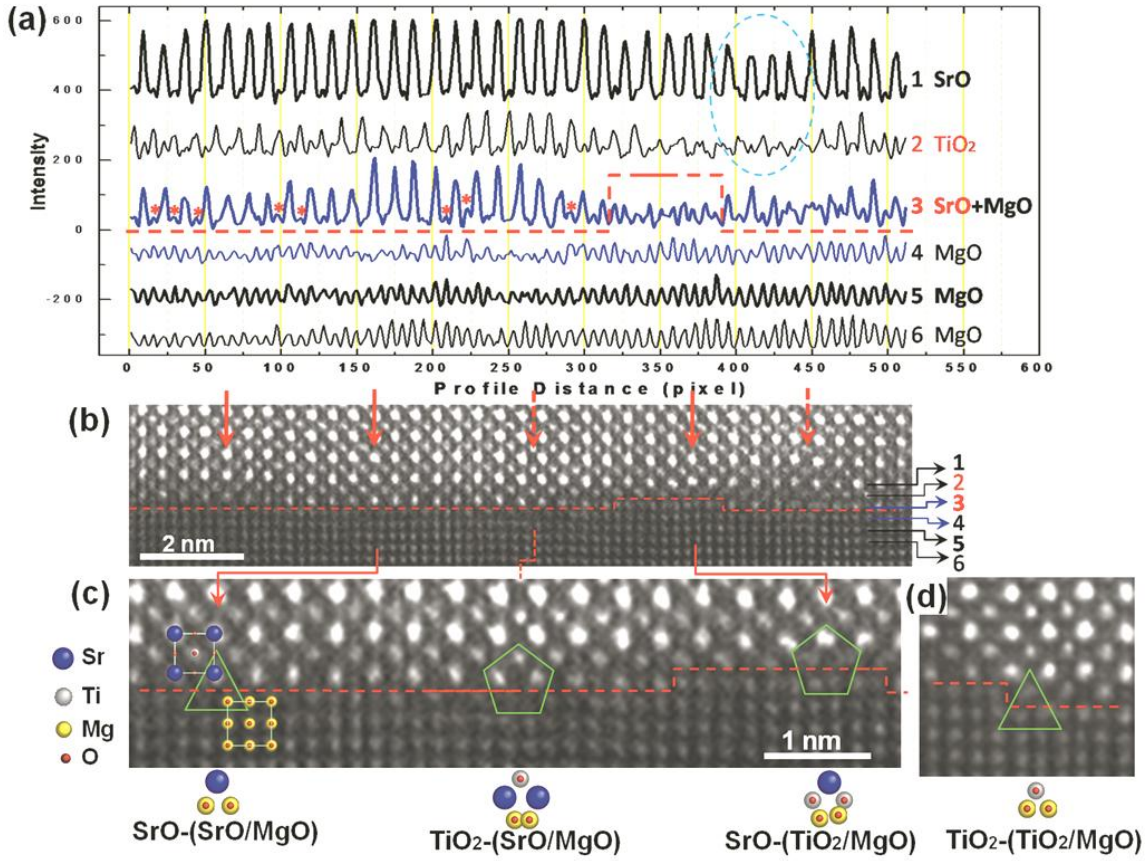

Figure 6.3. (a) Intensity line profiles along the six atomic planes noted as 1 to 6 at (b) the interface of STO/MgO in Fig. 6.1(b). The MgO substrate surface terrace with atomic-height steps is marked by a dotted line to guide the eye. The extra-half planes identified by GPA are marked by arrows, solid arrows represent SrO-planes and broken arrows are for TiO_2-planes. (c) Enlarged area from (b) shows three different dislocation core configurations. (d) The 4^{th} type of core configuration for the STO/MgO heterostructures from a different region of the specimen. Atomic-column-projection models of the four basic dislocation core configurations of the STO/MgO system are illustrated schematically to show their composition and core size.

This inconsistency suggests that the in real film growth, especially for those systems with comparable interface energy like the SrO/MgO (4.6 J/m^2) and the TiO_2/MgO (3.1 J/m^2)[214], other factors such as interfacial defects that are usually not taken into account in theoretical calculations can influence the growth mechanism and

the resulting interface structure. Previous studies have already pointed out that by tuning the interfacial chemistry it is possible to modify the strain distribution through relaxation [215].

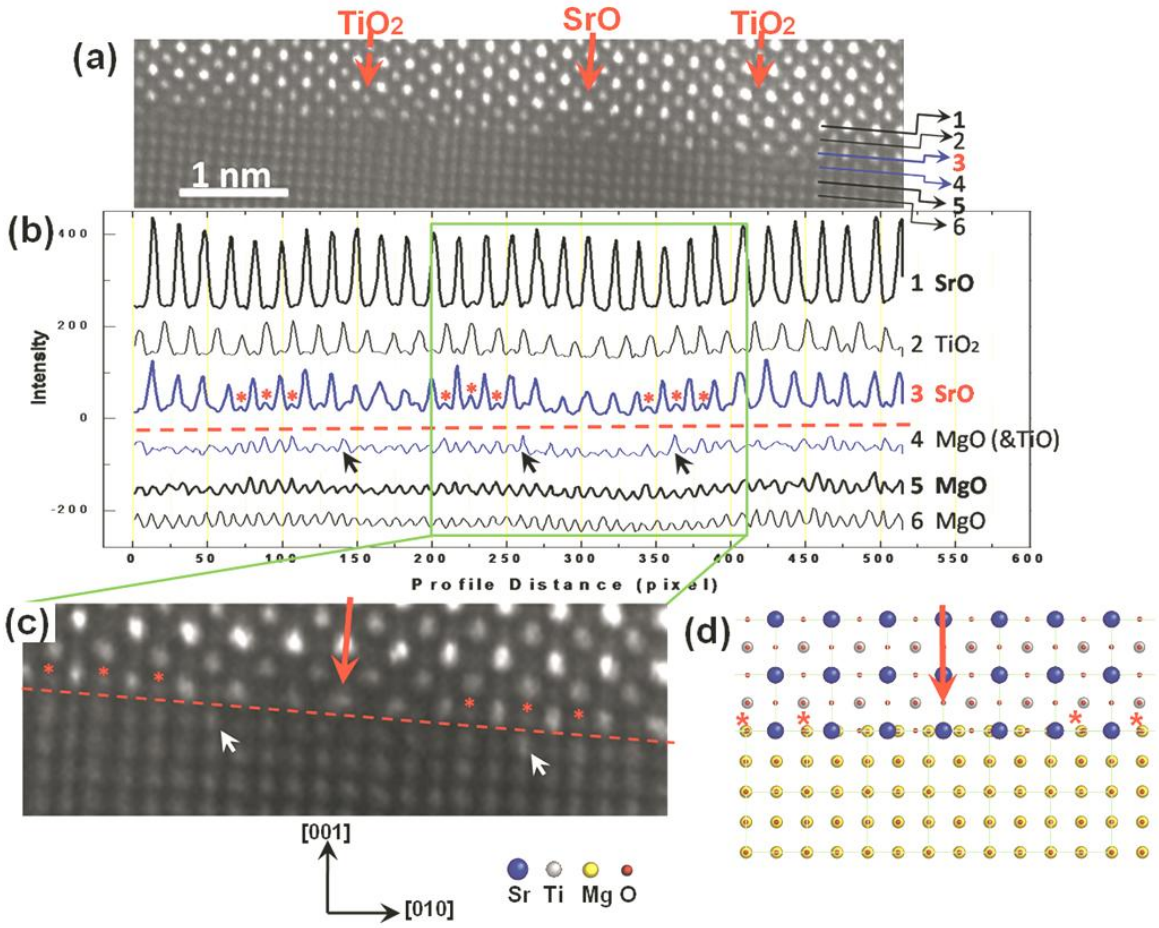

Figure 6.4. (a) The STEM image of a different region of the STO/MgO interface. The extra-half planes identified by GPA (not shown here) are marked by arrows. (b) The intensity line profiles of (a). Additional intensities in the starting SrO-plane and the surface MgO-plane marked by stars and arrows, respectively, suggest a certain extent of interfacial interdiffussion. (c) Enlarged dislocation core area from (b). (d) An atomic-projection model illustrates the interdiffussion observed in (c).

We explored the above issue by a careful study on the major interfacial defects at the heterointerface STO/MgO and found that the configuration of the dislocation cores is closely related to the local interfacial conditions, i.e. substrate surface terraces and possible substrate/film interdiffussion. In Fig. 6.3(b), it was found that as steps with atomic-scale-height emerge at the MgO-substrate surface, instead of maintaining the same type of starting plane and generating antiphase boundaries [15], the interface contact changes from SrO/MgO to TiO_2/MgO which also leads to a different core configuration. It should be noted that for both Fig. 6.3 and Fig. 6.4, the color-coded circles in the core models represent the dominant atom type in each atomic column; there could be intermixing along the incident e-beam direction. In fact, additional intensities in the starting SrO-layer (marked by stars in Fig. 6.3 and Fig. 6.4) and stronger intensities in the MgO-layers (pointed by arrows in Fig. 6.4) suggest possible interfacial interactions.

A typical case of this interface interdiffussion is shown in Fig. 6.5. The observed interdiffussion, up or down, at the interface suggest that they are more likely to happen at regions slightly away from the dislocation cores. Therefore, four basic misfit dislocation core configurations – SrO-(SrO/MgO), TiO_2-(TiO_2/MgO), SrO-(TiO_2/MgO) and TiO_2-(SrO/MgO) – depending on the interface types as well as the extra-half inserting planes, were observed in the specimen (Figs. 6.3(c) to 6.3(d)). In order to distinguish the two, different notations are adopted, '/' for interface and '-' for the extra-half inserting plane. For example, in Fig. 6.3(c), SrO-(SrO/MgO) stands for a dislocation core that is formed by inserting the SrO-plane on top of the heterogeneous interface contact of SrO/MgO. Since the interface contact of SrO/MgO was found

dominant in the STO/MgO system, the two core configurations of SrO-(SrO/MgO) and TiO_2-(SrO/MgO), with no preference between the two, are more often observed among all twenty images analyzed. Furthermore, it is interesting to see that the dislocation cores with the same type of initial film layer and of the extra-half inserting plane present a smaller core size (i.e. the three-atom-consisted core structure of SrO-(SrO/MgO) and TiO_2-(TiO_2/MgO)) compared to the ones that consisted of different planes (i.e. the SrO-(TiO_2/MgO) and TiO_2-(SrO/MgO) cores consisted by five atoms). This suggests a direct connection between the chemical disorder and lattice displacement at the dislocation core, i.e., a greater lattice distortion happens when more heterogeneous components are confined at the interface.

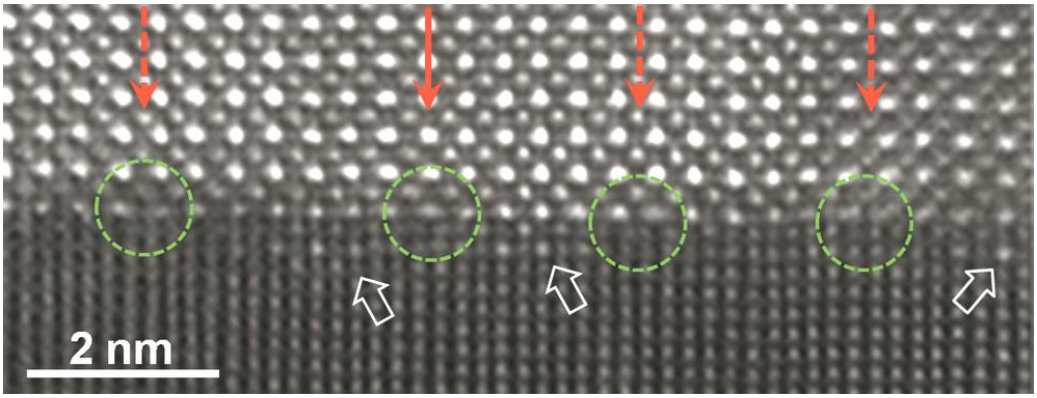

Figure 6.5. A typical STO/MgO interface region showing STO diffusion down into the substrate layers. The dislocation core positions are circled by dotted lines and the diffusion of STO into the substrate is noted by open arrows.

The above observed correlations between the real substrate surface conditions with the misfit dislocation position and core configuration are illustrated schematically by atomic models of the STO/MgO heterogeneous interface in Fig. 6.6. Under the ideal

condition (Fig. 6.6(a)), for the observed dominant interface contact of SrO/MgO in this study, the specific $14(020)_{STO}/13(020)_{MgO}$ domain matching is supposed to allow only one type of the dislocation core configuration, i.e. either the SrO-(SrO/MgO) or the TiO_2-(SrO/MgO). However, in reality the substrate surface is not perfectly smooth. Based on the observations in Fig. 6.3(c), a corresponding illustration is shown in Fig. 6.6(b) that shows that the emergence of atomic steps at the substrate surface could alternate the interface contact, and thus the core configuration changes accordingly.

In addition, interdiffussion can also happen at the substrate/film interface (e.g. Fig. 6.5). Interdiffussion brings additional compositional disorders to the interface chemistry, disturbing the ideal dislocation core periodicity (Fig. 6.6(c)), as well as the dislocation spacing. In summary, a certain amount of interdiffussion and atomic-height substrate steps were observed at the STO/MgO heterogeneous interface with a high density of misfit dislocations. Despite of the interfacial defects and rich dislocation core configurations, the absence of lattice defects such as antiphase boundaries or pores found in other PLD grown STO/MgO system [216] indicates the high quality of the STO epitaxial thin films observed in this study. It was suggested that a monolayer of TiO_2 needs to be deposited on the MgO (100) substrate prior to STO in order to achieve a two-dimensional film growth [213]. However, under the PLD conditions used in this study, there did not seem to be any problem for growing high quality STO film on MgO(100) with thicknesses ranging from 38 nm to over 150 nm.

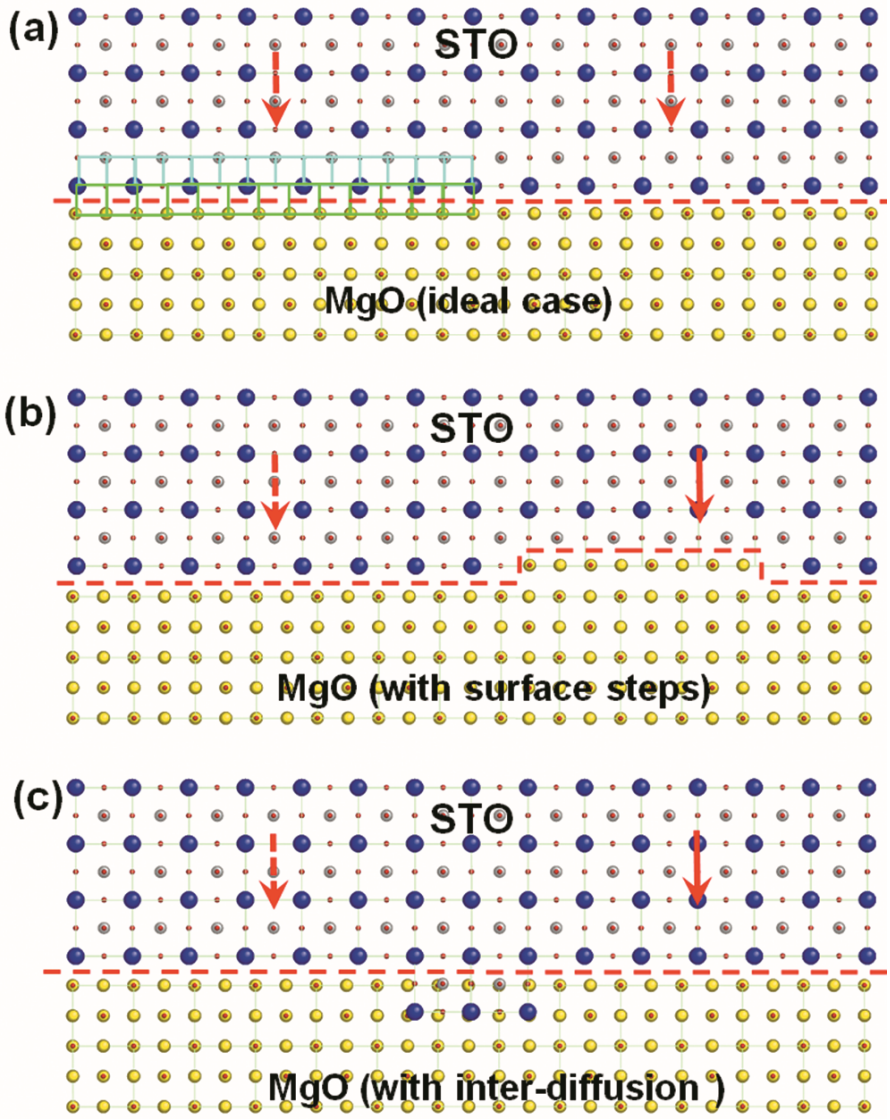

Figure 6.6. (a) The ideal condition of the 14(020)STO/13(020)MgO domain matching on a perfectly flat interface. Only one type of dislocation core configuration is expected. (b) The case of the MgO-substrate surface has an atomic-height step. The change of interface contact type alters core configuration. (c) The case of interdiffussion and its effect on dislocation core configuration.

For comparison, the reversed heterogeneous system MgO/STO was also studied using the STEM and GPA technique. A representative high-resolution Cs-corrected

STEM image of the MgO/STO(100) and the corresponding 020 Bragg image, phase image and E_{xx} strain map of the interface segment are shown in Figs. 6.7(a) to 6.7(d).

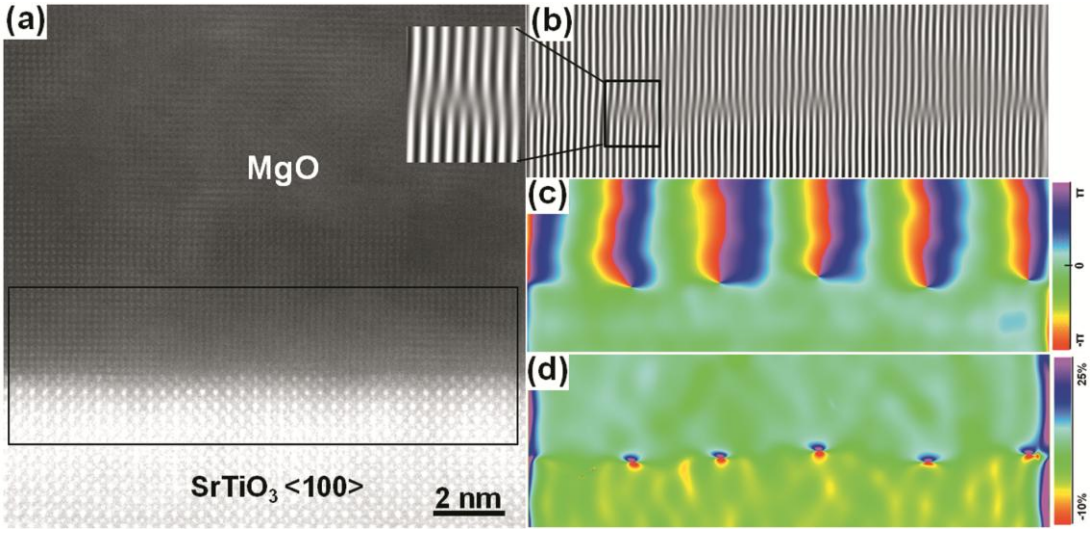

Figure 6.7. (a) Typical Cs-corrected STEM images of the MgO/STO(001) heterointerface along <100> zone axis. (b) Corresponding 020 Bragg image, (e) 020 geometric phase image and (g) the in-plane E_{xx} strain field map calculated using both 020 and 002 vectors. One misfit dislocation is enlarged to show the 'missing' (020) planes in the MgO thin film.

This 15-nm-thick MgO thin film deposited on a single crystal STO(001) substrate also shows high quality epitaxial growth and an atomically sharp interface. Similar to the former STO/MgO system, the average spacing between the misfit dislocations clearly located by the abrupt contrast in the 020 phase image (Fig. 6.7(c)) is about 2.70 nm, suggesting the STO/MgO also has a semi-coherent DME interface with a <100> misfit dislocation network. It is notable that the phase change across the STO/MgO dislocation is from $-\pi$ to π, opposite to the direction in the previous case of

MgO/STO (Fig. 6.1(c)), and corresponds to the 'missing' (020) planes in the MgO thin film as enlarged in Fig. 6.7(b).

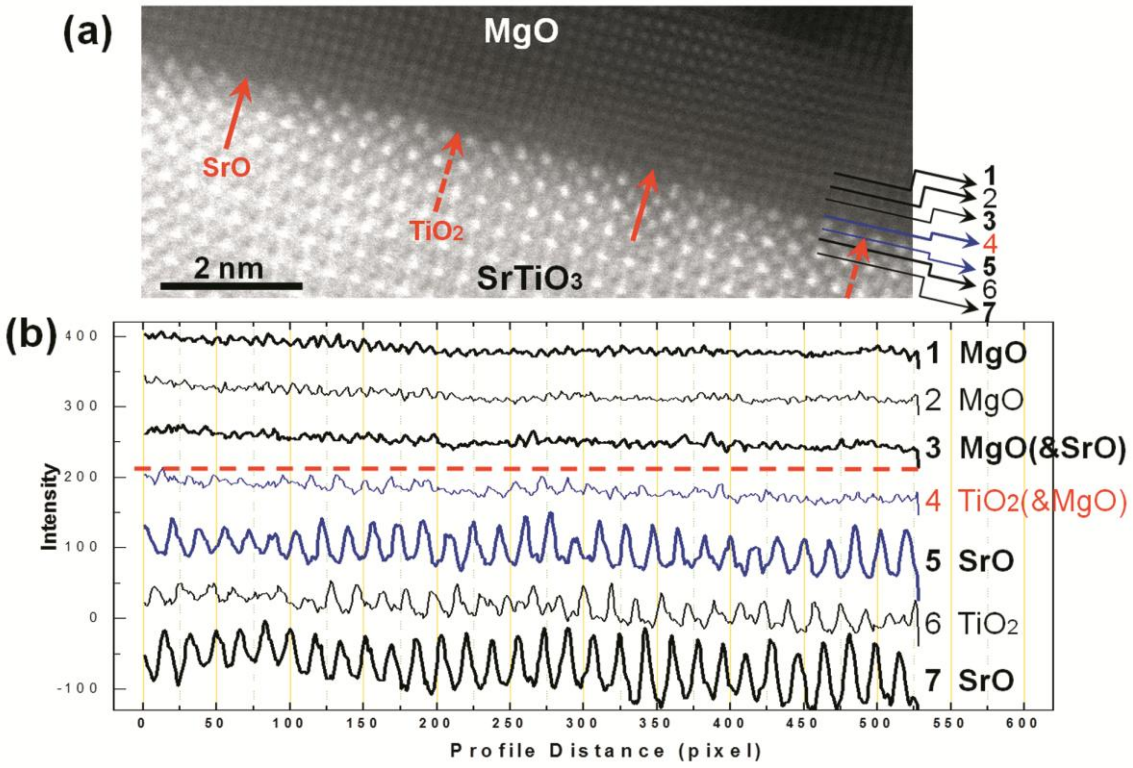

Figure 6.8. (a) The STEM image of a different region of the MgO/STO(001) interface. The extra-half planes identified by GPA (not shown here) are marked by arrows, solid arrows represent SrO-planes and broken arrows are for TiO_2-planes. (b) The intensity line profiles along the atomic planes in (a). It suggests an MgO/TiO_2 contact.

In Fig. 6.8(a), the extra-half planes in the STO substrate were marked by arrows to indicate the misfit dislocation cores. These misfit dislocations are generated to accommodate the lattice mismatch from the MgO film above. As in the reversed system, the type of the extra-half planes observed here still show a mixture of the SrO and TiO_2 planes. As for the interface contact, the image intensity profiles along the atomic planes

at this interface in Fig. 6.8(b) suggest a MgO/TiO_2 interface, which may be largely due to the fact that the termination layer of the STO(001) substrate is dominated by the TiO_2-plane and there is little surface modification prior to the deposition of the MgO film.

6.5 Conclusions

In summary, we used high resolution Cs-corrected STEM imaging and GPA to study the interface structure of two STO&MgO hetero-systems. Both thin films show excellent 14STO(020)/13MgO(020) domain-matching epitaxy (DME) with a high density <100> misfit dislocation network (dislocation spacing around 2.67 nm). The HR-STEM micrographs at the heterogeneous interfaces suggest that, in both cases, the type of extra-half planes at the dislocation core centre strongly depends on the real interfacial microstructures. The contact interface is dominated by SrO/MgO in the STO/MgO system, and by MgO/TiO_2 in the case of the MgO grown on STO. Further analysis of the dislocation core configuration of the STO/MgO interface revealed a highly sensitive interfacial environment, where minor geometrical (surface atomic-height steps) or compositional (localized interdiffussion) and/or charge perturbations could affect the interface contact, and therefore the dislocation core structure. The characterization method used in this work, Cs-corrected STEM combined with GPA processing can be applied in the study of nanostructures involving strain and stoichiometry modifications besides perovskite systems. The experimental observations

provide actual defect structures in atomic-scale that could be used for theoretical computation work.

CHAPTER VII

INTERFACE LATTICE DISPLACEMENT MEASUREMENT TO 1 PICOMETER BY GEOMETRIC PHASE ANALYSIS ON ABERRATION-CORRECTED HAADF STEM IMAGES

7.1 Overview

In this work, the accuracy of Geometric Phase Analysis (GPA) on aberration-corrected high-angle annular dark-field scanning transmission electron microscopy (Cs-corrected HAADF-STEM) images for lattice strain measurement at heterogeneous interfaces has been systematically investigated. Starting with an ideal crystal lattice of synthetic images, and then experimental HAADF images of a single-crystal lattice, we have quantitatively evaluated the inherent GPA processing artifacts and experimental errors due to STEM scanning distortions. Our results suggest that, with a properly chosen Fourier mask size and strain profile direction/width, 1 pm accuracy can be achieved for GPA strain quantification in the STEM fast-scan direction with a spatial resolution less than 1 nm. To demonstrate the effectiveness and reliability of the STEM-based GAP strain profile, we have applied it to two experimental heterointerfaces: the strained $LaAlO_3/SrTiO_3$ (LAO/STO) and the relaxed $SrTiO_3/MgO$ (STO/MgO). Interestingly, GPA strain mapping reveals a novel secondary relaxation mechanism in the LAO/STO heterostructures. Essential limitations in GPA are also discussed using the example of a $FeSe_{0.5}Te_{0.5}$(FST)/$SrTiO_3$ heterointerface. Although we focus on the

interfacial lattice strain in this paper, the approaches for strain error estimation and the fundamental discussions on line profiles can also be applied to other nanostructures with some modifications.

7.2 Introduction

The effects of lattice strain fields on the nature of heterogeneous interfaces have been a long-standing question in studies of thin film mechanical and physical properties [194, 217]. The film strain effect attracts extensive research interests owing to the recent discovery of exotic transport properties, e.g., insulator-metal transitions [218, 219], abnormal magnetoresistance [220] and superconductivity [221] in functional heterogeneous structures. For example, investigations of prototype perovskite $SrTiO_3$ (STO) showed that lattice distortion in favor of polarization-related tetragonality could enable room-temperature ferroelectricity [66]; studies on novel iron-based superconducting $Fe_{1+y}Te_{1-x}Se_x$ thin films found that interface strain modification [152] can either boost the critical superconducting transition temperature [33, 150] or destroy the superconductivity [151]. Control of the interface lattice mismatch strain requires an accurate knowledge of the actual strain field of the heterostructures in atomic scale.

Recent progress in digital image processing has enabled routine extraction and quantification of lattice parameters at an extremely high spatial resolution using dot-like high-resolution images. Geometric phase analysis (GPA) [108] and peak finding [106, 107] are the two main methods, working from Fourier space and real space, respectively. Despite

their algorithmic differences, the fundamental idea of image-based strain measurements is to identify the image contrast maxima as a periodic lattice and to calculate (and illustrate) the deviation of a real local lattice with respect to a reference crystal. These methods rely on one assumption that the image intensity peaks directly correspond to the positions of atomic columns in a given projection [107]. However, this assumption is not always valid, especially for phase-contrast-dominant high resolution transmission electron microscopy (HRTEM) which is known for its contrast reversal with sample thickness and microscope focus [119, 120] . In this work, high-angle annular dark-field scanning transmission electron microscopy (HAADF-STEM) has been chosen over HRTEM images in determining lattice strain at defective heterogeneous interfaces for the following reasons, (1) the contrast of STEM images is less sensitive to local sample variations; it has been experimentally confirmed that no contrast reversal in STEM up to a wide range of focus and foil thickness [121]; (2) STEM allows high resolution images to be taken from thicker foils to minimize surface relaxation [122, 123]; (3) Z-contrast STEM image adds another dimension for mapping lattice chemistry distribution at the same time.

The goal of this work is to experimentally assess the accuracy of GPA for the measurement of lattice strain at thin film heterogeneous interface using Cs-corrected HAADF-STEM images and to provide practical guidelines for strain profiling. A systematic evaluation has been conducted, starting with computer-generated images with ideally sharp contrast, free of any distortion (the perfect crystal lattice), which were used to explore the inherent inaccuracy of GPA digital processing. Next, GPA was applied on

the Cs-corrected STEM images of defect-free single-crystalline lattices (the experimental crystal lattice) to determine the error bar of GPA strain measurement introduced by STEM imaging. Scanning distortions in the slow-scan (the "fly-back" error [209, 210]) and in the fast-scan directions were examined with a complementary evaluation by the real space method. Then, two case studies, i.e. GPA strain mapping on Cs-corrected STEM images of two representative heterogeneous interfaces, the strained $LaAlO_3/SrTiO_3$ (LAO/STO) interface and the relaxed $SrTiO_3$/MgO (STO/MgO) interface, were presented. Last, limitations in GPA strain quantification were discussed in terms of the materials crystal structure studied.

7.3 Experimental

7.3.1. Synthetic images generated by computer

Artificial images of a two-dimensional dot-like lattice were generated using Origin Pro 8.5 (similar to [222]). To match with the experimental thin film samples, lattice symmetries of perovskite $SrTiO_3$ and rocksalt MgO in [100] zone axis were applied. As shown in Figs. 7.1(a) and enlarged 7.1(b), combining two of such dot contrast images with different lattice spacings, a heterogeneous interface with rigid contact is constructed under well defined in-plane x- and out-of-plane y-coordinates. Computed image #1 was designed as a coherent interface (within the field of view), with a small lattice differences between the substrate (23.50 pixel/unit-cell) and the film (23.33 pixel/unit-cell), as illustrated in the line profile across the interface in Fig. 7.1(c). Images of

incoherent interface with different misfit dislocation densities, i.e. computed images #2 and #3 (a model of the STO/MgO interface) were obtained by modifying the film lattice spacing with the respect to that of the substrate. Please note that there is no lattice strain being introduced in either side of the interface. All three computed images are in the size of 1024 × 1024 pixel.

7.3.2. Thin films and TEM samples preparation

Thin film samples were grown by a standard pulsed-laser deposition technique (with a KrF excimer laser λ = 248 nm) using commercial LAO and STO targets (CERAC, Inc.), a homemade $FeSe_{0.5}Te_{0.5}$ (nominal) target and commercial single crystal STO(100) and MgO(100) substrates. The depositions were carried out at the same substrate-to-target distance of 5 cm, target temperature of 780 °C, a laser energy of 300 mJ, a repetition rate of 2 Hz and an oxygen pressure of 27 Pa for the LAO and STO thin films. After 600 s and 720 s depositions, the LAO/STO and STO/MgO films were directly cooled down to room temperature in 4×10^4 Pa (300 Torr) of O_2 without post annealing. The $FeSe_{0.5}Te_{0.5}$ film was grown on single crystal STO(100) substrates in a controlled oxygen atmosphere (~10^{-2} Pa; details on target processing and deposition parameters can be found elsewhere [161]). The overall LAO, STO and $FeSe_{0.5}Te_{0.5}$ film thicknesses are around 50 nm, 40 nm and 150 nm, respectively. The overall microstructure properties of the LAO and STO films have been confirmed via X-ray diffraction (XRD) (BRUKER D8 powder X-ray diffractometer). The $FeSe_{0.5}Te_{0.5}$ film was examined by selected-area electron diffraction (SAED) using a JEOL JEM-2010

microscope. Cross-sectional specimens of the heterointerfaces were prepared through a conventional TEM sample preparation routine along <100> direction. Starting with cutting, gluing, the TEM specimens were then ground, tripod polished and further thinned in the center by dimpling. Ar ion milling was used to obtain a perforation and electron transparent thin area with a Gatan Precision Ion Polishing System (Gatan, Pleasanton, California). All TEM samples were plasma cleaned each time with a 25% O_2 and 75% Ar mixture before insertion into the microscope.

7.3.3. Cs-corrected STEM and quantitative image processing

In this work, TEAM 0.5 [135], a modified FEI Titan microscope with a special high-brightness Schottky-field emission electron source and an improved hexapole-type illumination aberration corrector, was employed. Technique details regarding to the microscope setup please see section 2.3.2.3. The microscope is equipped with a bottom mounted 2048 × 2048 pixel slow-scan CCD camera; all the HAADF images were recorded in a 1024 × 1024 pixel image size, using a dwell time of 10 μs (unless otherwise specified). TEM samples were left in the microscope for a sufficiently long time to reach thermal equilibrium (usually 1800 s to 3600 s until no noticeable drifting). The local TEM sample thickness was estimated by low-loss electron energy loss (EELS) spectra based on a calculation of the inelastic mean-free path derived from the effective sample atomic number (Digital Micrograph, the log-ratio routine).

In this work, a commercial program, a plug-in of Digital Micrograph (DM 1.8.3 package, HREM Research Inc.), was used for geometric phase analysis. Details of the

GPA algorithm please see section 2.3.3.2. A real space strain method, developed in-house, was also applied on the experimental crystal lattice to determine the error bar of the strain measurement as a function of Kernel size (and STEM scan direction and dwell time). This method consisted by three main steps, (1) sub-pixel peak fitting via 2D Gaussian functions; (2) lattice fitting via linear algebra; (3) conversion of discrete measurements into a 2D displacement image using Kernel Density Estimation (KDE). In the third step, a Gaussian kernel was adopted since it can be smoothly differentiated.

7.4 Results and discussion

7.4.1. GPA on computed images

We first investigated the factors contributing to the inherent inaccuracy of the digital processing GPA strain quantification using computed images. Starting with the simplest scenario of a coherent heterointerface in Fig. 7.1(a), the influences from one of the most important GPA processing parameters, the Fourier mask size, on strain mapping were studied. As shown in the power spectrum of the computed image #1 in Fig. 7.1(d), we tested the largest mask size possible $1/a_{sub}$, a small mask of $1/4a_{sub}$ and a mask size in between, $1/2a_{sub}$. The GPA strain maps of ε_{xx} (in-plane), ε_{yy} (out-of-plane) and ε_{xy} (shear strain) produced by these three masks using the substrate lattice as reference are presented in Figs. 7.2(a) to 7.2(i). Despite all images being generated from the same source image of Fig. 7.1(a), the strain maps become increasingly rougher, with increasing noise as the GPA mask size increases. For comparison, strain profiles across

the interface with a fixed width of 600 pixels were applied (see the example in Fig. 7.2(d)) and plotted in Figs. 7.3(a) to 7.3(c).

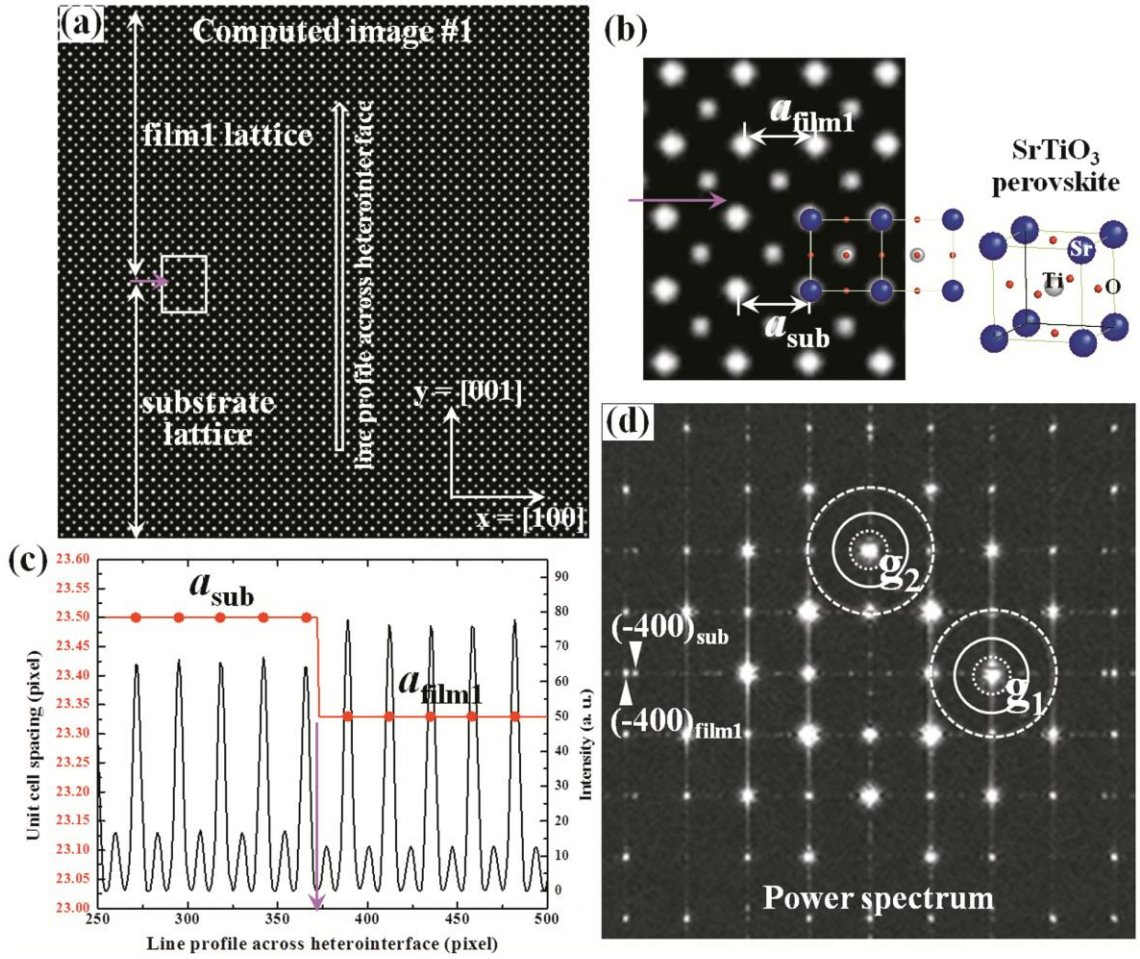

Figure 7.1. (a) The computed image #1, a computer-generated 2D lattice of a heterogeneous structure with a small lattice mismatch. The image is in <100>. (b) A magnified image of the rigid interface between film 1 and the substrate, both of which are in perovskite $SrTiO_3$ structure with contrast maxima at atomic positions. (c) Unit-cell spacing and intensity line profile along the y-direction across the interface. (d) The power spectrum of (a). The Fourier vectors selected for GPA are noted as g_1 and g_2. Three Fourier masks with different size are illustrated in circles.

Prior to discussing the mask size effect, it is noted that the profile direction and position can also affect the strain value extracted. Within a set of three strain profiles, for example in Fig. 7.2(j) of the medium mask, ε_{yy} presents more severe oscillations than the ε_{xx} and ε_{xy} even away from the interface. This is because the fact that the strain variations in ε_{xx} are along the direction parallel to the interface; but ε_{yy} oscillations are mainly perpendicular to the interface. When applying a line profile across the interface, the ε_{xx} oscillations cancel out among the 600 pixel sampling, while the variations in the ε_{yy} are preserved. If the line profile is carried out along the interface, the results will be reversed. For the shear strain ε_{xy}, although its variations have the same direction as ε_{yy}, they are essentially very small (in a range of ±0.01% in Fig. 7.3(c)) so the profile direction effect isn't obvious. Since the lattice strain of the heterogeneous interface is the main topic of this study, there are some "default" settings such as the profile direction that is always across the interface to show a comparison between the substrate and the film, similar to several previous studies [223-226]. Also, these ways of sampling can present some differences such as that the ε_{yy} profile often seems noisier than that of the ε_{xx}. Those phenomena can be different if one applies the strain profile in a different way on lattice images of other structures such as nanoparticles. But it is always important to know whether the strain variations are byproducts of a quantifying process or representative of the imaged lattice.

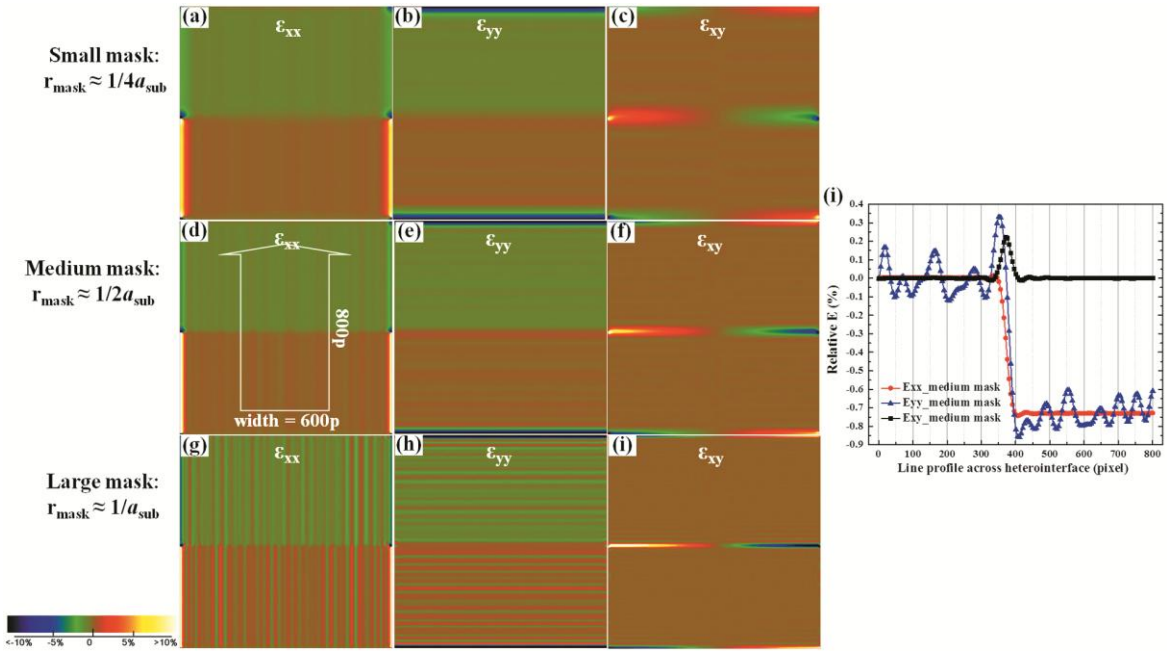

Figure 7.2. (a)-(b) The GPA ε_{xx} (in-plane), ε_{yy} (out-of-plane) and ε_{xy} (shear strain) maps of computed image #1 using the small mask. (d)-(f) The GPA maps using the medium mask and (g)-(i) using the large mask. (i) The strain profiles of the medium mask set of relative ε_{xx}, ε_{yy} and ε_{xy} obtained across the interface. The profile size is noted in (d).

To clarify the influence of the mask size on the strain profile, the substrate regions (marked by rectangles) in Figs. 7.3(a) to 7.3(c) were enlarged and presented in Figs. 7.3(d) to 7.3(f), in which the features of the strain profiles are directly related to the selection of mask size. In Fig. 7.3(d), all three in-plane strain ε_{xx} profiles exhibit in sinusoidal-wave-like oscillations with almost fixed frequencies that are proportional to their mask sizes. Meanwhile, the Fourier mask size is reciprocal to the spatial resolution of the strain measurement in real space. That is to say, the small mask (in black) produces a smooth strain field but with a low spatial resolution; whereas a large mask (in blue) boosts spatial resolution (short length scale of the fluctuations) and is accompanied with severe fluctuations, especially in ε_{yy} (for example in Fig. 7.3(e) where the strain

variations are not averaged out by sampling). Moreover, in Figs. 7.3(d) and 7.3(e), overshoots and undershoots were found (pointed by red open arrows) close to the interface (marked by purple arrows) regardless of the mask size. Since there is no strain in the original computed image, these abnormal high/low strains are processing artifacts, which are sensitive to image quality and can introduce significant errors [227]. And because they are located in the lattice layers next to the interface, it is necessary to quantitatively estimate their effective range from the interface. In Figs. 7.3(g) to 7.3(i), root-mean-square (RMS) variability of the strain profiles were calculated as a function of the data size, e.g., starting with the strain at pixel 120 to the interface, at pixel 121 to the interface etc., to determine the theoretical GPA accuracy as well as to find out at which point the RMS errors start rising due to the overshoots/undershoots. The RMS errors in the flat ranges are within 0.02%, 0.5% and 0.005% for the ε_{xx}, ε_{yy} and ε_{xy} profile strain, respectively, about zero in the reference substrate region. Again, the values of the error depend partially on the profile direction (and the profile width, which is discussed later). But, if a small Fourier mask (in black) is used, the GPA accuracy can be further improved to 0.01% of ε_{xx}, 0.05% of ε_{yy} and 0.002% of ε_{xy} that are all well within the 0.05% about zero. However, as marked in Figs. 7.3(g) and 7.3(i), the drawback of this mask selection is that the effects of the overshoots/undershoots on the strain error appear further from the interface, than that of the other two larger masks. On the contrary, if one wants to downsize the abnormal strain near the interface by choosing a large mask (e.g. the blue line in Fig. 7.3(g)), the measurement of an accurate strain in the second unit-cell layer can be achieved but at the cost of the overall accuracy. This

reflects the essential feature of local strain measurements, in which precision is a trade-off for spatial resolution. To balance the two, we suggest a medium mask size about twice of the substrate lattice parameter in real space (the red plots in Figs. 7.3(g) to 7.3(i)), which gives an overall theoretical GPA accuracy within 0.1% and a measurable range of the third unit-cell layer from the interface.

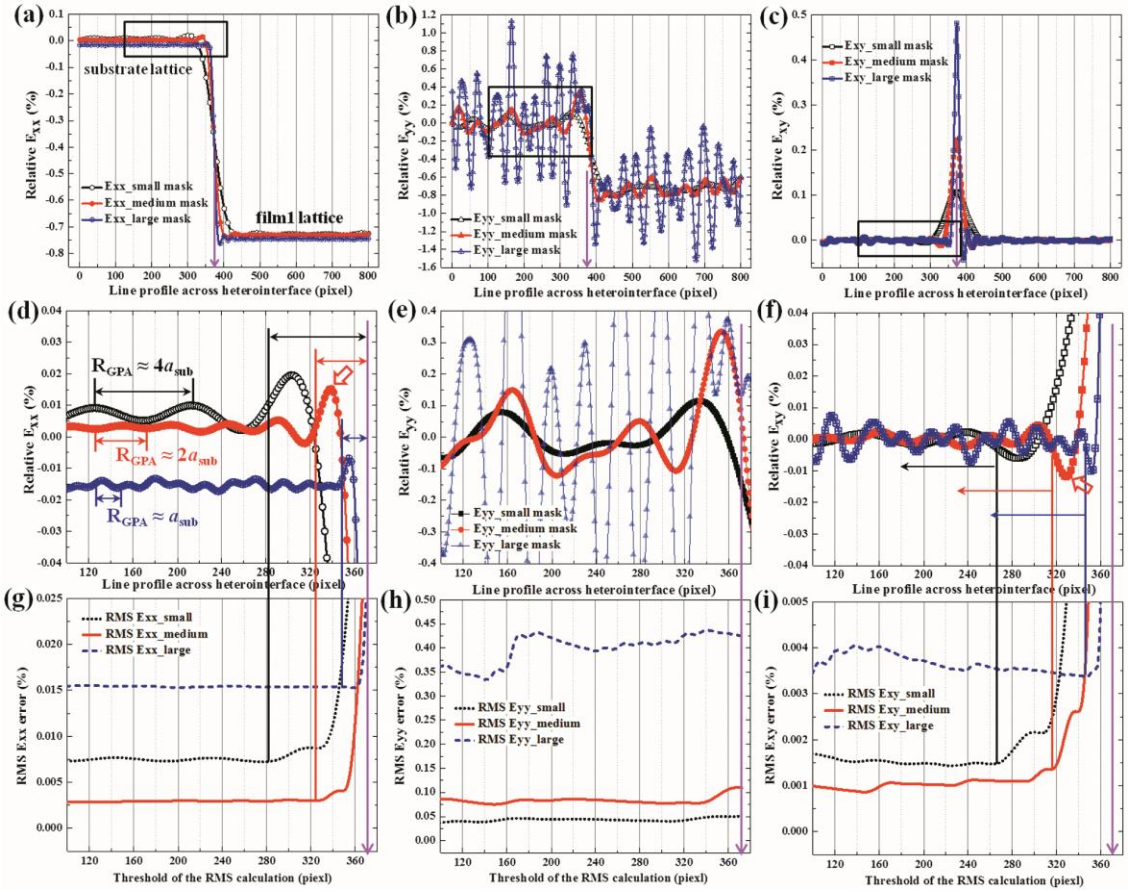

Figure 7.3. The effects of the Fourier mask size on (a) ε_{xx}, (b) ε_{yy} and (c) ε_{xy} strain profiles across the interface. (d)-(f) The enlarged rectangular regions in the substrate in (a)-(c). The GPA spatial resolutions are noted in (d). (g)-(i) The root-mean-square (RMS) of the strains in (d)-(f) as a function of the profile threshold.

In the above discussion, we found that not only the GPA processing parameters, e.g. the Fourier mask size affect the strain accuracy, but also how one surveys the strain maps and extracts the strain data. Besides the directions of the strain profile, the profile width as shown in Fig. 7.3(d) and its effect on strain value were studied. In Figs. 7.4(a) and 7.4(b), strain profiles of the ε_{xx} and ε_{yy} maps in Figs. 7.2(d) and 7.2(e) with different sampling widths are presented.

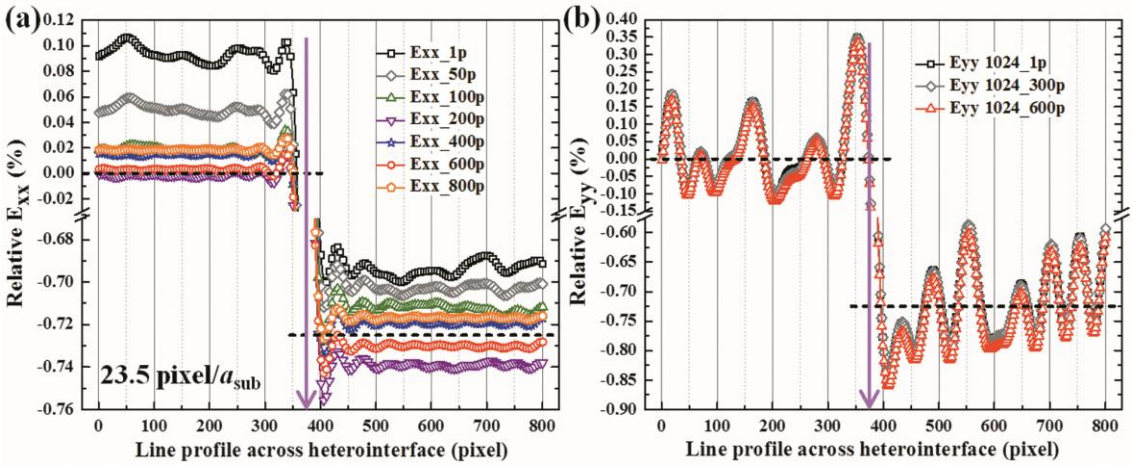

Figure 7.4. The effects of profile width on (a) the ε_{xx} strain of Fig. 7.2(d), (b) the ε_{yy} strain of Fig. 7.2(e) across the interface.

Compared to the known strain assigned in the lattice (marked as dashed-line to guide the view), for example in the substrate region in Fig. 7.4(a), the results given by profiles with small widths such as 1 pixel and 50 pixels show about 0.1% and 0.05% deviations that are obviously greater than that of other profiles (within 0.02%). The reason is that as shown in Fig. 7.3(d), the vertical ε_{xx} variations in Fig. 7.2(d) peak at a certain frequency of about $2a_{sub}$ (47 pixels). A profile width needs to be larger to avoid

the error of insufficient sampling. As suggested in Fig. 7.4(a), a profile width of 600 pixels is good for the images of 1024 pixels wide. In the case of the ε_{yy} strain profile, as shown in Fig. 7.4(b), plots with different widths are almost overlapped indicating the strain distribution is independent of the sampling width due to the profile direction.

Factors associated with the features of source images and how they interplay with the inherent GPA processing and strain profile parameters were also examined. Image resolution, i.e. the numbers of pixels per lattice period, is considered as one of the main requisites for image-based lattice strain measurement [98, 228]. To exclude possible influences in experimental imaging (such as recording media and TEM foil thickness [228]), computed images with low image resolutions of 512× 512 pixel and 256× 256 pixel were used to test the effect of image resolution alone. The GPA strain profile results showed that as long as the width of strain profiles is appropriate, the accuracy of the measured ε_{xx} and ε_{yy} strain barely changes with image size if at all. Here, a Fourier mask size of $1/2a_{sub}$ was fixed to test the effect of image resolution alone. Tailoring the computed image #1 (Fig. 7.1(a)) by a half to 512 × 512 pixel, the resulting ε_{xx} and ε_{yy} strain profiles are presented in Figs. 7.5(a) and 7.5(b), respectively. Although the results in Fig. 7.5(a) were from an image with the resolution twice lower than that of Fig. 7.4(a), as long as the width of strain profiles is appropriate, the accuracy of the measured ε_{xx} strain remains almost the same.

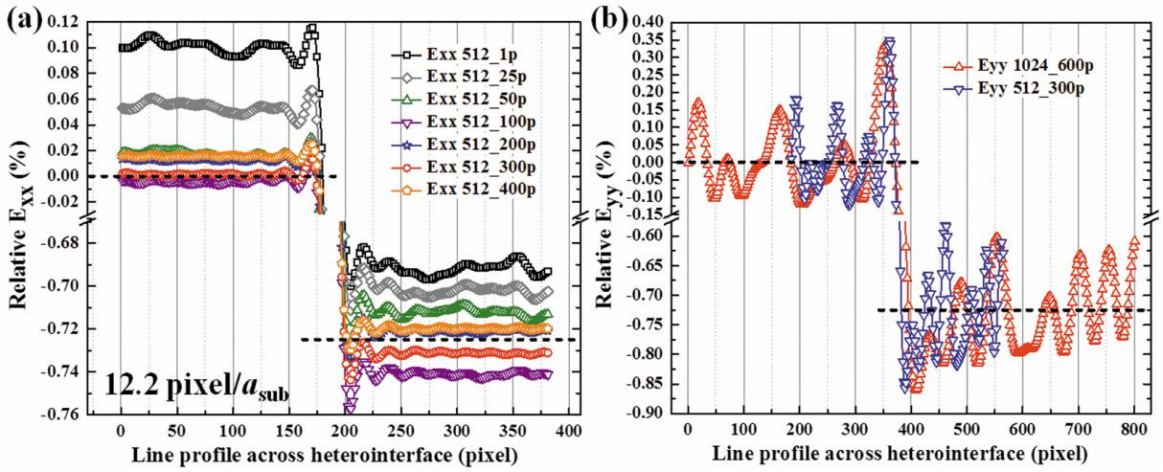

Figure 7.5. (a) The relative ε_{xx} strain profile as a function of profile width and (b) the ε_{yy} strain profiles of the computed image #1 of 512 × 512 pixel. The ε_{yy} strain profiles of the 1024 × 1024 pixel image #1 are also plotted for comparison.

It is also true for the image of 256× 256 pixel (about 6 pixel/unit-cell, see Fig. 7.6). In Fig. 7.5(b), the ε_{yy} strain of the 512 × 512 pixel image shows a higher oscillation frequency (actually is still associated with the mask size of $1/2a_{sub}$, but a_{sub} is half of that in the 1024 × 1024 pixel image); while the ε_{yy} deviation is still the same. In conclusion, the theoretical strain accuracy measured from the ideal crystal lattice does not affected by lowering the image resolution. Thus, in the case of ideal image quality, the accuracy of the GPA strain profile is independent of the image resolution as long as the lattice distortion is larger than one pixel.

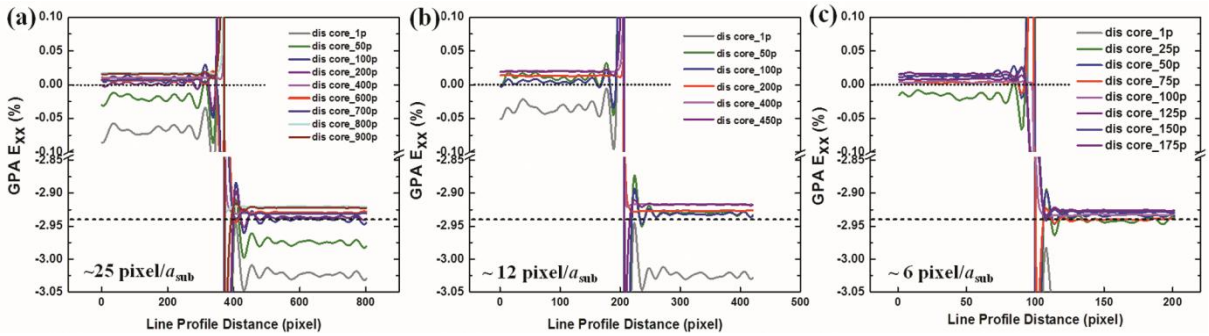

Figure 7.6. The relative ε_{xx} strain profiles as a function of profile width at the dislocation core of the computed image #3 with a size of (a) 1024 × 1024 pixel, (b) 512 × 512 pixel and 256 × 256 pixel.

Moreover, computed images with large lattice mismatches between the substrate and the film (i.e. a sudden lattice changes across the interface) have also been analyzed for the inherent GPA processing and strain profile accuracy. The GPA results using a mask size of $1/2a_{sub}$ on the computed image #2 are presented in Fig. 7.7. In this case, the film lattice parameter is approximately 22.81 pixel/unit-cell, giving a relative strain of -2.92% with respect to the substrate lattice. To quantify the in-plane strain with considering these dislocation cores, two ways of conducting the strain profile were performed, profiling at the position of the cores and in between them (arrows in Fig. 7.7(b)). As shown in Figs. 7.7(e) and 7.7(f), based on the results of different profile widths, placing the strain profile right at the core gives a better accuracy within 0.02% (once the width is larger than 50 pixels). Profiling in between the dislocations cores seems more sensitive to the change of the width that the 300-pixel-wide profile in the substrate region shows accuracy of 0.01% but the 400-pixel one only 0.03% (for the

dislocations about 400-pixel apart here). The results suggest that with a reasonable profile width, profiling right at the cores gives a better accuracy, within 0.02%.

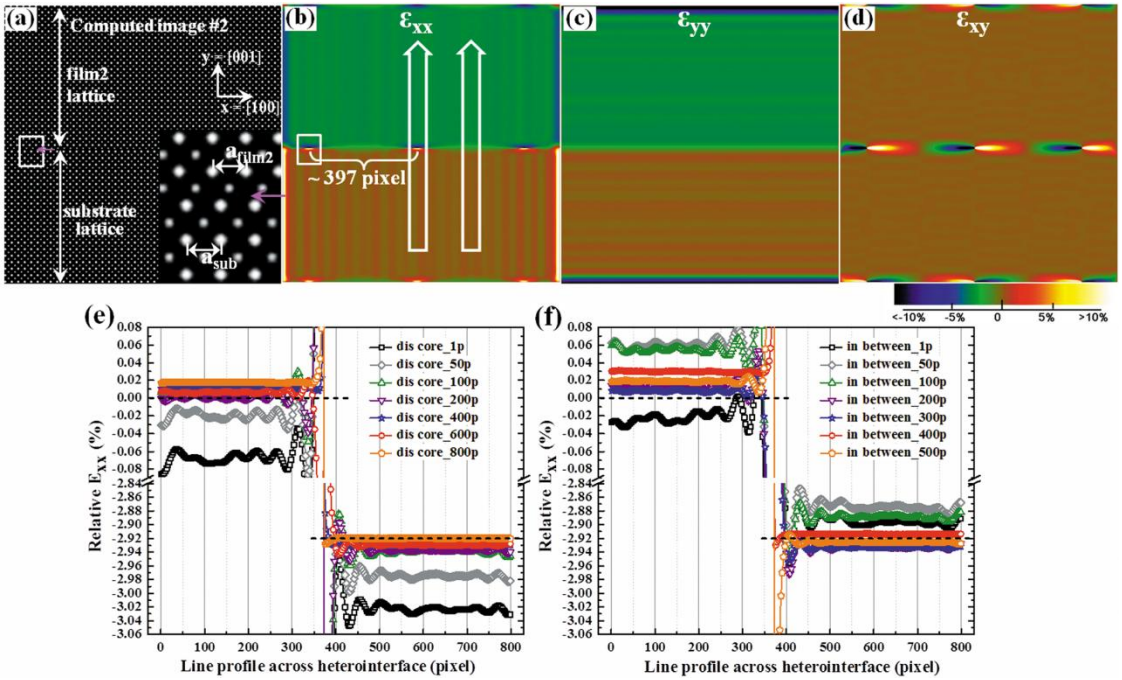

Figure 7.7. (a) The computed image #2 of a heterogeneous structure with a lattice mismatch of 2.92% in the film 2 with respect to the substrate. (b)-(d) The GPA ε_{xx} (in-plane), ε_{yy} (out-of-plane) and ε_{xy} (shear strain) maps of computed image #2using a Fourier mask of $1/2a_{sub}$. The relative ε_{xx} strain profiles of (b) as a function of profile width profiling (e) at the dislocation core and (f) in between the dislocations.

In Fig. 7.8, the GPA strain maps and profiles are presented for the computed image #3, a model of the STO/MgO interface, with a large lattice mismatch (film #3 has a relative strain of -7.31% to the substrate). Comparing the ε_{xx}, ε_{yy} and ε_{xy} maps of image #3 in Figs. 7.8(b) to 7.8(d) with that of image #1 in Figs. 7.2(d) to 7.2(f), there are six convergent regions, analogous to misfit dislocation cores, as the result of a relatively large lattice mismatch. These strain convergent regions are corresponding to 020 phase

jumps caused by a translation of half a-lattice fringe spacing in the top film lattice [108]. This is why the dislocation cores can be visualized in strain maps ε_{xx} and ε_{xy}, but not in ε_{yy} which is related only to the 002 lattice displacement.

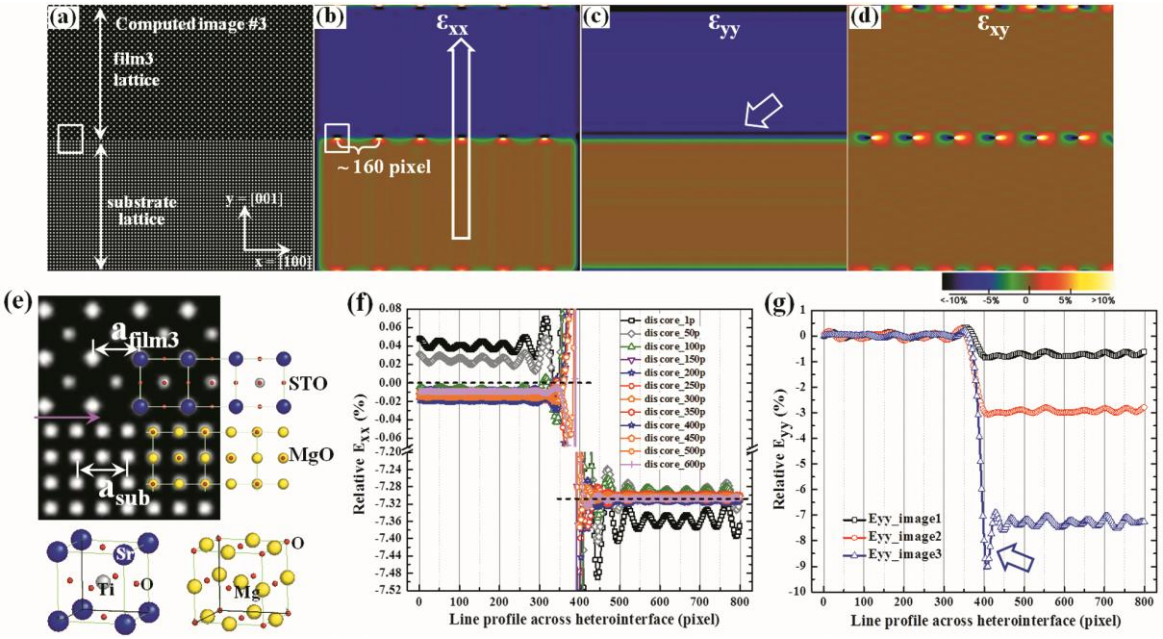

Figure 7.8. (a) The computed image #3 of the heterogeneous structure of STO/MgO in <100>. (b)-(d) The GPA ε_{xx} (in-plane), ε_{yy} (out-of-plane) and ε_{xy} (shear strain) maps of computed image #3using a Fourier mask of $1/2a_{sub}$. (e) An enlarged image of the rigid interface between film 3 and the MgO substrate with corresponding atomic models. (f) The relative ε_{xx} strain profiles of (b) at the dislocation core as a function of profile width. (g) The relative ε_{yy} strain profiles of Fig 7.2(e), Fig 7.9(c) and (c) across the interfaces. The severe undershoot in ε_{yy} of image #3 is marked by open arrows.

Following this observation, strain profiling was performed at the dislocation cores in the strain maps ε_{xx} of image #3 (Fig 7.8(f)), and the results show promising accuracy, despite a higher density of interfacial dislocation arrays. On the other hand, in Fig. 7.8(g), the out-of-plane ε_{yy} profile of image #3 presents a greater undershoot (not

wider though) in the STO film near the interface compared to that of the other two computed images. This processing artifact is likely due to the large lattice mismatch assigned in this interface (again, no lattice strain in the computed image). The interface model of image #3 also proves that GPA strain analysis isn't limited to local lattices that have identical symmetry as the reference, though centrosymmetric is necessary [119].

In a short summary of section 7.4.1, in the first part, four factors were studied using computer-generated images (the perfect crystal lattice): The Fourier mask size, strain profile width, source image resolution and misfit dislocations in the image-and their impacts on the inherent accuracy of the GPA digital processing for quantifying lattice strain at thin film heterogeneous interface. We found that the mask size is crucial to the inherent deviation of GPA, which is a trade-off of the spatial resolution of the measurement. To consider both, a medium mask size of $1/2a_{ref}$ is suggested. In the profile direction across the heterointerface, it allows a theoretical GPA accuracy of 0.005% for ε_{xx}, 0.1% for ε_{yy} and 0.001% for ε_{xy} (Figs. 7.3(g) to 7.3(i)) and a spatial resolution of $2a_{ref}$ (about 47 pixels in Fig. 7.3(d)). These GPA accuracies can be compromised if a small strain profile width is adopted. For an image of 1024 × 1024 pixel, an optimized profile width of 600 pixels is recommended (no less than 100 pixels). No additional error was found when there are large lattice mismatch and associated misfit dislocations in an interface lattice image, as long as the strain profiles are properly applied, i.e. at the dislocation core and with a sufficient width. If the image contrast is uniformly sharp throughout the field of view, the resolution of the image (the

number of pixel per lattice distance) is not a necessary requirement for high accuracy GPA strain measurements.

7.4.2. GPA on Cs-corrected HAADF-STEM images of single crystals

GPA is capable of measuring the local lattice in Fourier space at a high accuracy [139]. A precision of 3 pm was achieved in a GPA strain filed around dislocations using HRTEM [208]. Recent reports on STEM-image-based GPA precisions varies from 0.15% [229] to 0.40% [226]. In this section, Cs-corrected STEM images of single-crystalline substrate lattice far away from interfaces are used to determine the actual accuracy of STEM-GPA on interface strain quantification. Factors influencing the measurement precision are discussed.

STEM imaging is essentially different from TEM projections; the main artifact in STEM lattice images involves the distortions in the slow-scan direction, so called the "fly-back" error [209, 210]). This error can be clearly illustrated using GPA. In Fig. 7.9(a), a high resolution HADDF-STEM image was recorded by aligning the a-lattice axis of crystalline STO parallel to the fast scan direction (image resolution is 25.6 pixel/unit-cell, and image size 1024 × 1024 pixel). Using a Fourier mask of $1/2a_{STO}$, we obtained the GPA strain maps of ε_{xx} (a-lattice displacement), ε_{yy} (c-lattice displacement) and ε_{xy} (shear strain) in Figs. 7.9(b) to 7.9(d). Strain profiles were conducted along the out-of-plane c-direction to examine the lattice displacement across the ab-plane as in Figs. 7.2(d) to 7.2(f), and the results of relative strains are presented in Fig. 7.9(i). The root-mean-square (RMS) variation of the strain profiles was also calculated to estimate the

error, which presents a very high RMS for ε_{yy} of 1.30% about zero. This dramatic deviation was caused by the "flyback" error in the slow-scan direction, appearing as the horizontal stripes in the ε_{yy} strain map. Under the imaging direction in Fig. 7.9(a), it introduces severe artifacts in the measurement of the c-lattice displacement.

Different methodologies have been proposed to correct this systematic distortion, such as the digital correction algorithms [209]. Considering that the digital processing might have difficulty dealing with interfacial lattice jumps at interface defects, and that the "fly-back" error is sensitive to STEM scan direction [210], we adopted a simple solution of recording the same image twice with a 90 degree scan rotation, aligning the fast-scan direction parallel to the a- and c-direction, respectively. The second set of STEM image and GPA strain maps are shown in Figs. 7.9(e) to 7.9(h), with the ε_{xx} noted as ε_{xx}_90 to distinguish from the ε_{xx}_0 in Fig. 7.9(b). Note that since ε_{xx}_90 is profiled across the ab-plane (where the heterointerface lies in later interface applications), it represents the c-lattice displacement. Combining the two strain maps that are both in the fast-scan direction, we obtained quantitative relative a-lattice and c-lattice strains in Fig. 7.9(j). After eliminating the distortion in the slow-scan direction, in Fig. 7.9(j), a much lower RMS error of 0.22% (about zero) for the c-lattice strain has been achieved. In the case of the lattice shear distortion ε_{xy}, based on its definition of $\varepsilon_{xy} = ½ (\partial u_x(r)/\partial y + \partial u_y(r)/\partial x)$, the result has to be partially dependent on the slow-scan distortion in either imaging orientation.

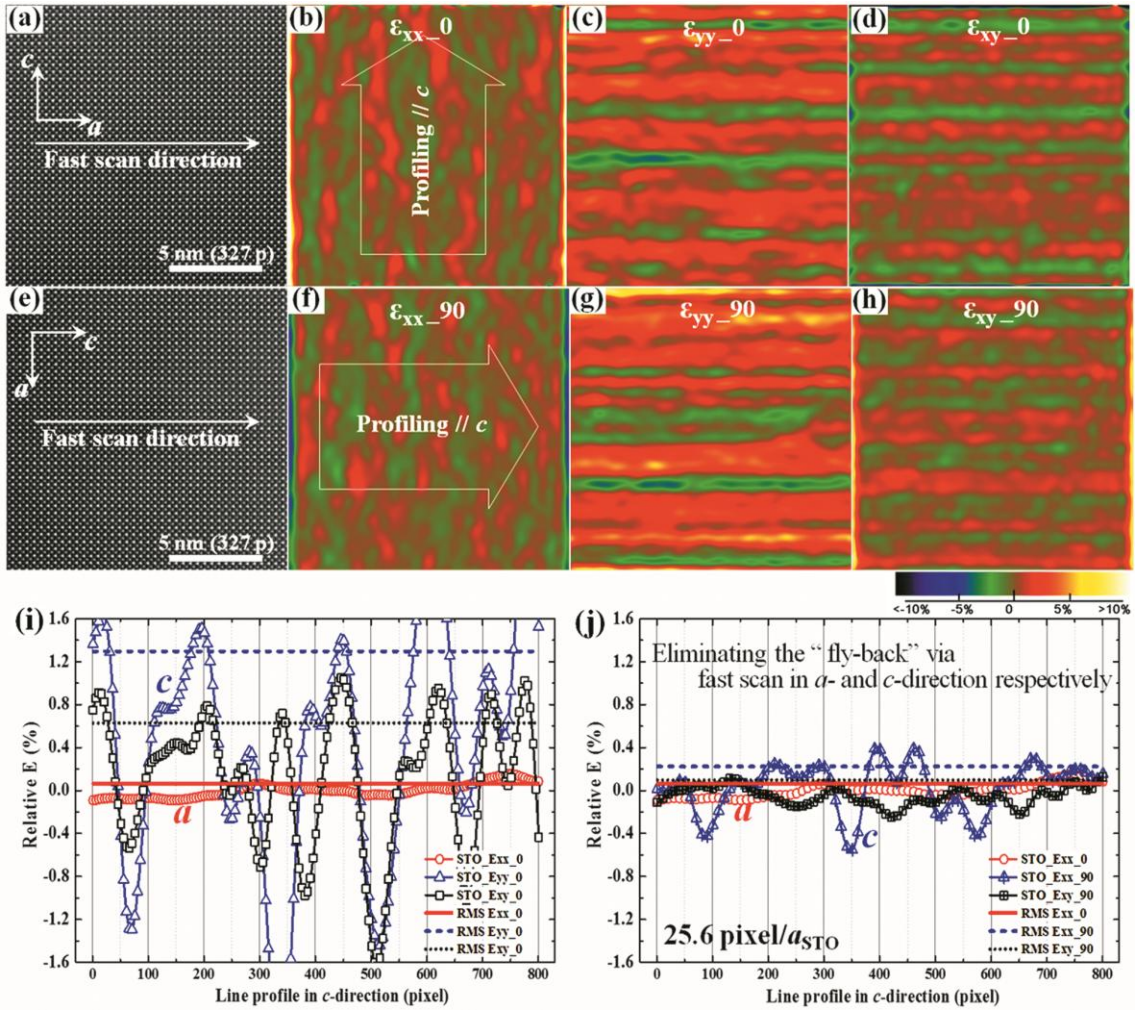

Figure 7.9. (a) A representative Cs-corrected STEM image of the STO substrate with *a*-lattice direction parallel to the fast scan direction in <100>. (b)-(d) The GPA ε_{xx}, ε_{yy} and ε_{xy} maps of (a) using a Fourier mask of $1/2a_{sub}$. (e) The STO substrate STEM image obtained with *c*-lattice direction aligning to the fast scan direction. (f)-(h) The GPA ε_{xx}, ε_{yy} and ε_{xy} maps of (e). (i) The relative strain profiles and RMS value of the strain maps of image (a). (j) The relative strain profiles and RMS value of the ε_{xx} in (b), the ε_{xx} in (f) and the ε_{xy} in (h). Note that both of the ε_{xx} in (b) and (f) are along the fast scan direction, and lead to small RMSs in *a*- and *c*-displacements.

One way to obtain full accuracy for ε_{xy} could be to take one term from each image (the $\partial u_x(r)/\partial y$ term from the x fast scan image, and the $\partial u_y(r)/\partial x$ term from the y

fast scan image), under an assumption that the two images are collected from the identical sample region. Since the two images were recorded sequentially rather than simultaneously, there is no guarantee for absolutely perfect alignment between the two. An alternative solution is to use the ε_{xy} obtained after the 90 degree rotation (noted as ε_{xy}_90 in Fig. 7.9(j), because some of the slow-scan distortion is canceled out along this profile direction. We repeated the above GPA profiles on several pairs of STEM images of the single-crystal STO taken under similar conditions, and found that the GPA accuracy using STEM images, as shown in Fig. 7.9(j) for example, is approximately within 0.25%.

To further verify the above error estimation, a real-space strain measurement method was also used to quantify the RMS strains in the above single crystal STEM images as a function of Kernel size (the Fourier mask in real space). Figs. 7.10(a) and 7.10(b) are a set of representative results obtained from a pair of STEM images before and after a 90 degree rotation. In both plots, the strains mapped along the fast-scan direction are in solid lines; the strains along the slow-scan direction are in dashed lines. For a Kernel size of two unit-cells, the RMS of the a-displacement in Fig. 7.10(a) and of the c-displacement in Fig. 7.10(b) are both well within 0.25%, agreeing with the above GPA assessment (Fig. 7.9(j)). The strain accuracy increases with the Kernel size, consistent with the effect of changing the Fourier mask size on GPA precision, as discussed above. Again, a larger Kernel size (or a smaller Fourier mask) leads to higher accuracy, but at the cost of spatial resolution. It is also noted that the RMS strains become almost constant as the Kernel size increases. We found that how fast and how

well the measured RMS strain approaches to zero depends greatly on the direction of the residual drift of the TEM sample. Even though we waited until there was no noticeable drift in the field of view, there is always some drift during the time required to obtain a STEM image.

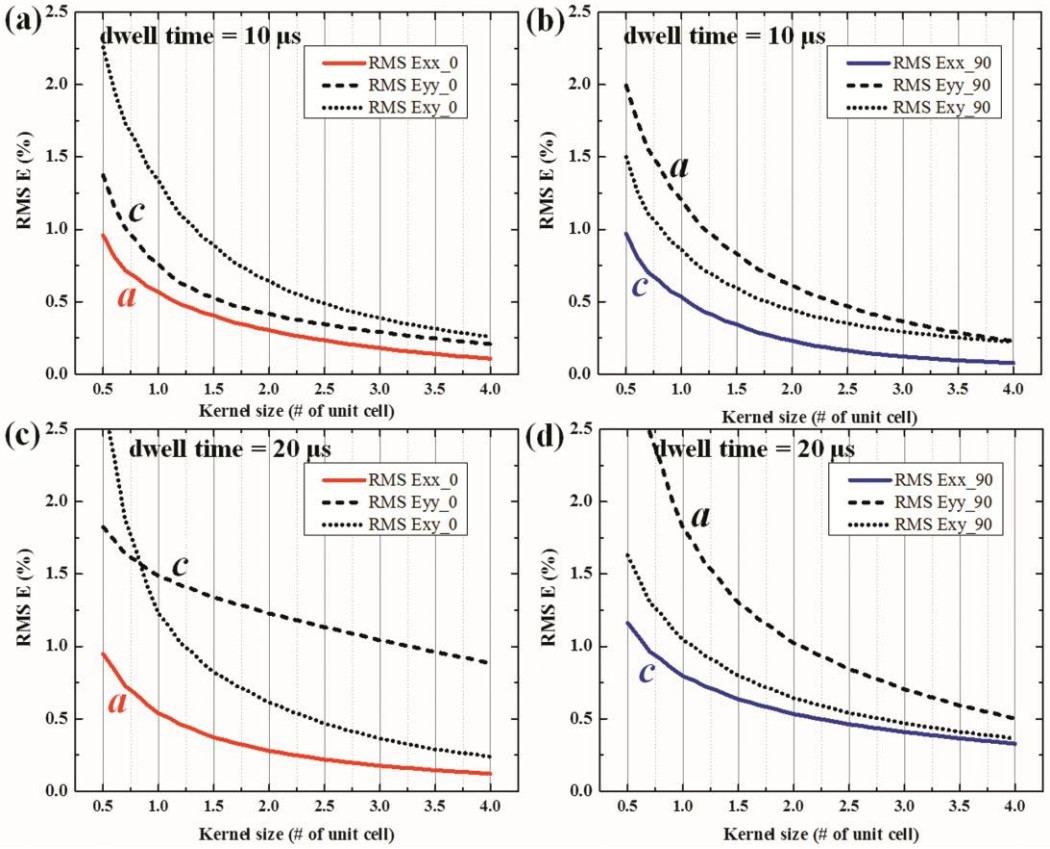

Figure 7.10. The experimental STEM-GPA accuracy assessed by real space strain measurements. The RMS strains as a function of Kernel size in a STEM image of the STO substrate with (a) *a*-lattice direction and (b) *c*-lattice direction parallel to the fast scan direction with the default dwell time of 10 µs. The RMS strains in a STO STEM image obtained with a dwell time of 20 µs with the fast scan direction in (c) *a*-lattice direction and (d) *c*-lattice direction.

For example, in the case of Fig. 7.9, the residual drift is mainly in the c-lattice direction, because the RMS strain of c-displacement is obviously larger when it is along the slow-scan direction in Fig. 7.9(i) than that of along the fast-scan direction in Fig. 7.9(j). An opposite example is the measurement in Figs. 7.10(a) and 7.10(b), where the direction of the residual sample drifts (defined as the drift that is not a linear function of time) is close to the a-lattice axis. When the sample drift direction aligns with the slow-scan direction, a large error appears. This could harm the accuracy even after using the 90-degree-rotation recording. As shown in Figs. 7.10(c) and 7.10(d), this set of RMS strains was measured from the STEM images obtained using a longer dwell time of 20 μs. After aligning the c-lattice axis to the fast-scan direction, the RMS strain of c-displacement decreases compared to that of in Fig. 7.10(c); the residual drift limits the accuracy to 0.35% regardless of the Kernel size. Thus, the residual sample drift in the STEM fast-scan direction (related to the dwell time) determines the scanning artifacts in this image-based lattice strain quantification.

As recalled from section 7.4.1, it is found that the resolution of the computed images does not affect the GPA strain accuracy; however, this is not the case for the experimental images. In Figs. 7.11(a) to 7.11(h), the GPA strain mappings and profiles of two STEM images with lower resolutions of 18.1 pixel/a_{STO} and 12.8 pixel/a_{STO}, respectively, are presented. The source STEM images were recorded around the same view field as Figs. 7.9(a) and 7.9(e). The 90-degree-rotation recording was also applied to minimize the slow-scan distortion. Comparing the strain profiles in Figs. 7.11(a) and 7.11(h) with that of in Fig. 7.9(j), the RMS of the a-lattice strain remains in the same

range; whereas, the RMS of the c-displacement increases as the image magnification decreases. It reaches 0.57% in Fig. 7.11(h), more than double the 0.22% error obtained in Fig. 7.9(j). By intensity line profile surveying, we found this accuracy degradation is closely related to the local image focus. The optimum focus of HAADF-STEM is a balance between a sharp probe and minimizing probe tails; in practice, the focus was chosen to maximize contrast [121]. For the high magnification STEM images (e.g. Figs. 7.9(a) and 7.9(e)), we tested STO regions with different sample thicknesses, estimated from 16 nm to 48 nm by EELS, and a strain RMS error within 0.25% can be achieved when the contrast is maximized by focus.

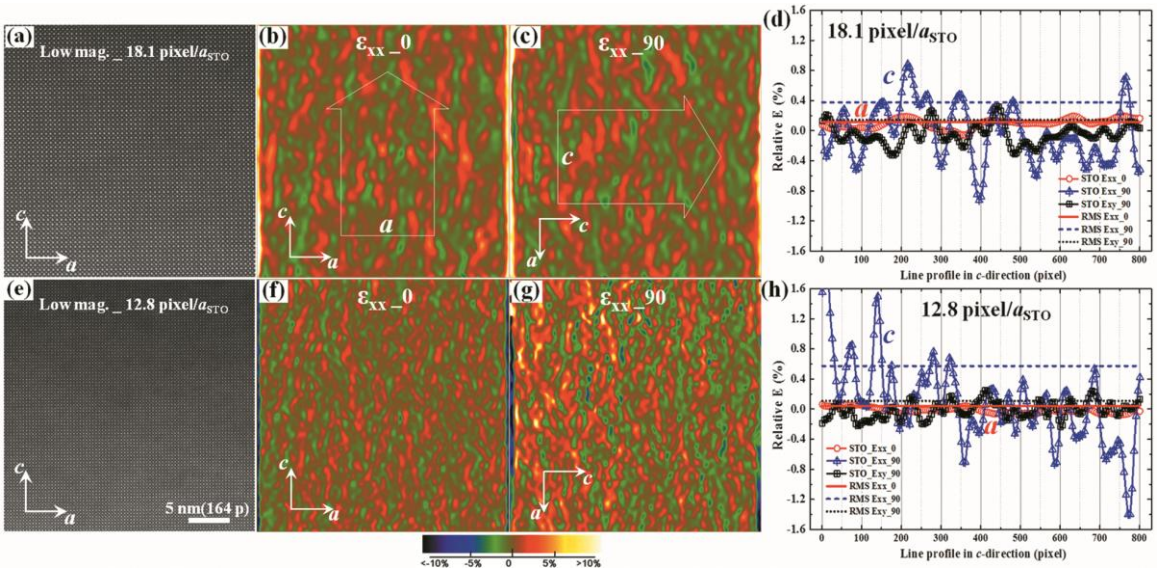

Figure 7.11. The effects of STEM image resolution on the actual GPA accuracy. (a) The STEM images with the same view field as Fig. 7.9(a) with lower resolution of 18.1 pixel/a_{STO}. (b)-(d) The a-lattice strain map, the c-lattice strain map and relative profiles in the out-of-plane directions. (e) The STO STEM images of 12.8 pixel/a_{STO} and (f)-(h) the corresponding GPA strain profile results. Note that the RMS of the c-displacement increases as the image magnification decreases.

However, in the case of the low magnification images, a uniform focus is difficult to obtain over a large field of view. Since the image-based lattice strain measurement depends on the positions of atomic columns (or contrast maxima), defocus caused by sample thickness variation introduces strain deviations at the edge of the image in Fig. 7.11(e) and increases the overall RMS error. Detailed comparisons of focused and unfocused local regions in low magnification STEM images are presented in Fig. 7.12.

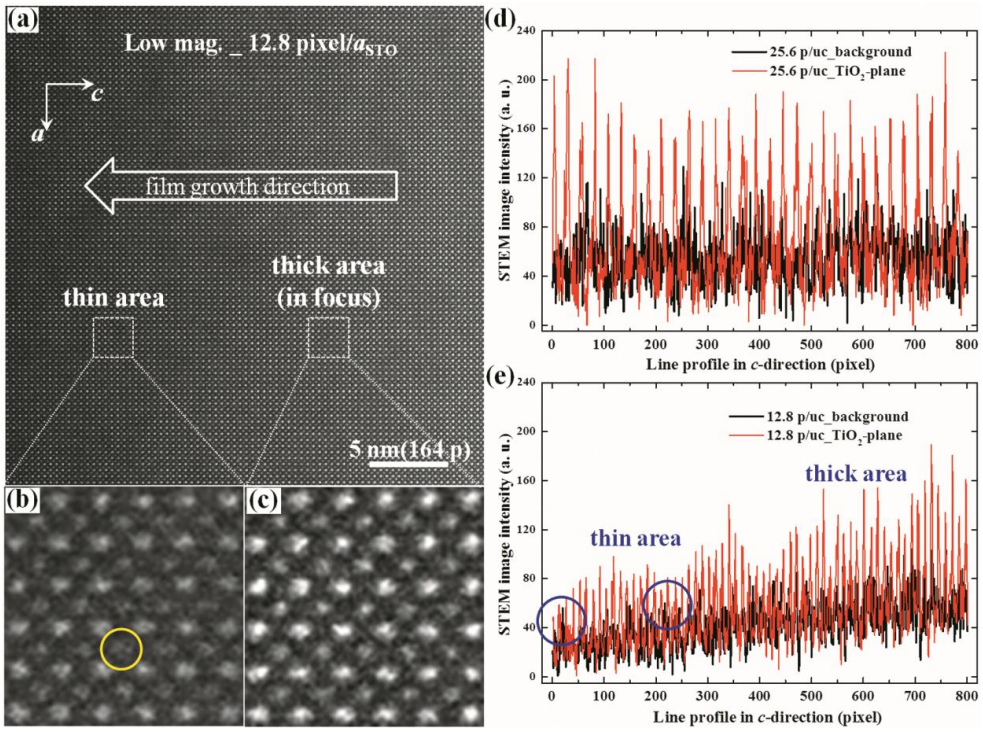

Figure 7.12. (a) The low magnification STEM images of STO substrate used as the source image for the strain map in Fig. 7.11(g). Enlarged lattice images of (b) the thin region and (c) the focused thicker region in (a). Intensity profiles of the image background and along the TiO_2-plane in (d) the high magnification image of Fig. 7.9(e) and in (e) the low magnification image Fig. 7.12(a) along the out-of-plane direction (film growth direction). Unfocused lattice with TiO_2-plane intensity comparable to the background is marked by circles.

In the low magnification image in Fig. 7.11(e) and Fig. 7.12(a), the field of view is much larger (about four times larger than Figs. 7.9(a) and 7.9(e)), and the optimum focus was achieved close to the center of the image. The local lattices of the unfocused thin edge and of the focused inner sample region are enlarged in Figs. 7.12(b) and 7.12(c). Comparing the image contrast variation across both Fig. 7.9(e) and Fig. 7.12(a) to the intensity profiles of Figs. 7.12(d) and 7.12(e), it is clear that the high magnification image has a relatively uniform sample thickness compared to that of the low magnification one, whose background intensity shows a clear increase. In Fig. 7.12(e), at the thin edge of the low magnification image (in circles), the intensity of TiO_2-atom columns become comparable to that of the background noise. This corresponds to the enlarged Fig. 7.12(b) where the focus is far from high contrast.

In fact, thickness and focus variations have been previously identified as main concerns in the HRTEM-based GPA [120, 227]. As for STEM, the maximum contrast criterion provides optimum focus at the region of interest; but some parts of the sample can be out of focus when the view field is large and the sample thickness is uneven or the foil is bending. In Fig. 7.11, the reason that the RMS of the a-displacement doesn't drop as much as the c-strain is because that the thickness variation in the cross-sectional TEM sample is mainly along the c direction (the out-of-plane film growth direction); whereas the sample thickness in the a direction is relatively uniform in the view field here. The RMS of the a-displacement could also be affected. Although STEM is more tolerant to contrast reversals from thickness/focus change, high-quality (not necessarily

high-resolution) lattice images with uniformly sharp contrast are still a prerequisite for accurate strain determination.

Based on the GPA strain profiles on Cs-corrected HAADF-STEM images of the single-crystal STO substrate lattice, an actual accuracy within 0.25% was determined for both a- and c-lattice displacements. Considering that STO bulk lattice parameter is about 0.3905 nm, the STEM-GPA precision is approximately 1 pm. This high accuracy can be experimentally achieved after eliminating the STEM slow-scan distortion by the 90-degree-rotation recording method. Two factors were found to play major roles in influencing the STEM-GPA precision: (1) the image focus and its degree of uniformity across the source STEM image; and (2) the residual sample drift in the STEM fast-scan direction. Unlike computer-generated images where the contrast is ideal, some regions of the experimental lattice images could be out of focus due to the sample thickness variation, especially when the field of view becomes large. Unfocused lattice images introduce uncertainties in atom column position, and thus errors in determining lattice displacement. If an optimum focus is satisfied across a region of interest, the strain measurement accuracy depends then mainly on the residual drift in the fast-scan direction. A simple way of checking, whether the sample has reached thermal equilibrium and whether the dwell time is appropriate in terms of balancing noise and drift, is to identify if the image is free of apparent strain in the crystalline lattice away from defects.

7.4.3. GPA on Cs-corrected HAADF-STEM images of heterointerfaces

In this part, we applied the above STEM-GPA strain profile to quantify the lattice strain of two representative heterostructures, the $LaAlO_3/SrTiO_3$ and the $SrTiO_3/MgO$ interfaces. The overall film crystallographic properties were first characterized by XRD θ-2θ scans (For XRD plots please see Fig. 7.13).

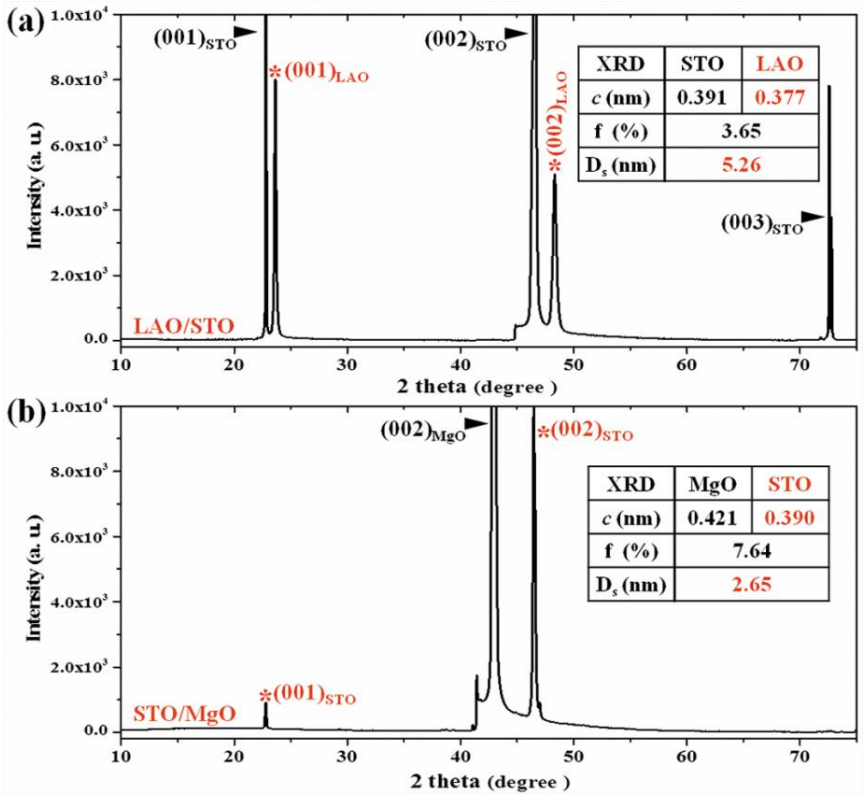

Figure 7.13. The XRD θ-2θ scans of (a) the $LaAlO_3/SrTiO_3$ and (b) the $SrTiO_3/MgO$ heterostructures.

Based on the sharp primary (00l) peaks, the out-of-plane lattice parameters (c) were calculated to be 0.377 nm and 0.390 nm for the LAO and the STO thin films respectively, calibrated based on the single crystal substrates. Assuming that the film

lattice parameter a is equal to c (cubic structure), the interface misfit rate ($f = 2(a_s-a_f)/(a_s+a_f)$) and corresponding misfit dislocation spacing ($D_s = (a_f \times a_s)/2(a_f - a_s)$) were calculated to be 3.65% and 5.26 nm for the $LaAlO_3/SrTiO_3$, and 7.64% and 2.65 nm for the $SrTiO_3$/MgO heterogeneous interface, respectively.

Fig. 7.14(a) is a representative cross-sectional STEM overview of the 50-nm-thick LAO epitaxial thin film on STO (100) substrate acquired in the <100> zone axis. Three misfit dislocations, marked by arrows, were found at the heterogeneous interface of LAO/STO with a dislocation spacing (D_s) of about 38 nm. This is much larger than the dislocation spacing of 5.26 nm estimated by XRD, which suggests a much smaller in-plane lattice mismatch between the LAO film and the STO substrate. To find out the actual lattice displacement of this strained heterogeneous interface, we applied the GPA strain profile to a high resolution STEM image of the interface Fig. 7.14(b). The GPA strain maps of ε_{xx}_0 (a-lattice displacement), ε_{xx}_90 (c-lattice displacement) and ε_{xy}_90 (shear strain) were generated using a Fourier mask of $1/2a_{STO}$ and presented in Figs. 7.14(c) to 7.14(e). Using a profile across the heterointerface with a width of 600 pixels (about 12 nm) suggested by the findings in section 7.4.1, the relative lattice strains with respect to the STO substrate are plotted in Fig. 7.14(f). It is interesting to see that the relative a-lattice strain, instead of showing an instantaneous jump as the c-lattice strain, shows a gradual decline across the heterointerface. The shear strain ε_{xy} oscillates about zero, indicating there is little out-of-plane rotation in both the film and substrate lattices.

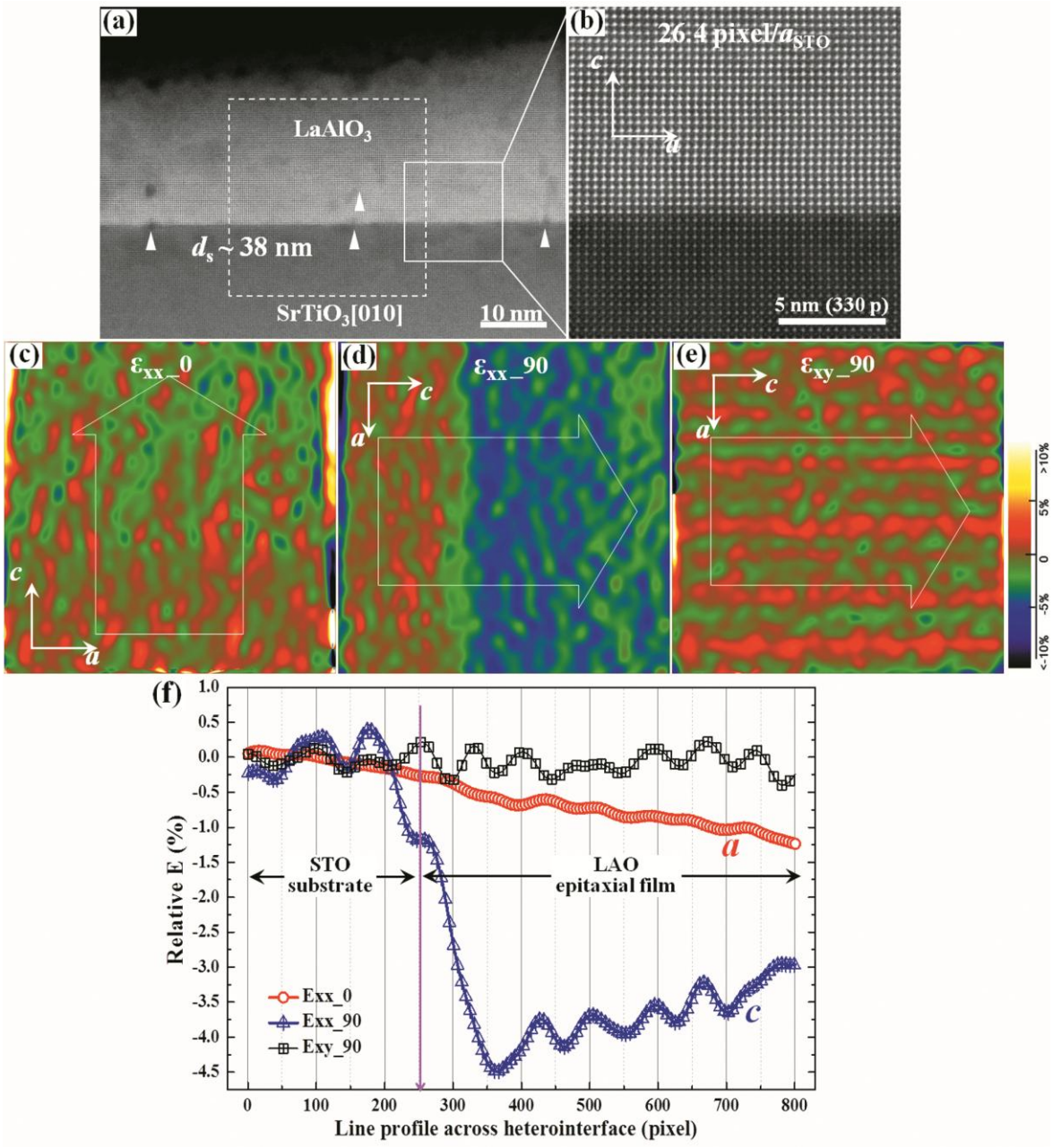

Figure 7.14. (a) A representative cross-sectional STEM overview of the 50-nm-thick LAO epitaxial thin film on STO (100) in the <100> zone axis. (b) A high resolution STEM image of the LAO/STO interface without dislocations. (c)-(e) The GPA *a*-lattice strain, the *c*-lattice strain and shear strain maps of (b). (f) The relative strain profiles of (c)-(e) across the heterointerface of LAO/STO.

To understand the above strain profiles, we re-plotted the relative a-lattice strain into the local a-lattice parameters as a function of the distance to the interface in nanometers in Fig. 7.15(a). The intensity profile across the LAO/STO interface was superimposed to illustrate the correlations between the value of a and the position of the local lattice. It is clear that near the interface of LAO/STO, indicated by a vertical arrow, the in-plane a-lattice relaxes in a gradual manner. To assess the a-lattice spacing near the heterointerface, considering that the overshoots/undershoots at interfaces are inherent GPA digital processing artifacts (e.g. Fig. 7.3(d)), the lattice regions within 1 nm to the interface (about $2a_{STO}$ the GPA spatial resolution) were excluded for the calculation. Then by averaging in selected regions in Fig. 7.14(a), the *a* of STO substrate was calculated as of 0.390 nm ± 0.001 nm, and of 0.387 nm ± 0.001 nm for the initial 8-nm-thick LAO film. The measured a of the substrate fits well with the XRD results and the STO bulk parameter; however, the a-value of our LAO film is considerably larger than its bulk counterpart (a_{LAO}^{bulk} = 0.379 nm). This strongly suggests that the initial film in-plane lattice is in a lateral tension, 2.09% larger than the LAO bulk parameter. Meanwhile, the results of the c-lattice spacing near the interface in Fig. 7.15(b) show that the initial film out-of-plane lattice (0.376 ± 0.001 nm) is slightly smaller than the bulk parameter, consistent with the lateral-tension-introduced out-of-plane compression in initial LAO film. When we repeated the above measurement in other STEM images of the LAO/STO interface (without misfit dislocations), even for the images with lower magnification, similar results on the local lattice parameters were obtained (Fig. 7.16). The STEM-GPA strain profile proved to be reproducible and reliable.

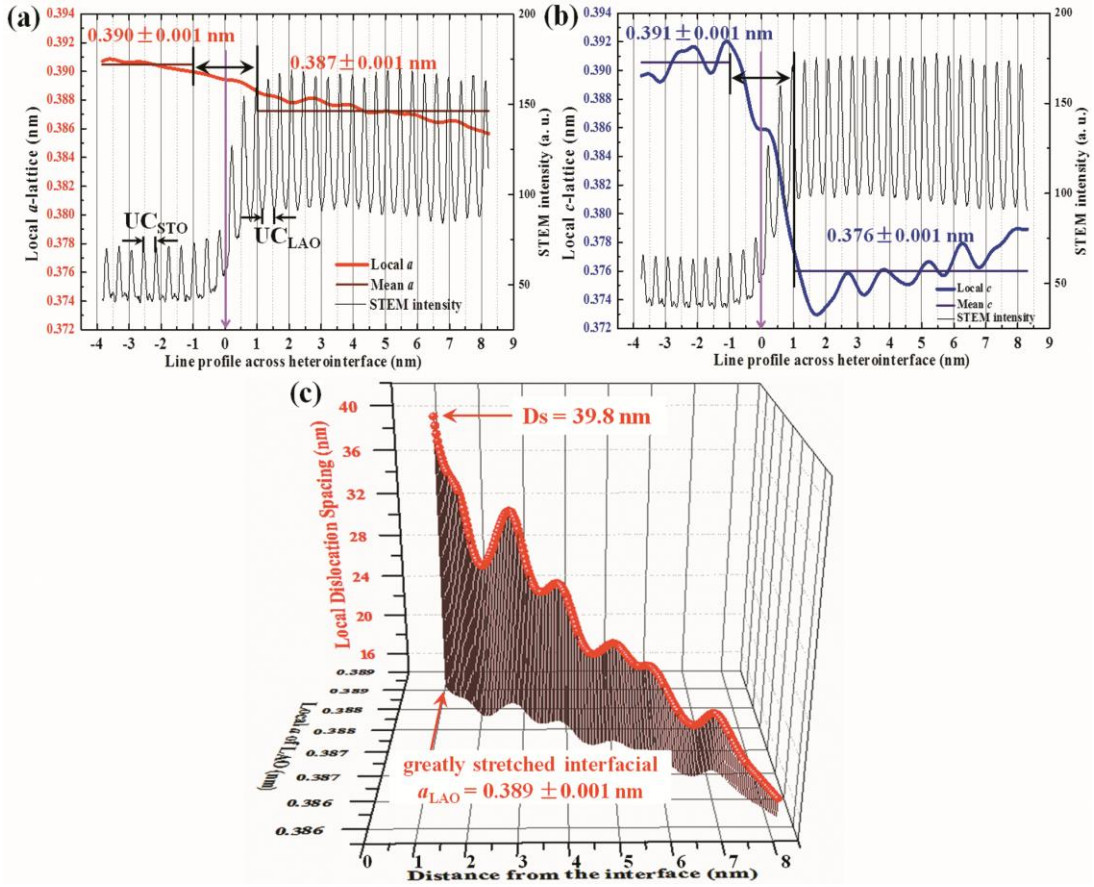

Figure 7.15. The local and mean (a) *a*-lattice parameters and (b) *c*-lattice parameters based on the strain profiles in Fig. 7.14(f) as a function of the distance to the interface in nanometers. The intensity profile across the LAO/STO interface was superimposed for the illustration of the position of local lattice. (c) The local dislocation spacing D_s as a function of the actual LAO film *a*-lattice from the interface.

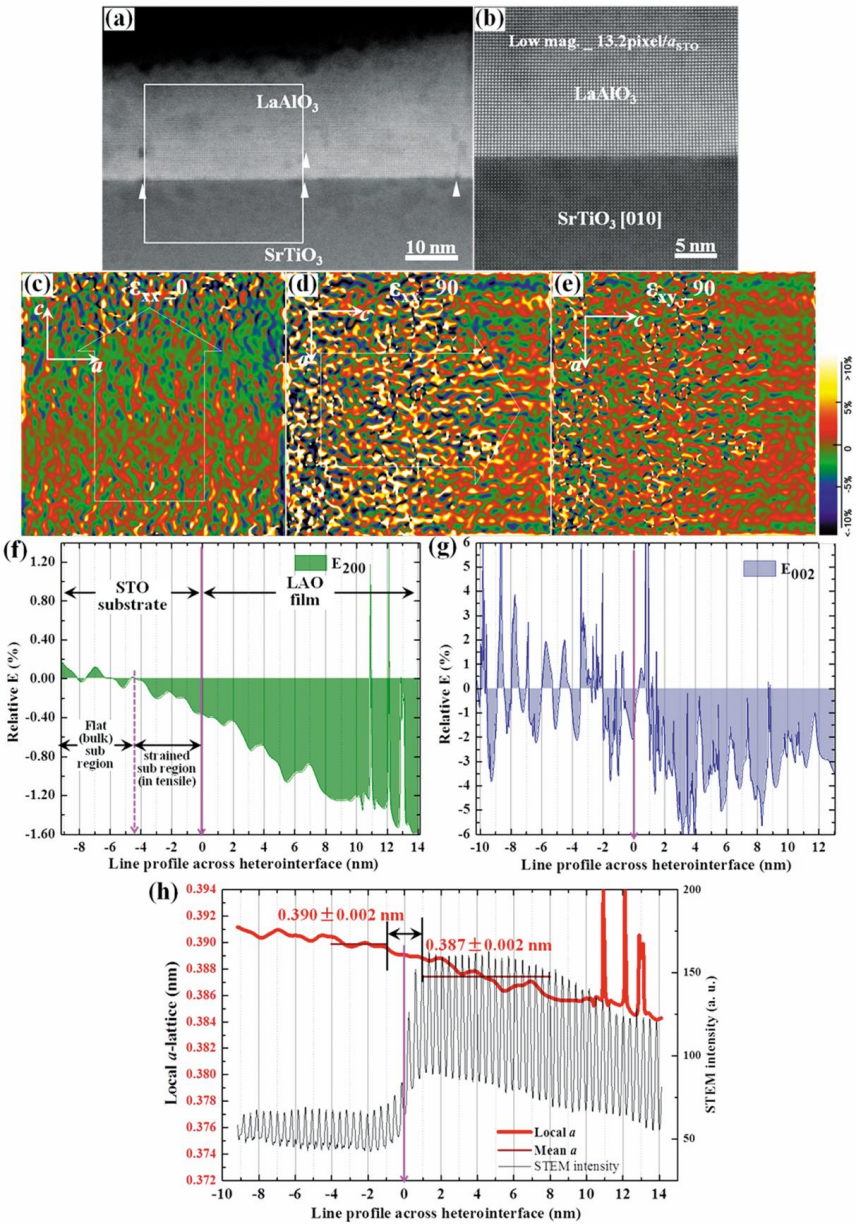

Figure 7.16. (a)A representative cross-sectional STEM overview of the 50-nm-thick LAO epitaxial thin film on STO (100) in the <100> zone axis. (b) A medium resolution STEM image of the LAO/STO interface without dislocations. (c)-(e) The GPA *a*-lattice strain, the *c*-lattice strain and shear strain maps of (b). The profile of (f) the relative *a*-lattice strain and (g) the *c*-lattice strain across the interface. (h) The local and mean *a*-lattice parameters as a function of the distance to the interface in nanometer, superimposed by image intensity profile. Due to a less uniform contrast in the lower magnification STEM image (b), the strain profile (f) and (g) is noisier than that of in Fig. 7.14.

Based on the local lattice parameters measured above, some important interface properties can be revealed. For example, the tetragonality of perovskite oxides, defined as c/a, is considered to be closely related to ferroelectric polarization [230]. Here, it yields a tetragonality value of $c/a \approx 1.03$ in the initial 8-nm-thick LAO film. In Fig. 7.15(c), we calculated the local dislocation spacing D_s as a function of the actual LAO film a-lattice from the interface. A D_s of about 40 nm was found as a result of the severely stretched interfacial film lattice; and this dislocation spacing is consistent with the spacing of 38 nm observed directly at the interface (Fig. 7.14(a)). Furthermore, it is noted that besides the misfit dislocations at the interface, additional dislocations are observed in the LAO thin film (Fig. 7.14(a)). We applied the GPA strain profile to a STEM image including these misfit dislocations (the view field is marked by a dashed square), and the results are presented in Fig. 7.17. It is interesting to see that the LAO film a-lattice strain no longer relaxes gradually, but instead jumps instantaneously across the misfit dislocations. Although this image is less uniform and gives a higher error in local lattice quantification, as shown in Fig. 7.17(g), the first-6-nm LAO layer has an a of 0.385 nm ± 0.002 nm, and it is relaxed to 0.380 nm ± 0.002 nm by generating the second misfit dislocation in the LAO film about 6 nm away from the interface. Combining the results in Fig. 7.14 and Fig. 7.17, a more complete in-plane film strain distribution can be obtained. Based on the local a-lattice, in strain map Fig. 7.17(b), the absolute LAO film lateral strains are 2.09% in between dislocations, 1.57% in the initial 6-nm LAO layers after relaxation by dislocations at the interface, and 0.26% after the secondary relaxation. Then, the LAO film is almost fully relaxed to the bulk parameter. These experimental

observations and quantifications provide an actual lattice strain distribution at the heterogeneous interface of LAO/STO.

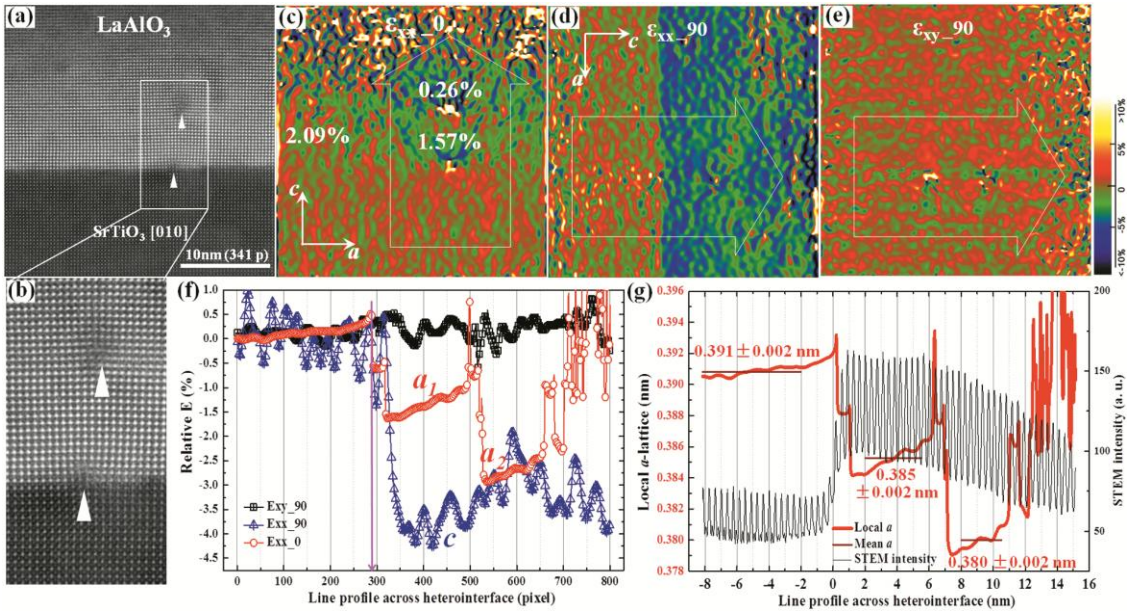

Figure 7.17. The secondary strain relaxation observed in LAO/STO GPA strain profiles on STEM images with misfit dislocations. (a) A STEM image of the LAO/STO interface with dislocations. The image is from view field marked by the dashed-square in Fig. 7.14(a). (b) The enlarged view of the dislocations. (c)-(e) The GPA *a*-lattice strain, the *c*-lattice strain and shear strain maps of (a). (f) The relative strain profiles of (c)-(e) across the heterointerface of LAO/STO. (g) The local and mean *a*-lattice parameters of (c) as a function of the distance to the interface in nanometers.

In the case of the heterointerface of STO/MgO, the results of GPA strain profile are in good agreement with the XRD prediction. A representative high resolution STEM image of the 40-nm-thick STO/MgO heterostructures in the <100> projection is presented in Fig. 7.18(a). The GPA strain maps were obtained in Figs. 7.18(b) to 7.18(d) using a Fourier mask of $1/2a_{MgO}$. In the strain map E_{xx}, the convergent region of strain

around the dislocation core clearly demonstrates that the dislocation spacing is about 2.63 nm, consistent with the value estimated from the XRD out-of-plane measurement (Fig. 7.13(b)). Strain profiles were also performed (as marked by the open arrows) and presented in Fig. 7.18(e).

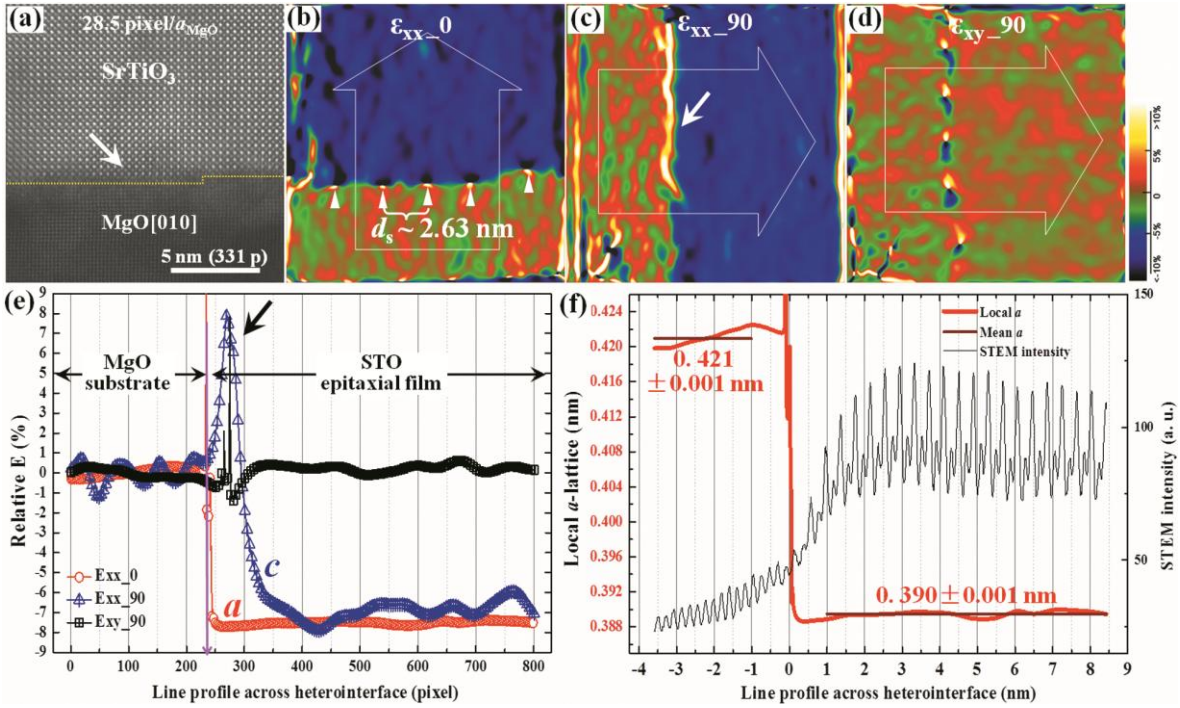

Figure 7.18. (a) A representative high resolution STEM image of the STO/MgO interface in <100>. (b)-(d) The GPA *a*-lattice strain, the *c*-lattice strain and shear strain maps of (a). (e) The relative strain profiles of (b)-(d) across the heterointerface of STO/MgO. (f) The local and mean *a*-lattice parameters of (c) as a function of the distance to the interface in nanometers. The interface steps and interdiffussion are marked by arrows.

Here, the STO film in-plane a-displacement drops immediately once across the interface and remains almost constant in the film. In Fig. 7.18(f), the mean *a* of the initial 8.5-nm-thick film is nearly the same as the bulk value, indicating a very small

residual lateral strain in the film. The out-of-plane c-displacement shares a similar trend as that of the *a*. In Fig. 7.18(e), the dramatic overshoot near the interface reflects the actual interface imperfections of MgO substrate surface terraces and interdiffussion (marked by arrows). For detailed discussions on the misfit dislocations and associated interface defects of the STO/MgO heterostructures please see [231]). Thus, based on the GPA strain profiles above, we found that at the STO/MgO heterointerface the lateral film strain has been relaxed by generating a high density of misfit dislocations, presenting a prototype domain-matching epitaxy (DME) [10].

7.4.4. Discussions on limitation

In addition to the trade-off between the spatial resolution and the precision, which is a feature of local measurement averaging, there are some essential limitations in GPA strain profiles. One of the limitations is due to the nature of the GPA method, which is basically a comparison process. Since it measures a relative lattice parameter with respect to a selected reference, the observed structure needs to be fairly similar to the reference.

An example to demonstrate the limitation of GPA is shown in our attempt to quantify the heterointerface of $FeSe_{0.5}Te_{0.5}$(FST)/STO in Fig. 7.19. In this case, as shown in the enlarged <100> projection Fig. 7.19(b) (the film unit cell is marked by a rectangular), the $FeSe_{0.5}Te_{0.5}$ film has a P4/nmm tetragonal structure (space group #129 [26]). The lattice parameters of the $FeSe_{0.5}Te_{0.5}$ film were found to be a_{FST} = 0.380 nm, c_{FST} = 0.586 from electron diffraction [93]. Comparing with the perovskite STO substrate (bulk

a_{STO} = c_{STO} = 0.390 nm), c_{FST} is about 1.5 times larger than c_{STO}. From the power spectrum in Fig. 7.19(c), the choice of Fourier vectors g_1 = $[020]_{STO}$* and g_2 = $[002]_{STO}$*(close to the $(003)_{FST}$ reflection) can still be satisfied using a mask size of $1/2a_{STO}$. However, as shown in the relative strains obtained from the GPA maps (Figs. 7.19(d) to 7.19(f)), in Fig. 7.19(g), the out-of-plane c-displacement presents severe oscillations. As we transfer the relative strains into local lattice parameters in Fig. 7.19(f), the mean a of the initial 9-nm-thick FST film is 0.379 nm ± 0.001 nm, consistent with the SAED results; whereas, the local c-parameter in the film is too random to make further reasonable calculation. If the difference between the structure being measured and the reference is larger or smaller than half of the reference lattice parameter (i.e. half of the periodicity π), there will be phase jumps (discontinuities) in the phase image due to a phase restriction of $-\pi$ to π in the GPA algorithm [108]. In practice, this leads to noisy strain maps with overshoots/undershoots in every unit-cell.

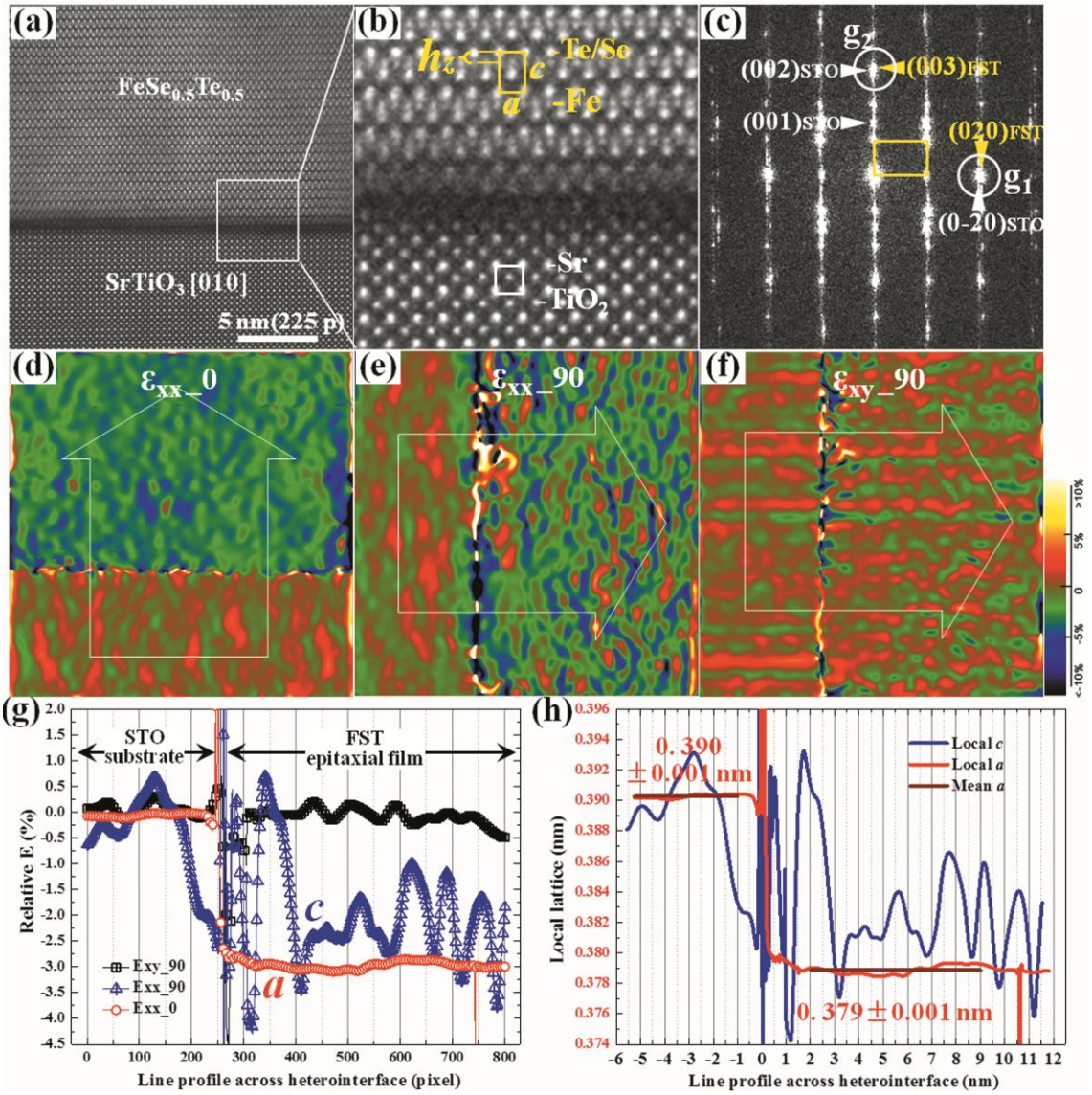

Figure 7.19. (a) A representative high resolution STEM image of the $FeSe_{0.5}Te_{0.5}$/STO interface in <100>. (b) The enlarged view of the $FeSe_{0.5}Te_{0.5}$ and STO lattice with marked unit-cell. (c) The power spectrum of (a). The Fourier vectors $g_1 = [020]_{STO}$* and $g_2 = [002]_{STO}$* were selected for GPA. (d)-(f) The GPA *a*-lattice strain, the *c*-lattice strain and shear strain maps of (a) using a mask size of $1/2a_{STO}$. (g) The relative strain profiles of (d)-(f) across the heterointerface of FST/STO. (g) The local and mean *a*-lattice and *c*-lattice parameters as a function of the distance to the interface in nanometers.

Moreover, due to the periodic nature of the GPA methodology, lattice distortion within a single unit cell can't be quantified. The chalcogen height (h_z), defined as the vertical distance of the Se/Te-plane above the Fe-plane (marked in Fig. 7.19(b)), is one of the most important lattice parameters for the Fe-based superconductors [232]. It would be a valuable complement to the diffraction methods if h_z can be quantified using the image-based measurement at a higher spatial resolution. However, as shown in the GPA strain profile in Fig. 7.19, the h_z depending on the atom coordinates within a unit cell is beyond the capability of GPA.

7.5 Conclusions

In this work, the accuracy and reliability of using GPA method to measure interface lattice strain were systematically investigated, using both computer-generated and experimental Cs-corrected HAADF-STEM images of single-crystalline lattices and heterogeneous interfaces with different lattice misfits. The conclusions and guidelines identified are follows:

1. The inherent accuracy and spatial resolution of the GPA method depends greatly on the mask size, the strain profile direction and width, but not on the image resolution (with ideal contrast). A medium mask size of $1/2a_{ref}$ is suggested to balance precision and resolution for local measurement. Strain profile widths approaching 1-pixel should be avoided; sufficient sampling is necessary to obtain representative strain profiles across a heterointerface.

2. An experimental strain accuracy within 0.25% (lattice precision of 1 pm) was achieved in STEM-image-based GPA after eliminating the STEM slow-scan distortion by recording two images with scan directions 90 degrees apart. A good consistency check is to identify if the image in fast-scan direction is free of apparent strain in the crystalline lattice away from defects.

3. The size of the field of view for GPA strain quantification with high precision is limited by the degree of uniformity in the STEM image contrast of the sample. Special care needs to be taken in TEM foil preparation for a uniform sample thickness.

4. The STEM-GPA strain profile has been proven effective in quantifying the lattice displacement fields of the partially strained LAO/STO heterointerface with a secondary relaxation mechanism, and of the fully relaxed STO/MgO heterostructures with a high density of interface misfit dislocations. Repeating the GPA processing in STEM images obtained under different imaging conditions (focus, view fields, magnification etc.) provides a better understanding of the overall strain field.

5. STEM images, especially the Cs-corrected HAADF images, are reliable sources for image- based lattice strain quantification. Although thickness/focus variations could affect the image contrast from one region to another (and then the overall accuracy), they are not very detrimental to the GPA strain profile. However, there are some fundamental limitations when applying GPA to a structure whose lattice parameter is very different from the available reference lattice.

CHAPTER VIII

SUMMARY AND FUTURE WORK

In this dissertation, we employed the state-of-the-art aberration-corrected scanning transmission electron microscopy and systematically investigated the defect structure and associated lattice strain of a few functional heterogeneous epitaxial thin films. The actual interface structures of studied heterosystems display rich defective atomic arrangements that are closely related to the film global epitaxial quality. The microstructure and inhomogeneous lattice strain at the unique heterogeneous interface can be understood through faithful atomic-scale characterization in order to achieve improved film functionality and rational interface device design.

The spatial relationship of the intrinsic chemical inhomogeneity of Te, Se and the interstitial iron Fe(2) in the $Fe_{1+y}Te_{1-x}Se_x$ epitaxial system has been established by determining the overall film stoichiometry using EDX and by in-depth atomic-column-by-atomic-column Cs-corrected STEM characterization. Our results demonstrated that the deposition atmosphere could affect - film local stoichiometry inhomogeneity, and thus the superconducting transition temperature. Tunable and enhanced flux-pinning effects have been achieved in YBCO conventional lateral heterostructures and the novel vertical aligned nanocomposites. Interface defects and associated strain field generated to relax the lattice mismatch have been identified as flux-pinning defects, whose nature, density and distribution can be modified through interface engineering. In particular, to understand one of the most important interfacial defects, the misfit dislocations, detailed

interfacial analysis has been conducted on prototype perovskite STO/MgO epitaxial film. Our atomic characterization has revealed a highly sensitive heterogeneous interfacial environment, where minor geometrical or compositional and/or charge perturbations could affect the interface contact, and therefore the dislocation core configurations.

Interface strain is another major topic in epitaxial thin film study. Understanding its effects to film quality and functionality relies on a precise measurement at actual heterogeneous interface. In this dissertation, we systematically investigated the accuracy and reliability STEM-based GPA method for quantifying interface lattice strain. An experimental strain accuracy of 1 pm with a spatial resolution less than 1 nm has been established after eliminating the STEM slow-scan distortion, by recording two images with scan directions 90 degrees apart. Applications of this optimized strain measurement method have demonstrated an unexpected secondary relaxation mechanism at a LAO/STO heterointerface.

Cs-corrected STEM imaging in combine with quantitative digital imaging processing is a powerful tool for revealing the actual interface structure in atomic scale. The future research can be focused on these aspects:

1. Incorporating of electronic property characterization techniques such as electron energy loss spectroscopy (EELS) into the current chemical and lattice displacement field at heterogeneous interface, to achieve a multi-dimension microstructure characterization.

2. Incorporating of ab initio computations such as density functional calculation based on the experimentally determined atom arrangement of interface structures, to understand the atomic origin of film physical properties.

REFERENCES

1. M. Ohring: Materials science of thin films: Deposition and structure (Academic Press, 2002).

2. L. Royer: The regular combining of different types of crystal. *Comptes Rendus Hebdomadaires Des Seances De L Academie Des Sciences* **180**, 2050 (1925).

3. P.J. Bedrossian: Sibinding and nucleation on Si(100). *Phys. Rev. Lett.* **74**, 3648 (1995).

4. S. Clarke, M.R. Wilby and D.D. Vvedensky: Theory of homoepitaxy on Si(001):1. Kinetics during growth. *Surf. Sci.* **255**, 91 (1991).

5. N. Reyren, S. Thiel, A.D. Caviglia, L.F. Kourkoutis, G. Hammerl, C. Richter, C.W. Schneider, T. Kopp, A.S. Ruetschi, D. Jaccard, M. Gabay, D.A. Muller, J.M. Triscone and J. Mannhart: Superconducting interfaces between insulating oxides. *Science* **317**, 1196 (2007).

6. A. Ohtomo and H.Y. Hwang: A high-mobility electron gas at the LaAlO3/SrTiO3 heterointerface. *Nature* **427**, 423 (2004).

7. A. Chen, H. Zhou, Z. Bi, Y. Zhu, Z. Luo, A. Bayraktaroglu, J. Philips, C. E., J. MacManusDriscoll, S.J. Pennycook, J. Narayan, Q. Jia and H. Wang: A new class of room-temperature multiferroic thin films with bismuth-based supercell structure. *Adv. Mater.* **25**, 1028 (2013).

8. R. Hull and J.C. Bean: Misfit dislocations in lattice-mismatched epitaxial-films. *Crit. Rev. Solid State Mat. Sci.* **17**, 507 (1992).

9. J.S. Speck and W. Pompe: Domain configurations due to multiple misfit relaxation mechanisms in epitaxial ferroelectric thin-films .1. Theory. *J. Appl. Phys.* **76**, 466 (1994).

10. J. Narayan and B.C. Larson: Domain epitaxy: A unified paradigm for thin film growth. *J. Appl. Phys.* **93**, 278 (2003).

11. B.W. Dodson: Nature of misfit dislocation sources in strained-layer semiconductor structures. *Appl. Phys. Lett.* **53**, 394 (1988).

12. D. Kienzle, B. Quezada and L. Marks: SrTiO3 (001) (root 13 x root 13) R33.7 degrees surface reconstruction. *Microsc. Microanal.* **15**, 1022 (2009).

13. M.W. Chu, I. Szafraniak, R. Scholz, C. Harnagea, D. Hesse, M. Alexe and U. Gosele: Impact of misfit dislocations on the polarization instability of epitaxial nanostructured ferroelectric perovskites. *Nat. Mater.* **3**, 87 (2004).

14. D.B. Keith, B. K Tanner: High resolution X-ray diffractometry and topography (Bristol, PA : Taylor & Francis, 1998).

15. S.B. Mi, C.L. Jia, M.I. Faley, U. Poppe and K. Urban: High-resolution electron microscopy of microstructure of SrTiO3/BaZrO3 bilayer thin films on MgO substrates. *J. Cryst. Growth* **300**, 478 (2007).

16. M. Huijben, A. Brinkman, G. Koster, G. Rijnders, H. Hilgenkamp and D.H.A. Blank: Structure-property relation of SrTiO3/LaAlO3 interfaces. *Adv. Mater.* **21**, 1665 (2009).

17. S.P. Alpay, I.B. Misirlioglu, V. Nagarajan and R. Ramesh: Can interface dislocations degrade ferroelectric properties? *Appl. Phys. Lett.* **85**, 2044 (2004).

18. M. Arredondo, Q.M. Ramasse, M. Weyland, R. Mahjoub, I. Vrejoiu, D. Hesse, N.D. Browning, M. Alexe, P. Munroe and V. Nagarajan: Direct evidence for cation non-stoichiometry and cottrell atmospheres around dislocation cores in functional oxide interfaces. *Adv. Mater.* **22**, 2430 (2010).

19. Y. Lin and C.L. Chen: Interface effects on highly epitaxial ferroelectric thin films. *J. Mater. Sci.* **44**, 5274 (2009).

20. T. Riedl, T. Gemming, K. Dorr, M. Luysberg and K. Wetzig: Mn valency at La(0.7)Sr(0.3)MnO(3)/SrTiO(3) (001) thin film interfaces. *Microsc. Microanal.* **15**, 213 (2009).

21. J.W. Matthews and A.E. Blakeslee: Defects in epitaxial multilayers .1. Misfit dislocations. *J. Cryst. Growth* **27**, 118 (1974).

22. J.P. Hirth and R.C. Pond: Steps, dislocations and disconnections as interface defects relating to structure and phase transformations. *Acta Mater.* **44**, 4749 (1996).

23. Y. Kamihara, T. Watanabe, M. Hirano and H. Hosono: Iron-based layered superconductor La[O1-xFx]FeAs (x=0.05-0.12) with T-c=26 K. *Journal of the American Chemical Society* **130**, 3296 (2008).

24. Mazin, II: Superconductivity gets an iron boost. *Nature* **464**, 183 (2010).

25. D.C. Johnston: The puzzle of high temperature superconductivity in layered iron pnictides and chalcogenides. *Adv. Phys.* **59**, 803 (2010).

26. M. Tegel, C. Lohnert and D. Johrendt: The crystal structure of FeSe(0.44)Te(0.56). *Solid State Commun.* **150**, 383 (2010).

27. F.C. Hsu, J.Y. Luo, K.W. Yeh, T.K. Chen, T.W. Huang, P.M. Wu, Y.C. Lee, Y.L. Huang, Y.Y. Chu, D.C. Yan and M.K. Wu: Superconductivity in the PbO-type structure alpha-FeSe. *Proc. Natl. Acad. Sci. U. S. A.* **105**, 14262 (2008).

28. K.W. Yeh, T.W. Huang, Y.L. Huang, T.K. Chen, F.C. Hsu, P.M. Wu, Y.C. Lee, Y.Y. Chu, C.L. Chen, J.Y. Luo, D.C. Yan and M.K. Wu: Tellurium substitution effect on superconductivity of the alpha-phase iron selenide. *Epl* **84**, (2008).

29. W. Bao, Y. Qiu, Q. Huang, M.A. Green, P. Zajdel, M.R. Fitzsimmons, M. Zhernenkov, S. Chang, M.H. Fang, B. Qian, E.K. Vehstedt, J.H. Yang, H.M. Pham, L. Spinu and Z.Q. Mao: Tunable (delta pi, delta pi)-type antiferromagnetic order in alpha-Fe(Te,Se) superconductors. *Phys. Rev. Lett.* **102**, (2009).

30. J.S. Wen, G.Y. Xu, G.D. Gu, J.M. Tranquada and R.J. Birgeneau: Interplay between magnetism and superconductivity in iron-chalcogenide superconductors: Crystal growth and characterizations. *Rep. Prog. Phys.* **74**, (2011).

31. A. Martinelli, A. Palenzona, M. Tropeano, C. Ferdeghini, M. Putti, M.R. Cimberle, T.D. Nguyen, M. Affronte and C. Ritter: From antiferromagnetism to superconductivity in Fe(1+y)Te(1-x)Se(x) (0 <= x <= 0.20): Neutron powder diffraction analysis. *Phys. Rev. B* **81**, (2010).

32. T. Katase, Y. Ishimaru, A. Tsukamoto, H. Hiramatsu, T. Kamiya, K. Tanabe and H. Hosono: Advantageous grain boundaries in iron pnictide superconductors. *Nat. Commun.* **2**, (2011).

33. E. Bellingeri, I. Pallecchi, R. Buzio, A. Gerbi, D. Marre, M.R. Cimberle, M. Tropeano, M. Putti, A. Palenzona and C. Ferdeghini: T(c)=21 K in epitaxial FeSe(0.5)Te(0.5) thin films with biaxial compressive strain. *Appl. Phys. Lett.* **96**, (2010).

34. T.G. Kumary, D.K. Baisnab, J. Janaki, A. Mani, A.T. Satya, R.M. Sarguna, P.K. Ajikumar, A.K. Tyagi and A. Bharathi: Superconducting Fe(1+delta)Se(1-x)Te(x) thin films: Growth, characterization and properties. *Supercond. Sci. Technol.* **22**, (2009).

35. M. Dawber, K.M. Rabe and J.F. Scott: Physics of thin-film ferroelectric oxides. *Rev. Mod. Phys.* **77**, 1083 (2005).

36. X.B. He, G.R. Li, J.D. Zhang, A.B. Karki, R.Y. Jin, B.C. Sales, A.S. Sefat, M.A. McGuire, D. Mandrus and E.W. Plummer: Nanoscale chemical phase separation in FeTe(0.55)Se(0.45) as seen via scanning tunneling spectroscopy. *Phys. Rev. B* **83**, (2011).

37. C. de la Cruz, Q. Huang, J.W. Lynn, J.Y. Li, W. Ratcliff, J.L. Zarestky, H.A. Mook, G.F. Chen, J.L. Luo, N.L. Wang and P.C. Dai: Magnetic order close to superconductivity in the iron-based layered LaO(1-x)F(x)FeAs systems. *Nature* **453**, 899 (2008).

38. M.K. Wu, J.R. Ashburn, C.J. Torng, P.H. Hor, R.L. Meng, L. Gao, Z.J. Huang, Y.Q. Wang and C.W. Chu: Superconductivity at 93-K in a new mixed-phase Y-Ba-Cu-O compound system at ambient pressure. *Phys. Rev. Lett.* **58**, 908 (1987).

39. T.J. Doi, T. Yuasa, T. Ozawa and K. Higashiyama: Transport critical-current densities in uniaxially and biaxially oriented Tl-1(Ba0.8Sr0.2)(2)Ca2Cu3O9 superconducting films on ag and srtio3 substrates prepared by a spray-pyrolysis method. *Jpn. J. Appl. Phys. Part 1 - Regul. Pap. Short Notes Rev. Pap.* **33**, 5692 (1994).

40. K. Li and J.E. Johnson: Properties of ion-beam deposited YBCO thin-films. *IEEE Trans. Magn.* **27**, 1463 (1991).

41. M. Schieber, Y. Ariel, M. Schwartz, M. Levinsky, S.S.M. Maharizy, B.L. Zhou and S.C. Han: Laser ablated YBCO films on buffer layers of YSZ and SrTiO3 deposited on sapphire and MgO substrates (Adam Hilger Ltd, 1991).

42. M.W. Rupich, D.T. Verebelyi, W. Zhang, T. Kodenkandath and X.P. Li: Metalorganic deposition of YBCO films for second-generation high-temperature superconductor wires. *MRS Bull.* **29**, 572 (2004).

43. A. Ibi, H. Fukushima, R. Kuriki, S. Miyata, K. Takahashi, H. Kobayashi, M. Konishi, T. Watanabe, Y. Yamada and Y. Shiohara: Development of long YBCO coated conductors by IBAD-PLD method. *Physica C* **445**, 525 (2006).

44. M.P. Paranthaman and T. Izumi: High-performance YBCO-coated superconductor wires. *MRS Bull.* **29**, 533 (2004).

45. S.R. Foltyn, L. Civale, J.L. Macmanus-Driscoll, Q.X. Jia, B. Maiorov, H. Wang and M. Maley: Materials science challenges for high-temperature superconducting wire. *Nat. Mater.* **6**, 631 (2007).

46. S.R. Foltyn, P.N. Arendt, Q.X. Jia, H. Wang, J.L. MacManus-Driscoll, S. Kreiskott, R.F. DePaula, L. Stan, J.R. Groves and P.C. Dowden: Strongly coupled critical current density values achieved in Y1Ba2Cu3O7-delta

coated conductors with near-single-crystal texture. *Appl. Phys. Lett.* **82**, 4519 (2003).

47. M. Charalambous, J. Chaussy and P. Lejay: Evidence from resistivity measurements along the c-axis for a transition within the vortex state for h-parallel-to-ab in single-crystal YBa2Cu3O7. *Phys. Rev. B* **45**, 5091 (1992).

48. G. Blatter, M.V. Feigelman, V.B. Geshkenbein, A.I. Larkin and V.M. Vinokur: Vortices in high-temperature superconductors. *Rev. Mod. Phys.* **66**, 1125 (1994).

49. T.L. Hylton and M.R. Beasley: Flux-pinning mechanisms in thin-films of YBa2Ca3Ox. *Phys. Rev. B* **41**, 11669 (1990).

50. Z.L. Wang, A. Goyal and D.M. Kroeger: Structural and chemical disorder near the Y2BaCuO5/YBa2Cu3O7-delta interface and its possible relation to the flux-pinning behavior in melt-textured YBa2Cu3O7-delta. *Phys. Rev. B* **47**, 5373 (1993).

51. B. Keimer, F. Dogan, I.A. Aksay, R.W. Erwin, J.W. Lynn and M. Sarikaya: Inclined-field structure, morphology, and pinning of the vortex lattice in microtwinned YBa2Cu3O7. *Science* **262**, 83 (1993).

52. C.P. Poole, H.A. Farach and R.J. Creswick: Superconductivity (Academic Press, 1995).

53. J.L. Macmanus-Driscoll, S.R. Foltyn, Q.X. Jia, H. Wang, A. Serquis, L. Civale, B. Maiorov, M.E. Hawley, M.P. Maley and D.E. Peterson: Strongly enhanced current densities in superconducting coated conductors of YBa2Cu3O7-x+BaZrO3. *Nat. Mater.* **3**, 439 (2004).

54. H. Wang, A. Serquis, B. Maiorov, L. Civale, Q.X. Jia, P.N. Arendt, S.R. Foltyn, J.L. MacManus-Driscoll and X. Zhang: Microstructure and transport properties of Y-rich YBa2Cu3O7-delta thin films. *J. Appl. Phys.* **100**, (2006).

55. C.V. Varanasi, J. Burke, L. Brunke, H. Wang, M. Sumption and P.N. Barnes: Enhancement and angular dependence of transport critical current density in pulsed laser deposited YBa2Cu3O7-x+BaSnO3 films in applied magnetic fields. *J. Appl. Phys.* **102**, (2007).

56. P.N. Barnes, T.J. Haugan, C.V. Varanasi and T.A. Campbell: Flux pinning behavior of incomplete multilayered lattice structures in YBa(2)Cu(3)O(7-d). *Appl. Phys. Lett.* **85**, 4088 (2004).

57. H.Y. Wang and J. Wang: Interfacial Defects and Flux-Pinning Effects in Nanostructured YBa2Cu3O Thin Films. *IEEE Trans. Appl. Supercond.* **19**, 3395 (2009).

58. S.R. Foltyn, H. Wang, L. Civale, Q.X. Jia, P.N. Arendt, B. Maiorov, Y. Li, M.P. Maley and J.L. MacManus-Driscoll: Overcoming the barrier to 1000 A/cm width superconducting coatings. *Appl. Phys. Lett.* **87**, (2005).

59. T. Haugan, P.N. Barnes, R. Wheeler, F. Meisenkothen and M. Sumption: Addition of nanoparticle dispersions to enhance flux pinning of the YBa2Cu3O7-x superconductor. *Nature* **430**, 867 (2004).

60. B. Maiorov, S.A. Baily, H. Zhou, O. Ugurlu, J.A. Kennison, P.C. Dowden, T.G. Holesinger, S.R. Foltyn and L. Civale: Synergetic combination of different types of defect to optimize pinning landscape using BaZrO3-doped YBa2Cu3O7. *Nat. Mater.* **8**, 398 (2009).

61. S. Kang, A. Goyal, J. Li, P. Martin, A. Ijaduola, J.R. Thompson and M. Paranthaman: Flux-pinning characteristics as a function of density of columnar defects comprised of self-assembled nanodots and nanorods in epitaxial YBa2Cu3O7-delta films for coated conductor applications. *Physica C* **457**, 41 (2007).

62. S. Kang, K.J. Leonard, P.M. Martin, J. Li and A. Goyal: Strong enhancement of flux pinning in YBa2Cu3O7-delta multilayers with columnar defects comprised of self-assembled BaZrO3 nanodots. *Supercond. Sci. Technol.* **20**, 11 (2007).

63. B. Roas, L. Schultz and G. Endres: Epitaxial-growth of YBa2Cu3O7-x thin-films by a laser evaporation process. *Appl. Phys. Lett.* **53**, 1557 (1988).

64. P. Chaudhari, R.H. Koch, R.B. Laibowitz, T.R. McGuire and R.J. Gambino: Critical-current measurements in epitaxial-films of YBa2Cu3O7-x compound. *Phys. Rev. Lett.* **58**, 2684 (1987).

65. D. Larbalestier, A. Gurevich, D.M. Feldmann and A. Polyanskii: High-Tc superconducting materials for electric power applications. *Nature* **414**, 368 (2001).

66. Y.S. Kim, D.J. Kim, T.H. Kim, T.W. Noh, J.S. Choi, B.H. Park and J.G. Yoon: Observation of room-temperature ferroelectricity in tetragonal strontium titanate thin films on SrTiO3 (001) substrates. *Appl. Phys. Lett.* **91**, (2007).

67. Z.L. Zhang, W. Sigle and W. Kurtz: HRTEM and EELS study of screw dislocation cores in SrTiO3. *Phys. Rev. B* **69**, (2004).

68. C.L. Jia, A. Thust and K. Urban: Atomic-scale analysis of the oxygen configuration at a SrTiO3 dislocation core. *Phys. Rev. Lett.* **95**, 2255061 (2005).

69. R.F. Klie, W. Walkosz, G. Yang and Y. Zhao: Aberration-corrected Z-contrast imaging of SrTiO3 dislocation cores. *J. Electron Microsc.* **58**, 185 (2009).

70. E. Ruska: The development of the electron-microscope and of electron-microscopy. *Bioscience Reports* **7**, 607 (1987).

71. M. von Ardenne: The scanning electron microscope. *Zeitschrift Fur Physik* **109**, 553 (1938).

72. J.W. Menter: The direct study by electron microscopy of crystal lattices and their imperfections. *Proceedings of the Royal Society of London Series a-Mathematical and Physical Sciences* **236**, 119 (1956).

73. J.C. Yang, M.W. Small, R.V. Grieshaber and R.G. Nuzzo: Recent developments and applications of electron microscopy to heterogeneous catalysis. *Chem. Soc. Rev.* **41**, 8179 (2012).

74. O. Scherzer: Errors of electron lenses. *Zeitschrift fur Physik* **101**, 593 (1936).

75. O. Scherzer: Spharische und chromatische korrektur von elektronen-linsen. *Optik* **2**, 114 (1947).

76. K.W. Urban: Studying atomic structures by aberration-corrected transmission electron microscopy. *Science* **321**, 506 (2008).

77. K. Urban, L. Houben, C.L. Jia, M. Lentzen, S.B. Mi, A. Thust and K. Tillmann: Atomic-resolution aberration-corrected transmission electron microscopy, in advances in imaging and electron physics (P. W. Hawkes, 2008)

78. K.W. Urban: Is science prepared for atomic-resolution electron microscopy? *Nat. Mater.* **8**, 260 (2009).

79. W.M.J. Coene, A. Thust, M. deBeeck and D. VanDyck: Maximum-likelihood method for focus-variation image reconstruction in high resolution transmission electron microscopy. *Ultramicroscopy* **64**, 109 (1996).

80. C. Kisielowski, C.J.D. Hetherington, Y.C. Wang, R. Kilaas, M.A. O'Keefe and A. Thust: Imaging columns of the light elements carbon, nitrogen and oxygen with sub angstrom resolution. *Ultramicroscopy* **89**, 243 (2001).

81. G. Van Tendeloo, S. Bals, S. Van Aert, J. Verbeeck and D. Van Dyck: Advanced electron microscopy for advanced materials. *Adv. Mater.* **24**, 5655 (2012).

82. O.L. Krivanek, N. Dellby and A.R. Lupini: Towards sub-angstrom electron beams. *Ultramicroscopy* **78**, 1 (1999).

83. A. Hashimoto, K. Suenaga, A. Gloter, K. Urita and S. Iijima: Direct evidence for atomic defects in graphene layers. *Nature* **430**, 870 (2004).

84. O.L. Krivanek, M.F. Chisholm, V. Nicolosi, T.J. Pennycook, G.J. Corbin, N. Dellby, M.F. Murfitt, C.S. Own, Z.S. Szilagyi, M.P. Oxley, S.T. Pantelides and S.J. Pennycook: Atom-by-atom structural and chemical analysis by annular dark-field electron microscopy. *Nature* **464**, 571 (2010).

85. M. Varela, J. Gazquez and S.J. Pennycook: STEM-EELS imaging of complex oxides and interfaces. *MRS Bull.* **37**, 29 (2012).

86. M. Varela, J. Gazquez, A.R. Lupini, J.T. Luck, M.A. Torija, M. Sharma, C. Leighton, M.D. Biegalski, H.M. Christen, M. Murfitt, N. Dellby, O. Krivanek and S.J. Pennycook: Applications of aberration corrected scanning transmission electron microscopy and electron energy loss spectroscopy to thin oxide films and interfaces. *Int. J. Mater. Res.* **101**, 21 (2010).

87. O.L. Krivanek, N. Dellby, M.F. Murfitt and Iop: Aberration-corrected scanning transmission electron microscopy of semiconductors (17th International Conference on Microscopy of Semiconducting Materials, 2011).

88. S. Kadkhodazadeh: High resolution STEM of quantum dots and quantum wires. *Micron* **44**, 75 (2013).

89. W. Zhou, I.E. Wachs and C.J. Kiely: Nanostructural and chemical characterization of supported metal oxide catalysts by aberration corrected analytical electron microscopy. *Curr. Opin. Solid State Mat. Sci.* **16**, 10 (2012).

90. M. Varela, A.R. Lupini, S.J. Pennycook, Z. Sefrioui and J. Santamaria: Nanoscale analysis of YBa2Cu3O7-x/La0.67Ca0.33MnO3 interfaces. *Solid-State Electron.* **47**, 2245 (2003).

91. C. Visani, J. Tornos, N.M. Nemes, M. Rocci, C. Leon, J. Santamaria, S.G.E. te Velthuis, Y. Liu, A. Hoffmann, J.W. Freeland, M. Garcia-Hernandez, M.R. Fitzsimmons, B.J. Kirby, M. Varela and S.J. Pennycook: Symmetrical interfacial reconstruction and magnetism in La0.7Ca0.3MnO3/YBa2Cu3O7/La0.7Ca0.3MnO3 heterostructures. *Phys. Rev. B* **84**, (2011).

92. Y.Y. Zhu, C.F. Tsai and H.Y. Wang: Atomic interface sequence, misfit strain relaxation and intrinsic flux-pinning defects in different YBa2Cu3O7-delta heterogeneous systems. *Supercond. Sci. Technol.* **26**, (2013).

93. Y. Zhu, L. Chen, J. Ciston and H. Wang: Atomic-scale investigations of intrinsic chemical inhomogeneity in superconducting Fe1+ySe1-xTex epitaxial films. *J. Phys. Chem. C* **Accepted**, (2013).

94. Y.J. Kim, R.Z. Tao, R.F. Klie and D.N. Seidman: Direct atomic-scale imaging of hydrogen and oxygen interstitials in pure niobium using atom-probe tomography and aberration-corrected scanning transmission electron microscopy. *ACS Nano* **7**, 732 (2013).

95. J. Garcia-Barriocanal, A. Rivera-Calzada, M. Varela, Z. Sefrioui, E. Iborra, C. Leon, S.J. Pennycook and J. Santamaria: Colossal ionic conductivity at interfaces of epitaxial ZrO(2): Y(2)O(3)/SrTiO(3) heterostructures. *Science* **321**, 676 (2008).

96. L.F. Kourkoutis, H.L. Xin, T. Higuchi, Y. Hotta, J.H. Lee, Y. Hikita, D.G. Schlom, H.Y. Hwang and D.A. Muller: Atomic-resolution spectroscopic imaging of oxide interfaces. *Philosophical Magazine* **90**, 4731 (2010).

97. S. Van Aert, J. Verbeeck, R. Erni, S. Bals, M. Luysberg, D. Van Dyck and G. Van Tendeloo: Quantitative atomic resolution mapping using high-angle annular dark field scanning transmission electron microscopy. *Ultramicroscopy* **109**, 1236 (2009).

98. A.Y. Borisevich, H.J. Chang, M. Huijben, M.P. Oxley, S. Okamoto, M.K. Niranjan, J.D. Burton, E.Y. Tsymbal, Y.h. chu, p. yu, r. ramesh, s.v. kalinin and s.j. pennycook: suppression of octahedral tilts and associated changes in electronic properties at epitaxial oxide heterostructure interfaces. *Phys. Rev. Lett.* **105**, (2010).

99. A.Y. Borisevich, A.R. Lupini, J. He, E.A. Eliseev, A.N. Morozovska, G.S. Svechnikov, P. Yu, Y.H. Chu, R. Ramesh, S.T. Pantelides, S.V. Kalinin and S.J. Pennycook: Interface dipole between two metallic oxides caused by localized oxygen vacancies. *Phys. Rev. B* **86**, (2012).

100. C.L. Jia, J. Barthel, F. Gunkel, R. Dittmann, S. Hoffmann-Eifert, L. Houben, M. Lentzen and A. Thust: Atomic-scale measurement of structure and chemistry of a single-unit-cell layer of LaAlO3 embedded in SrTiO3. *Microsc. Microanal.* **19**, 310 (2013).

101. H.J. Chang, S.V. Kalinin, A.N. Morozovska, M. Huijben, Y.H. Chu, P. Yu, R. Ramesh, E.A. Eliseev, G.S. Svechnikov, S.J. Pennycook and A.Y. Borisevich: Atomically resolved mapping of polarization and electric fields

across ferroelectric/oxide interfaces by Z-contrast imaging. *Adv. Mater.* **23**, 2474 (2011).

102. R. Srinivasan, R. Banerjee, J.Y. Hwang, G.B. Viswanathan, J. Tiley, D.M. Dimiduk and H.L. Fraser: Atomic scale structure and chemical composition across order-disorder interfaces. *Phys. Rev. Lett.* **102**, (2009).

103. M. Lopez-Haro, J.M. Cies, S. Trasobares, J.A. Perez-Omil, J.J. Delgado, S. Bernal, P. Bayle-Guillemaud, O. Stephan, K. Yoshida, E.D. Boyes, P.L. Gai and J.J. Calvino: Imaging Nanostructural modifications induced by electronic metal-support interaction effects at Au parallel to cerium-based oxide nanointerfaces. *ACS Nano* **6**, 6812 (2012).

104. D.M. Kepaptsoglou, K. Hadidi, O.M. Lovvik, A. Magraso, T. Norby, A.E. Gunnaes, A. Olsen and Q.M. Ramasse: Interfacial charge transfer and chemical bonding in a Ni-LaNbO4 cermet for proton-conducting solid-oxide fuel cell anodes. *Chem. Mat.* **24**, 4152 (2012).

105. J.M. Yang, J.W. Kim, A. Wilke, O. Seifarth, T. Schroeder and Ieee: Interface analysis of epi-Si(111)/Y2O3/Pr2O3/Si(111) heterostructures (18th Ieee International Symposium on the Physical and Failure Analysis of Integrated Circuits, 2011).

106. P. Bayle, T. Deutsch, B. Gilles, F. Lancon, A. Marty and J. Thibault: Quantitative-analysis of the deformation and chemical profiles of strained multilayers. *Ultramicroscopy* **56**, 94 (1994).

107. R. Bierwolf, M. Hohenstein, F. Phillipp, O. Brandt, G.E. Crook and K. Ploog: Direct measurement of local lattice-distortions in strained layer structures by hrem. *Ultramicroscopy* **49**, 273 (1993).

108. M.J. Hytch, E. Snoeck and R. Kilaas: Quantitative measurement of displacement and strain fields from HREM micrographs. *Ultramicroscopy* **74**, 131 (1998).

109. A.Z. Moshfegh: PVD growth method: Physics and technology (Academic Press, 2004).

110. D. Dijkkamp, T. Venkatesan, X.D. Wu, S.A. Shaheen, N. Jisrawi, Y.H. Minlee, W.L. McLean and M. Croft: Preparation of Y-Ba-Cu oxide superconductor thin-films using pulsed laser evaporation from high-tc bulk material. *Appl. Phys. Lett.* **51**, 619 (1987).

111. I.W. Boyd: Thin film growth by pulsed laser deposition. *Ceram. Int.* **22**, 429 (1996).

112. C. Belouet: Pulsed laser-assisted deposition of thin films - Principle and industrial perspectives. *Vide-Science Technique Et Applications* **53**, 421 (1998).

113. F.E. Fernandez, M. Pumarol, A. Martinez, W.Y. Jia, Y.Y. Wang, E. Rodriguez and H.A. Mourad: Advances in pulsed laser deposition growth of nitride thin films, in laser applications in microelectronic and optoelectronic manufacturing iv (Academic Press, 1999)

114. H.M. Christen and G. Eres: Recent advances in pulsed-laser deposition of complex oxides. *J. Phys.-Condes. Matter* **20**, (2008).

115. V.M. Kaganer, R. Kohler, M. Schmidbauer, R. Opitz and B. Jenichen: X-ray diffraction peaks due to misfit dislocations in heteroepitaxial structures. *Phys. Rev. B* **55**, 1793 (1997).

116. N.B. Bolotina: X-ray diffraction analysis of modulated crystals: Review. *Crystallogr. Rep.* **52**, 647 (2007).

117. A.Y. Nikulin, A.W. Stevenson, H. Hashizume, D. Cookson, G. Hobler and S.W. Wilkins: Model-independent determination of 2D strain distribution in ion-implanted silicon crystals from X-ray diffraction data. *Semicond. Sci. Technol.* **12**, 350 (1997).

118. D.B. Williams and C.B. Carter: Transmission electron microscopy: A textbook for materials science (Plenum Press, 1996)

119. M.J. Hytch and T. Plamann: Imaging conditions for reliable measurement of displacement and strain in high-resolution electron microscopy. *Ultramicroscopy* **87**, 199 (2001).

120. E. Guerrero, P. Galindo, A. Yanez, T. Ben and S.I. Molina: Error quantification in strain mapping methods. *Microsc. Microanal.* **13**, 320 (2007).

121. D.O. Klenov and S. Stemmer: Contributions to the contrast in experimental high-angle annular dark-field images. *Ultramicroscopy* **106**, 889 (2006).

122. C.T. Chou, S.C. Anderson, D.J.H. Cockayne, A.Z. Sikorski and M.R. Vaughan: Surface relaxation of strained heterostructures revealed by Bragg line splitting in lacbed patterns. *Ultramicroscopy* **55**, 334 (1994).

123. D. Jacob, Y. Androussi, T. Benabbas, P. Francois and A. Lefebvre: Surface relaxation of strained semiconductor heterostructures revealed by finite-element calculations and transmission electron microscopy. *Philos. Mag. A-Phys. Condens. Matter Struct. Defect Mech. Prop.* **78**, 879 (1998).

124. A.V. Crewe, J. Wall and J. Langmore: Visibility of single atoms. *Science* **168**, 1338 (1970).

125. S.J. Pennycook and P.D. Nellist: Z-contrast scanning transmission electron microscopy, in impact of electron and scanning probe microscopy on materials research (Springer,1999)

126. R. Erni, M.D. Rossell, C. Kisielowski and U. Dahmen: Atomic-resolution imaging with a sub-50-pm electron probe. *Phys. Rev. Lett.* **102**, 0961011 (2009).

127. N. Alem, R. Erni, C. Kisielowski, M.D. Rossell, W. Gannett and A. Zettl: Atomically thin hexagonal boron nitride probed by ultrahigh-resolution transmission electron microscopy. *Phys. Rev. B* **80**, (2009).

128. P.D. Nellist and S.J. Pennycook: The principles and interpretation of annular dark-field Z-contrast imaging, (Advances in imaging and electron physics, 2000)

129. J.M. Cowley: Image contrast in a transmission scanning electron microscope. *Appl. Phys. Lett.* **15**, 58 (1969).

130. P. Hartel, H. Rose and C. Dinges: Conditions and reasons for incoherent imaging in STEM. *Ultramicroscopy* **63**, 93 (1996).

131. M. Varela, A.R. Lupini, K. van Benthem, A.Y. Borisevich, M.F. Chisholm, N. Shibata, E. Abe and S.J. Pennycook: Materials characterization in the aberration-corrected scanning transmission electron microscope. *Ann. Rev. Mater. Res.* **35**, 539 (2005).

132. Y. Liao: Practical electron microscopy and database (Academic Press, 2006).

133. H. Rose: Outline of a spherically corrected semiaplanatic medium-voltage transmission electron-microscope. *Optik* **85**, 19 (1990).

134. S.J. Pennycook, M. Varela, C.J.D. Hetherington and A.I. Kirkland: Materials advances through aberration-corrected electron microscopy. *MRS Bull.* **31**, 36 (2006).

135. U. Dahmen, R. Erni, V. Radmilovic, C. Kisielowski, M.D. Rossell and P. Denes: Background, status and future of the transmission electron aberration-corrected microscope project. *Philos. Trans. R. Soc. A-Math. Phys. Eng. Sci.* **367**, 3795 (2009).

136. F. Zemlin: Practical procedure for alignment of a high-resolution electron-microscope. *Ultramicroscopy* **4**, 241 (1979).

137. C. Kisielowski, B. Freitag, M. Bischoff, H. van Lin, S. Lazar, G. Knippels, P. Tiemeijer, M. van der Stam, S. von Harrach, M. Stekelenburg, M. Haider, S. Uhlemann, H. Muller, P. Hartel, B. Kabius, D. Miller, I. Petrov, E.A. Olson, T. Donchev, E.A. Kenik, A.R. Lupini, J. Bentley, S.J. Pennycook, I.M. Anderson, A.M. Minor, A.K. Schmid, T. Duden, V. Radmilovic, Q.M. Ramasse, M. Watanabe, R. Erni, E.A. Stach, P. Denes and U. Dahmen: Detection of single atoms and buried defects in three dimensions by aberration-corrected electron microscope with 0.5-angstrom information limit. *Microsc. Microanal.* **14**, 469 (2008).

138. B. Rafferty, P.D. Nellist and S.J. Pennycook: On the origin of transverse incoherence in Z-contrast STEM. *J. Electron Microsc.* **50**, 227 (2001).

139. J.L. Rouviere and E. Sarigiannidou: Theoretical discussions on the geometrical phase analysis. *Ultramicroscopy* **106**, 1 (2005).

140. A. Cho: The Hot Question: How new are the new superconductors? *Science* **320**, 870 (2008).

141. S. Medvedev, T.M. McQueen, I.A. Troyan, T. Palasyuk, M.I. Eremets, R.J. Cava, S. Naghavi, F. Casper, V. Ksenofontov, G. Wortmann and C. Felser: Electronic and magnetic phase diagram of beta-Fe(1.01)Se with superconductivity at 36.7 K under pressure. *Nat. Mater.* **8**, 630 (2009).

142. A. Wittlin, P. Aleshkevych, H. Przybylinska, D.J. Gawryluk, P. Dluzewski, M. Berkowski, R. Puzniak, M.U. Gutowska and A. Wisniewski: Microstructural magnetic phases in superconducting FeTe0.65Se0.35. *Supercond. Sci. Technol.* **25**, (2012).

143. T.M. McQueen, Q. Huang, V. Ksenofontov, C. Felser, Q. Xu, H. Zandbergen, Y.S. Hor, J. Allred, A.J. Williams, D. Qu, J. Checkelsky, N.P. Ong and R.J. Cava: Extreme sensitivity of superconductivity to stoichiometry in Fe(1+delta)Se. *Phys. Rev. B* **79**, (2009).

144. W. Schuster, H. Mikler and K.L. Komarek: Transition metal-chalcogen systems .7. Iron-selenium phase-diagram. *Mon. Chem.* **110**, 1153 (1979).

145. S. Rossler, D. Cherian, S. Harikrishnan, H.L. Bhat, S. Elizabeth, J.A. Mydosh, L.H. Tjeng, F. Steglich and S. Wirth: Disorder-driven electronic localization and phase separation in superconducting Fe(1+y)Te(0.5)Se(0.5) single crystals. *Phys. Rev. B* **82**, (2010).

146. D. Fruchart, P. Convert, P. Wolfers, R. Madar, J.P. Senateur and R. Fruchart: Antiferromagnetic structure of Fe1.125Te following a monoclinic deformation. *Mater. Res. Bull.* **10**, 169 (1975).

147. A. Kumar, A. Pal, R.P. Tandon and V.P.S. Awana: Role of interstitial "caged" Fe in the superconductivity of FeTe(1/2)Se(1/2). *Solid State Commun.* **151**, 1767 (2011).

148. R. Viennois, E. Giannini, D. van der Marel and R. Cerny: Effect of Fe excess on structural, magnetic and superconducting properties of single-crystalline Fe(1+x)Te(1-y)Se(y). *J. Solid State Chem.* **183**, 769 (2010).

149. T. Gebre, G. Li, J.B. Whalen, B.S. Conner, H.D. Zhou, G. Grissonnanche, M.K. Kostov, A. Gurevich, T. Siegrist and L. Balicas: Disorder-dependent superconducting phase diagram at high magnetic fields in Fe1+ySexTe1-x (x similar to 0.4). *Phys. Rev. B* **84**, (2011).

150. W.D. Si, Z.W. Lin, Q. Jie, W.G. Yin, J. Zhou, G.D. Gu, P.D. Johnson and Q. Li: Enhanced superconducting transition temperature in FeSe(0.5)Te(0.5) thin films. *Appl. Phys. Lett.* **95**, (2009).

151. S.X. Huang, C.L. Chien, V. Thampy and C. Broholm: Control of tetrahedral coordination and superconductivity in FeSe0.5Te0.5 thin films. *Phys. Rev. Lett.* **104**, (2010).

152. M.J. Wang, J.Y. Luo, T.W. Huang, H.H. Chang, T.K. Chen, F.C. Hsu, C.T. Wu, P.M. Wu, A.M. Chang and M.K. Wu: Crystal orientation and thickness dependence of the superconducting transition temperature of tetragonal FeSe(1-x) thin films. *Phys. Rev. Lett.* **103**, (2009).

153. R. Khasanov, M. Bendele, A. Amato, P. Babkevich, A.T. Boothroyd, A. Cervellino, K. Conder, S.N. Gvasaliya, H. Keller, H.H. Klauss, H. Luetkens, V. Pomjakushin, E. Pomjakushina and B. Roessli: Coexistence of incommensurate magnetism and superconductivity in Fe(1+y)SexTe(1-x). *Phys. Rev. B* **80**, (2009).

154. T.J. Liu, J. Hu, B. Qian, D. Fobes, Z.Q. Mao, W. Bao, M. Reehuis, S.A.J. Kimber, K. Prokes, S. Matas, D.N. Argyriou, A. Hiess, A. Rotaru, H. Pham, L. Spinu, Y. Qiu, V. Thampy, A.T. Savici, J.A. Rodriguez and C. Broholm: From (pi,0) magnetic order to superconductivity with (pi,pi) magnetic resonance in Fe1.02Te1-xSex. *Nat. Mater.* **9**, 716 (2010).

155. T.J. Liu, X. Ke, B. Qian, J. Hu, D. Fobes, E.K. Vehstedt, H. Pham, J.H. Yang, M.H. Fang, L. Spinu, P. Schiffer, Y. Liu and Z.Q. Mao: Charge-carrier localization induced by excess Fe in the superconductor Fe1+yTe1-xSex. *Phys. Rev. B* **80**, (2009).

156. S.C. Speller, C. Aksoy, M. Saydam, H. Taylor, G. Burnell, A.T. Boothroyd and C.R.M. Grovenor: Analysis of FeySe1-xTex thin films grown by radio frequency sputtering. *Supercond. Sci. Technol.* **24**, (2011).

157. H.F. Hu, J.M. Zuo, J.S. Wen, Z.J. Xu, Z.W. Lin, Q. Li, G.D. Gu, W.K. Park and L.H. Greene: Phase separation in the iron chalcogenide superconductor Fe(1+y)Te(x)Se(1-x). *New J. Phys.* **13**, (2011).

158. D. Louca, K. Horigane, A. Llobet, R. Arita, S. Ji, N. Katayama, S. Konbu, K. Nakamura, T.Y. Koo, P. Tong and K. Yamada: Local atomic structure of superconducting FeSe1-xTex. *Phys. Rev. B* **81**, (2010).

159. X.B. He, G.R. Li, J.D. Zhang, A.B. Karki, R.Y. Jin, B.C. Sales, A.S. Sefat, M.A. McGuire, D. Mandrus and E.W. Plummer: Nanoscale chemical phase separation in FeTe0.55Se0.45 as seen via scanning tunneling spectroscopy. *Phys. Rev. B* **83**, (2011).

160. Y.M. Qiu, W. Bao, Y. Zhao, C. Broholm, V. Stanev, Z. Tesanovic, Y.C. Gasparovic, S. Chang, J. Hu, B. Qian, M.H. Fang and Z.Q. Mao: Spin gap and resonance at the nesting wave vector in superconducting FeSe(0.4)Te(0.6). *Phys. Rev. Lett.* **103**, (2009).

161. L. Chen, C.F. Tsai, Y.Y. Zhu, A.P. Chen, Z.X. Bi, J. Lee and H.Y. Wang: Enhanced flux pinning properties in superconducting FeSe0.5Te0.5 thin films with secondary phases. *Superconductor Science & Technology* **25**, 025020 (2012).

162. D. Abou-Ras, R. Caballero, C.H. Fischer, C.A. Kaufmann, I. Lauermann, R. Mainz, H. Monig, A. Schopke, C. Stephan, C. Streeck, S. Schorr, A. Eicke, M. Dobeli, B. Gade, J. Hinrichs, T. Nunney, H. Dijkstra, V. Hoffmann, D. Klemm, V. Efimova, A. Bergmaier, G. Dollinger, T. Wirth, W. Unger, A.A. Rockett, A. Perez-Rodriguez, J. Alvarez-Garcia, V. Izquierdo-Roca, T. Schmid, P.P. Choi, M. Muller, F. Bertram, J. Christen, H. Khatri, R.W. Collins, S. Marsillac and I. Kotschau: Comprehensive comparison of various techniques for the analysis of elemental distributions in thin films. *Microsc. Microanal.* **17**, 728 (2011).

163. P.J. Phillips, M. De Graef, L. Kovarik, A. Agrawal, W. Windl and M.J. Mills: Atomic-resolution defect contrast in low angle annular dark-field STEM. *Ultramicroscopy* **116**, 47 (2012).

164. S. Lee, J. Jiang, J.D. Weiss, C.M. Folkman, C.W. Bark, C. Tarantini, A. Xu, D. Abraimov, A. Polyanskii, C.T. Nelson, Y. Zhang, S.H. Baek, H.W. Jang, A. Yamamoto, F. Kametani, X.Q. Pan, E.E. Hellstrom, A. Gurevich, C.B. Eom and D.C. Larbalestier: Weak-link behavior of grain boundaries in superconducting Ba(Fe(1-x)Co(x))(2)As(2) bicrystals. *Applied Physics Letters* **95**, 212505 (2009).

165. R.F. Loane, P. Xu and J. Silcox: Incoherent imaging of zone axis crystals with ADF STEM. *Ultramicroscopy* **40**, 121 (1992).

166. A.C. Diebold, B. Foran, C. Kisielowski, D.A. Muller, S.J. Pennycook, E. Principe and S. Stemmer: Thin dielectric film thickness determination by advanced transmission electron microscopy. *Microsc. Microanal.* **9**, 493 (2003).

167. J. Tersoff and F.K. Legoues: Competing relaxation mechanisms in strained layers. *Phys. Rev. Lett.* **72**, 3570 (1994).

168. J.R. Clem: 2-Dimensional vortices in a stack of thin superconducting films - a model for high-temperature superconducting multilayers. *Phys. Rev. B* **43**, 7837 (1991).

169. C. Tsai, Y. Zhu, L. Chen and H. Wang: Flux pinning properties in YBCO thin films with self-aligned magnetic nanoparticles. *IEEE Trans. Appl. Supercond.* **21**, 2749 (2011).

170. F.C. Klaassen, G. Doornbos, J.M. Huijbregtse, R.C.F. van der Geest, B. Dam and R. Griessen: Vortex pinning by natural linear defects in thin films of YBa(2)Cu(3)O(7-delta). *Phys. Rev. B* **64**, (2001).

171. B. Dam, J.M. Huijbregtse, F.C. Klaassen, R.C.F. van der Geest, G. Doornbos, J.H. Rector, A.M. Testa, S. Freisem, J.C. Martinez, B. Stauble-Pumpin and R. Griessen: Origin of high critical currents in YBa2Cu3O7-delta superconducting thin films. *Nature* **399**, 439 (1999).

172. S.R. Foltyn, H. Wang, L. Civale, B. Maiorov and Q.X. Jia: The role of interfacial defects in enhancing the critical current density of YBa2Cu3O7-delta coatings. *Supercond. Sci. Technol.* **22**, (2009).

173. J. Wang, J.H. Kwon, J. Yoon, H. Wang, T.J. Haugan, F.J. Baca, N.A. Pierce and P.N. BarneS: Flux pinning in YBa(2)Cu(3)O(7-delta) thin film samples linked to stacking fault density. *Appl. Phys. Lett.* **92**, (2008).

174. H. Yamada, H. Yamasaki, K. Develos-Bagarinao, Y. Nakagawa, Y. Mawatari, J.C. Nie, H. Obara and S. Kosaka: Flux pinning centres correlated along the c-axis in PLD-YBCO films. *Supercond. Sci. Technol.* **17**, 58 (2004).

175. R. Ramesh, A. Inam, D.M. Hwang, T.S. Ravi, T. Sands, X.X. Xi, X.D. Wu, Q. Li, T. Venkatesan and R. Kilaas: The atomic-structure of growth interfaces in Y-Ba-Cu-O thin-films. *J. Mater. Res.* **6**, 2264 (1991).

176. L.E.C. Vandeleemput, P.J.M. Vanbentum, F. Driessen, J.W. Gerritsen, H. Vankempen, L.W.M. Schreurs and P. Bennema: Morphology and surface-topology of YBa2Cu3O7-x crystals - theory and STM observations. *J. Cryst. Growth* **98**, 551 (1989).

177. J.M. Huijbregtse, J.H. Rector and B. Dam: Effect of the two (100) SrTiO3 substrate terminations on the nucleation and growth of YBa2Cu3O7-delta thin films. *Physica C* **351**, 183 (2001).

178. S.J. Pennycook, M.F. Chisholm, D.E. Jesson, R. Feenstra, S. Zhu, X.Y. Zheng and D.J. Lowndes: Growth and relaxation mechanisms of YBa2Cu3O7-x films. *Physica C* **202**, 1 (1992).

179. R.Y. Guo, A.S. Bhalla, L.E. Cross and R. Roy: Surface crystallographic structure compatibility between substrates and high T(c) (YBCO) thin-films. *J. Mater. Res.* **9**, 1644 (1994).

180. C. Tsai, Y. Zhu, L. Chen and H. Wang: Correlation between flux pinning properties and interfacial defects in YBa2Cu3O7-delta/CeO2 multilayer thin films. *IEEE Trans. Appl. Supercond.* **21**, 2758 (2011).

181. F. Heidelbach, H.R. Wenk, R.E. Muenchausen, S. Foltyn, N. Nogar and A.D. Rollett: Textures of laser ablated superconducting thin-films of YBa2Cu3O7-delta as a function of deposition temperature. *J. Mater. Res.* **7**, 549 (1992).

182. J.G. Wen, C. Traeholt, H.W. Zandbergen, K. Joosse, E. Reuvekamp and H. Rogalla: A HREM study of the atomic-structure and the growth-mechanism at the YBa2Cu3O7 YSZ interface. *Physica C* **218**, 29 (1993).

183. J.G. Wen, C. Traeholt and H.W. Zandbergen: Stacking-sequence of YBa2Cu3O7 thin-film on SrTiO3 substrate. *Physica C* **205**, 354 (1993).

184. S.N. Basu, A.H. Carim and T.E. Mitchell: A TEM study of microstructures of YBa2Cu3O7-x thin-films deposited on LaAlO3 by laser ablation. *J. Mater. Res.* **6**, 1823 (1991).

185. C. Traeholt, J.G. Wen, V. Svetchnikov and H.W. Zandbergen: HREM study of the YBCO/MgO interface on an atomic-scale. *Physica C* **230**, 297 (1994).

186. X.Y. Zheng, D.H. Lowndes, S. Zhu, J.D. Budai and R.J. Warmack: Early stages of YBa2Cu3O7-delta epitaxial-growth on MgO and SrTiO3. *Phys. Rev. B* **45**, 7584 (1992).

187. H.W. Zandbergen, R. Gronsky, K. Wang and G. Thomas: Structure of (CuO)2 double-layers in superconducting YBa2Cu3O7. *Nature* **331**, 596 (1988).

188. P. Marsh, R.M. Fleming, M.L. Mandich, A.M. Desantolo, J. Kwo, M. Hong and L.J. Martinezmiranda: Crystal-structure of the 80-K superconductor YBA2CU4O8. *Nature* **334**, 141 (1988).

189. J. Karpinski, E. Kaldis, S. Rusiecki, E. Jilek, P. Fischer, P. Bordet, C. Chaillout, J. Chenavas, J.L. Hodeau and M. Marezio: 2 New bulk superconducting phases in the Y-Ba-Cu-O system - YBa2Cu3.5O7+x (Tc approximately 40-K) and YBa2Cu4O8+x (Tc approximately 80-K). *Journal of the Less-Common Metals* **150**, 129 (1989).

190. G. Van Tendeloo, H.W. Zandbergen, J. Vanlanduyt and S. Amelinckx: Electron-microscopy of high-tc superconductors. *Mater. Charact.* **27**, 59 (1991).

191. G. Van Tendeloo, T. Krekels and S. Amelinckx: A novel type of dislocation in YBA2CU3+XO7+X. *Philos. Mag. Lett.* **63**, 189 (1991).

192. A. Llordes, A. Palau, J. Gazquez, M. Coll, R. Vlad, A. Pomar, J. Arbiol, R. Guzman, S. Ye, V. Rouco, F. Sandiumenge, S. Ricart, T. Puig, M. Varela, D. Chateigner, J. Vanacken, J. Gutierrez, V. Moshchalkov, G. Deutscher, C. Magen and X. Obradors: Nanoscale strain-induced pair suppression as a vortex-pinning mechanism in high-temperature superconductors. *Nat. Mater.* **11**, 329 (2012).

193. K. Matsumoto and P. Mele: Artificial pinning center technology to enhance vortex pinning in YBCO coated conductors. *Supercond. Sci. Technol.* **23**, (2010).

194. D. Balzar, P.A. Ramakrishnan and A.M. Hermann: Defect-related lattice strain and the transition temperature in ferroelectric thin films. *Phys. Rev. B* **70**, 0921031 (2004).

195. E. Dagotto: Complexity in strongly correlated electronic systems. *Science* **309**, 257 (2005).

196. J.W. Reiner, F.J. Walker and C.H. Ahn: Materials science atomically engineered oxide interfaces. *Science* **323**, 1018 (2009).

197. K. Szot, W. Speier, G. Bihlmayer and R. Waser: Switching the electrical resistance of individual dislocations in single-crystalline SrTiO3. *Nat. Mater.* **5**, 312 (2006).

198. H. Li, A.L. Roytburd, S.P. Alpay, T.D. Tran, L. Salamanca-Riba and R. Ramesh: Dependence of dielectric properties on internal stresses in epitaxial barium strontium titanate thin films. *Appl. Phys. Lett.* **78**, 2354 (2001).

199. R. Escamilla, T. Akachi, R. Gomez, V. Marquina, M.L. Marquina and R. Ridaura: Suppression of T-c in the (Y0.9Ca0.1)Ba2Cu4-xFexO8 system. *Supercond. Sci. Technol.* **15**, 1074 (2002).

200. D.G. Schlom, L.Q. Chen, C.B. Eom, K.M. Rabe, S.K. Streiffer and J.M. Triscone: Strain tuning of ferroelectric thin films. *Ann. Rev. Mater. Res.* **37**, 589 (2007).

201. P. Casek, S. Bouette-Russo, F. Finocchi and C. Noguera: SrTiO3(001) thin films on MgO(001): A theoretical study. *Phys. Rev. B* **69**, 0854111 (2004).

202. C. Cheng, K. Kunc, G. Kresse and J. Hafner: SrTiO3/MgO(001) and MgO/SrTiO3(001) systems: Energetics and stresses. *Phys. Rev. B* **66**, 0854191 (2002).

203. F. Ernst: Metal-oxide interfaces. *Mater. Sci. Eng. R-Rep.* **14**, 97 (1995).

204. L. Fitting, S. Thiel, A. Schmehl, J. Mannhart and D.A. Muller: Subtleties in ADF imaging and spatially resolved EELS: A case study of low-angle twist boundaries in SrTiO3. *Ultramicroscopy* **106**, 1053 (2006).

205. Z.L. Zhang, W. Sigle and M. Ruhle: Atomic and electronic characterization of the a 100 dislocation core in SrTiO3. *Phys. Rev. B* **66**, 0941081 (2002).

206. A.M. Sanchez, J.G. Lozano, R. Garcia, M. Herrera, S. Ruffenach, O. Briot and D. Gonzalez: Strain mapping at the atomic scale in highly mismatched heterointerfaces. *Adv. Funct. Mater.* **17**, 2588 (2007).

207. Z.S. Dong and C.W. Zhao: Measurement of strain fields in an edge dislocation. *Physica B* **405**, 171 (2010).

208. M.J. Hytch, J.L. Putaux and J.M. Penisson: Measurement of the displacement field of dislocations to 0.03 angstrom by electron microscopy. *Nature* **423**, 270 (2003).

209. A.M. Sanchez, P.L. Galindo, S. Kret, M. Falke, R. Beanland and P.J. Goodhew: An approach to the systematic distortion correction in aberration-corrected HAADF images. *J. Microsc.-Oxf.* **221**, 1 (2006).

210. J.H. Chung, G.D. Lian and L. Rabenberg: Practical and reproducible mapping of strains in Si devices using geometric phase analysis of annular dark-field images from scanning transmission electron microscopy. *IEEE Electron Device Lett.* **31**, 854 (2010).

211. S. Cazottes, Z.L. Zhang, R. Daniel, J.S. Chawla, D. Gall and G. Dehm: Structural characterization of a Cu/MgO(001) interface using Cs-corrected HRTEM. *Thin Solid Films* **519**, 1662 (2010).

212. C.L. Jia, S.B. Mi, K. Urban, I. Vrejoiu, M. Alexe and D. Hesse: Effect of a single dislocation in a heterostructure layer on the local polarization of a ferroelectric layer. *Phys. Rev. Lett.* **102**, 1176011 (2009).

213. S.R.C. McMitchell, Y.Y. Tse, H. Bouyanfif, T.J. Jackson, I.P. Jones and M.J. Lancaster: Two-dimensional growth of SrTiO3 thin films on (001) MgO substrates using pulsed laser deposition and reflection high energy electron diffraction. *Appl. Phys. Lett.* **95**, 1741021 (2009).

214. D.C. Sayle and G.W. Watson: The atomistic structures of MgO/SrTiO3(001) and BaO/SrTiO3(001) using simulated amorphization and recrystallization. *J. Phys. Chem. B* **105**, 5506 (2001).

215. D.W. Kim, D.H. Kim, B.S. Kang, T.W. Noh, D.R. Lee and K.B. Lee: Roles of the first atomic layers in growth of SrTiO3 films on LaAlO3 substrates. *Appl. Phys. Lett.* **74**, 2176 (1999).

216. Y.Y. Tse, S.R.C. McMitchell, T.J. Jackson, I.P. Jones and A. Genc: Microstructural investigation of strontium titanate films grown by interval pulsed laser deposition (Electron Microscopy and Analysis Group Conference 2009, 2010)

217. F. Kirscht, B. Snegirev, P. Zaumseil, G. Kissinger, K. Takashima, P. Wildes and J. Hennessy: Lattice strain and defects in epitaxial silicon wafers, (Proceedings of the Electrochemical Society Symposium on Diagnostic Techniques for Semiconductor Materials and Devices, 1997).

218. S. Thiel, G. Hammerl, A. Schmehl, C.W. Schneider and J. Mannhart: Tunable quasi-two-dimensional electron gases in oxide heterostructures. *Science* **313**, 1942 (2006).

219. C. Cen, S. Thiel, G. Hammerl, C.W. Schneider, K.E. Andersen, C.S. Hellberg, J. Mannhart and J. Levy: Nanoscale control of an interfacial metal-insulator transition at room temperature. *Nat. Mater.* **7**, 298 (2008).

220. J.M. Harris, Y.F. Yan, P. Matl, N.P. Ong, P.W. Anderson, T. Kimura and K. Kitazawa: Violation of kohlers rule in the normal-state magnetoresistance of YBA2CU3O7-delta and LA2SRXCUO4. *Phys. Rev. Lett.* **75**, 1391 (1995).

221. K. Ueno, S. Nakamura, H. Shimotani, A. Ohtomo, N. Kimura, T. Nojima, H. Aoki, Y. Iwasa and M. Kawasaki: Electric-field-induced superconductivity in an insulator. *Nat. Mater.* **7**, 855 (2008).

222. W.J. Chang and T.D. Brown: Reliability of the CFTM and GPA methods for strain analysis at ultra-thin layers. *Micron* **42**, 392 (2011).

223. W. Zhou, W. Tang and K.M. Lau: A strain relief mode at interface of GaSb/GaAs grown by metalorganic chemical vapor deposition. *Appl. Phys. Lett.* **99**, (2011).

224. T. Kiguchi, K. Aoyagi, Y. Ehara, H. Funakubo, T. Yamada, N. Usami and T.J. Konno: Configuration and local elastic interaction of ferroelectric domains and misfit dislocation in PbTiO(3)/SrTiO(3) epitaxial thin films. *Sci. Technol. Adv. Mater.* **12**, (2011).

225. Y. Wang, P. Ruterana, L. Desplanque, S. El Kazzi and X. Wallart: Strain relief at the GaSb/GaAs interface versus substrate surface treatment and AlSb interlayers thickness. *J. Appl. Phys.* **109**, (2011).

226. S.H. Vajargah, M. Couillard, K. Cui, S.G. Tavakoli, B. Robinson, R.N. Kleiman, J.S. Preston and G.A. Botton: Strain relief and AlSb buffer layer morphology in GaSb heteroepitaxial films grown on Si as revealed by high-angle annular dark-field scanning transmission electron microscopy. *Appl. Phys. Lett.* **98**, (2011).

227. J.H. Chung and L. Rabenberg: Effects of strain gradients on strain measurements using geometrical phase analysis in the transmission electron microscope. *Ultramicroscopy* **108**, 1595 (2008).

228. H. Seitz, K. Ahlborn, M. Seibt and W. Schroter: Sensitivity limits of strain mapping procedures using high-resolution electron microscopy. *J. Microsc.-Oxf.* **190**, 184 (1998).

229. D. Diercks, G. Lian, J. Chung and M. Kaufman: Comparison of convergent beam electron diffraction and geometric phase analysis for strain measurement in a strained silicon device. *J. Microsc.*. **241**, 195 (2011).

230. R.E. Cohen: Origin of ferroelectricity in perovskite oxides. *Nature* **358**, 136 (1992).

231. Y. Zhu, C. Song, A.M. Minor and H. Wang: Cs-corrected STEM investigation of dislocation core configurations at a SrTiO3/MgO heterogeneous interface. *Microsc. Microanal.* **In press**, (2013).

232. Y. Mizuguchi, Y. Hara, K. Deguchi, S. Tsuda, T. Yamaguchi, K. Takeda, H. Kotegawa, H. Tou and Y. Takano: Anion height dependence of T(c) for the Fe-based superconductor. *Superconductor Science & Technology* **23**, 054013 (2010).